THESIS ON POWER ENGINEERING,
ELECTRICAL ENGINEERING, MINING ENGINEERING D55

Analysis and Development of Inductive Current Sensor for Power Line On-Line Measurements of Fast Transients

LAURI KÜTT

TUT PRESS

TALLINNA TEHNIKAÜLIKOOL
TALLINN UNIVERSITY OF TECHNOLOGY

Department of Fundamentals of Electrical Engineering and Electrical Machines

Dissertation was accepted for defence of the degree of Doctor of Philosophy on May 15, 2011.

Supervisor: Professor Jaan Järvik, Department of Department of Fundamentals of Electrical Engineering and Electric Machines, Tallinn University of Technology.

Opponents: Dr. Herwig Renner, Graz University of Technology, Austria

Dr. David Raisz, Budapest University of Technology and Economics, Hungary

Defence of the Thesis: June 15, 2012, 16:00, as part of: "12th International Symposium Topical Problems in the Field of Electrical and Power Engineering" and "Doctoral School of Energy and Geotechnology II", Kuressaare, Conference Center Hotel "Meri".

Authors declaration:

Hereby I declare that this Doctoral Thesis, my original investigation and achievement, submitted for the doctoral degree at Tallinn University of Technology, has not been submitted for any academic degree.

Lauri Kütt

May 15th, 2012

Copyright: Lauri Kütt, 2012

ISSN 1406-474X

ISBN 978-9949-23-301-4 (publication)

ISBN 978-9949-23-302-1 (PDF)

ENERGEETIKA. ELEKTROTEHNIKA. MÄENDUS D55

Induktiivse voolutajuri uurimine ja välja töötamine kiirete siirdeprotsesside mõõtmiseks elektrivõrgus

LAURI KÜTT

TTÜ KIRJASTUS

Contents

Contents 5
Symbol index 8
List of abbreviations 14
Acknowledgements 15
1 Introduction 17
1.1 Supply reliability and methods of diagnostics 17
1.2 Potential of on-line power line diagnostics 19
1.3 Fault locating principles using fault-initiated fast transients 23
1.4 Pre-fault condition detection 26
1.5 On-line monitoring system architecture overview 27
1.6 Sensors for fast transients on-line measurement 29
1.7 Air-core magnetic field sensors 30
1.8 State of the art and thesis objectives 31
1.9 Scientific contribution presented in the thesis 34
2 Fast transients in power networks 35
2.1 Measurement of fast transients 35
2.1.1 Partial discharge transient measurement 35
2.1.2 Fault transient waveform measurement 36
2.2 Frequency spectrum analysis of transient signals 37
2.2.1 Fast transient signal waveforms, windows of analysis and frequency spectrum 39
2.3 Digital low-pass filter characteristics 41
2.4 Bandwidth analysis 43
2.4.1 Partial discharge signal waveforms and analysis 44
2.4.2 Fault signal waveforms and analysis 46
2.4.3 Discussion 48
2.5 High-frequency transients' propagation on power lines 48
2.6 Pulsed signal measurement criteria 51
2.7 Summary of sensor operating bandwidth criteria 52
3 Air-core inductive sensor and its low-frequency model 53
3.1 Magnetic field around a wire 53
3.2 Magnetic flux and output of inductive loop sensor 54
3.3 Number of turns and mutual inductance 56
3.4 Summary 59
4 Medium-frequency model of air-core sensor 60
4.1 Components in medium-frequency model 60
4.1.1 Inductance of the sensor 61
4.1.2 Capacitance of the sensors 66
4.1.3 Coil wire resistance 70
4.1.4 Termination resistor 71
4.1.5 Measurement system 71

4.2 Sensor model as second order transfer function 73
4.2.1 Transfer function in Laplace domain 73
4.2.2 Calculation of the transfer function 74
4.2.3 Poles and zeros of the model 77
4.3 Characteristics of the sensor based on the transfer function analysis 78
4.3.1 Resonance and damping 79
4.3.2 Effect of poles and zeros on system behaviour 80
4.3.3 Damping and effect on bandwidth 83
4.4 Summary 86
5 Air-core sensor high-frequency model 87
5.1 Overview of high-frequency stray components 87
5.2 Skin effect 91
5.2.1 Analytical approach 91
5.2.2 Circuit representation 92
5.2.3 Skin effect on practical wires 95
5.2.4 Simulation results and conclusions 98
5.3 Terminating resistance properties 99
5.4 Effect of measurement system connection 102
5.5 Capacitance effects of the sensor coil 106
5.5.1 Capacitive coupling to wire 106
5.5.2 Shielding of the sensor 108
5.6 Transmission line effects of the sensor coil 115
5.7 Summary 118
6 Sensor design criteria and methods 119
6.1 Requirements for a sensor and design procedures 120
6.2 Sensor geometry design 121
6.3 Sensitivity of the sensor coil 122
6.4 Sensor electrical design based on determination of inductance 124
6.4.1 Inductance of multi-turn coil 124
6.4.2 Coil parameters selection 127
6.5 Sensor electrical design based on sensitivity criteria 130
6.6 Discussion 132
7 Verification of the sensor by laboratory measurements 133
7.1 Inductive sensor coil preparation and parameter identification 133
7.1.1 Construction of the sensor coil 133
7.1.2 Measurement of inductance, capacitance, wire resistance 134
7.1.3 Transfer plots sensors characteristic verification 135
7.2 Partial discharge transients measurement 137
7.2.1 Measurement set-up 137
7.2.2 Calibration of the sensor 140
7.2.3 Calibration of the high-voltage line measurements 142
7.2.4 Measurement of high-voltage partial discharges 146
7.3 Conclusions 147

8 Conclusions and discussion 148
8.1 Key results of the work 148
8.2 Future research and development 149
9 Abstract 151
References 154
10 Kokkuvõte 164
Author's publications 168
APPENDIX / LISA A. Curriculum Vitae 170
APPENDIX / LISA B. Elulookirjeldus 173
APPENDIX C. Dissertations Defended on Power Engineering, Electrical Engineering, Mining Engineering in Tallinn University of Technology

Symbol index

1. Units and constants

This thesis is written on base of SI-units. All formulas, calculations and measurement results have been presented only using SI-units and the derived SI-units.

List of constants used in this thesis

Symbol	Description	Value
μ_0	Magnetic permeability of free space	$4 \cdot \pi \cdot 10^{-7}$ H/m
ε_0	Dielectric permittivity of free space	$8{,}85 \cdot 10^{-12}$ F/m

2. General assignments

$u(t)$, u	voltage as function in time t
$i(t)$, i	current as function in time t
$U(s)$, U	voltage as function of complex Laplace variable s
Lower "$_D$"	marks discrete signals and characteristics, as in $x_D[n]$
(t)	specifies continuous function of variable "t"
$[n]$	specifies discrete function of variable "n"
A	area
e	electromotive force
f	frequency
H	magnetic field, scalar
h	height dimension, height
$\vec{H}$	magnetic field vector
k	count value
l	longitudinal dimension, length
L	inductance
M	mutual inductance
n	count value
$\vec{R}$	radius vector
r	radius
t	time
w	number of turns

3. Specific assignments

$\dot{B}$	time-differential of magnetic flux density
υ	is speed of wave propagation
Φ	magnetic flux
ρ	characteristic resistance of the wire
α	attenuation constant
$\Delta\varphi_{GD}$	phase shift due to group delay

$\mu_{a,air}$	absolute magnetic permittivity for air
Δf	DTFT spectrum frequency resolution
α_L	empirical skin effect inductance coefficient
ω_n	natural angular oscillating frequency
ω_{pn}	angular frequency of a n-th pole
α_R	empirical skin effect resistance coefficient
ε_r	relative dielectric permittivity
$\boldsymbol{A}$	normal vector of an area
A_{loop}	magnetic sensor loop area
A_w	cross-section area of the coil wire
$A_{w,eqv}$	effective area of the wire
$\boldsymbol{B}$	magnetic flux density vector
B	magnetic flux density, scalar
C'_S	sensor self-capacitance per unit length
C'_{Ss}	sensor-to-shield capacitance per unit length
C'_{TT}	coil turn-to-turn capacitance per unit length
C'_W -	cable capacitance per unit length
C_C	coil self-capacitance in general term
C_E	equivalent capacitance
C_{GE}	capacitive coupling of measurement system ground to real earth/common ground
C'_k	value of transmission path
C_{line}'	line-to-ground capacitance per line unit length
$C_{LS,T}$	per-turn line-to-shield capacitance
C_M	measurement device input capacitance
C_M	measurement circuitry input differential mode capacitance
C_{MD}	differential measurement input capacitance
C_{MG}	measurement device input common mode capacitance (towards ground)
C_{MG}	input capacitance to ground plain
C_{probe}	probe capacitance
C_S	sensor equivalent stray capacitance
$C_{S,M}$	is the combined capacitance of coil and measurement system
C_{Sdiff}	coil loading capacitance for differential mode
C_{Ss}	Sensor coil to shield capacitance
$C_{SS,T}$	per-turn shield-to-sensor capacitance
C_{SW}	capacitance between the sensor coil and the power line wire
C_T	terminating resistor stray capacitance
C_{tt}	is turn-to-turn capacitance
C_W	connecting wires or cables capacitance

C_W	measurement circuitry input connection wires stray capacitance
$\boldsymbol{D}$	denominator expression
d_C	coil total thickness
D'_k	value of transmission path cofactor
$d\boldsymbol{L}_k$	current vector element length
$d\boldsymbol{L}'_k$	dispositioned current element vector
e	electromotive force
E_{sig}	signal energy
$F(s)$	function of complex number s
f_{pk}	frequency of a pole
f_{res}	natural oscillating frequency
F_s	sampling frequency
f_{tresp}	resonant transient oscillation frequency
f_{zk}	frequency of a zero
G_D	group delay
G_L	conductance representing an inductance L value in Laplace domain
G_{line}'	line-to-ground conductance per line unit length
G_{Lt}	conductance representing an inductance L value in time domain
G_R	conductance representing a resistance R value in Laplace domain
G_{Rt}	conductance representing a resistance R value in time domain
$\boldsymbol{H}$	magnetic field intensity vector
$h_{\mu s}$	microstrip line height above ground plain
h_C	coil height
$h_{line,C}$	distance of power line from sensor coil
h_r	height to distance of circle
I	scalar current value
$i_{line,mag}$	magnitude value of current of a line being measured
$i_{line,RMS}$	RMS value of current in wire being measured by an inductive sensor
$I_{s(n)}$	current of a conducting cylinder, layer n
$i_{sh,l}$	left side shield current
$i_{sh,r}$	right side shield currents
j	complex operator
J	current density
$J(r)$	current density distribution function
K_L	is the correction function for inductance
K_S	sensor sensitivity factor
K_w	is the correction function for number of turns
L'_S	sensor self-inductance per unit length
l_C	coil length
L_{GE}	Inductance of the grounding wire connecting measurement system

	ground to real earth/common ground
l_{lfk}	is distance on power line from fault location to the substation
l_{line}	power line wire length
L_{line}'	line wire series inductance per line unit length
L_{loop}	inductance of a single-turn loop
$L_{Ring\,k}$	internal inductance of the rings in skin effect model
LR_{skin}	skin effect inductance ratio
L_S	sensor equivalent series inductance
$L_{S,T}$	winding inductance per turn value
L_W	measurement circuitry input connection wires stray inductance
l_W	length of connecting wires/cable
$l_{w,loop}$	length of wire in single loop
$l_{w,loop}$	length of wire of a single loop
L_{wDC}	is the wire self-inductance at DC
l_{wire}	coil winding wire total length
M	mutual inductance
M_{loop}	mutual inductance for a single loop
M_S	sensor coil to power line wire mutual inductance
$M_{S,T}$	per-turn mutual inductance
M_{TT}	mutual inductance between turns
N	count end value
$\boldsymbol{N}$	numerator expression
$\boldsymbol{P}^3$	poles' polynomial of 3rd degree
$\boldsymbol{P}_C$	poles' polynomial of sensor coil
$\boldsymbol{P}_{LC}$	poles' polynomial of *LC*-filter
p_m	equation system poles
p_w	winding by pitch
$\boldsymbol{R}_k$	radius vector
R'_{SSkin}	sensor skin resistance per unit length
R'_{wDC}	wire DC resistance value per unit length
r_C	coil radius
R_E	equivalent resistance
r_{line}	power line wire with radius
R_{line}'	line wire series inductance per line unit length
R_M	measurement device input resistance
RR_C	shape ratio of the sensor coil
$R_{Ring\,k}$	resistance on the ladder diagram
RR_{skin}	skin effect resistance ratio
R_S	sensor winding wire equivalent series resistance
$r_{s(n)}$	radius of a conducting cylinder, layer n

R_{skin}	skin effect resistance
$R_{SSkin,T}$	per-turn skin resistance
R_T	terminating resistor resistance value
r_w	wire radius
R_{wDC}	is the wire resistance at DC
s	Laplace complex operator $s = \sigma + j\omega$, where σ and ω – real values
s	complex number; $s = \sigma + j\omega$
$s_{\mu s}$	separation distance
s_{Ss}	separation distance
s_w	spacing between two wires
$TF(s)$	transfer function
t_s	duration of time of the sampled signal
U_{db}	voltage value in decibels
U_{in}	input voltage value
$U_{in,LC}$	input voltage of LC-filter
U_{out}	output voltage value
$u_{out,int}$	instantaneous voltage value of the integrator output
$U_{out,LC}$	output voltage of LC-filter
$u_{out,RMS}$	sensor voltage output RMS value
U_{ref}	reference voltage value
w	number of turns
w_{corr}	corrected number of turns
$X(s)$	input function
x_a, y_a, z_a	coordinates in observation point “a”
x_b, y_b, z_b	coordinates in observation point “b”
x_c, y_c, z_c	coordinates in observation point “c”
$X_D[k]$	k-th sample of discrete frequency spectrum X_D
$x_D[n]$	n-th sample of discrete signal x_D
x_k, y_k, z_k	coordinates in observation point “k”
Y	conductance
$Y(s)$	output function
Z^3	zeros’ polynomial of 3rd degree
Z_C	zeros’ polynomial of sensor coil
Z_{line}	characteristic impedance of the transmission line
z_n	are equation system zeros
Z_S	sensor impedance
Z_{S0}	wave impedance of the sensor coil
Z_{skin}	complex skin impedance
Z_{Sskin}	complex skin impedance
γ	propagation constant
$\delta_{\max}$	is defined by formula (5.2) as skin depth at the maximum frequency

	$f_{\max}$ the skin resistance is observed
$\Delta\varphi_{FD}$	filter characteristic phase shift
$\Delta\varphi_{OUT}$	filter phase shift
ξ	damping factor
σ	characteristic conductance of material
φ_i	angle between radius vector $\boldsymbol{R}_i$ and current element vector $d\boldsymbol{L}_i$

List of abbreviations

Abbrevation	Description
AC	Alternating current
Active RC-filter	Filter with operational amplifier component
B-dot sensor	Inductive magnetic field sensor consisting of a single wire loop
CT	Current transformer (with iron core)
DAC	Digital to analog converter
DC	Direct current
DTFT	Discrete time Fourier Transform
EHV	Extra-high voltage, voltage range 300 kV and beyond
EMF	Electromotive force
ESL	Equivalent series inductance
EU	European Union
FEM	Finite Element Method
FIR	Finite order digital filter
FPGA	Field programmable gate array
GIS	Geographic information system
HV	High voltage, voltage range 35 … 300 kV
HFCT	High frequency current transformer
LC circuit	Resonant circuit with inductive and capacitive components
LC-filter	Passive inductor-capacitor filter circuit
LRC circuit	Circuit with inductive, resistive and capacitive components
Matlab	Science and engineering programming environment software
MV	Medium voltage, voltage range 1 … 35 kV
PD	Partial discharge
RC-filter	Passive resistor-capacitor filter circuit
RMS	Root mean square
TDR	Time-domain reflectometry
TOA	Time of arrival
UHF	Ultra-high frequency
VT	Voltage transformer (with iron-core)

Acknowledgements

This work would have never been completed unless for the valuable and excellent support I have got during the doctoral studies and writing of the thesis. There are very many people to thank, so I please forgive me if I have missed some of you, nevertheless you still have my gratitude!

The greatest thanks have to be said to my supervisor prof. Jaan Järvik, for providing me the opportunity to carry out my doctoral studies, for the assistance and support during the studies and thesis work. Greatest thanks also go to prof. Matti Lehtonen from Aalto University, for providing me the opportunity to stay and carry out my studies in Aalto University, and providing me much insight to high-frequency diagnostics in power networks.

For the initiation of the topic to study and supporting my research on the practical side, I would like especially to thank Kalle Arulaane from Liewenthal Electronics, and ass. prof. Jako Kilter from Tallinn University of Technology (TUT). I would have not been able to make it so far without their contribution on showing me the practical role and possibilities ahead. For valuable discussions, I would like to thank ass. prof. Aleksander Kilk, prof. Kuno Janson, ass. prof. Rein Oidram and ass. prof. Toomas Ruuben from TUT.

For the direct effort to content of this thesis, I would like to specially thank Muhammad Shafiq from Aalto University for valuable discussions and measurements, some of the data presented in this thesis has been available through cooperation with him. Special thanks also to Heigo Mõlder, for because of him this thesis has 3D images and field simulation graphics. For the direct review and evaluation of the content of the thesis I would like to express thanks to my colleagues prof. Anouar Belachen and Tiiu Sakkos.

This thesis would not have been completed without support for measurement and laboratory access. Most effort in this was provided by Tatu Nieminen and Petri Hyvärinen in Aalto University. For the measurement support in TUT, I would like to thank Dmitri Vinnikov and Tanel Jalakas for their support on measurement equipment, and Raul Land for providing support on high-frequency measurements. Thanks go also to Rantelon Ltd, for providing a good tool for inductance and capacitance measurements.

Some of the excellent discussions have been provided to me by Estonian distribution network operator (EE Jaotusvõrk OÜ) thanks to Mart Haavik, and Helen Networks in Helsinki, thanks to Pirjo Heine.

Heaviest financial support of my doctoral thesis has been provided by TUT by Doctoral School of Energy- and Geotechnology II – project and Archimedes foundation with DoRa Programme (both of these are financed by the EU). I would like to express gratitude to Eesti Energia AS and Mati Jostov Foundation, for providing the scholarships through the TUT. Thanks also go to TUT Research and Development office for the support.

Finally I would like to express my greatest thanks to my family, for the support and encouragement throughout the years of my studies.

Lauri Kütt

This research was supported by European Social Fund's Studies and Internationalization Programme DoRa.

1 Introduction

1.1 Supply reliability and methods of diagnostics

Electric energy transmission system today is facing continuously growing challenges towards improving power quality and supply reliability for the customers. Requirements for avoiding loss of electric power supply are becoming stricter and even the smallest duration of unexpected outage is not tolerated. Power transmission system carrying electric power from, for example, power plant to the customer electric appliance is composed of vast number of components – there are generators, circuit breakers, wires, insulators and many more. Reliability of each of these components is essentially very high but the power network nevertheless can be extremely vulnerable – breakdown of even a single component can lead to outage lasting for days. Following component breakdown, the power is switched off immediately; if the power network operator is acting quickly, outage duration is only the time needed for finding damaged component and repairing it.

Every supply interruption brings with itself customer discontent and also economic losses. Amount of inconvenience to customers from private household to large enterprises is naturally in direct dependence of the fault duration. Faults in power network are major causes for the effects like voltage dips and transients in the power networks, which at first can be considered a milder compared to outage, but nevertheless can bring along significant damage. Economic effect due to fault events is quite enormous – the EU studies from 2008 [64] indicate that total loss due to power supply outages and bad power quality can be up to 0,15 trillions € annually for the EU countries, interruptions and voltage dips accounting for roughly 50% of total loss. This means that improvements of even fractions of percent could mean significant effect of overall economy and prevention of faults in this view is extremely important.

In terms of fault prevention, supply interruptions can be divided into two groups based on the possibilities to prevent their occurrence. First group are the unpredictable faults, such as ones caused by human intervention and natural phenomena, and mostly mechanical type electrical component failures (metal vague, overstress etc). These faults are highly unpredictable as they provide no electrical indication of possible problem before the fault occurs. Second group are most of the insulation breakdown faults that are one of the most common breakdown causes for the power network. Prior to complete breakdown these faults often present some electrical phenomena which can be detected. Typical insulation breakdown is indicated by miniature and fast discharge phenomena, called partial discharges. If such events were properly detected in advance, they could provide a location to repair before unexpected power outage could occur due to complete breakdown.

For both faults of predictable and unpredictable nature accurate fault locating presents an important aspect of keeping the fault duration low. There is much

improvement to be done in this field, as even at present level of technology the distribution networks are often not equipped with measurement devices capable of providing location of the fault to repair. Most common fault locating algorithms implemented are relying on complex analysis of strong post-fault short-circuit currents, but their accuracy and capabilities can depend on the types of fault. This means that locations of some types of faults are not resolved even with the fault locating equipment and still time-consuming manual operations are required for identifying the location of the problem. A solution to this would be addition of high-frequency transient analysis-based fault locating methods that take into account the immediate fault initiated transient, not relying of long-time fault occurrence.

Smart grid technologies and small scale renewable production units are most often using power electronics, incapable of surviving long-time fault currents, reaching above tens of times the normal operating values. Traditional solution to the short-circuit protection is often found in the inertia of the system and the fact, that the fault currents will commonly be present in the supply network at least some hundreds of microseconds later after the fault. Prior to the fault currents, the fault-initiated transients travelling close to speed of light have already reached the equipment, and these are usually not yet harmful. If a protection system would be capable of monitoring such events, significantly faster and effective protection functions could be implemented [101].

The partial discharge events as well fault initiated transients in power networks are therefore very important to keep an eye on, for providing the essential input for condition monitoring of the power network. The most successful way of improving power supply reliability would be to implement a constant monitoring of the events, as precise moment of neither fault nor partial discharge occurrence can be estimated. Term for this type of condition monitoring in power network is called on-line monitoring, capable of providing information about power lines state at any time.

Measurement of very fast transients (that the fault-initiated transients as well as partial discharge traces are) presents a major challenge for measurement equipment present in substations today. Namely, the measurement devices in substations have been designed for observation of the low-frequency phenomena, close to mains 50 (or 60) Hz frequency. Fault-initiated transients or traces of partial discharges on the other hand are very high frequency events, with frequency components reaching into tens and even hundreds of MHz. For such measurements some new measurement instruments are necessary. The power network diagnostics can be carried out with more accuracy, the more accurate the measurements are. Having a sensor that is capable of capturing high frequency transients is thus a key component for providing fast and correct power network state information.

1.2 Potential of on-line power line diagnostics

For identifying the potential benefits of added power network diagnostics, fault statistics of Estonian Distribution Network fault statistics from year of 2010 could be studied. This statistics provides information on the medium-voltage (MV) feeder switch-off events and also reflects the nature of Estonian distribution lines, as in the rural areas the MV power lines are most often overhead lines. In the urban areas most of the MV lines are cable lines and most of the customers of the distribution network are also in urban areas. In rural areas power lines tend to be quite long and run through rough terrain including forests, swamps and there are many faults due to factors of nature.

During 2010, there were total of 12 209 faults in Estonian distribution network MV feeders registered that lead to the complete power switch-off. The main events leading to the power outage have been described in Figure 1.1 with typical fault event description and symptoms described in Table 1.1.

Table 1.1. Most common faults on medium-voltage power lines and fault symptoms.

Fault event description	Typical fault symptoms
Ageing	Broken insulator and power line wire ties; broken insulators and wires; transformer faults; mostly involving old power lines.
Birds and animals	Trees on power lines due to beavers' activity; birds on insulators; wire breaking due to heavy birds landing; rodents on insulators and in substations.
Icing	Wires having excessive sag and shorting due to ice; broken wires due to mass of ice; broken old power line masts; trees leaning on power lines due to mass of snow and ice.
Lightning	Broken insulators, burnt wire when outage has occurred at the same time that there was a thunderstorm in the area.
Search for fault locations	Search for single-phase earth fault by switching off one line section and making a trial powering to observe, if the fault has passed or is still present.
Storm	Trees on power lines; broken wires and power line masts. Faults that are associated with higher than 15 m/s average wind speed in the area.
Trees on power lines	Trees falling or leaning on power lines, both storm and non-storm weather related.
Unknown	Fault due to unknown reason.

It can be seen that if the fault count is observed, over 50% of switch-off are caused by trees on power lines, lightning and unknown reasons. In Estonia there are many overhead lines passing through forests, so trees on power lines are quite common type of faults. Although the line passage required for keeping clean is 10 meters

(by government regulation [88]), the trees can taller than that and falling of trees on the power line is therefore still very likely.

Another view can be taken on the fault duration of different types of faults, presented in Figure 1.2. This picture is different compared to the event count statistics, as the duration for repairing the fault will be dependent of various non-trivial factors. The total duration of supply interruption was over 54 000 hours.

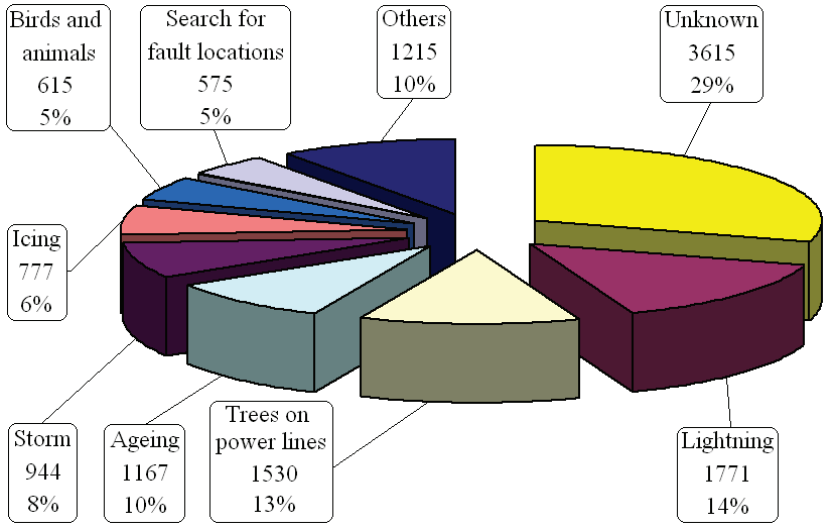

Figure 1.1. Overview of event count statistics.

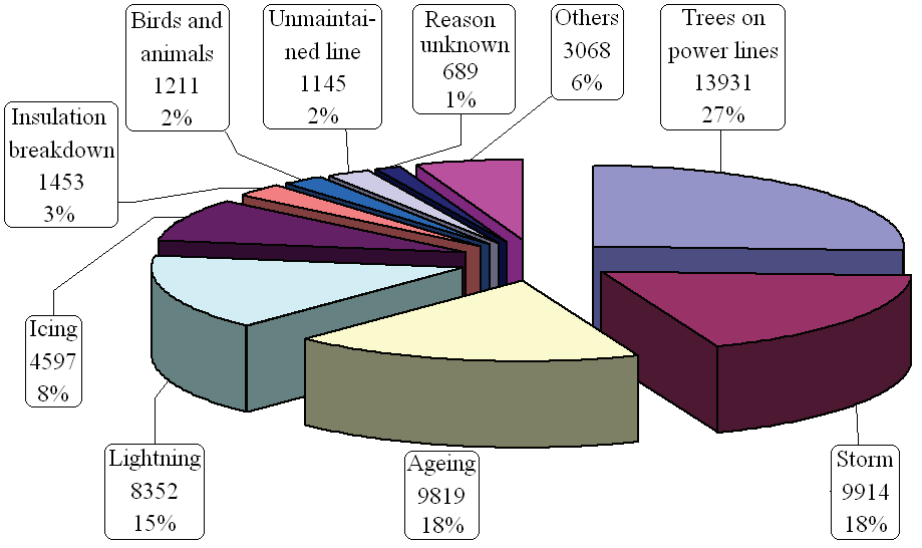

Figure 1.2. Fault duration statistics for different fault types (duration presented in hours).

It should be pointed out that trees on power lines, storm and lightning are accounting for 60% of the total outage duration. Main reason for that is that when there is a major storm, all the repair crews are usually rather busy for weeks. Response time to a single fault is then rather long and can reach up to one week. When there is a tree on the power line, it is often difficult to determine its location and searching for the fault location alone can require several hours. Reason for ageing faults high duration is for example problems with older cables where cable sleeves have had problems and their repair is time-consuming. It should be pointed out that unknown fault events provide only 1% of fault duration while the unknown switch-off event count was 29% of all the faults. Reason for this is that the unknown faults are mostly momentary, disappearing after the initial switch-off and after automatic switch-on the fault is no longer seen. Still they provide much stress to the customer, who has to suffer unexpected short-time outage but it also causes voltage sags for all the customers of the same substation.

Moving to the more potential field of usage of on-line monitoring technologies, the substation overall fault count for the year 2010 could be observed on Figure 1.3. This diagram presents the count of different feeders that had a particular number of outages during the year. While outage count of 1...3 very likely indicates some random events on the power line, 5 and more outages for the year indicate some systematic problems with the power line and equipment condition. Number of such feeders in this condition is 605, which is quite high count.

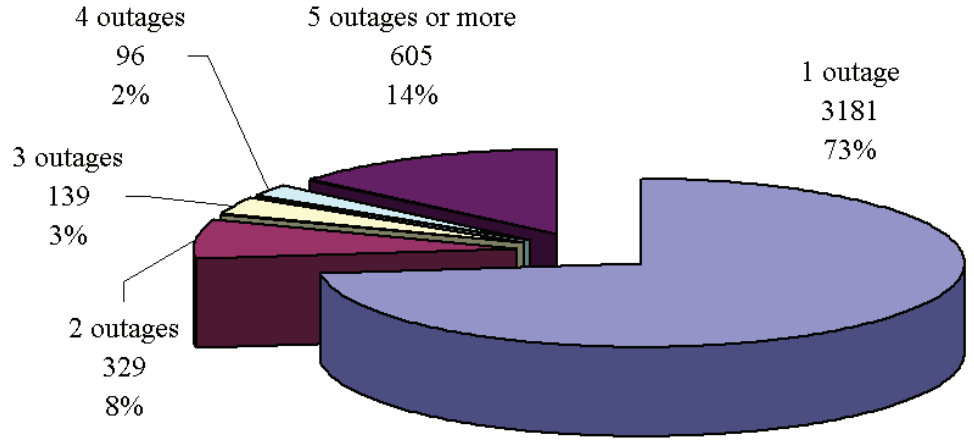

Figure 1.3. Feeder overall fault count per year 2010.

The fault count statistics for the feeders with 5 or more outages in 2010 is presented in Figure 1.4. It can be observed that the number of faults with unknown duration is 3024, which is 83% of all the unknown faults in the feeders (referring to statistics in Figure 1.1).

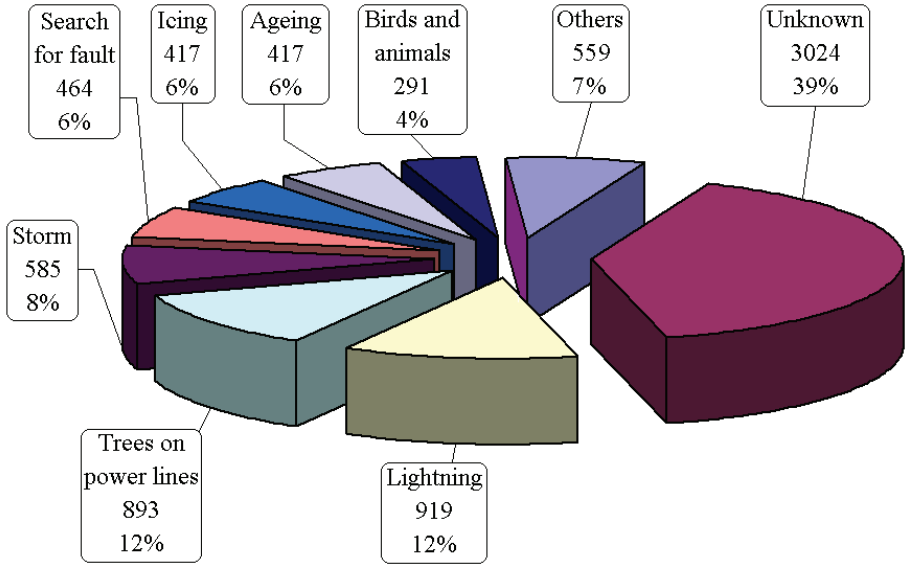

Figure 1.4. Event count statistics for feeders with 5 or more faults in 2010.

One other reason for switch-off is also search for fault location, which was also performed for over 80% of the feeders presented. The fault duration statistics presented in Figure 1.5 indicate, that most of fault outage time is still due to trees on power lines, storms and lightning. Unknown faults account only for 1% of the total outage time, so in statistics of undelivered power and customers not served this makes up only an unrecognizably small part of overall statistics.

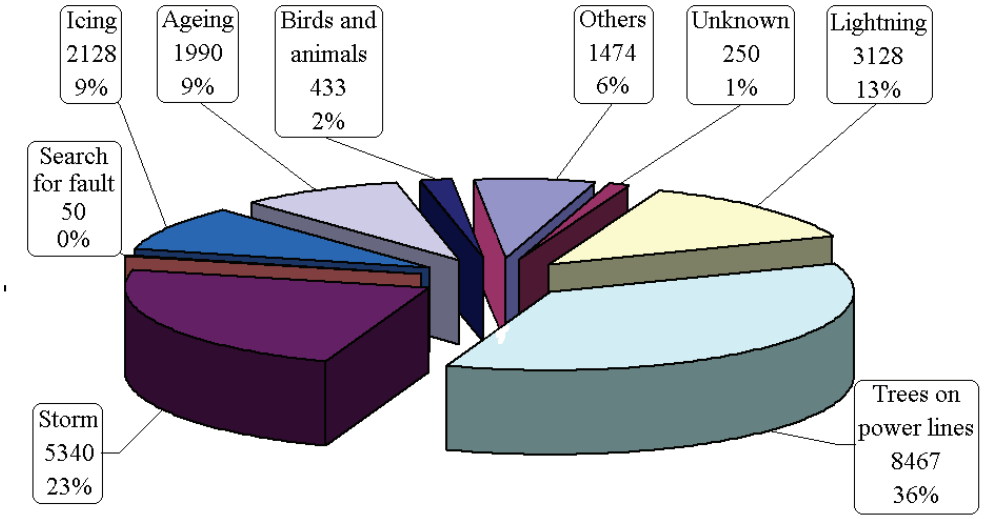

Figure 1.5. Event duration statistics for feeders with 5 or more faults in 2010.

If the fault is not present after the initial switch-off and automatic repowering, it makes the fault extremely difficult to find and repair. However, this does not mean that the fault will not be present again. The potential of on-line monitoring system can be especially stressed out for the feeders with many unknown faults, as detecting the type of fault and determining its location are very important for eliminating such faults.

The faults that are momentary due to non-random problem usually evolve into more serious faults, which eventually still lead to longer power outage. For example, there could be a tree in the forest, bending more and more on the power lines. Some random momentary short-circuits could burn some smaller branches but the tree is still there, bending more on the power lines. Soon much of the tree will be leaning on the power lines and may cause breaking of power line wires, power line poles etc. that are much more difficult, time-consuming and expensive to fix. Locating such faults in advance gives not only relief on the power quality aspects, but also can save a lot of resources.

Applying the on-line monitoring system does not mean that the faults will be completely eliminated. However, it is very likely that very many of the previously unknown faults will have a reason and repair before evolving into more severe problems. Also, an on-line monitoring system equipped with fault locating functionality can provide information about the problem location and thus reduce the outage times significantly. This could be very beneficial also during storms, where there are highly many faults in the network and responding to the faults depends on the fact if there is some information about problematic location.

1.3 Fault locating principles using fault-initiated fast transients

The fault initiated transients originate from the fast drop of voltage in the location of the fault. Rate of voltage variation in the location of the transient can reach into hundreds of kilo-volts per microsecond, with the whole voltage drop event lasting even less than a microsecond. The voltage drop will cause charge movement from the power line wire to the place of the fault, creating a sharp current waveform on the power line wire. Combination of voltage and current waveform has rather good propagation properties as it inhibits properties of an electromagnetic wave moving on a transmission line. The speed for propagation of such electromagnetic travelling wave is determined by the permeability and permittivity of the medium of the transmission line, also equal to the speed of light at that specific medium. For an overhead power line, for example, the propagation speed of such wave is close to $3 \cdot 10^8$ m/s.

The A-type [16] travelling wave fault locating uses the travelling wave reflection from a place of impedance discontinuity, such that are for example, substation busbars and fault location itself. Travelling time from one location to another is quite significant on power lines, and the polarity of the wave changes with every

reflection (see Figure 1.6). This causes a signal to appear if measured at substation, resembling a periodic oscillation, with frequency of this process providing information about the fault location [35]. This method is usable for high-voltage, point-to-point lines, but usually not for distribution lines. Reason for the latter is the large number of points where the wave could be reflected from.

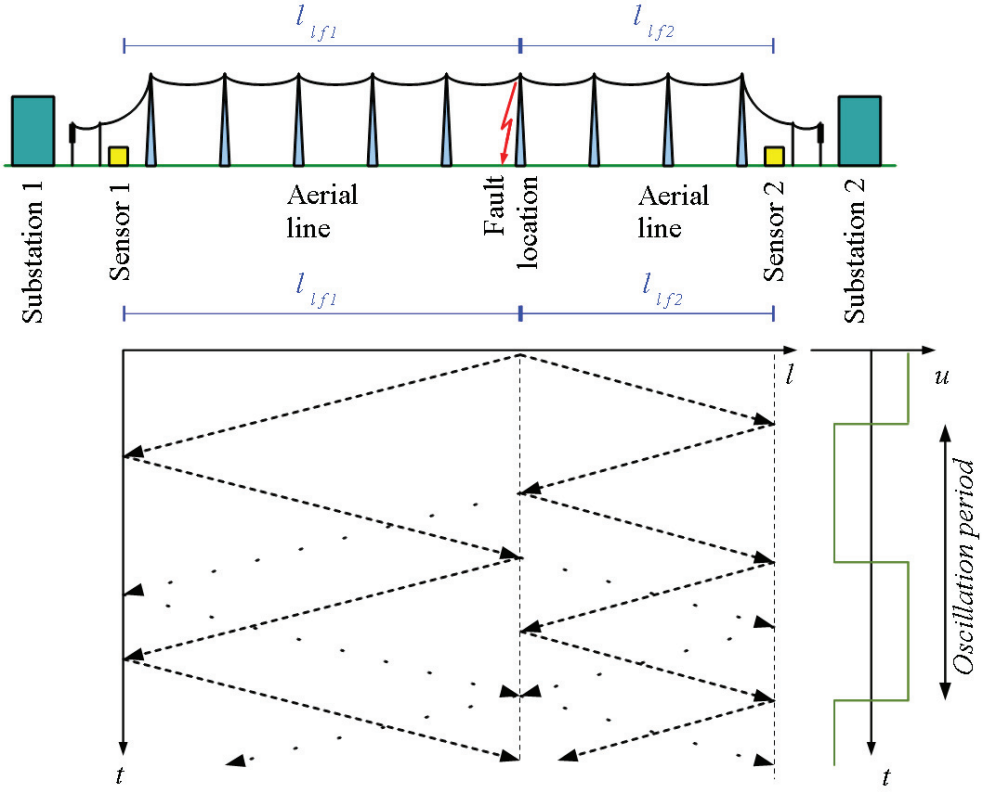

Figure 1.6. Overview if the A-type travelling wave fault locating principles.

As an example of A-type fault locating method using travelling waves in Figure 1.6, result of voltage measurement has been provided from substation "2". The time for the wave to travel from fault location is

$$t_2 = \frac{l_{lf2}}{\upsilon}, \tag{1.1}$$

where υ is speed of wave propagation, l_{lf2} is distance on power line from fault location to the substation.

The reflections in the substation occur at times t_2, $3t_2$, $5t_2$, $7t_2$ etc., as the wave has to travel to the fault location and back before the next reflection. Observing the period between the two reflections will provide an indication of the fault location.

There are rather many complexities for the usage of A-type for the distribution networks [72] including multiple branches and discontinuities, every one of which is causing reflections in addition to the fault location and substation. Eventually, this will render the reflections from the fault and substation to disappear in noise from other reflections on the line.

More suitable for the distribution networks is the D-type principle [123], which uses observation for travelling wave at two ends of the power line with fault in the middle (see Figure 1.7). The time of arrival for such a travelling wave is determined by distance of measurement site from fault location, arrival of fault initiated transient to substations "1" and "2" occur at time of (1.1)

$$t_1 = \frac{l_{lf1}}{\upsilon},$$

$$t_2 = \frac{l_{lf2}}{\upsilon}$$

after the fault event.

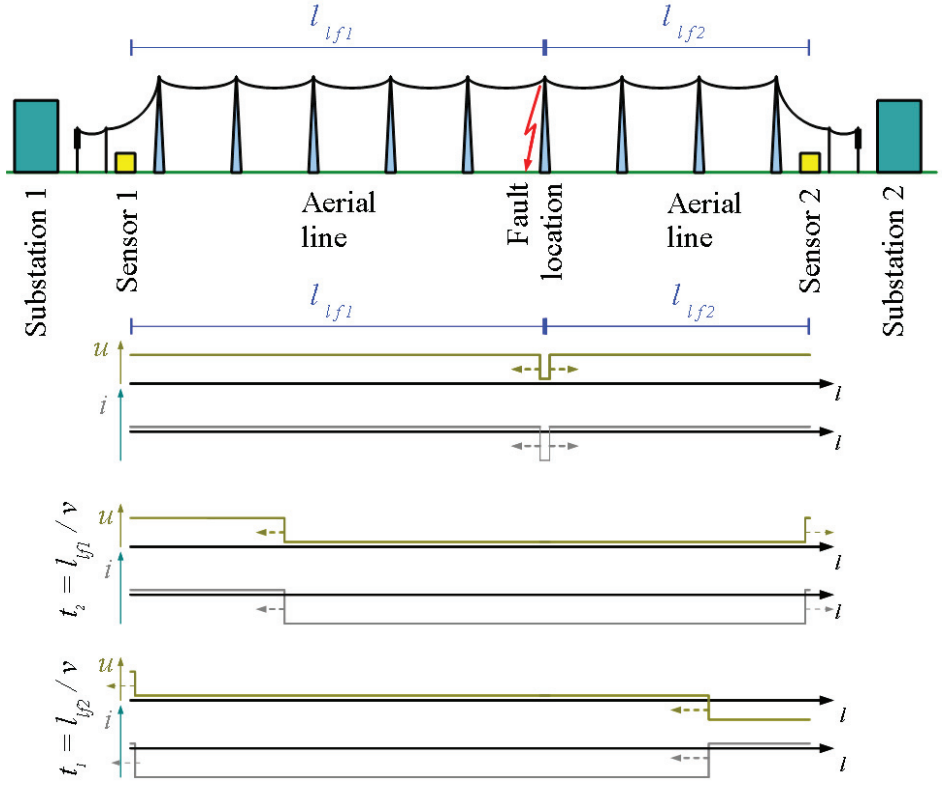

Figure 1.7. Overview if the D-type travelling wave fault locating principles.

If time in two measurement locations is synchronized, line length is known and the difference of time of arrival is observed, the fault locating can be very precise. This is described by formula [25]

$$l_{lf2} = \left(\frac{t_2 - t_1}{2} \right) \cdot \upsilon + \frac{l_{lf1} + l_{lf2}}{2}, \tag{1.2}$$

where $l_{lf1} + l_{lf2}$ is the line length.

There are several limitations that can harm the travelling wave measurement outcome and correct estimation of time of arrival (TOA) [16] [123]. Usually the distribution networks have a topology with highly many branches and connections, causing reflections proprietary to the electromagnetic travelling waves. This can weaken the transient signal itself; distort the waveform edge shape and many more. The overhead line and ground do not form a perfect medium for the travelling wave, causing also distortions to the travelling wave. These and many more effects make the TOA measurement rather complex, if all the effects are taken into account for more accurate results. Accurate measurements for waveform edge shape restoration are essential for this purpose. Research done indicates rather successful results on HV transmission lines measured with bandwidth range of 500 kHz [123], 625 kHz [34] [105], 1 MHz [123] and 5 MHz [60], while for use in distribution networks the bandwidth of 500 kHz [12] [76], 625 kHz [112] and over 10 MHz has been indicated [24] [81].

1.4 Pre-fault condition detection

The partial discharge (PD) is actually a miniature electrical breakdown phenomenon, presenting a dielectric overstress, limited to only very local range and limited charge. Such events are common, for example, when there is presence of impurities or voids in the dielectric material. Partial discharges are present at all voltage levels, but with higher voltages the dielectric stress is higher and the partial discharge phenomenon therefore more intense.

Due to aging but also manufacturing impurities, the dielectric insulation material will have various defects including cracks, voids etc. There are several types of PD occurring due to insulation damage, most common types present on a cable assembly are sliding discharge, floating discharge, cavity discharge and protrusion discharge [11]. Every type of discharge produces its characteristic patterns [78] [14] and intensity. Partial discharge is good for diagnostics of power lines with covered overhead conductors, for example trees leaning on the power line can provide quite intense PD activity [43].

The partial discharge phenomena holds some energy, and the energy released in the dielectric material would cause further deterioration. Water treeing [32] is one example of PD effects, damaging the insulation in time until the complete breakdown. As the material is suffering more damage and more defects, the intensity of partial discharges increases until it develops into electric arc, damaging the

insulation permanently. The sign of soon-to-happen breakdown is therefore a PD occurrence with growing intensity. It is interesting to note from research that the PD intensity will grow as defects elaborate; however there will be a drop of intensity before the final breakdown [78]. This assures that accurate measurement and monitoring is one of very essential aspects to determine the soon-to-happen breakdown signature. While the PD activity can be measured form a very low intensity, the PD indicating danger to the insulation would be quite strong. Still, the PD even duration remains usually in less than some microseconds, with weaker PD having shorter duration. This indicates the need for a very fast monitoring and measurement system.

In the literature, there is some information available about the required bandwidth for measurements of PD produced transients. The estimations on the most suitable bandwidth for the partial discharge measurements start from 20 MHz [57]. In [106] the estimations for the required bandwidth propose limits over 35 MHz, analysis has been based on basis of real signal observations and spectral analysis. An analysis of frequency spectrum of PD calibration pulses [95] but also more practical tests [7] presents that main content of the PD pulse would remain below 60 MHz. Also a suitable bandwidth of 100 MHz is indicated [92] [102], but without references to practical measurements. Theoretical approach to measurement bandwidth presents that as the bandwidth of the measurement equipment increases, weaker PD signal traces can be monitored for example 1 MHz would adequate for 0,1 pC detection, while with 350 MHz the limit will be down to nearly 0,01 pC [13]. Due to very high frequencies there are also examples of UHF RF measurements [8] [51] with results of traces of PD at several hundred MHz.

Although there is material available on the bandwidth for measurement, there is still lack of sources describing the effect of bandwidth for the measurement accuracy. The effect of bandwidth on the measurement accuracy of both PD as well as fault-initiated transients will be discussed further in this thesis.

1.5 On-line monitoring system architecture overview

A proposed power line on-line monitoring system (Figure 1.8) would consist of following functional blocks:

1) sensor unit for accurate measurements of the transients on the power line;
2) signal processing unit necessary to perform analysis of the transient recorded;
3) diagnostics algorithm processing unit for making decisions on the power line status based on conclusions from transient latest recordings or from event database;

4) communication with other devices in order to provide reference input from or output to other devices for the ability of performing more complex analysis.

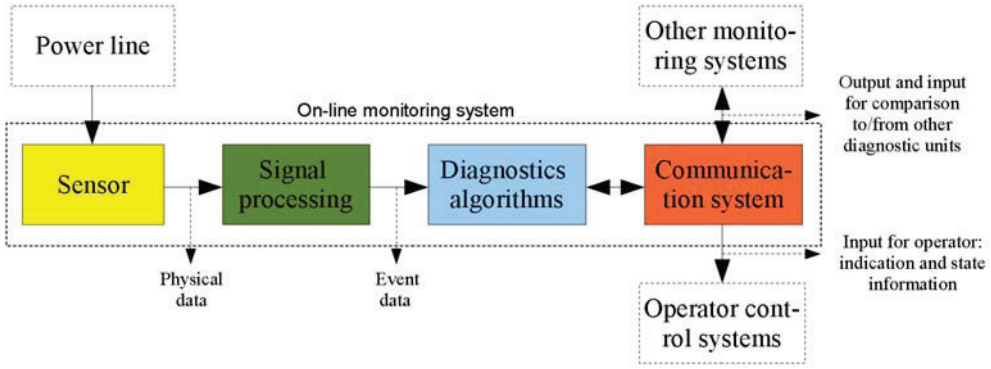

Figure 1.8. Overview of the on-line power line monitoring system structure.

Starting from the last one, communication is needed for indicating the network status to the operator, but also communication form other units can increase the accuracy of the diagnosis. For example, this is the case, when a diagnostics unit is measuring and operating on the one end of the power line, but the information is shared also with the diagnostics device that is measuring and operating on the other end of power line. Communication is also required towards an interface to indicate the network status on an operator's GIS (Geographic Information System) software user interface.

Diagnostics algorithms are required to observe the output of the signal processing unit and determine the state of the power system by the statistical or preset level data. For example, the state of cable health, as described above, can be identified by observing the PD intensity over a longer time period. This requires data storage and some database processing power. For fault locating, there is a need to analyze the time of arrival of the travelling waves and provide a decision on the fault geographical location.

Signal processing is needed for the essential conversion and conditioning of the signal obtained from high-frequency sensor, with the target to convert the signal into different type of information about transient event origin (PD / fault initiated / disturbance), quantity (PD intensity) etc. Such functionality includes amplification of the output of the sensor measuring the high-frequency transients, filtering, conversion and digital signal processing features. Signal processing functionality should be able to detect the event of PD or fault on a power line, qualify it and quantize it. These actions require very fast operations and the systems built with it could be based on, for example, FPGAs offering very fast parallel processing capabilities [24].

Sensor should be able to provide the electric output to the signal processing unit with such rate and precision that the parts of transient with most valuable for

diagnostics (transient waveform edges, waveform overall shape and transient energy estimation) would be captured intact. This means that the sensor should have enough bandwidth and sensitivity to capture the short PD events and /or fault initiated transients. The measurement sensor has a critical role in the diagnostics system, as the output of units using sensor data can not be more accurate than the sensor itself.

The equipment and systems in power distribution substations today is by many criteria not suitable for providing the required functionality, such as

- most accurate measurements are carried out at mains frequencies, conventional current and voltage transformers are not capable of high-frequency transient measurements;
- signal processing systems and analog inputs are targeted for bandwidth up to 10 kHz;
- relay protection systems do not provide capabilities necessary for using comprehensive event database and rely on rather strong signals' processing.

This means that the on-line monitoring system device would have to be a separate device to reach its potential, not so much a new feature to the already existing relay protection hardware. Of course, functionalities of on-line monitoring can be included in the relay protection systems, but very likely the hardware would have to see significant changes. In this thesis the on-line measurements are observed as being independent from the requirements for the relay protection class devices.

1.6 Sensors for fast transients on-line measurement

The electromagnetic travelling wave, carrying the transient, has always two quantities involved – voltage and current. For diagnostics, there are options to use either the voltage measurements, current measurements, or both.

Fast measurement of voltage can be achieved via capacitive coupling to the power line wire. Some sensors available [81] provide quite compact form, including a capacitive divider and providing bandwidth up to 100 MHz. There are also capacitive voltage transformers for extra-high voltage (EHV) lines, capable of reaching bandwidths above 500 kHz [36], which still is quite insufficient for capturing the high-frequency transients. For the uncoupled method of transient voltage measurement there are some quite expensive sensor technologies available, employing optical influences of electric field on light including Kerr effect [37] and Pockels effect [38].

For current measurements there are several options available. One of the simplest and common ones is to use a shunt resistor connected in series on the power line being measured, which then provides a voltage signal proportional to the current measured, however this is rather expensive for high-voltage applications. It is usual

that in substations feeder currents are measured using different voltage transformers. Conventional substation equipment is using iron-core inductive transformers, which have relatively low bandwidth, usually less than 100 kHz. For wider bandwidth measurements several other solutions are available. Devices based on Hall-effect are making their way into high-voltage measurement systems [74]. Hall-effect is feasible as it allows miniature sensors with rather good performance, but they are rather expensive in high-voltage applications. Air-core [117] and also ferrite core [110] Rogowski coils are identified as having very good performance at ranges above 1 MHz frequencies. At the same time, the Rogowski coils are appreciated for their small price. Using a simpler magnetic sensor [97] has also been proposed for high-speed current transient current measurements. Good side of the Hall effect and inductive current sensors is that the current measurement is provided while being uncoupled from the power line. There are also high-frequency current transformers (HFCT) with bandwidth up to hundred MHz, however these are extremely expensive and usually applied in scientific measurements only.

For measurement on EHV lines, for providing isolation and excellent decoupling from high voltage, an optical signal and power links can be used [5]. Another way would be to use a totally decoupled design of monitoring and measurement system, mounted on a power line wire and communicating by radio channel [29]. Fully optical effect current sensors are used in EHV measurements, employing measurement of Faraday effect to determine the current value [28]. The optical transducers once again are more expensive, as they require precise lasers for providing accurate measurements.

In summary, there is a quite large variety of sensing technologies available that would be able to provide means for measuring the high-frequency transients. In practice there would be many aspects to consider for selecting the best technology. The common aspects evaluated in practical applications are functionality, robustness, reliability, ease of maintenance and installation, precision and of course, price. For fulfilling these conditions, the air-core inductive sensors would have to be promoted and in this thesis the air-core inductive sensors are observed.

1.7 Air-core magnetic field sensors

There is a proverb in Estonian – "A good child has many names" – and this certainly applies to the air-core magnetic sensors. *B-dot sensor*, *I-dot sensor*, *electrically short loop antenna*, *Rogowski coil* – these are the most common names found in literature, although with some differences. The pure B-dot sensor is considered a single-turn magnetic loop, and its name is originating from time-differential marking with a dot on B (magnetic flux) if Faraday's law is observed

$$e = -M \cdot \frac{dB}{dT} = -M \cdot \dot{B} \tag{1.3}$$

A name also used for a single-turn loop is *electrically short loop antenna* [54]. Sensors having multiple turns are just named multiturn B-dot sensor [20]. In other

case, the Rogowski coil (also specified as I-dot sensor) can also be represented as series of B-dot sensors mounted around a wire being measured in a circular position [71] [89]. The naming issue is such, that there is no perfect name for the sensor, so in this thesis the multi-turn sensor is just called the inductive current sensor.

Best features of air-core inductive sensors are listed as high linearity, lack of saturation effects, high bandwidth, accuracy but also being lightweight [117] [118]. Range of applications in power systems where the inductive sensors have significant benefits compared to iron core current transformers include current transformer calibration, protection of the power system [17] [118], measurement of high-voltage inverters [109], lightning current measurements [27], partial discharge measurements [50] and many more. The air-core magnetic field sensors have even been referred as unsuitable for precise measurements at mains frequency due to sensitivity to external high-frequency interference although with careful shielding such problems are indicated as insignificant [84]. For current measurements, the magnetic field sensors are much more convenient and flexible [116], for example, than shunts. Flexibility can be added to Rogowski coil by split-core design [5] and with flexible former [87] [117], allowing convenient mounting on the wire and in tight places. The application of fast transients' measurement for the power systems is considered perfectly suitable for air-core sensors (especially Rogowski type) [21] [22] [108]. For measurement of partial discharges, examples of a B-dot sensor are also available [92].

1.8 State of the art and thesis objectives

Many researchers have described the operation of an air-core inductive current sensor for the measurement of high-speed transients on power lines. The challenge is to combine the insulation requirements of the HV applications and high-speed response of the sensor. Different effects of the sensor behaviour have been studied using different models and approach. It has to be said that results presented in publications are rather good, presenting the potential of the inductive sensors.

The high-frequency operation of the induction sensors has been considered in different levels. In simplest division, there are transmission line and lumped model approaches, which both are presented as the solution to describe the sensor behaviour.

Most commonly found transmission line approach applies particularly for the Rogowski coils, [71] [86] describing the sensor coil as a series of winding turns, each having a part of the coil overall inductance, combined with coil self-capacitance presented as series turn-to-turn capacitance. There is only one occasion of model presented with a capacitive coupling between line and sensor [45]. The transmission line model has been observed for various influences, including effect of placement toward the wire [39] [65] [86] for Rogowski coil.

It could be noted, that some papers are presented in a mixed style, observing some characteristics from transmission line model and other from the lumped circuit model [45] [86] [108]. However as such models are not presented derived or dependent from each other, it would be a reason to suspect that the approach taken would actually be insufficient to describe the high-frequency operation completely.

Lumped model approaches [10] [11] [45] [58] [62] [92] [108] use an inductive sensor coil model, presented with mutual induction coupling as a source, total coil inductance, total coil self-capacitance and wire resistance. This can be added passive integration component as termination resistor [114], passive integration with *RC*-filter [18] and active integration component as active *RC*-filter [85] or combination of all of the aforementioned ones [10] [45] [125]. The output active integration is specifically important for the measurements at low-frequency [58] [116], as the current variation rate is very small and the output voltage is also extremely low. Complex behaviour of such electric circuits has been presented as the time-domain [114] differential equation based or frequency domain transfer function based [10] models. The terminating resistor has a determining role in defining the bandwidth as well as response [55], the self-integration region being also defined by the coil terminating resistor value [10] gathers lot of attention from investigators. An approach explaining the effect of adding the low-value terminating resistor to the inductive sensor is that it makes its operation comparable to true current transformer [116].

There is also controversy to be pointed out from the inductive sensor measurement methods, which in scientific sense are likely not able to provide accurate results in high frequency operation. One of the common ones is the connection of sensor to the input of oscilloscope (should have input impedance of $Z_{in} = 50$ ohm) [86]. It should be noted that when the wire connecting to oscilloscope is short, it will most probably act as loading capacitance, which will undoubtedly affect the results. Although measurement loading of the sensor coil is not presented in various papers [6], it should be considered one of the key influences to the measurement results.

Literature sources describing the high-frequency operation are inconsistent also on their targets. In several cases, authors observe the resonant behaviour of the sensor, neglecting the measurement integrity and phase response [86] [92] [94]. In case of time-domain analysis using differential equations, the full response characteristics of the sensor coil are typically not presented [26] [80] [114]. It could be suspected that most authors would target measurement of some pulsed phenomenon (many have identified their intent to measure for example partial discharge (PD) pulses. For such measurements however, phase and amplitude plot required states are not observed by most authors at all. The self-integration operation mode range [10] [113] that is presented as the operating bandwidth is observed most commonly as stable magnitude response range [19] [122]. There are usually only little remarks about the phase response [6] [55] [109] to the measurement results, the stable phase plot is practically not targeted by the researchers. One approach taken is also a simulation-based determination of terminating resistor resistance value [71].

Determination of the sensor coil parameters value is discussed at range of different levels. The sensor self-capacitance is investigated for the Rogowski coil type sensor, using models of coaxial cable [93]. The sensor-to-wire capacitance is presented in [45] as model of wire above ground, which in calculations is not accurate at all. For power electronics measurements with relatively low voltages present, the effect of capacitive coupling is very small and this is suggested to be insignificant even to equip the sensor with shielding [87].

In [6] a Rogowski air-core sensor is presented with self-integrating bandwidth from 1 to 770 MHz, which on the other hand could be considered a bit too high operation for the inductive sensor. A self-integrating magnetic loop for high-frequency pulse measurement has been presented in [96] with operating frequency range starting from 800 kHz (while upper frequency has not been described), with sensitivity of 0,235 V/A. For lightning current measurements, an air-core self-integrating sensor has been described having bandwidth from 783 Hz to 25,3 MHz, but the wide bandwidth has also a set-back as the sensor has a rather low sensitivity of 0,0322 V/kA [20] (due to value of lightning currents, this could be acceptable for the application). One of the best cases for the measurement of high-frequency transients is actually not air-core coil, but a ferrite core sensor with bandwidth ranging from 800 kHz to 106 MHz [110] and from 232 to 120 MHz [107] with sensitivity indicated at 2,22 V/A. Same authors have also proposed a sensor with bandwidth from 296 kHz to 120 MHz, with sensitivity even higher, at 3,27 V/A (also with ferrite core) [111]. The stability of the phase response graph indicated is however of question, as it is said to be varying less than 1,5 degrees. Later in this thesis it can be seen, that this is even theoretically very difficult to achieve.

In literature available today aspects of the high-frequency measurements of inductive sensors have not been fully resolved. There are several controversies in the research results and also the approaches defining the sensor coil operation at high frequencies are a matter of dispute. In order to shed light on the matters, intention of this thesis is to provide some organization of the phenomena associated with the inductive sensor operation and present a design of an inductive sensor capable of carrying out the high-frequency transients' measurements in power systems. In more detail, the main objectives of this thesis can be listed as:

1) to identify the bandwidth limits required for carrying out accurate fast transients measurements;
2) to identify and present effects of key elements defining the operation of an inductive sensor for the design of an inductive sensor;
3) to create a high-frequency model of an inductive sensor, capable of presenting sensor operation above 30 MHz;
4) to propose of design methodology for designing an inductive sensor suitable for carrying out fast transients measurements;

5) verification of the proposed methodology by measurements on the actual sensor completed by the proposed design.

1.9 Scientific contribution presented in the thesis

Main scientific contribution presented in this thesis is:

- determining the bandwidth needed to measure the fast transients by a direct signal comparison and selective filtering (Chapter 2: Fast transients in power networks);
- defining more accurate high-speed model for more accurate measurements above the frequency range of 30 MHz (Chapter 5: Air-core sensor high-frequency model).
- detailed analysis on the effect of skin effect resistance to the operation of air-core inductive sensor (Chapter 5.2: Skin effect);
- detailed analysis on terminating resistance stray inductance to the operation of air-core inductive sensor (Chapter 5.3: Terminating resistance properties);
- detailed analysis on connection wires to the operation of air-core inductive sensor (Chapter 5.4: Effect of measurement system connection);
- detailed analysis on capacitive coupling effects to operation of air-core inductive sensor (Chapter 5.5: Capacitance effects of the sensor coil);
- identification of sensor design criteria and (Chapter 6: Sensor design criteria and methods);
- proposition of a design method of a shielded multi-turn inductive sensor coil, based on inductance design aspects (Chapter 6.4: Sensor electrical design);
- proposition of a design method of a shielded multi-turn inductive sensor coil, based on sensitivity design aspects (Chapter 6.4: Sensor electrical design);
- verification of designed sensor by measuring its transfer characteristics, and identifying the components of the sensor coil high-frequency model (Chapter 7: Verification of the sensor by laboratory measurements);
- verification of sensor operation and capabilities in laboratory testing, comparing the waveforms from reference measurements and inductive sensor output (Chapter Chapter 7: Verification of the sensor by laboratory measurements).

2 Fast transients in power networks

The high-frequency transients in power lines mostly have pulsed nature, it means that they do not repeat in time with the same characteristic waveform. Most often serious faults occur when two electrical conductors in the power line come together and/or if either of the conductors comes in contact with earth. In these cases, the most characteristic transient is caused by the transition of voltage between the affected conductors to zero (or close-to zero value). The voltage variation rate is very high and can reach thousands of volts per microsecond (see example on Figure 2.6), while the transient itself could last only less than 100 ns.

The phenomenon most often associated with pre-fault physical insulation break-down process, partial discharge (PD), is in electrical sense very similar to the fault transient process, only in sense of physical quantities and energy much weaker. The duration of the PD event can be extremely short (few nanoseconds) and its amplitude very low (few to few tens of volts) (see example in Figure 2.4).

All this makes the measurement more complex, as the accurate measurement would require capturing the wide range of high frequency components with very good sensitivity. A question arises about selection of frequency components that would hold the most important value for recording pulse waveform with high accuracy. The following analysis is observing the measurement of the pulsed fast transients, and presenting the effects to the accuracy of the measurement by limitation of bandwidth for measurement.

2.1 Measurement of fast transients

In this chapter, several measurements are presented referring to simulation of faulty events in laboratory conditions. Due to high voltage present on power lines and high supply reliability requirements, it is rather difficult to conduct measurements of actual transient phenomena on real power networks. The laboratory fault simulations present one of the most suitable cases of producing fast transients. In real world effects like skin-effect, coupling, ground path etc., cause attenuations for high frequencies, especially considering that the power lines are not intended for the high-frequency signals transmission.

2.1.1 Partial discharge transient measurement

Simulation of the partial discharge (PD) signal was carried out in the High Voltage Laboratory of Aalto University, Finland.

The measurement setup was relatively simple and consisted only of a partial discharge characteristic pulse source, a voltage probe for measurements and load resistor to match the source output impedance (Figure 2.1).

A partial discharge calibrator CAL1E from Power Diagnostix was used as a PD source. For measurement and recording LeCroy Wavesurfer 24Xs type

oscilloscope was used, which provided 400 MHz analog bandwidth, equipped with LeCroy PP009 voltage probes that provide 500 MHz bandwidth (–3 dB).

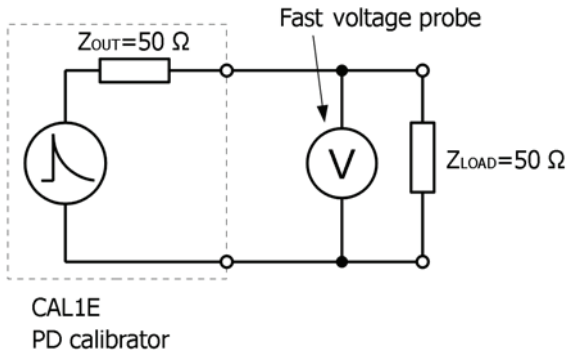

Figure 2.1. PD waveform measurement setup.

The captured PD transient waveform is presented in Figure 2.4 and its frequency content in Figure 2.5 in "2.2.1. Fast transient signal waveforms, windows of analysis and frequency spectrum". The signal waveform presents some indications of PD calibrator output oscillations, which actually are rather useful in the present analysis – namely the real PD measurements contain often quite high-frequency oscillations.

2.1.2 Fault transient waveform measurement

The simulation of earth fault transient was carried out in Tallinn University of Technology with a special transmission line set-up representing overhead power line (see Figure 2.2 and Figure 2.3). The simulated fault represented a single-phase earth fault for a power line, having momentary voltage of 1000 V on the faulty phase wire.

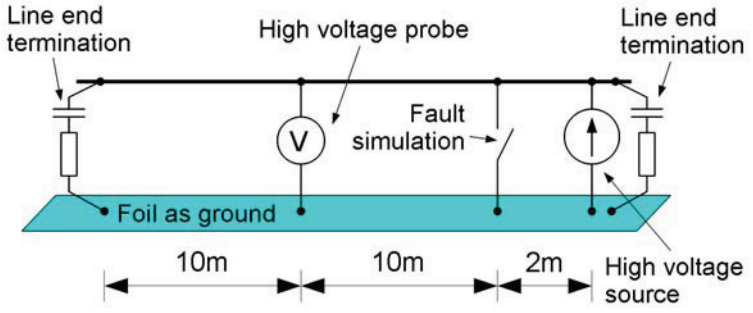

Figure 2.2. Fault transient waveform recording setup.

The power line model was created as a straight wire held at a constant height of 1 m above metal foil acting as ground. The line was energized using Megger MIT1020 isolation tester and charged to 1000 V. For keeping the reflections from line ends at a low level, an AC-type termination was used in the test line active

section ends. To observe the transient most directly, a high-voltage wide bandwidth probe Testec HVP15-HF was used for capturing the voltage between the power line wire and the grounding foil. This probe specified bandwidth was to be 50 MHz (–3 dB), though measurement results show that it captured signals having nearly 200 MHz bandwidth. This could also mean that there is some high-frequency phenomenon that was not captured due to probe overstress. For measurement and recording, Agilent InfiniVision MSO6104A oscilloscope with analog channels' bandwidth of 1 GHz was used.

Measurement point was set up at distance of 10 m from the fault simulation location and 10 m away from the line end in order to prohibit the reflections from affecting the measurements in the most important time-frame. The fault was simulated by establishing low-inductance connection between the wire and the ground foil.

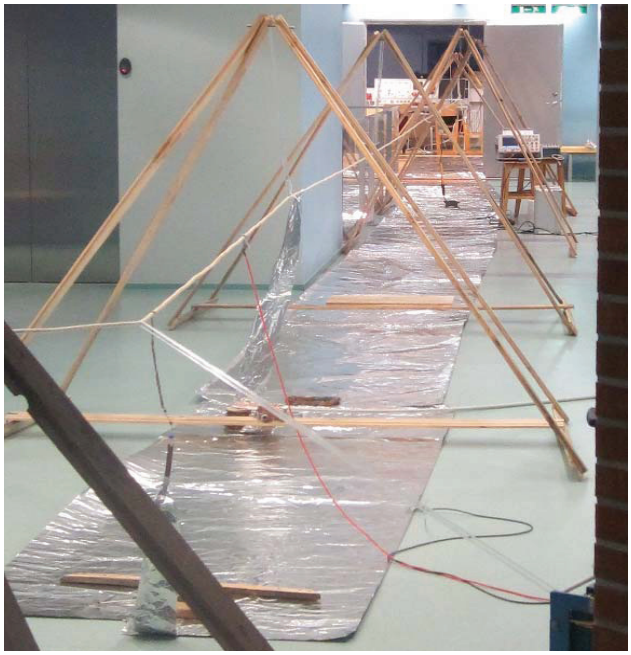

Figure 2.3. Measurement setup overview.

The captured fault transient waveform is presented in Figure 2.6 and its frequency content in Figure 2.7 in chapter "2.2.1. Fast transient signal waveforms, windows of analysis and frequency spectrum".

2.2 Frequency spectrum analysis of transient signals

The frequency spectrum of the two test fault signals are presented in figures below. As the most relevant part of the signals will remain in the frequency range up to 200 MHz, and the probes used in this test also are not capable of providing reliable results in higher frequency, only the spectrum up to 200 MHz is focused on.

The frequency spectrum can be obtained by conducting Fourier' transform on the signal observed. For the discrete signals with length of N samples, the discrete time Fourier transform (DTFT) can be calculated as [53]

$$X_D[k] = \sum_{n=0}^{N-1} x_D[n] e^{-j \cdot 2\pi \cdot k \cdot n / N} , \tag{2.1}$$

where $k = 0; 1; \ldots ; N-1$ and n is the index of the sample in the signal.

The resulting $X(k)$ is a function of index k and the length of the resulting array is the same as the signal length. This result is symmetrical in the frequency range ($0 \ldots F_s$), where F_s is the sampling frequency. In practical applications, only one half of the spectrum is observed as it represents a mirror image up to the frequency $F_s / 2$. This however reveals, that when the number of discrete frequencies is N and the highest frequency is the sampling frequency, the DTFT resolution, or the smallest frequency deviation distinguishable, is defined as

$$\Delta f = \frac{F_s}{2N} . \tag{2.2}$$

For example, for signal with 1024 samples and sampling rate of 2048 MHz, the resolution of the DTFT is 1 MHz. This is clearly observable also in the results presented within this thesis. In this view, it would be good to have signals with more length as these provide a better resolution.

Another property to be pointed out is that DTFT as well as continuous-time Fourier transform indicates the averaged intensity values for different frequency components in the signal for the duration of time of the sampled signal t_s

$$t_s = \frac{N}{F_s} . \tag{2.3}$$

For periodic signals, this is not an issue; however, as in this case the signals are of pulse-nature, the intensity of the momentarily occurring very intense transients vanishes in noise when longer sampled signals are observed. For the pulsed signals analysis, this is contradictory to the previously established relation, which states that the frequency resolution would be finer, if the signal was longer. In this thesis the observation needs to focus on the particular momentary events. Thus, only the vicinity of the signals, related to the fault events, are observed in detail. It is more reasonable to define a shorter section of the signal for analysis that only contains the information on the transient analyzed. Such window of analysis presents the section of signal that is focused in more detail.

This analysis uses an approach to better define the signals frequency components. In order to achieve better separation on the frequency scale, the signals selected in the window are repeated periodically. It provides better resolution of frequency, but as the initial signal is repeated, there is no new information contained in the

repetition and the most the frequency components remain at zero. For analysis, this presents a better overview of the actual signal content for visualization.

2.2.1 Fast transient signal waveforms, windows of analysis and frequency spectrum

The waveform of PD signal measurement and the section of the signal processed (window) are presented in Figure 2.4 altogether with the DTFT plot in Figure 2.5 of the signal in the processing window. It can be observed, that the suitable length of window is 512 samples long as this length of signal presents the most valuable parts of transient. Frequency plot has been presented with intention to point out the particular frequency resolution values of the DTFT on Figure 2.5.

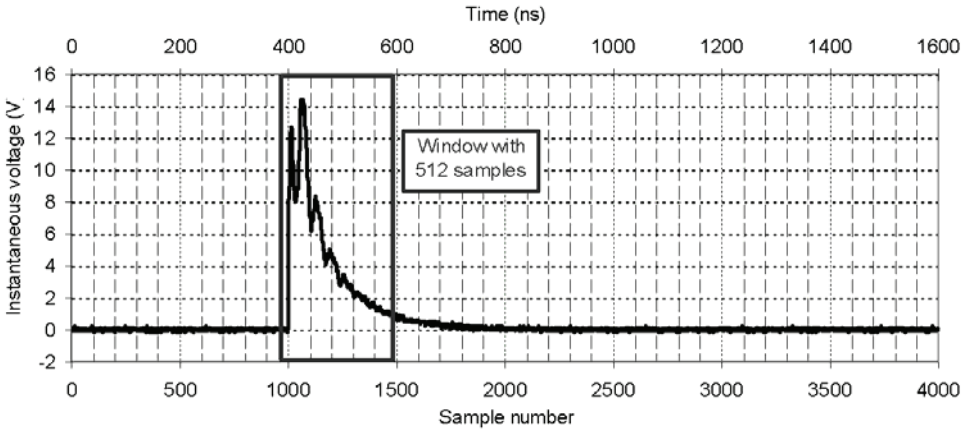

Figure 2.4. PD signal with window indicating observed transient region, F_s = 2,5 GS/s.

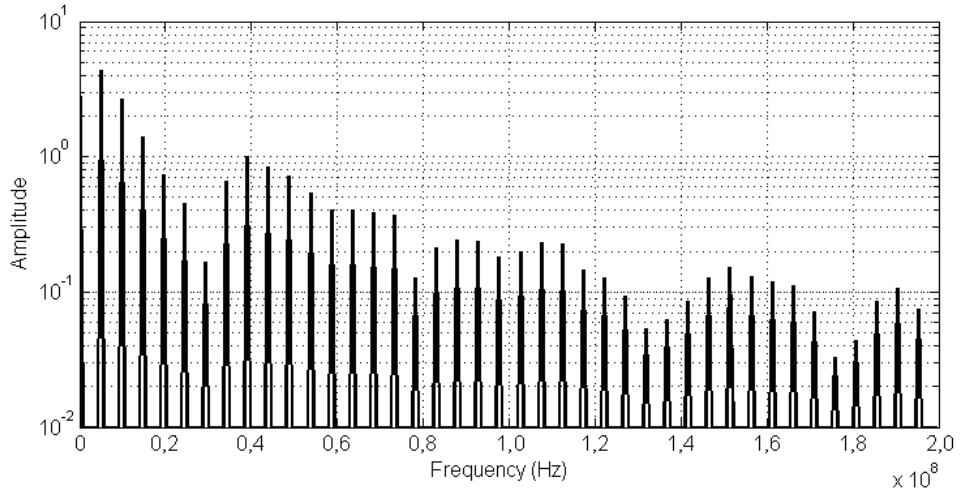

Figure 2.5. PD signal initial DTFT plot in frequency range 0 … 200 MHz.

Similarly, the waveform of fault transient measurement and section of signal processed (window) are presented in Figure 2.6 with the DTFT plot for the signal in window in Figure 2.7. Here also the suitable length of the window is 512 samples long as this length of the signal presents the most valuable parts of the recorded transient.

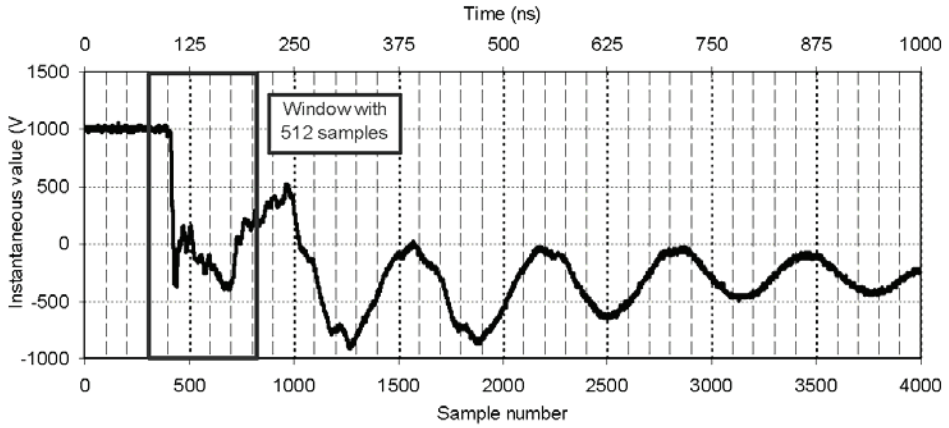

Figure 2.6. Fault signal with window indicating observed transient region, F_s = 4 GS/s.

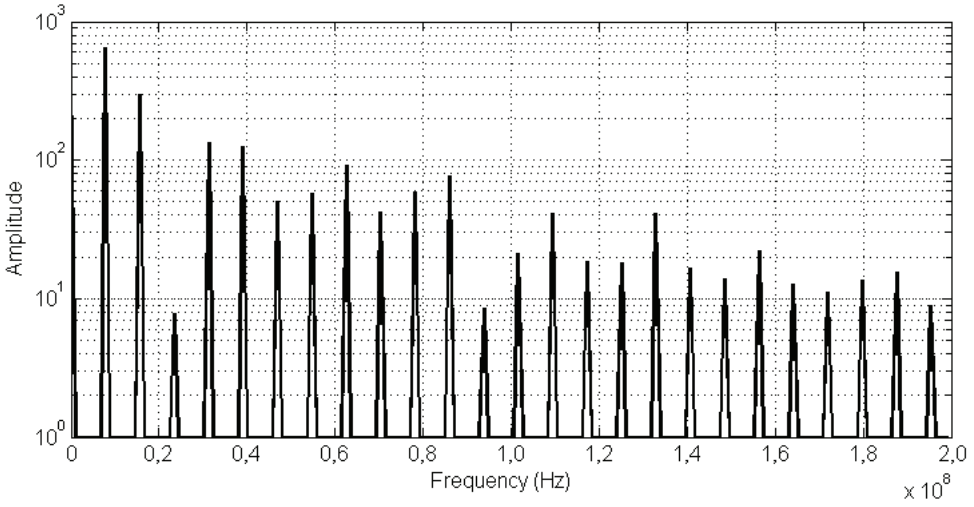

Figure 2.7. Fault signal initial DTFT plot in frequency range 0 … 200 MHz.

As expected, the frequency spectrum graphs present too much information, which makes it rather difficult to determine the precise bandwidth requirements for the sensor to measure such signals. One of the methods for sufficient bandwidth estimation is known as spectral energy density analysis [49]. The energy of the signal is calculated for all the frequencies present in the signal spectrum as an

integral over the full signal bandwidth, or in discrete form, as a sum of all the frequency components

$$E_{sig} = \int_{-\infty}^{\infty} \left|X(f)\right|^2 df = \sum_{k=0}^{N} \left|X_k(k)\right|^2 . \tag{2.4}$$

In theory, the higher the signal spectral energy is compared to the original signal, the more important information about the signal is contained. This means, that when the signal lost significant portion of energy due to filtering, it also lost the information about the signal original waveform, and as long as the filtered signal energy levels are high, the signal should be same as the original. In further analysis presented below it can be seen however that observing the energy of the signal alone is not sufficient to describe the bandwidth content in the present case. Thus a different method is used which employs digital filtering. A comparison of the filtered transients to the original recorded waveform is presented.

2.3 Digital low-pass filter characteristics

Digital filters are most suitable for processing signals in sampled forms. There is a variety of finite order filters (FIR) that are capable of very effective signal filtering and provide excellent passband and stopband characteristics [49]. In the present task, digital filters are synthesized using Matlab tools, and the fast transients signals measured are processed with the filters having different bandwidth. This way, a comparison of the output of a sensor with limited bandwidth can be provided. The task is to find out, at which bandwidth limit the filtered signal waveform still resembles the original waveform. This way, the estimations about required sensor bandwidth can be given.

For every filter, including both analog and digital filter types, there is a specific phase characteristic involved. Digital filters inherit a constant processing delay because of data storage events during the processing, this is also known as group delay G_D. For the ideal filter, the value of the group delay should be constant for all the frequencies. The phase plot of the digital filter also includes the processing delay and this should be taken into account while observing the phase plots.

A phase shift caused by group delay can be calculated for every frequency as a fraction of full cycle (2π radians or 360º). In degrees, it can be calculated as

$$\Delta\varphi_{GD} = -\frac{G_D}{\frac{1}{f}} \cdot 360 = -G_D \cdot f \cdot 360 , \tag{2.5}$$

where f is the frequency observed.

For example, if $G_D = 10$ ns, then for $f = 1$ MHz the phase shift due to group delay is –3,6º (lagging); however, at $f = 100$ MHz the delay is –360º (lagging). Thus the digital filter phase characteristic can present significant phase shift just because of

the processing delay. The actual filter phase shift can be defined as the filter characteristic phase shift $\Delta\varphi_{FD}$ without the group delay phase shift

$$\Delta\varphi_{FD} = \Delta\varphi_{OUT} - \Delta\varphi_{GD}\,. \tag{2.6}$$

The example below presents the case of the filter implemented in this analysis. The filter is designed with 200 MHz highest passband limit and 250 MHz as the lowest stopband limit (the transition frequency, i.e the difference in frequency from passband limit to stopband limit, is 50 MHz). The filter output phase shift as well as the phase characteristics due to the group delay is presented in Figure 2.8 and Figure 2.9. As a reference, a group delay plot has been presented, showing the steady group delay for most of the passband. Significant phase shift can be observed when approaching the passband upper limit, and at the limit frequency the phase shift is approximately 70º.

The first purpose of such filter in the context of this analysis is to provide a verification of the bandwidth of the signals needed for measurements. This is done by comparing a signal that has been passed through a filter with a specific bandwidth limit, with an original signal measured. Such comparison sets quite high requirements to the filter phase plot, as the filtered signal should not be distorted to make a valid comparison. The phase shift of the filter at passband limit has been observed at a maximum of 70º with an increase towards the stopband and the transition area attenuation is changing rapidly to –40 dB. This means that the stopband attenuation is damping the signal components that could provide distortions quite effectively. It can therefore be concluded that the filter presented is quite suitable for making the comparison, as it does not produce significant distortions to the filtered signal that is being observed within the passband region.

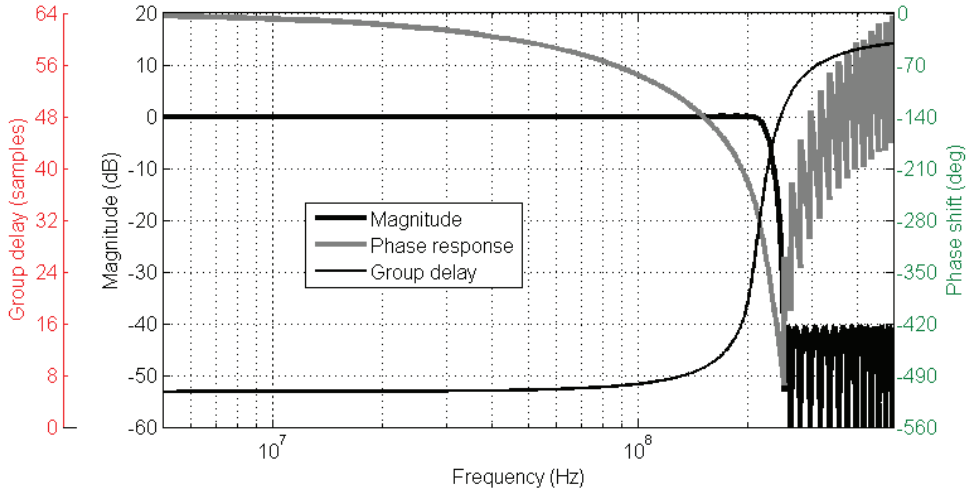

Figure 2.8. Filter frequency plot with magnitude and phase responses and group delay. Note that 0 dB means no attenuation and –40 dB means 100 times attenuation.

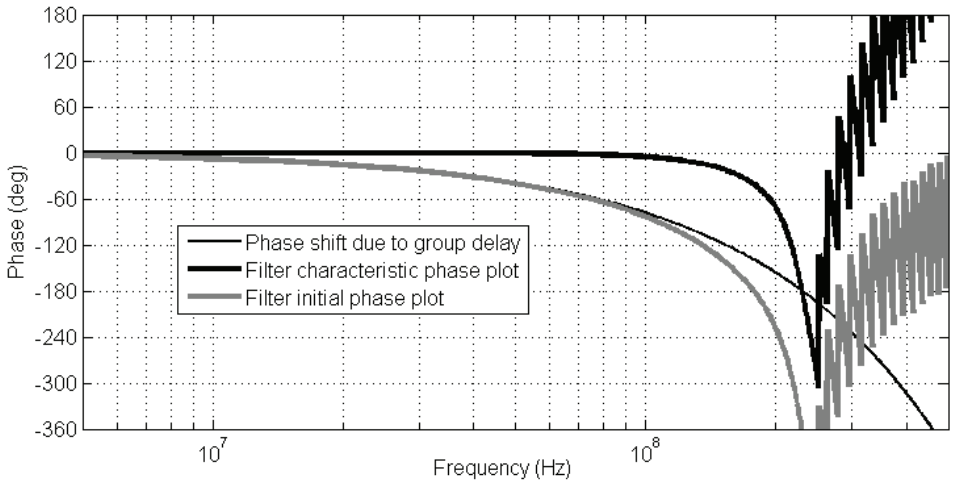

Figure 2.9. Filter phase plot details and filter phase characteristics.

2.4 Bandwidth analysis

The following section focuses on the trial method for determining the bandwidth, which the sensor used for capturing PD and fault signals should provide in order to guarantee accurate measurements.

This method itself is rather straightforward and uses Matlab provided functions to design a minimum phase lowpass FIR digital filter. The filter characteristics for testing each of the frequency limits are stated in Table 2.1. The first filter has passband limit frequency at 200 MHz for testing the effect of digital filter on the signal. It should be noted, that the lower design frequency of the filter increases the group delay. For more efficient signal analysis the group delay is compensated for most effective visual comparison of the original and filtered signals. All the filters designed have basically the same characteristics as described above in "2.3. Digital low-pass filter characteristics".

Table 2.1. Filter parameters for determining the bandwidth upper limit of signals for measurement.

Upper passband frequency (MHz)	Attenuation in passband, max (dB)	Attenuation in stopband, min (dB)	Stopband lower limit (MHz)
200	–0,1	–40	250
90	–0,1	–40	130
70	–0,1	–40	100
50	–0,1	–40	75
30	–0,1	–40	50

2.4.1 Partial discharge signal waveforms and analysis

PD signals processed with digital filters are presented below in Figure 2.10 for bandwidths of 70 to 200 MHz. The signal waveforms with filtering bandwidth ranging from 30 to 70 MHz are presented in Figure 2.11.

The signal waveforms processed with filters having bandwidth above 70 MHz show quite good results. The similarity between the measured and the filtered signal shows quite good match, although major distortions can be seen due to filter processing delay. It could be said, that even the 50 MHz bandwidth could provide sufficient accuracy, as the signal waveform resembles the original. Limiting the bandwidth further to 30 MHz will cause the signal to be heavily distorted and valuable information on short-duration transients can be completely lost. Based on the graphs above, it could be stated that 70 MHz bandwidth is sufficient for quite precise PD measurements. However, if we look at the graph on Figure 2.12, it can be noted that the real bandwidth reaches up to 90 MHz in this case. It is due to the filter transition band properties that there are still such high frequencies included.

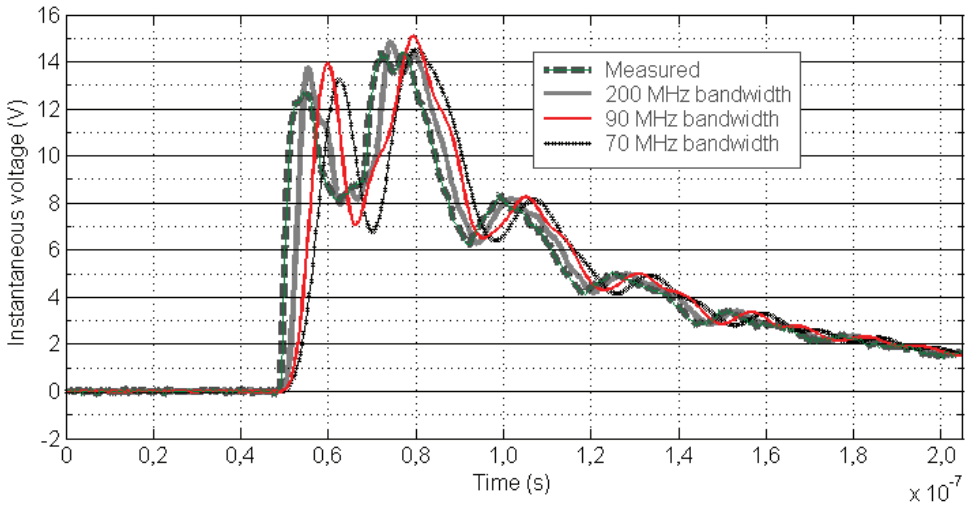

Figure 2.10. PD signal waveforms filtered at 200; 90 and 70 MHz.

As a comparison to the taken approach to use filtering to determine the actual bandwidth, Table 2.2 presents the PD signal spectral energy calculations for analysis. Observing the spectral energy content, not much change can be seen as the change at 30 MHz is less than 5%. An anomaly to the overall trend is the energy increase at frequency of 50 MHz as here it is higher than for 70 MHz. This can be related to the impulse response characteristics of the filter.

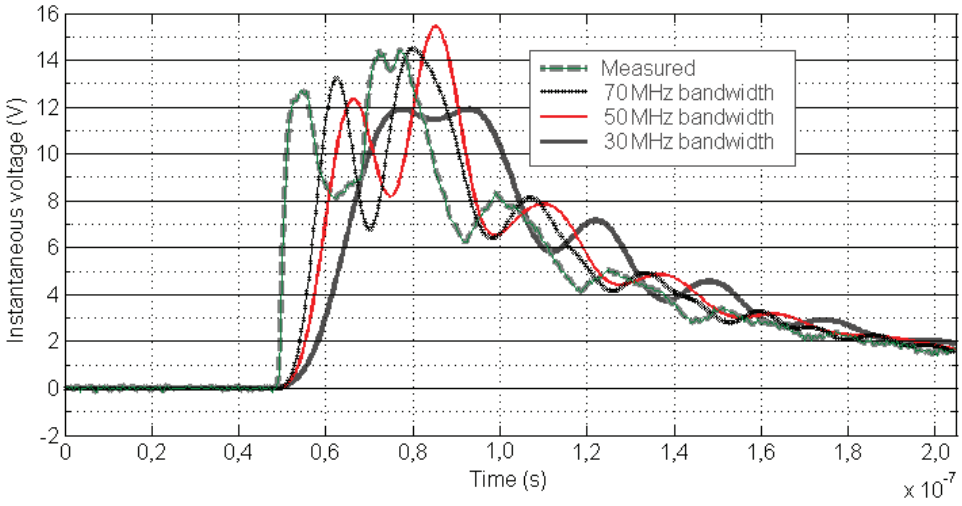

Figure 2.11. PD signal waveforms filtered at 70; 50 and 30 MHz.

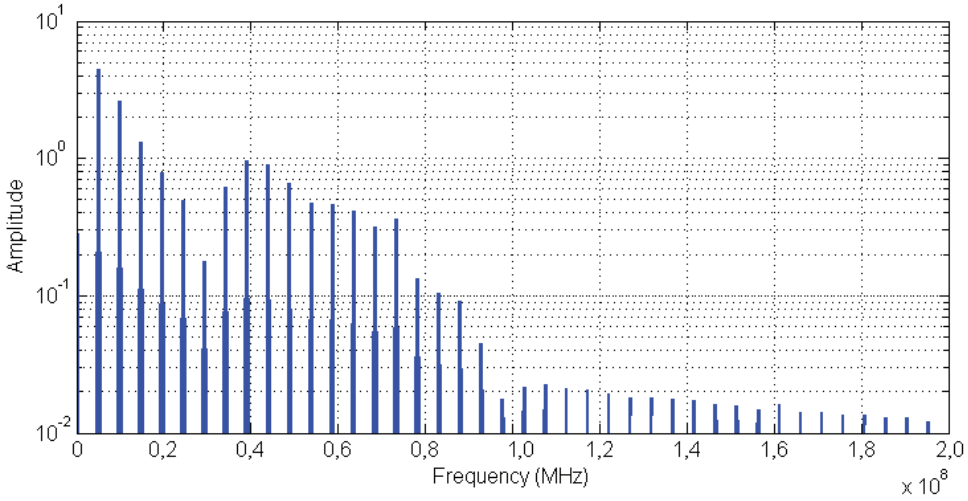

Figure 2.12. PD signal frequency plot after filtering with 70 MHz filter.

Table 2.2. PD signal spectral energy values.

Filtering bandwidth (MHz)	Signal energy level (V^2)	Part of original
Original	105,5	100%
200	105,0	99,5%
90	104,5	99,1%
70	103,4	98,0%
50	103,8	98,4%
30	100,9	95,6%

2.4.2 Fault signal waveforms and analysis

The recorded fault signals processed with digital filters are presented below in Figure 2.13 for the bandwidths of 70 to 200 MHz. The signal waveforms with bandwidth range from 30 to 70 MHz are presented in Figure 2.14. One should consider that the initial transient visible in Figure 2.13 and Figure 2.14 before 20 ns is due to the filtering process of the initial step; this can be ignored in the further analysis.

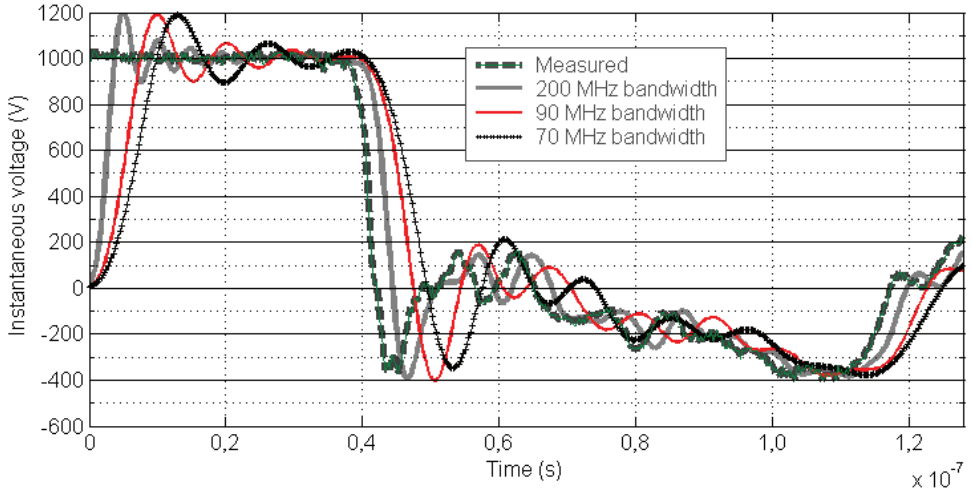

Figure 2.13. Fault signal waveforms filtered at 200, 90, and 70 MHz.

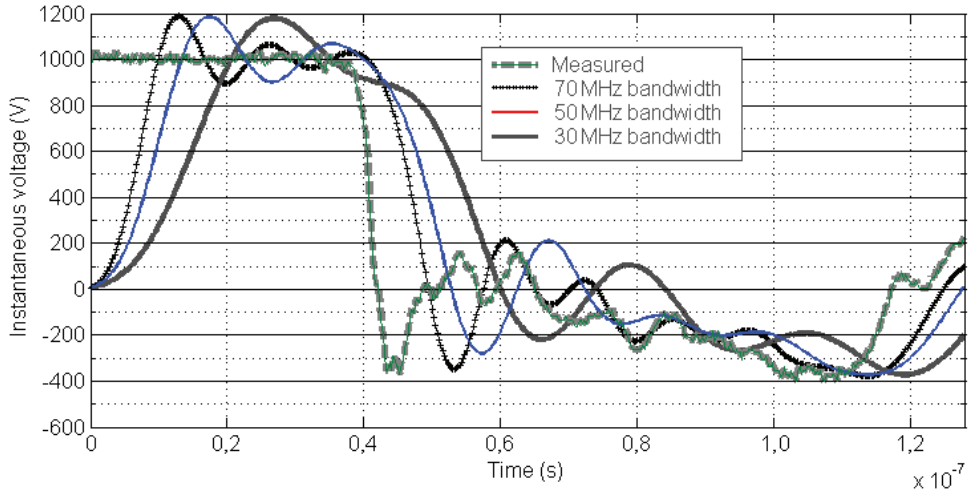

Figure 2.14. Fault signal waveforms filtered at 70, 50, and 30 MHz.

One of the physical phenomena of particular interest for the measurement of the fault transient to observe during is travelling wave edge shape, as this would

provide information about the fault location and causes. For example, determining the exact time of arrival of the fault transient travelling wave can be done more precisely, the sharper the rise of the wave edge is. In this view, the waveform of the transient filtered with bandwidth higher than 70 MHz seems most suitable. Filtering with 90 MHz can still provide nice match of the slope. For a reference, the fault signal frequency plot after filtering with 90 MHz filter is presented in Figure 2.15.

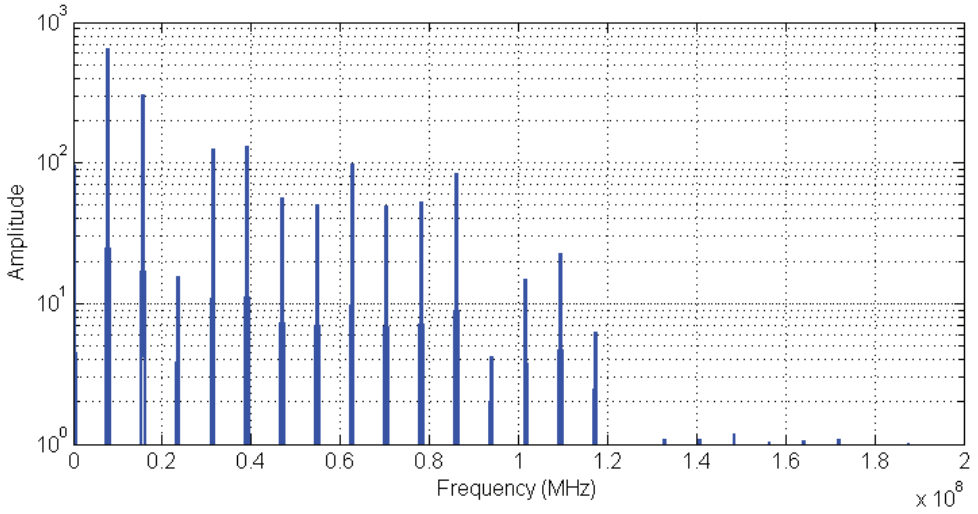

Figure 2.15. Fault signal frequency plot after filtering with 90 MHz filter.

As in the case of PD waveform filtering, also here the frequency plot still contains significant traces of signal components with frequency over 90 MHz.

The fault signal spectral energy calculations have been presented in Table 2.3. As here also the lower frequency components dominate, it is very difficult to determine when the most valuable information is lost.

Table 2.3. Fault signal spectral energy values.

Filtering bandwidth (MHz)	Signal energy level (V^2)	Part of original
Original	$7{,}91 \cdot 10^5$	100%
200	$7{,}86 \cdot 10^5$	99,4%
90	$7{,}72 \cdot 10^5$	97,6%
70	$7{,}63 \cdot 10^5$	96,5%
50	$7{,}52 \cdot 10^5$	95,1%
30	$7{,}29 \cdot 10^5$	92,2%

2.4.3 Discussion

As it could be seen from the results above, the necessary bandwidth to accurately record the fast transients reaches above 70 MHz and even 100 MHz bandwidth could be recommended. It confirms the expectations from [95] that the bandwidth of such signals would be in range over 50 MHz.

The grid protection methods of the conventional substations rely on relatively slow occurring transient processes. Thus, the bandwidth of the measurement devices found in substations today – the iron-core voltage transformers (VT) and current transformers (CT) – are not able to reach higher than some (or some tens) kHz. Detecting the PD and the fault originated travelling wave transients can be quite out of reach using conventional CTs and VTs; however obtaining a transducer that would have the characteristics of the classical units but also high bandwidth can be very costly.

Another topic is also the low-frequency limit, necessary for carrying out the measurements of the fast transients. In the analysis presented, the frequency components below 5 MHz (Figure 2.12) and 7 MHz (Figure 2.15) were not visible and the DC component in the FFT plots was just representing the average of the signal observed in the window. The relatively large frequency component steps are present due to very high sampling frequency that in a real system would be rather difficult to implement. When the sampling frequency of the analog-to-digital converter was lower, the frequency resolution will also become more accurate. In this view it would be rather more suitable, for example, to limit the lower bandwidth at 100 kHz … 1 MHz. In this thesis, as more accuracy can be achieved using high-speed measurement equipment, the lower bandwidth of 1 MHz is targeted.

2.5 High-frequency transients' propagation on power lines

As the frequency of the electrical voltage and current variation becomes close to the wavelength of the variation frequency, the electrical voltage and current will propagate along the transmission medium as an electromagnetic wave. The wavelength for a particular frequency f can be calculated as

$$\lambda = \frac{\upsilon}{f}, \tag{2.7}$$

where υ is the wave propagation velocity in the specific medium.

For example, for the overhead lines with the wave propagation velocity of $299 \cdot 10^6$ m/s, at frequency 1 MHz the wavelength is

$$\lambda = \frac{299 \cdot 10^6}{1 \cdot 10^6} = 2{,}99 \cdot 10^2 \,\mathrm{m} \cdot$$

Similarly, for 100 MHz frequency the wavelength would be ≈ 3 m. For power transmission lines, basically every line section has more length than the presented

wavelength and in this case the high-speed transient should be observed as propagation of an electromagnetic wave.

In case of power transmission lines, the propagation medium is the power line itself and this is actually a rather good path for the high-frequency signals. It can be observed as an array of sections of distributed components, like inductance of the transmission line wire, capacitance of the transmission line wire to the ground, but also some line series resistance and some small conductance to ground (see Figure 2.16) are present.

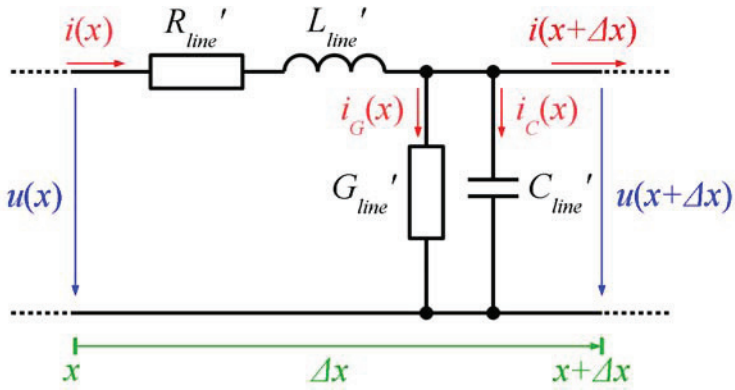

Figure 2.16. Section of a transmission line wire as model with distributed components; R_{line}' – line wire series inductance per line unit length; L_{line}' – line wire series inductance per line unit length; C_{line}' – line-to-ground capacitance per line unit length; G_{line}' – line-to-ground conductance per line unit length.

The propagation of an electromagnetic wave along the transmission line (also known as travelling waves) is described by the wave equations or Telegraph equations [63] as

$$-\frac{\partial u}{\partial x} = R_{line}'\, i(x) + L'_{line}\,\frac{di(x)}{dt}, \tag{2.8}$$

$$-\frac{\partial i}{\partial x} = G_{line}'\, u(x) + C_{line}'\,\frac{du(x)}{dt}, \tag{2.9}$$

where $di(x)/dt$ is the current variation rate at a geographical location x and similarly $du(x)/dt$ is the voltage variation rate at a geographical location x.

As a solution to these equations, the relation between the current and voltage of the travelling wave can be presented as characteristic impedance of the transmission line Z_{line}

$$\frac{u(x)}{i(x)} = Z_{line} = \sqrt{\frac{R_{line}' + j\cdot\omega\cdot L_{line}'}{G_{line}' + j\cdot\omega\cdot C_{line}'}}\,. \tag{2.10}$$

Some conclusions can be presented observing the line as lossless line, i.e. the lossy components $R_{line}' = 0$ and $G_{line}' = 0$, in which case

$$\frac{u(x)}{i(x)} = Z_{line} = \sqrt{\frac{L_{line}'}{C_{line}'}} \tag{2.11}$$

and the wave propagation speed

$$\upsilon = \sqrt{L_{line}' \cdot C_{line}'}\,. \tag{2.12}$$

Both the line inductance and line capacitance are determined by the line physical geometry [48], therefore there are rather large differences for the characteristics of cable lines and overhead lines. Typical values for the power lines would be

- $Z_{line} \approx 400\ \Omega$, $\upsilon \approx 299 \cdot 10^8$ m/s for the overhead lines;
- $Z_{line} \approx 40\ \Omega$, $\upsilon \approx 150 \cdot 10^8$ m/s for the cable lines.

For a lossless line, the electromagnetic wave would propagate over the transmission line without distortions. This provides the perquisite of fast transient measurement in some remote part of the transmission network, as the transient would also reach the location with the same voltage and current momentary values' relation as provided by (2.11).

In the real network the losses cannot be avoided and thus several loss effects have to be taken into account in (2.10). Due to loss, the voltage and current of the electromagnetic wave will have a phase shift; the propagation speed is varying at different frequencies [63]; the propagation function will also have an attenuation part, which will decrease the magnitude of the wave etc. The losses bringing the most attenuation are [75]:

- skin effect, increases the series resistance of the transmission line; dependent on the square root of frequency;
- surface roughness, due to the skin effect the conductor surface quality becomes highly important; increases the series resistance of the transmission line as frequency is growing;
- the dielectric losses due to a current passing through dielectric, in linear relation to the frequency;
- radiation losses, due to spreading of the electromagnetic field in the free space surrounding the transmission line.

For the overhead power lines significant wave distortion is also brought due to ground effects, like ground stratification [3], [4], cross-talk [83] etc.

The mechanisms of losses and distortions are rather difficult to observe and predict, especially considering the variable construction of the transmission lines. There are methods available to calibrate the measurement system based on the

measurement results themselves, for example time-domain reflectometry (TDR) [44] has been implemented with rather good results. Results of the TDR method heavily depend on the accuracy of the measurement results. It means that the output of the sensor should be as little distorted as possible, in order to provide an accurate measurements of high-speed transients.

Higher frequency signal components have higher attenuation constant. This means that in the vicinity of the fault or PD, the high-frequency components are strongest. As the transient pulse is propagating along the transmission line, the lower frequency signal components become more significant, as the energy of the high-frequency components decreases. This means that the sensor should have good sensitivity in both low and high frequency operating range, as the measurement location is further away from the sensor.

2.6 Pulsed signal measurement criteria

Every measurement system and sensor can be described with a transfer function, which presents the relation of input of the sensor to the output of the sensor. There are two types of transfer characteristics – magnitude transfer characteristics and phase response characteristics. First one presents the relation of physical quantity measured to the output quantity of the sensor, while the second one presents the phase shift in the output of the sensor compared to the measured quantity (in case of sine waveform). Phase shift essentially presents the delay between input and output of a circuit. For example, when there is a phase shift of 90 degrees, the output of a circuit is delayed by quarter of an oscillating cycle. At 10 kHz this would mean delay of 25 μs, but at 1 MHz the delay would be 0,25 μs.

Both the trace of partial discharge as well as fault-initiated transients have pulsed nature. This means that they emerge only momentarily, however they contain high number of different very high frequency components. Pulse shape is highly dependent on the amplitude and on the exact timing of each individual frequency component. For example, if some frequency components are damped more, the pulse shape is altered and if one frequency is delayed more than some other frequency present in the pulse, the pulse shape is also modified.

This presents two essential conditions for the measurements of pulsed signals. First requirement is based on amplitude – the measurement system amplitude response should be stable and at the same value for all the frequencies present in the pulse. The second one concerns the phase response of the measured signal – the phase shift in the operating bandwidth should be stable at 0 degrees for the full bandwidth range. In this way, the least distorted measurement can be provided (see Figure 2.17).

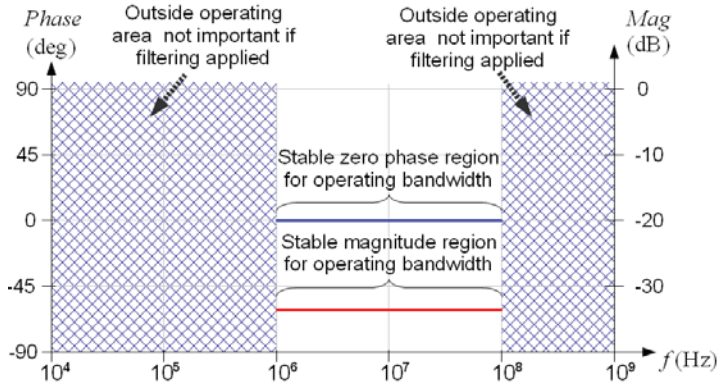

Figure 2.17. Magnitude and phase response requirements for pulsed signal measurement.

2.7 Summary of sensor operating bandwidth criteria

In this chapter the transients' effective high-frequency components were described and analysis of the measured transients revealed that the target bandwidth should reach from 1 MHz up to 100 MHz. The lower bandwidth limit depends on the measurements system digital-to-analog acquisition and sampling frequency and within this thesis the lower bandwidth is observed at 1 MHz. Highest frequency for the sensor has been presented at 100 MHz, which should be adequate for capturing the fast transients with rather good accuracy. Due to different distortions, the accuracy of the sensor output has critical importance and pulsed measurements are especially difficult in this sense.

As a requirement to the sensor for measuring pulsed signals, the phase and amplitude response of the sensor should be stable in the full operating range. In addition, the phase response of the sensor should provide 0 degrees phase shift for the specified operating range. This will be one of the most important criteria in the sensor design presented in this thesis.

3 Air-core inductive sensor and its low-frequency model

3.1 Magnetic field around a wire

Every conductor with some current passing through it has also a magnetic field around it. The relation can be calculated with the Biot-Savart-Laplace Law [48]

$$\boldsymbol{H} = \frac{1}{4\pi}\int_a^b \frac{I \cdot d\boldsymbol{L}_k \times \boldsymbol{R}_k}{\left|\boldsymbol{R}_k\right|^2}, \tag{3.1}$$

where $\boldsymbol{H}$ – magnetic field intensity vector; I – scalar current value; $d\boldsymbol{L}_k$ – current vector element length; $\boldsymbol{R}_k$ – radius vector leading from current point to observation point; $(x_c; y_c; z_c)$ – coordinates at a point "c", where the field is observed; $(x_k; y_k; z_k)$ – coordinates at field source point "k"; $d\boldsymbol{L}'_k$ – dispositioned current element vector $d\boldsymbol{L}_k$ (Figure 3.1).

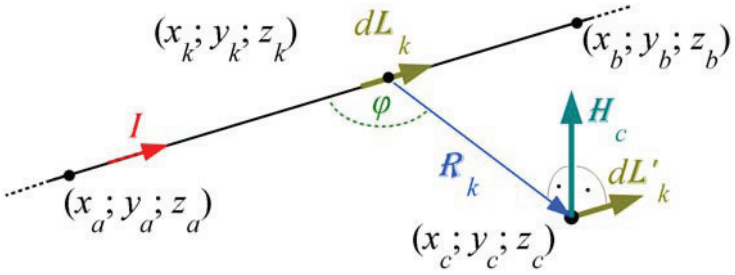

Figure 3.1. Biot-Savart-Laplace law calculation example.

The main conclusions for the fast transients measurement application by the Biot-Savart-Laplace law would be

1) intensity of the magnetic field around a conductor is directly proportional to the current passing through the conductor; (in higher frequencies this applies to the immediate near-field zone);
2) intensity of the magnetic field decays in relation to the distance of the observation point from the current. In scalar form, the magnetic field intensity around a round, straight wire can be calculated as

$$H = \frac{I}{2\pi \cdot h}, \tag{3.2}$$

where h – distance of observation point from the wire.

In this thesis, the wire where current is measured is always assumed to have a perfect round shape and to be infinitely long and straight.

3) direction of a magnetic field around a round conductor is always perpendicular to the direction of current movement and the radius from the current to the observation point;

For measurement of the current, it offers a rather straightforward method – if one would measure the magnetic field around the conductor, the magnetic field intensity would provide the information about the value of current in the conductor. This applies also for higher frequency measurements.

Total magnetic field effect in an environment is described by magnetic flux density $\boldsymbol{B}$, also defined as

$$\boldsymbol{B} = \mu_a \cdot \boldsymbol{H}\,, \tag{3.3}$$

where μ_a is the absolute magnetic permeability of the environment (scalar quantity).

In vector representation this is an indication, that the magnetic flux density vector has the same direction as the magnetic field vector. Magnetic flux density in the vicinity of a current-carrying wire can be calculated in scalar form as

$$B = \mu_a \cdot H = \frac{\mu_a \cdot I}{2\pi \cdot h}. \tag{3.4}$$

For air, the absolute magnetic permittivity $\mu_{a,air}$ can be considered equal to permeability of free space μ_0, that is

$$\mu_{a,air} \approx \mu_0 = 4 \cdot \pi \cdot 10^{-7}\ \text{H/m}. \tag{3.5}$$

3.2 Magnetic flux and output of inductive loop sensor

A quantity of magnetic flux, passing through an area A is determined by magnetic flux density and the loop area

$$\Phi = \oint_{Aloop} \boldsymbol{B} \cdot d\boldsymbol{A}\,, \tag{3.6}$$

where $\boldsymbol{B}$ – magnetic flux density; A_{loop} – magnetic sensor loop area; $\boldsymbol{A}$ – smallest piece of the loop area with its normal vector.

It provides that result of multiplication between $\boldsymbol{B}$ and $\boldsymbol{A}$ is the largest, when the vectors are in same orientation, i.e. the angle between direction of magnetic flux density (also the direction of magnetic field) and direction of normal vector of loop area is zero.

Every conductive loop being subjected to variable magnetic flux provides an electromotive force. This is described by Faraday's law

$$e = -\frac{d\Phi}{dt}, \tag{3.7}$$

where e – electromotive force (EMF); Φ – magnetic flux through loop; t – time.

This means that the electromotive force depends on the rate of change of the flux linkage acquired by the coil loop area. It provides a simple relation – the faster the change, the more there is output EMF. However, it also presents trivial method of how to monitor the current by observing the magnetic field intensity around a wire. For making a simplest inductive current sensor, nothing more is needed than a loop of some wire, placed in the area with changing magnetic field effect and a sensitive voltmeter, connected to the ends of the loop, as in Figure 3.2.

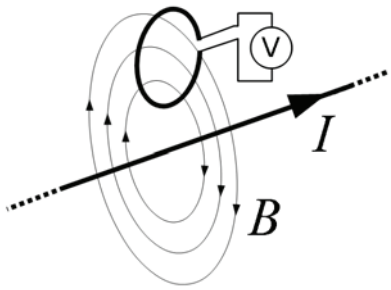

Figure 3.2. Simplest inductive loop current sensor.

In terms of sensitivity of such simple sensor following (3.7) focus should be paid on the value of magnetic flux for making some some introductory conclusions.

First conclusion based on the (3.6) is that orientation of a loop, that would hold as much of the magnetic flux as possible (this means would achieve as much output as possible from magnetic field around the wire) should be perpendicular to the wire. Because of this, it is assumed in this thesis that the inductive sensor coil is always perpendicular to the magnetic field around the wire. In more detail, it is assumed that every turn of the inductive sensor winding is perpendicular to the magnetic field surrounding the wire.

Second, as observed previously, the magnetic loop flux density around the wire follows a relation to distance from wire (3.4). To obtain a total magnetic flux, (3.6) refers to integration based on the shape of area. It suggests that for every shape of loop, there should be a separate formula to calculate the flux through loop. Calculation formulas [30] [47] [91] for some common shapes of loops using (3.6) have been presented in Table 3.1.

Table 3.1. Magnetic flux values for common shapes.

Geometrical representation	Expression for flux calculation
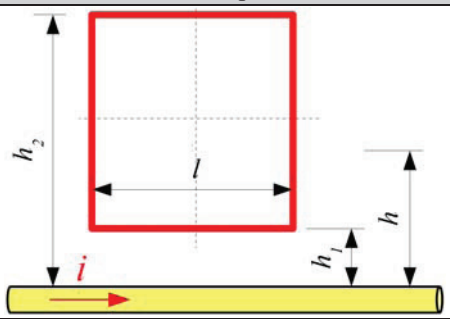	Rectangular loop $\Phi = \frac{\mu_0 \cdot l \cdot I}{2\pi} \ln \frac{h_2}{h_1}$ (3.8)
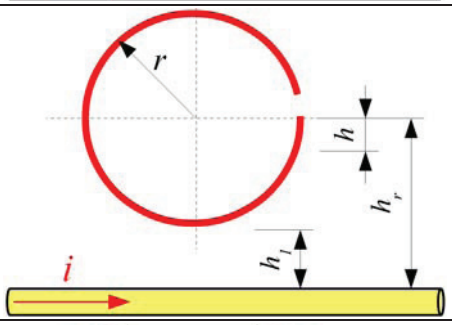	Circular loop $\Phi = \frac{\mu_0 \cdot I}{2}\left(h_r - \sqrt{h_r^{\,2} - r^2}\right)$ (3.9)
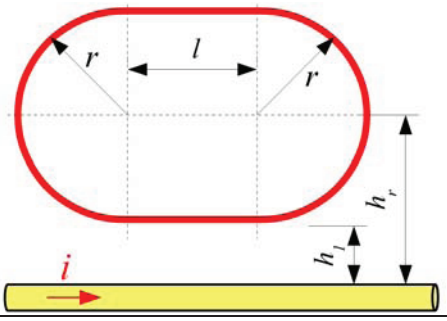	Oval loop $\Phi = \frac{\mu_0 \cdot l \cdot I}{2\pi}\left[\ln \frac{h_2}{h_1} + \pi\left(h_r - \sqrt{h_r^{\,2} - r^2}\right)\right]$ (3.10)

3.3 Number of turns and mutual inductance

Previously the discussion has been about one loop and in essence it is sufficient to estimate the overall sensitivity of the composed sensor coil. If a sensor coil has multiple turns in winding, due to geometry, all the loops in coil can be considered as series connected, so the induced voltage in the coil terminals due to flux change is sum of voltage of all loops. If all turns of coil are exactly the same in shape, there is exactly the same flux through all turns in coil and

$$e = -\sum_{n=1}^{w} \frac{d\Phi_n}{dt} = -\frac{w \cdot d\Phi}{dt}, \tag{3.11}$$

where w – number of turns in coil.

In order to increase the sensitivity of the coil, one could add greater number of turns, all perpendicular to the wire where current is measured. This approach is taken with Rogowski coil, where all the loops are placed around the wire perimeter (see Figure 3.3), at the same time keeping all loops perpendicular to the wire.

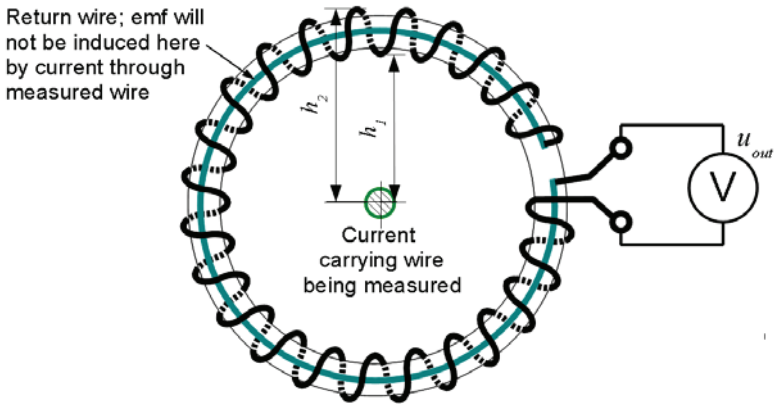

Figure 3.3. Rogowski coil geometry.

It is possible to have a sensor with thousands of turns, but clearly at such high number of turns, there will be questions regarding capacitance and inductance. At low frequency operation, the reactance due to capacitance of the coil is very high (> 1 MΩ) and at the same time the reactance due to inductance is very low (< 10 Ω). In this case their effect is very small and when the sensor coil operation is observed only at low frequencies, the effects due to inductance and capacitance of the coil can be neglected.

Physical expression of inductance in form

$$e = -L\frac{di}{dt} \tag{3.12}$$

sets the relation between the current variation in time and voltage. Using this relation, it is appropriate to define a mutual inductance M as relation between the current passing through the wire observed and the output of the inductive sensor coil as

$$e = -M\ \frac{di}{dt}. \tag{3.13}$$

Taking into account (3.11) and a relation between flux Φ and current I, the value for M can be expressed more precisely. However, as expression of Φ is changing with shape of the loop, the value of M is also different for each shape. For example, for a rectangular loop with flux of

$$\Phi = \frac{\mu_0 \cdot w \cdot l \cdot I}{2\pi} \ln \frac{h_2}{h_1}, \tag{3.8}$$

mutual inductance expression is

$$M = \frac{\mu_0 \cdot w \cdot l}{2\pi} \ln \frac{h_2}{h_1}. \tag{3.14}$$

Mutual inductance is also expressed in henries (H) like regular inductance. Standard unit for inductance can be defined by voltage, current and time [33] as

$$1\,\mathrm{H} = \frac{1\,\mathrm{V} \cdot 1\,\mathrm{s}}{1\,\mathrm{A}}, \tag{3.15}$$

which sets a relation between the current variation rate and the induced voltage value. Output of the inductive sensor coils at low frequencies is indeed a derivative of the variation rate of current, meaning stronger output in case of higher frequencies.

The simplest model of the inductive current sensor can be represented as a voltage source with output in relation to measured current as in a measurement system on Figure 3.4. The external measurement device is presented as voltmeter with internal resistance R_M. Value of R_M is expected to be very large, so that it does not affect the output in this stage. For example, oscilloscope probes have resistance in range of 1 MΩ, which presents a very light load for the sensor coil.

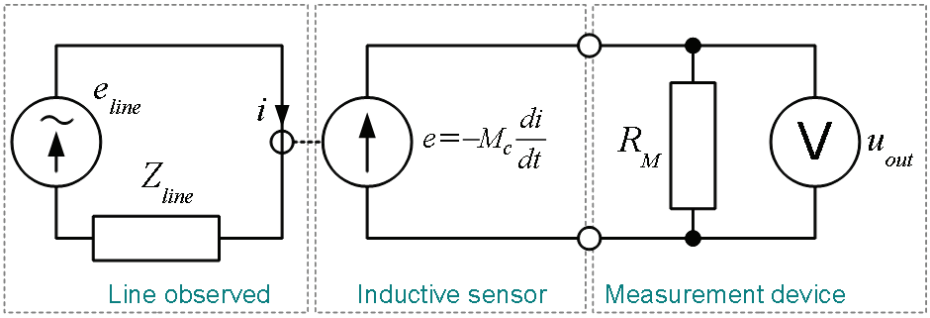

Figure 3.4. Measurement system model circuit for low-frequency operation.

Due to the differentiating nature of inductive sensors, sensitivity characteristics provided for a steady-state, sine waveform measurements is defined as relation to frequency [100]

$$u_{out,RMS} = K_S \cdot i_{line,RMS} \cdot f, \tag{3.16}$$

where $u_{out,RMS}$ – sensor voltage output RMS value; $i_{line,RMS}$ – RMS value of current passing by wire being measured by an inductive sensor; f – frequency of the current measured (Hz); K_S – sensor sensitivity factor (in units V/(A·Hz)).

Air-core inductive sensors such as Rogowski coils implemented for the mains measurements require amplifiers of the output signal due to their relatively low sensitivity compared to other ferromagnetic current transducers (like conventional current transformers). As the inductive sensor output is a differentiation product of the current passing through the wire, integration of (3.13) is performed to obtain the actual current value

$$i = -\frac{1}{M}\int e\, dt\,. \tag{3.17}$$

The amplification and integration of the output has been one of the most common topics in the scientific papers relating to Rogowski air-core inductive sensors [6] [10] [17] [18] [58] [61] [85] [87] [116] [117].

3.4 Summary

The low-frequency inductive sensor model provides the ideal case of the sensor coil operation. It has to be stressed out that this model presents the sensor operation only for low frequencies. The capacitance and inductance have been neglected due to their small effect and this makes the model very simple. As the frequency of the measured current is increasing, effects from inductance and capacitance will be having much greater role and a more complicated model has to be used for describing the operation.

The results obtained with low frequency operation analysis of the inductive sensor however present the basis for calculating the shape of loop. More sensitive the loop is at low frequency, more sensitive it is also for the higher frequency ranges. This means that the mutual inductance value used afterwards will be the same regardless of the frequency of current observed.

4 Medium-frequency model of air-core sensor

The limiting frequency for taking the medium-frequency model of the inductive sensor coil into use depends on several aspects. Most important criteria are associated with the values of reactive components present in the physical build of the coil. Every wire holds some inductance and every two wires some capacitance, the sensor coil presents some self-inductance and self-capacitance.

For low frequency operation, the reactance of an inductive coil is very small compared to other effects; similarly, reactance provided by very small self-capacitance is very high for the low frequency. It could be said that the limits of usage of medium-frequency model would start from 50 kHz. As the frequency rises the reactance values will provide more effect to the operation of the coil. Eventually, the self-inductance and self-capacitance will determine the sensor coil's operation at higher frequency range.

4.1 Components in medium-frequency model

A model with lumped components [10] [93] [125] (Figure 4.1) conforms to actual sensor physical operation – when a high-speed current pulse passes the sensor over a wire being measured, energy is stored in the coil's magnetic field and after this magnetic field of the coil is decaying, as magnetic field energy is used from the coil by external circuitry and stored in the coil's self-capacitance. The energy exchange between the coil self-capacitance and self-inductance can result in resonance.

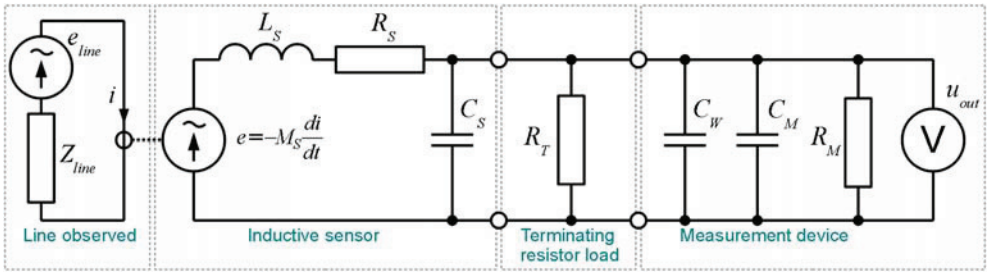

Figure 4.1. Sensor coil medium frequency model.

The model for the medium frequency coil operation (Figure 4.1) [44] [68] [93] [109] is a simple second-order circuit of coil-to-wire mutual inductance M_S, equivalent series inductance L_S and equivalent stray capacitance C_S. The winding wire equivalent series resistance R_S is small, but it is useful to include it also to the medium-frequency model. The sensor coils' mutual inductance is the sum of mutual inductance of the turns and is presented as a source e in the circuit of coils self-components. However, in this circuit model, external components loading the coil also need to be taken into account. First of all, the measurement device is now represented with both resistance R_M and capacitance C_M, and connecting wires or cables have capacitance C_W. Because of resonance, pulse response can have an

oscillating result and for decaying this damping or terminating resistor R_T is added to the circuit. Some authors have suggested some modifications to the model, for example in [97] a model without self-capacitance has been proposed, although it would be insufficient for the medium-frequency analysis.

Following discussion will explain roles and quantities of each of the components present in the sensor model. After this, role on the operation of the sensor coil for each of the components is introduced, as the medium-frequency model analysis will actually present the expected operation bandwidth.

4.1.1 Inductance of the sensor

Sensor coil inductance is one of the terms that describes the coil behaviour and by indirect means, also the coil sensitivity. Inductance by a definition [48] is a relation between current passing through the wire of the coil and magnetic flux as

$$L = \frac{\Phi}{i}, \tag{4.1}$$

where Φ is total flux of coil invoked by current i.

Following examples in "3.2. Magnetic flux and output of inductive loop sensor" it is clear that every geometrical shape produces its own magnetic flux. Inductance calculations therefore present rather complex relations in dependence of geometrical dimensions of the coil.

One of most notable works of inductance calculations have been made by Grover [42], who has presented quite complex calculations using value tables. Exact derivations of loop inductance can be also seen in [79], however for both rectangular coils and circular loops the integration result is again highly complex. Results of calculations using such formulas are presented as references in comparison later in this chapter. Quite common approach to find inductance is also to use empirical formulas for a specified shape and range of dimensions, which might be good in practice, but are not generally acceptable for more detailed analysis. More universal methods for inductance calculations have been presented by Wheeler [119], who has proposed quite short formulas compared to Grover's. The formulas are following general physical geometry characteristics such as main outline dimensions, wire radius and coil length.

The basic weakness of the simplified inductance calculations is that they tend to be inaccurate for the coils with high number of turns. Most trivial induction calculation for multi-turn coils has been presented with using single loop inductance and number of turns squared as [79]

$$L = w^2 \cdot L_{loop}, \tag{4.2}$$

where w – number of turns, L_{loop} – inductance of a single-turn loop.

Such calculation in essence is not capable of including the 3-dimensional field representation with the larger number of turns, therefore it is expected to provide a considerable error for coils having high number of turns. Later in this work it is presented, that it would be reasonable to implement coils with number of turns greater than 10 for achieving good sensitivity. This means that for the basis for the inductance calculations Wheeler's formulas are appropriate, as these consider the effects of higher number of turns in a coil.

As a general approach with inductance both Wheeler's and Grover's calculations, different formulas are provided for short and long coils. The limitation for long coils is that its thickness should exceed its cross-sectional dimensions [120].

The coil geometry outlines presented in Figure 4.2 will be used for inductance analysis, but also for self-capacitance analysis in "4.1.2. Capacitance of the sensors". The main dimensions used in calculations are coil radius r_C or coil length l_C and height h_C, coil total thickness d_C. Wire is described by radius r_w and winding by pitch p_w.

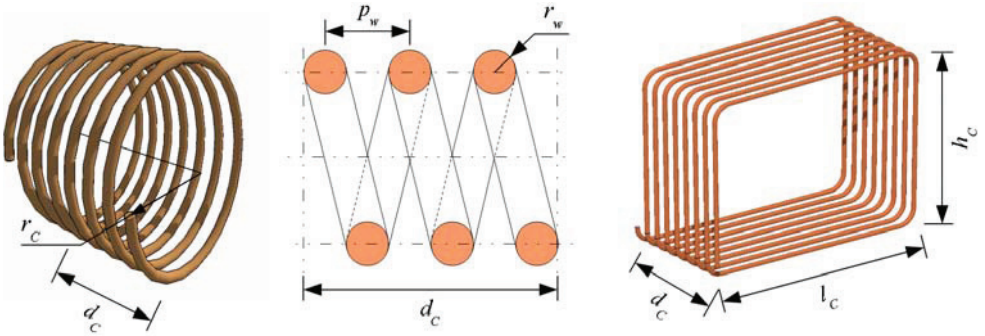

Figure 4.2. Coil geometrical parameters overview for circular and rectangular coils, and coil wire parameters and pitch definition.

Circular coil

When coil wire radius is significantly smaller than loop radius ($r_w << r_C$), inductance of a circular loop can be calculated approximately as [79]

$$L_{loop} = \mu_0 \cdot r_C \cdot \left[\ln\left(\frac{8 \cdot r_C}{r_w} \right) - 2 \right]. \tag{4.3}$$

This relation presents a small variation in loop inductance when the wire diameter is changing. In the sensor application, the expected wire radius is 0,2 mm and coil radius over 3 cm. Calculation results for different wires and coil radiuses has been presented in Table 4.1, along with variation range of inductance when moving from smallest wire diameter to largest wire diameter.

For reference with multi-turn coil calculation formulas, also the simple-case inductance values by (4.2) are provided for a coil with $w = 10$ turns. In this case it is rather trivial, as loop inductance values would have to be multiplied by 100.

Table 4.1. Inductance of a loop for various wire radiuses and coil radiuses.

r_w (mm)	0,05	0,10	0,20	Variation range for loop inductance due to r_w	0,05	0,10	0,20
r_C (mm)	Inductance of loop (4.3) (μH)				Inductance of coil (μH) with $w = 10$ (4.2)		
15	0,109	0,096	0,083	24,0%	10,9	9,6	8,3
25	0,198	0,176	0,154	22,0%	19,8	17,6	15,4
50	0,439	0,395	0,352	19,8%	43,9	39,5	35,2
100	0,965	0,878	0,791	18,0%	96,5	87,8	79,1

As it can be seen from the Table 4.1 the inductance variation due to change of wire radius in these cases remains at 20% range. Effect of wire tends to decrease as the coil dimensions are increasing.

For a multi-turn coil, one could use inductance formula provided by Wheeler [119] for short coils (as the sensor coil is expected to be *short* with $r_C > d_C$)

$$L = \mu_0 \cdot w^2 \cdot r_C \cdot \left[\ln\left(1 + \frac{\pi \cdot r_C}{d_C}\right) + \frac{1}{2{,}3 + \frac{1{,}6 \cdot d_C}{r_C} + 0{,}44\left(\frac{d_C}{r_C}\right)^2} \right], \qquad (4.4)$$

which does not include the effect of wire radius. To explain the effect of the (4.4), sample calculations have been carried out based on the same coil radius data as above. Difference here though is the physical thickness of coils growing with increase of number of turns. In the calculated example below, coil thickness is assumed for a close-packed coil with extremely thin wire insulation as

$$d_C = r_w \cdot w. \qquad (4.5)$$

Calculation results for close-packed coils with $w = 10$ turns are presented in Table 4.2. This table also presents a difference to calculations by (4.2).

Table 4.2. Inductance of a close-packed coil of 10 turns for various wire radiuses.

r_w (mm)	0,05	0,1	0,2	Variation range for loop inductance due to r_w	0,05	0,1	0,2
r_C (mm)	Inductance of coil with $w = 10$ (4.4) (μH)				Comparison to results by (4.2) (see Table 4.1)		
15	8,11	6,83	5,59	31,1%	74,4%	71,2%	67,4%
25	15,1	13,0	10,8	28,2%	76,4%	73,6%	70,3%
50	34,5	30,2	25,9	25,0%	78,7%	76,4%	73,6%
100	77,7	69,1	60,4	22,3%	80,6%	78,7%	76,4%

It can be seen that for the close-packed coil, the inductance variation calculated for a multi-turn coil will be higher than for a loop calculation.

Another result to point out from Table 4.2 is that the comparison to ideal loop inductance case is presenting quite same range difference, in present case the average difference is 74,8%. This trend continues also for a larger number of turns and for all the coil radius and wire radius values presented. This relation becomes very useful later when the sensor coil design is discussed in "6.4. Sensor electrical design".

For design aspects, it is also valuable to point out that formula (4.4) can be used to present the effect of increased wire pitch to the overall inductance. In Table 4.3 similar coils to the ones presented above have been used, and as comparison a close-packed coil with pitch equal to wire diameter (for r_w = 0,2 mm wire) has been provided.

Table 4.3. Inductance of a coil of 10 turns for various wire pitch values.

Winding pitch p_w (mm)	0,4	1,0	2,0	4,0	Inductance variation (close-packed vs. p_w = 4 mm)
Thickness d_C (mm)	3,6	9,0	18,0	36,0	
r_C (mm)	Inductance of coil (μH) with w = 10				
15	5,59	4,19	3,09	2,13	61,9%
25	10,84	8,43	6,48	4,71	56,6%
50	25,91	20,96	16,86	12,97	50,0%
100	60,42	50,38	41,93	33,72	44,2%

Having a coil of greater length than close-packed coil will bring benefit in decreased inductance value. The decrease of close to 2 times compared to the close-packed coil can be achieved when the pitch is 4 mm, which in implementation would mean quite thick coil. Furthermore, the decrease of inductance due to added pitch shows decreasing trend as the coil radius is increasing.

Rectangle coil

The discussion about circular coil inductance can be also widened for the rectangle coil shapes. A rectangle loop inductance can be calculated as [79]

$$L_{loop} = \frac{\mu_0}{\pi}\left[-h_C \cdot \ln\left(1+\sqrt{1+\left(\frac{l_C}{h_C}\right)^2}\right) + h_C \ln\frac{2l_C}{r_w} - \right.$$
$$\left. -l_C \cdot \ln\left(1+\sqrt{1+\left(\frac{h_C}{l_C}\right)^2}\right) + l_C \ln\frac{2h_C}{r_w} + 2\sqrt{h_C{}^2 + l_C{}^2} - 2l_C - 2h_C \right], \quad (4.6)$$

which is quite complicated for a more general analysis. One simplification that can be made, is to observe a square coil, where length and height of the coil are equal ($l_C = h_C$). In case $r_w << l_C$ (4.6) can be reduced to [79]

$$L_{loop} = \frac{2 \cdot \mu_0 \cdot l_C}{\pi} \left[\ln\left(\frac{l_C}{r_w}\right) - 0{,}774 \right]. \tag{4.7}$$

The loop inductance for the square coil presents similar relation to coil wire size as results for the circular coil in Table 4.1.

Inductance of a multi-turn square coil can be found by [119]

$$L = \frac{2 \cdot \mu_0 \cdot w^2 \cdot l_C}{\pi} \cdot \left[\ln\left(1 + \frac{\pi \cdot l_C}{2 \cdot d_C}\right) + \frac{1}{3{,}64 + \frac{4 \cdot d_C}{l_C} + 0{,}51\left(\frac{2 \cdot d_C}{l_C}\right)^2} \right] \tag{4.8}$$

and this is very similar to the circular coil inductance formula (4.4). A valuable point to investigate here again is the relation of applying loop inductance from (4.7) and coil inductance value by (4.2). Calculation values for such analysis have been provided in Table 4.4.

Table 4.4. Inductance of a close-packed square coil of 10 turns for various wire radiuses.

r_w (mm)	0,05	0,1	0,2	Variation range for inductance due to r_w	0,05	0,1	0,2
l_C (mm)	Inductance of coil (μH) by (4.8) with w = 10				Comparison to results by (4.7) and (4.2)		
15	9,93	8,30	6,69	31,1%	73,6%	70,1%	65,7%
25	18,6	15,8	13,1	28,2%	75,7%	72,8%	69,1%
50	42,7	37,2	31,7	25,0%	78,1%	75,7%	72,8%
100	96,4	85,4	74,3	22,3%	80,1%	78,1%	75,7%

The average difference from calculation with (4.8) according to Table 4.4 is 74%. Like in case of results presented in Table 4.2, for all coil and wire radius values and variety of number of turns, the difference to such comparison still remains almost the same. The simplifications that can this can provide for the sensor coil design procedures are described further in “6.4. Sensor electrical design”.

As for rectangular coils that are not square-shaped, there seems not to be a simpler universal inductance calculation than (4.6). Reason for this is the vast variety possible coil length l_C to coil height h_C ratio values. For sensor application though, some shape forms could be analyzed to determine the effect of shape to the inductance value. In the next example, a set of different loop shapes are compared against a square loop with side length of 100 mm. All rectangular loop shapes are selected in a way that the loop area would remain the same. Calculations results of

such loops' inductance are presented in Table 4.5 and Figure 4.3, using formula (4.6) and wire radius $r_w = 0{,}1$ mm. The ratio of the rise of the inductance when using the non-rectangular coil is presented as relative inductance.

Table 4.5. Inductance of rectangular loop and relative inductance compared to square loop.

l_C (mm)	h_C (mm)	Shape ratio l_C / h_C	Inductance L_{loop} (μH)	Relative inductance compared to square coil
100,0	100,0	1,0	0,491	1,00
109,9	91,0	1,2	0,493	1,00
122,0	82,0	1,5	0,499	1,02
133,3	75,0	1,8	0,508	1,04
158,7	63,0	2,5	0,536	1,09
200,0	50,0	4,0	0,594	1,21
312,5	32,0	9,8	0,778	1,59
400,0	25,0	16,0	0,925	1,89

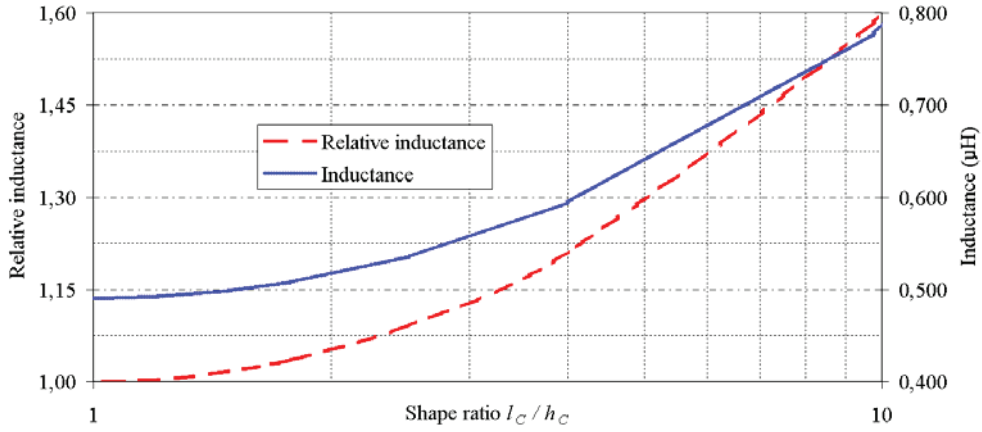

Figure 4.3. Inductance of rectangular loop and relative inductance compared to square loop.

Based on results from Table 4.5 and observable from Figure 4.3 it can be concluded that the shape ratio of the rectangle loop has relatively weak influence on the value of loop inductance. Shape ratio l_C / h_C of 4 will increase the inductance value by roughly 20%; as all expected sensor coil shapes should have shape ratio less than 4, the inductance increase due to stretching of the rectangular loop should provide only minor influence.

4.1.2 Capacitance of the sensors

The turn-to-turn capacitance has been first investigated by engineers interested in evaluation of high-frequency performance of solenoids for radio-communication devices. There are both empirical [69] [70] and analytical [77] approaches

presented, discussed also below in this chapter. Today more interest for coil capacitance calculation has been shown by researchers of power electronics [67] [40] to provide a better approach for inductive components modelling. For the sensor approach, both of these approaches are analyzed but rather controversly, none of them seem to provide satisfying solution about the coil self-capacitance values. Therefore, some practical measurements have been presented, to provide some starting points for coil capacitance assessment.

The analysis here is limited by some borders of the inductive sensor application presented in context of this thesis. Namely, the small wire dimensions refer to the possibility to have the coils made as single-layer coils. It can be shown, that this kind of approach is actually beneficial to the coil capacitance estimations for the sensor coil design.

Analytical approaches

One of the essential works for coils self-capacitance as been presented in the work of Palermo [77], providing a good overview of the previous achievements and providing an approach to observe the self-capacitance C_C of the coil as capacitance of parallel rings, having the capacitance between them just as a capacitance of 2-wire transmission line. This calculation uses a formula

$$C_C = \frac{l_w \cdot \pi \cdot \varepsilon}{\operatorname{acosh}\left(\frac{p_w}{2 \cdot r_w}\right)} = \frac{2 \cdot \pi^2 \cdot \varepsilon \cdot r_C}{\ln\left(\frac{p_w}{2 \cdot r_w} + \sqrt{\left(\frac{p_w}{2 \cdot r_w}\right)^2 - 1}\right)}, \tag{4.9}$$

where l_w – winding wire length of single turn, for a circular coil $l_w = 2 \cdot \pi \cdot r_C$.

Equation (4.9) as well as author itself [77] state, that there is evidence that the coil capacitance is independent of number of turns and rather most important factors are pitch and wire diameter. It has to be agreed that the wire diameter might be one of the aspects that defines the capacitance, a point that is neglected, for example, in [69] [70]. The transmission line approach has seen much criticism [69] [70] [73] and same papers present, that the capacitance of the coil is relatively constant for various parameters, like coil pitch p_w.

Analytical approach is picked up where it was left off, in a new round in [40] [41] [67]. This time the transmission line capacitance is defined for the turn-to-turn capacitance, however the turn-to-turn capacitance is presented as a chain of capacitors connected in series (see Figure 4.4), and sum of capacitance is

$$C_C = \frac{C_{tt}}{w - 1}, \tag{4.10}$$

where C_{tt} is turn-to-turn capacitance calculated with the same equation as (4.9).

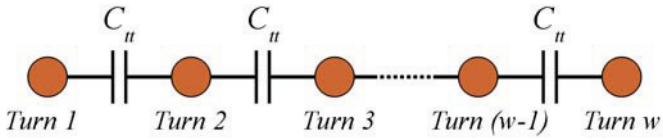

Figure 4.4. Concept of distributed capacitance as presented in [40].

Turn-to-turn capacitance has also been presented for the distributed line models of inductive coils [31]. It is on the other hand in some occasions presented [93] that value for this capacitance is so small that it does not need to be taken into account.

The approach of chained capacitors has a definite controversy to the measurement results (see below in this chapter), as it refers that the capacitance should decrease very fast when the number of turns is increased. Results do not confirm the validity of this even for a lower number of turns, therefore such equation cannot very likely be used for reliable estimation of self-capacitance of the air-core sensor coils.

A more complex self-capacitance analytical approach is presented in [73], but its complexity and the fact that its calculation relies on input from values on graphs, makes it quite inaccessible for more general analysis.

Empirical approaches

One of the well known formulas for air-core coil self-capacitance calculation is provided by Medhurst [69] [70]. This empirical formula is provided as a result of a larger practical investigation, carried out on a variety of coils of different geometrical build-up. The coil total capacitance estimation given as

$$C_C = 2 \cdot r_C \left(0{,}1126 \cdot \frac{d_C}{2 \cdot r_C} + 0{,}08 + \frac{0{,}27}{\sqrt{d_C / 2 \cdot r_C}} \right) \tag{4.11}$$

presents a very simple formula using coil thickness and coil radius as main variables.

Engineers in the high-frequency fields, also working with different inductive coils, rely on different tables and empirical formulas with many different coefficients. Such data is updated from time to time to provide better correlation when there is more data available. In the ultra-high-frequency engineering fields some more detailed FEM-software tools are used, which take all field effects into account based on the geometry, and can provide solutions to designed geometries.

Practical testing

When the authors of previously discussed methods present practical measurement results to prove their validity, it though cannot be validated for coil forms investigated for inductive sensors within this thesis. Instead, in this thesis, some measurement-based simple estimation on capacitance is used, as there are quite

large differences when comparing the results of proposed theoretical approaches to the measurement results.

Measurements were carried out using test setup presented in Figure 4.5. To eliminate the effect of external components to as much as possible extent, coils under testing were excited using magnetic field coupling and this way there was no galvanic coupling the signal generator or cables. Only differential active probe was connected to the output, whose capacitance was confirmed to be 0,9 pF in testing.

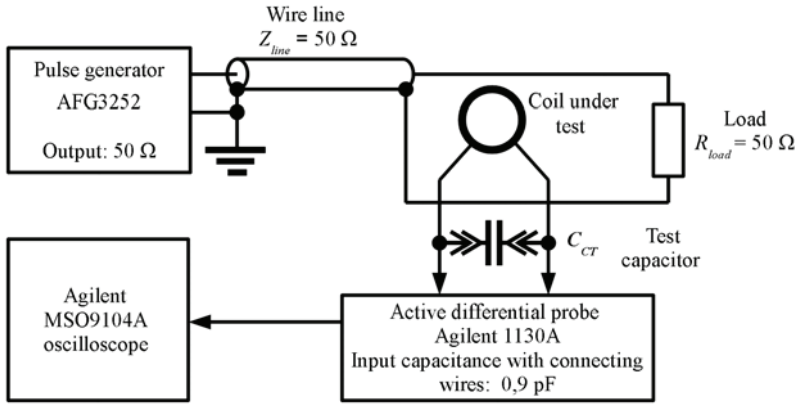

Figure 4.5. Coil self-capacitance measurement setup overview.

The coils were loaded by only probe and then also additional capacitance was added. For excitation, square-wave pulses from the signal generator were provided in a loop near the coil itself, and oscillation frequency of the impulse response of the coil was recorded [82]. By measuring the coil inductance accurately with precise meter, the variable to determine from the testing results was coil self-capacitance (plus probe capacitance, which was subtracted later). Capacitance was calculated by

$$C_C = \frac{1}{4 \cdot \pi^2 \cdot L \cdot f_{tresp}{}^2} - C_{probe}, \tag{4.12}$$

where C_{probe} – probe capacitance, f_{tresp} – resonant transient oscillation frequency of the coil.

For practical measurements of capacitance, some round and rectangle coil shapes have been analyzed. Outlines of the coils observed for self-capacitance have been presented in Figure 4.6 and the coils' geometrical data is presented in Table 4.6 along with measurement results.

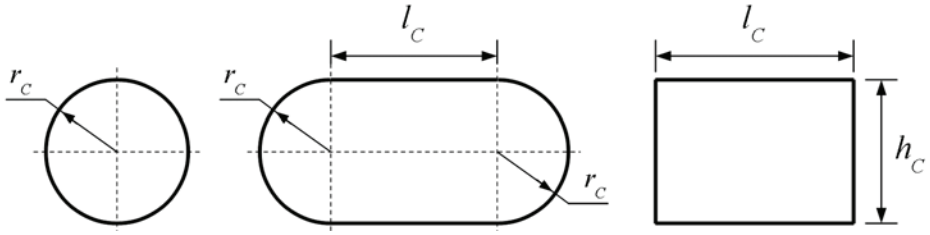

Figure 4.6. Outlines of coils used for measurement of self-capacitance.

Table 4.6. Comparison of coil self-capacitance measurement results and calculations with (4.10), (4.11).

Coil dimensions						Measured capacitance (pF)	Capacitance by (4.10) (pF)	Capacitance by (4.11) (pF)
r_C (mm)	l_C (mm)	h_C (mm)	p_w (mm)	r_w (mm)	w			
50	-	-	8	0,25	4	1,34	0,840	6,58
50	-	-	4	0,25	4	1,28	1,05	8,73
50	-	-	4	0,25	10	1,77	0,351	5,71
50	-	-	2	0,25	10	1,98	0,470	7,37
50	-	-	0,6	0,25	10	4,10	1,55	12,5
50	-	-	0,6	0,1	10	2,19	0,551	12,5
50	-	-	0,3	0,1	50	2,69	0,185	8,01
-	55	50	8	0,1	4	1,02	0,562	-
-	105	20	8	0,1	4	1,08	0,669	-
12,5	75	-	8	0,1	4	1,14	0,610	-

Measurement results of the coil self-capacitance in present that the expected value for a multi-turn coil of different shapes is expected to remain from 1 up to 4 pF. This is kept in mind for this work; coils with low number of turns could be observed with 2 pF and coils with high number of turns will be referred to have around 3 pF of self-capacitance. It should be pointed out that in present case assuming 2 pF for coil self-capacitance provides less error than using both (4.10) or (4.11) for calculations.

4.1.3 Coil wire resistance

For the medium-frequency model, it is sufficient to specify the wire resistance as wire DC resistance. This can be calculated as

$$R_S = \frac{l_{w,loop} \cdot w \cdot \rho}{A_w}, \tag{4.13}$$

where $l_{w,loop}$ – length of wire in single loop; w – number of loops (turns) in coil; ρ – characteristic resistance of the wire; A_w – cross-section area of the coil wire.

The coil resistance is quite small, and generally its resistance is less than the value of the terminating resistor. In high-frequency model, this resistance is increasing

due to skin-effect (see “5.2. Skin effect”) which causes current to be diverted only to the outer layers of the wire. It should be noted that at frequencies the medium frequency model is targeting, the skin effect for most wire dimensions is quite small and this can be neglected.

4.1.4 Termination resistor

A termination or damping resistor is an external component to the inductive sensor system. Usually in the system, coil is fixed by its geometrical characteristics and measurement system relies on parameters of components available. In this view, terminating resistor is a component that is most variable by the designer of the system containing inductive sensor and it does provide several possibilities for shaping the frequency response of the sensor.

The terminating resistor does have to be selected carefully and it has been widely discussed in many papers [71] [93] [111] dealing with circuit models of inductive sensors. Still, in the papers available mostly trivial analysis for a proper value of the terminating resistance can be seen. Having very small value of resistance on one hand seems to provide a very wide bandwidth for measurement [93] [111], however this is also the factor that significantly decreases the output sensitivity. When using coil without termination resistor, or when its resistance value is very high, the output oscillations of the LC-circuit are not damped, thus the output of the sensor coil will be very noisy.

Selection of the terminating resistance value is also a task of great importance to the sensor design and will be discussed in detail in “4.3.3. Damping and effect on bandwidth”.

4.1.5 Measurement system

Measurement system medium-frequency model consists of its equivalent resistance and capacitance. Latter is chosen as most measurement units available exhibit capacitive nature at their input. Based on discussion in “4.1.2. Capacitance of the sensors”, sensor coil’s self-capacitance is in range of $2 \ldots 3$ pF. This means for example that if an oscilloscope probe having capacitance of 10 pF is connected to the coils output, it will present significant effect to the coils behaviour. Cables connecting sensor coil to the measurement device can also exhibit significant capacitance.

Measurement system inclusion most directly affects the coil operation. Capacitance of the external components is critical in calculation of circuits’s resonance (see Figure 4.7) and frequency response of the overall system. Medium-frequency model provides quite simple way for doing this – capacitances of measurement system can be simply added together with the coil self-capacitance. Resistance of the measurement system is significantly higher (typically > 1 MΩ) than, for example, terminating resistance (typically < 1 kΩ) and thus the overall coil loading

resistance is practically not affected by the inclusion of the measurement system resistance.

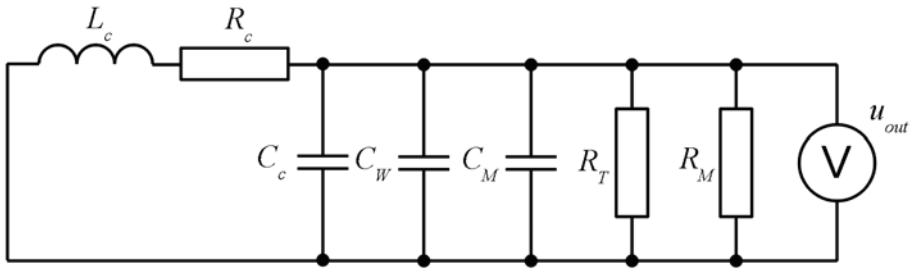

Figure 4.7. Coil resonant LRC circuit model with measurement system.

Most material available on inductive sensor models neglects the capacitance of the measurement system, with few exceptions the model circuits are described with measurement impedance [108]. In [113] a model is described with external capacitance, but it is not clear if this represents measurement system. In [17] it is stated that overall capacitance includes output cable capacitance, which indeed is a parameter of measurement system. Both measurement system capacitance and resistance are provided in [39]. A scarce model of sensor with capacitive load is provided in [9]. Measurement system resistance is usually quite high and its effect is very small, thus it can be neglected. Still [22] provides the model with measurement resistance, in [96] it is referred to as input resistance.

A solution to make the measurement system with as little effect as possible would be to use low-capacitance measurement devices, having only few picofarads of input capacitance. Active and differential probes for laboratory use provide as low as less than 1 pF input [1]. High-speed operational amplifiers, as well as digital to analog converters (DAC-s) also provide input capacitance in range from 2 to 5 pF [2].

One often overlooked aspect in the sensor coil measurement system is the capacitance of the cables. Assuming coil output wires with radius r_w of 0,2 mm are in parallel with spacing $s_w = 10$ mm, using cable insulation material relative dielectric permittivity value of 4 the cable capacitance per unit length can be calculated as [48]

$$C'_W \approx \frac{\pi \cdot \varepsilon_w \cdot \varepsilon_0}{\cosh^{-1}\left(\frac{s_w}{2 \cdot r_w}\right)} = 28{,}4 \text{ pF/m}. \tag{4.14}$$

The wire with length of only 3 cm would produce around 1 pF additional capacitance. Considering the single-layer coil total self-capacitance also in the range of couple picofarads, this can already provide significant effect to the system behaviour. Only way to minimize the effect of connecting wires is to keep these as short as possible.

4.2 Sensor model as second order transfer function

Observing inductive and capacitive non-linear components in the model circuit, one has to create quite difficult equations using integral and differential products of current and voltage of the components. Such time-varying formulas have been presented in several sources [19] [109] [111], however further analysis using such complex representation is difficult. In present case, it is much more beneficial to turn to models in frequency domain (known also as Laplace domain). This way, much about the properties of the sensor can be concluded and approximations can be made more easily where applicable.

4.2.1 Transfer function in Laplace domain

Laplace transform presents a rather good method to analyze solutions to differential and integral equations. In this way, all functions in time are transferred to functions in complex frequency as [53]

$$F(s) = \int_{-\infty}^{\infty} f(t) \cdot e^{-st} dt \,, \tag{4.15}$$

where $f(t)$ – function of time; $F(s)$ – function of complex number s; $s = \sigma + j\omega$, where σ and ω are real values.

The complex number s in engineering applications is called complex frequency and this provides a good ground for frequency analysis, hence also named *frequency domain analysis*. The Laplace transform can be applied to both signals, systems, physical quantities and also to electric circuit components. It should be pointed out that later in text, Laplace transformation is not exquisitely performed. Instead, time values (like $u(t)$) are considered to have been transformed to frequency domain when they are noted as $U(s)$. In another expression

$$u(t) \xrightarrow{L} U(s) \,. \tag{4.16}$$

Inverse Laplace transform from frequency domain to time domain is be expressed as

$$U(s) \xrightarrow{L^{-1}} u(t) \,. \tag{4.17}$$

Instead of Kirchhoff's laws, a different method for the circuit behaviour is used, observing transfer function of the circuit, which sets a relation between some input and some output values as

$$Y(s) = TF(s) \cdot X(s) \,, \tag{4.18}$$

where $Y(s)$ – output function; $TF(s)$ – transfer function; $X(s)$ – input function.

In context of this work, $X(s)$ and $Y(s)$ represent signals while $TF(s)$ presents the properties of an electrical circuit. Transfer function further analysis is made upon this function's numerator and denominator analysis

$$TF(s) = \frac{N}{D} = \frac{(s + z_0)(s + z_1)...(s + z_n)}{(s + p_0)(s + p_1)...(s + p_m)}, \tag{4.19}$$

where N – numerator expression; D – denominator expression; $z_0 ... z_n$ are equation system zeros and $p_0 ... p_m$ – equation system poles, n – number of zeros in equation system and m – number of poles in equation system.

Poles in this representation are the solutions to equation

$$(s + p_0)(s + p_1)...(s + p_m) = 0 \tag{4.20}$$

and zeros are solutions to the equation

$$(s + z_0)(s + z_1)...(s + z_n) = 0\,. \tag{4.21}$$

Basically, the poles represent integration products while zeros represent differentiation products. Analysis on values for poles and zeros is used for observing the transfer function behaviour for different operating frequencies and the system dynamics.

4.2.2 Calculation of the transfer function

A method for calculating transfer function for a magnetic loop sensor circuit model used in this thesis is based on topological formulas, idea that was introduced by S. J. Mason [66]. The topological formula approach is one of the simplest ways of establishing transfer functions of a circuit. Circuit dynamics information is provided, when the transfer function is build using elements of Laplace transform. This provides healthy simplification, as the differential equations of the system can be avoided in the calculations.

The transmission function will be built in a form

$$TF = \frac{N}{D}, \tag{4.22}$$

where N – numerator, D – denominator.

In present case voltage transfer is calculated, input of the circuit will be a source with the equivalent conductance of ∞ (infinity). Output of the circuit would be a voltmeter with equivalent conductance of 0. The circuit model representation for voltage transfer calculation is presented in Figure 4.8. In this model, all similar components are grouped, meaning capacitors in parallel are represented as C_E ($= C_S + C_W + C_M$) and resistors in parallel are R_E ($= R_T \| R_M$).

To start with, it should be specified that the calculations will be based on conductance values, which requires substitutions as specified in Table 4.7.

Table 4.7. Conductance values of different components.

Component	Conductance in time domain	Conductance in Laplace domain
Resistance	$G_{Rt} = \frac{1}{R}$	$G_R = \frac{1}{R}$
Capacitance	$G_{Ct} = j \cdot \omega \cdot C$	$G_C = s \cdot C$
Inductance	$G_{Lt} = \frac{1}{j \cdot \omega \cdot L}$	$G_L = \frac{1}{s \cdot L}$

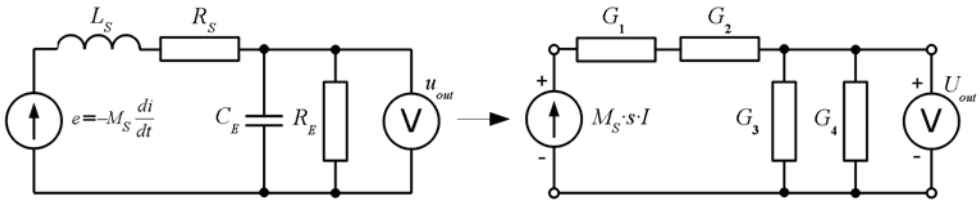

Figure 4.8. Transformation of the sensor model circuit.

Development of the transfer function can start with denominator N expression. Denominator overall expression can be written as

$$D = \sum C'_k D'_k , \tag{4.23}$$

where C'_k is value of transmission path and D'_k is its cofactor.

To find the conductance of transmission path the source and meter should be replaced with equivalent conductances. Three points in the circuit can now be identified, that are not short-circuited. Let us mark these points as "a", "b", and "c" (see Figure 4.9).

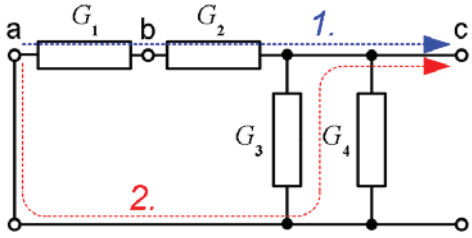

Figure 4.9. Calculation of transmission path conductance paths.

Next, a source point and target point should be specified. Let the source point be "a" and target "c". In this way, two paths from "a" to "b" can be identified:

- Path "1." is through G_1 and G_2 in series, providing $C'_1 = G_1 \cdot G_2$.
- Path "2." is through G_3, G_4 in parallel, providing $C'_2 = G_3 + G_4$.

To find cofactors, the taken path should be short-circuited. Resulting circuits for both paths are presented in Figure 4.10.

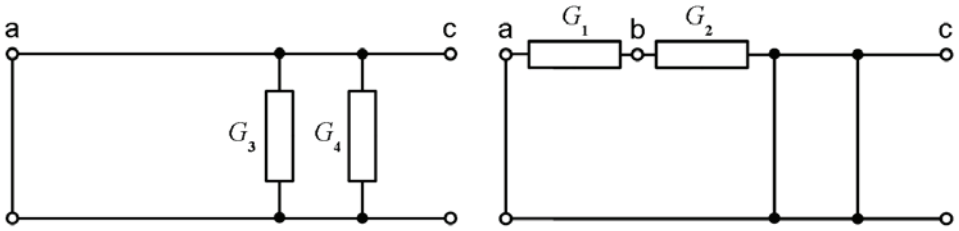

Figure 4.10. Cofactor schematic for path "1." (on the right) and for path "2." (on the left).

It can be observed, that the circuit of first schematic does not provide any points that are not short-circuited, providing cofactor $D'_1 = 1$. For the second path, there is a point "b" in the circuit, that is not short-circuited to "a" or "c". Connection from "a" to "b" is by a path through G_1 and G_2 in parallel (this also equals to two paths – through G_1 and G_2, which are summed together), which provides cofactor of $D'_2 = G_1 + G_2$. Value of denominator in this case is

$$D = C'_1 \cdot D'_1 + C'_2 \cdot D'_2 = G_1 \cdot G_2 + (G_3 + G_4)(G_1 + G_2). \tag{4.24}$$

Next, the numerator is searched in similar form as denominator (4.23)

$$N = \sum C'_k D'_k, \tag{4.25}$$

To find the numerator, the original circuit should be observed. Now, all paths from source to voltmeter should be found. In this circuit, only one path can be identified (see Figure 4.11).

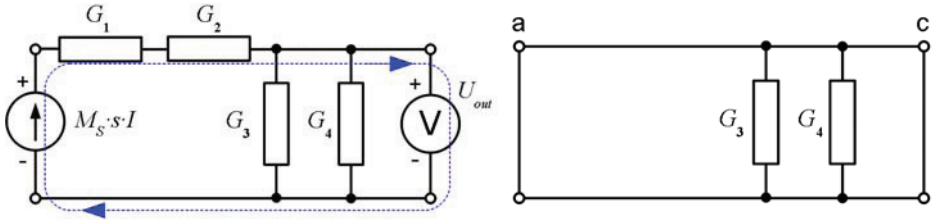

Figure 4.11. Calculation of transmission chain conductance for numerator (on the left) and cofactor circuit for numerator (on the right).

All values of conductances along this path should be multiplied, in this path it provides $C'_1 = G_1 \cdot G_2$. To find the cofactor, the taken path should be shorted (see Figure 4.11). It can be observed, that the circuit of first schematic does not provide any points that are not short-circuited, providing cofactor $D'_1 = 1$. The resulting numerator is

$$N = C'_1 \cdot D'_1 = G_1 \cdot G_2. \tag{4.26}$$

Resulting transfer function is

$$TF = \frac{N}{D} = \frac{G_1 \cdot G_2}{G_1 \cdot G_2 + (G_3 + G_4)(G_1 + G_2)} \tag{4.27}$$

representing the circuit's transfer function with unit value input. The source specifies the input value, this means that the output can be obtained when circuit transfer function is multiplied with input value

$$U_{out}(s) = U_{in}(s) \cdot TF = s \cdot M_S \cdot I(s) \cdot TF, \tag{4.28}$$

where U_{in} is the source voltage value, $U_{in} = s \cdot M_S \cdot I$.

Now, the conductances used can be replaced by actual values based on circuit components

$$U_{out}(s) = \frac{s \cdot M_S \cdot I(s) \cdot \frac{1}{s \cdot L_S} \cdot \frac{1}{R_S}}{\frac{1}{s \cdot L_S} \cdot \frac{1}{R_S} + \frac{1}{s \cdot L_S} \cdot \frac{1}{R_E} + \frac{1}{s \cdot L_S} \cdot s \cdot C + \frac{1}{R_S} \cdot \frac{1}{R_E} + \frac{1}{R_S} \cdot s \cdot C}, \tag{4.29}$$

which can be further developed into

$$U_{out}(s) = \frac{s \cdot M_S \cdot I(s)}{L_S \cdot C_E \left[s^2 + \left(\frac{1}{R_E \cdot C_E} + \frac{R_S}{L_S} \right) s + \left(\frac{1 + \frac{R_S}{R_E}}{L_S \cdot C_E} \right) \right]}. \tag{4.30}$$

Other transfer functions referred in this paper are calculated using the same method. However, in text the transfer function is not specified, only the resulting forms of transfer function are provided.

4.2.3 Poles and zeros of the model

For analysis of the circuit behaviour poles and zeros for the circuit transfer function should be known. These are the solutions to the transfer function numerator and denominator polynomials as presented in (4.20) and (4.21). For solving such equations, (4.30) can be rewritten as

$$U_{out}(s) = \frac{s \cdot M_S \cdot I(s)}{L_S \cdot C_E \left[s^2 + \left(\frac{L_S + R_S \cdot R_E \cdot C_E}{R_E \cdot C_E \cdot L_S} \right) s + \left(\frac{R_S + R_E}{R_E \cdot L_S \cdot C_E} \right) \right]}. \tag{4.31}$$

There is one zero for this function, at frequency $z_1 = 0$. Frequencies of poles can be found at frequencies of

$$p_1, p_2 = \frac{-\frac{L_S + R_S \cdot R_E \cdot C_E}{R_E \cdot C_E \cdot L_S} \pm \sqrt{\left(\frac{L_S + R_S \cdot R_E \cdot C_E}{R_E \cdot C_E \cdot L_S} \right)^2 - 4 \left(\frac{R_S + R_E}{R_E \cdot L_S \cdot C_E} \right)}}{2}. \tag{4.32}$$

Providing expected values of $C_E \approx 10^{-11}$ F and $L_S \approx 10^{-4}$ H, some simplification can be made. Observing the terms under square root, the function can be simplified without significant error

$$p_1, p_2 = \frac{-\frac{L_S + R_S \cdot R_E \cdot C_E}{R_E \cdot C_E \cdot L_S} \pm \sqrt{\left[\frac{L_S + R_S \cdot R_E \cdot C_E}{R_E \cdot C_E \cdot L_S} - \frac{2\left(R_S + R_E\right)}{L_S + R_S \cdot R_E \cdot C_E}\right]^2}}{2}. \quad (4.33)$$

Using this, the poles of the system can be calculated as

$$p_1 = -\frac{R_S + R_E}{L_S + R_C \cdot R_E \cdot C_E}, \quad (4.34)$$

$$p_2 = -\frac{L_S + R_S \cdot R_E \cdot C_E}{R_E \cdot C_E \cdot L_S} - \frac{R_S + R_E}{L_S + R_S \cdot R_E \cdot C_E}. \quad (4.35)$$

These poles present the angular frequency value, for obtaining frequency values of poles these have to be divided by 2π:

$$f_{p1} = \frac{\omega_{p1}}{2\pi} = \frac{1}{2\pi} \cdot \frac{R_S + R_E}{L_S + R_S \cdot R_E \cdot C_E}, \quad (4.36)$$

$$f_{p2} = \frac{\omega_{p2}}{2\pi} = \frac{1}{2\pi}\left(\frac{L_S + R_S \cdot R_E \cdot C_E}{R_E \cdot C_E \cdot L_S} + \frac{R_S + R_E}{L_S + R_S \cdot R_E \cdot C_E}\right). \quad (4.37)$$

A simplification to the frequency calculations has been presented in [111]

$$f_{p2} \approx \frac{1}{2\pi} \frac{L_S + R_S \cdot R_E \cdot C_E}{R_E \cdot C_E \cdot L_S}, \quad (4.38)$$

as it can be expected that for the sensor design the bandwidth is quite wide, this means also that the lower frequency is very low compared to high frequency and this simplification would provide only an error below 1%. The representation (4.37) can be rather useful for understanding design aspects of the sensor coil.

4.3 Characteristics of the sensor based on the transfer function analysis

Second order transfer function can be written as [53]

$$TF(s) = \frac{{\omega_n}^2}{s^2 + 2 \cdot \xi \cdot \omega_n \cdot s + \omega_n}, \quad (4.39)$$

where ω_n – natural angular oscillating frequency; ξ – damping factor.

In case of the medium-frequency inductive sensor model, the characteristic factors ω_n and ξ can be defined from the transfer function model from (4.30)

$$U_{out}(s) = \frac{\frac{s \cdot M_S}{L_S \cdot C_E}}{s^2 + \left(\frac{1}{R_E \cdot C_E} + \frac{R_S}{L_S}\right)s + \left(1 + \frac{R_S}{R_E}\right) \cdot \frac{1}{L_S \cdot C_E}} I(s), \tag{4.40}$$

from which the value for the term ω_n can be expressed as

$$\omega_n = \frac{1}{\sqrt{L_S \cdot C_E}} \cdot \tag{4.41}$$

The part of the $TF(s)$ defining the damping rate

$$\left(\frac{1}{R_E \cdot C_S} + \frac{R_S}{L_S}\right) = \frac{L_S + R_S \cdot R_E \cdot C_E}{R_E \cdot C_E \cdot L_S} = 2 \cdot \zeta \cdot \omega_n \tag{4.42}$$

can be expanded into

$$2 \cdot \zeta = \frac{\sqrt{L_S} \cdot \sqrt{L_S} + R_S \cdot R_E \cdot \sqrt{C_E} \cdot \sqrt{C_E}}{R_E \cdot \sqrt{L_S} \cdot \sqrt{C_E}} = \frac{1}{R_E}\sqrt{\frac{L_S}{C_E}} + \frac{R_S \cdot R_E}{R_E}\sqrt{\frac{C_E}{L_S}}. \tag{4.43}$$

Investigating the terms described for the sensor coils intended for quite high frequency measurements, the expected values for C_E are in range of 10 pF and L_S in 10 μH. The expected values for the described parts of equation are

$$\sqrt{\frac{L_S}{C_E}} \approx 10^3 \; ; \sqrt{\frac{C_E}{L_S}} \approx 10^{-3} \cdot \tag{4.44}$$

This means that the second part of the sum is expected to provide only a fraction of the first part of sum. It is safe to define, that it does not provide significant error if damping factor was defined as

$$\xi \approx \frac{1}{2 \cdot R_E}\sqrt{\frac{L_S}{C_E}}. \tag{4.45}$$

4.3.1 Resonance and damping

Resonance of the second order circuit is seen when two poles provide conjugate complex pair. This means that when solving the characteristic equation in the denominator

$$s^2 + 2 \cdot \xi \cdot \omega_n \cdot s + \omega_n = 0 \tag{4.46}$$

provides poles at

$$p_1, p_2 = -\zeta \cdot \omega_n \pm j \cdot \omega_n \sqrt{1 - \xi^2} \tag{4.47}$$

and damping rate $\xi < 1$. In this case the circuit is defined as undamped and has some decaying oscillations until limiting value $\xi = 0$, when the oscillations are undamped. Damping factor below zero, i.e. $\xi < 0$ causes the circuit to be unstable; however in case of inductive sensor this is rather impossible. The expected minimum value for damping in case of real coil will be well below 1, but as there is always some R_T value, so the $\xi > 0$ will always be guaranteed.

For second order circuits, damping $\xi = 1$ defines the limit where oscillations do not occur if the system is subjected to step or impulse. When $\xi \geq 1$, the poles of the circuit do not provide complex part as $(1 - \xi) < 0$ and the square root of this provides always *j*. The expression for poles can be simplified to

$$p_1, p_2 = -\zeta \cdot \omega_n \pm \omega_n \sqrt{\xi^2 - 1}\,. \tag{4.48}$$

It can be seen from (4.48) that the higher the damping rate, the more there is difference between frequencies of the two poles.

4.3.2 Effect of poles and zeros on system behaviour

Analysis on transfer function based on presentation (4.19) provides overview of the most critical aspects of the circuit behaviour. Such characteristics can be, for example, magnitude response, phase response, damping/decay, stability, overshoot, delay and many more. Within this thesis, attention is paid to the actual frequency and phase response, poles and zeros are the values that help to determine the response of the circuit for a wide range of frequencies.

The frequency plots used hereafter are presented on logarithmic scale, with both frequency and magnitude axis having a logarithmic representation. In terms of frequency, the units observed and compared are *decades* (dec), this means 10 times increase of frequency. For example, one decade further from 217 Hz is 2170 Hz. Decades can be handled just as linear values, 1 + 1 decade means 10 times frequency increase, with additional 10 times frequency increase resulting in 100 times frequency increase.

Transfer rate of input to the output of the circuit is presented on magnitude plot. In most direct approach, assuming sine-wave input with amplitude value 1 to the circuit, the value found on magnitude plot can be found also in the output. For pulsed measurement application, one has to take the magnitude transfer rate in account in wide bandwidth, as a pulse provides a variety of different frequency components. The value of transfer rate can vary from very small values to very large values; therefore it is useful to provide this in logarithmic scale. Common logarithmic values found on the magnitude plot are decibels, the units for ratio to reference

$$U_{dB} = 20\log\left(\frac{U}{U_{ref}}\right), \tag{4.49}$$

where U_{dB} – voltage value in decibels; U – observed voltage value; U_{ref} – reference voltage value.

In the magnitude transfer analysis it is reasonable to assume $U_{ref} = 1$ V. On decibel scale, when observing voltage or current, +20 dB means 10 times stronger (10 V) and –20 dB means 10 times weaker (0,1 V).

Every zero and pole provide opposite effects to each other. A zero of the transfer function provides a growing transfer rate on the magnitude plot at +20 dB/dec. This means that when at frequency 10 Hz the transfer rate is 0,001 (–60 dB), then at frequency 100 Hz it would be 0,01 (–40 dB) and at frequency 1000 Hz this would be 0,1 (–20 dB). Effect of zero (same applies to poles) on asymptotic plot starts from the frequency of zero and can be represented as a +20 dB/dec line (see Figure 4.12).

Frequency of zero can be calculated as

$$f_{zn} = -\frac{z_n}{2\pi}, \tag{4.50}$$

where z_n is the n-th solution to the zeros polynomial (4.21).

A pole of the transfer function provides a decreasing transfer rate on the magnitude plot at –20 dB/dec. This means that when at frequency 10 Hz the transfer rate is 10 (+20 dB), then at frequency 100 Hz it would be 1 (0 dB) and at frequency 1000 Hz this would be 0,01 (–40 dB). Effect of pole on asymptotic plot starts from the frequency of pole and can be represented as a –20 dB/dec line (see Figure 4.12).

Frequency of pole can be calculated as

$$f_{pn} = -\frac{p_n}{2\pi}, \tag{4.51}$$

where p_n is the n-th solution to the poles polynomial (4.20).

An example of poles' and zeros' effects to magnitude plot can be observed on Figure 4.12. The magnitude is provided on logarithmic axis, with decibel and relative scale.

Phase shift due to signal moving through the circuit can be observed on phase plot. As for magnitude plot, in ideal case when there is sine-wave input, the value of phase shift applying to the plot can be found by the value on phase plot. Phase in this thesis is observed in degrees, as this provides some better overview compared to radian values.

Effect of poles and zeros on phase frequency plot starts one decade before the actual frequency of pole or zero and ends one decade after the frequency of pole or zero. Due to every zero, the phase plot is affected by added phase by +90 degrees, and this is added during two decades. Due to every pole, the phase plot is affected

by decrease of phase by 90 degrees, and this is added during two decades. Such variation in phase shift is provided on a sample plot on Figure 4.13.

An asymptotic plot is the approximate representation of the circuit behaviour, and it is closest to the real circuit behaviour when the zeros are apart from each other and also when the poles are apart from each other, and provided zeros' and poles' polynomials have real solutions. In resonance cases the asymptotic plot produces significant error; however further away from the resonance frequency the plot can be quite close to the real behaviour.

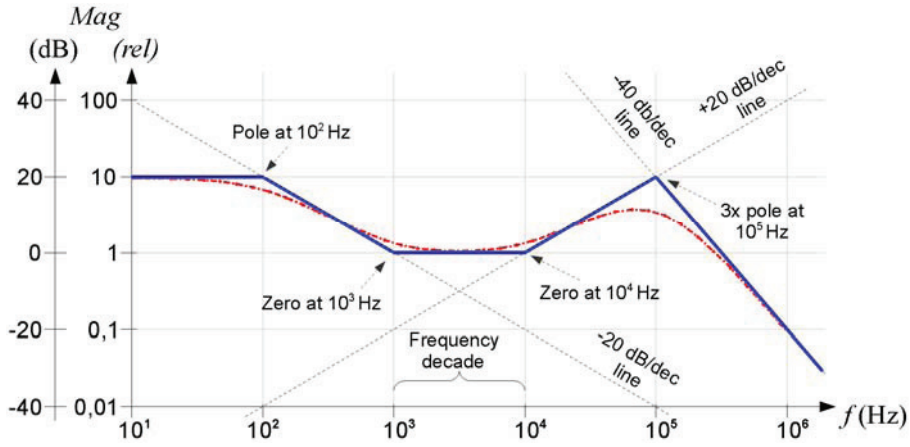

Figure 4.12. Asymptotic plot of effects of poles and zeros on magnitude plot. Blue line represents asymptotic plot and red line represents actual simulation results.

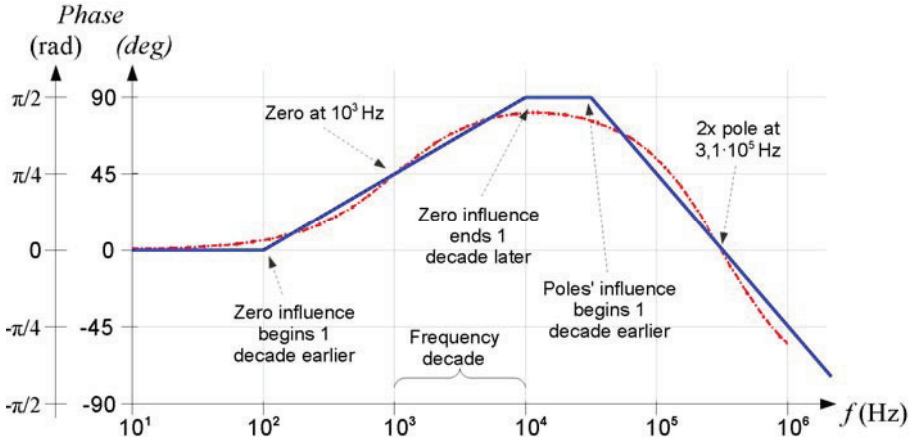

Figure 4.13. Asymptotic plot of effects of poles and zeros on phase plot. Blue line represents asymptotic plot and red line represents actual simulation results.

4.3.3 Damping and effect on bandwidth

The need for integration of the undamped inductive sensors has been discussed by various authors [10] [61]. Below resonance frequency, the undamped sensor coil operates similar to manner of the low-frequency model. For this model, a relation was established that the output of the coil is related to the rate of change of measured current as

$$e = -M_S \frac{di}{dt}. \tag{3.13}$$

Based on this formula, sensor with integrated output should, by mathematical approach, be able to replicate the measured high-frequency current waveform. Most direct approach to achieve this is to add an integrating unit to the output of the coil. In this way

$$u_{out,\mathrm{int}} = \int e\, dt = -M_S \int \frac{di}{dt} dt = -M_S \cdot i, \tag{4.52}$$

where i – instantaneous current value; $u_{out,int}$ – instantaneous voltage value of the integrator output.

There is also another option to provide the integration of the input current. Following discussion in [10] [93], adding a termination resistor R_T can be used to introduce a *self-integrating* operating area to the inductive sensor transfer response. This is far cheaper and more reliable option than using external active integrators. As discussed above, adding a termination resistor for damping is mandatory for keeping the noise level of the sensor output low. However, when the resistor is selected with care, it can make big difference to the sensor operating frequency range.

By (4.43), the damping rate is increased as the resistance of R_T is decreased. In addition, by (4.48), lower R_T resistance also means that the poles of the inductive sensor transfer function are further away from each other. This is also addressed in more detail in [107], by specifying the operating bandwidth the frequency region between two poles. However, for providing more accurate sensor, an improvement to this could be proposed, if also phase frequency plot is taken into account, to guarantee better match to (4.52).

Figure 4.14 presents an overview of the amplitude and phase plot of the self-integrating operating range. In literature [10] [93] [107] condition for self-integrating region is specified as stable magnitude plot area and this ranges from pole at $f_{p1} \ldots f_{p2}$. For observing the properties of phase plot, one should take into account that the effect of pole for phase shift starts at one decade earlier and ends one decade later than the pole frequency. Thus, the phase asymptotical plot will be stable only at frequency above $10 \cdot f_{p1}$ and below $f_{p1}/10$. In order to fulfill the requirements for pulse measurement presented in "2.7. Summary of sensor operating bandwidth criteria", it will be the requirement for poles' placement.

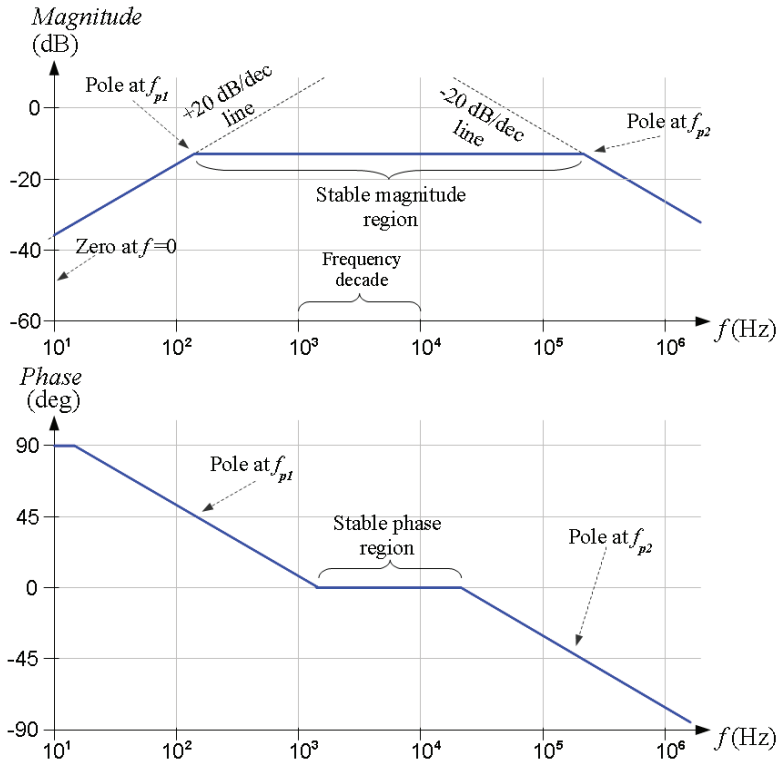

Figure 4.14. Self-integrating region specification with magnitude and phase frequency plots.

Still, in papers available there is not much consideration towards real capabilities and requirements for estimating the needed sensor operating bandwidth. The simple inductive sensor is not capable of reaching up to several hundreds MHz, so it does not provide any benefits of stretching the higher operating bandwidth that far. The transient waveforms presented in "2. Fast transients in power networks" refer that it is reasonable to keep the highest operating frequency at 100 MHz.

An example of frequency magnitude and phase plot for a second-order system with variable R_T value (thus also varying damping rate ξ value) is presented in Figure 4.15. The base values for the circuits simulated are presented in Table 4.8. Circuit being processed is an equivalent to circular coil with diameter of 100 mm, having 10 turns. Table also provides information about calculated actual frequency values for poles. It can be seen, that the poles could be located even at several GHz with same L_S and C_S values. This is useful for noting for later, when in sensor design discussions in "6.4. Sensor electrical design".

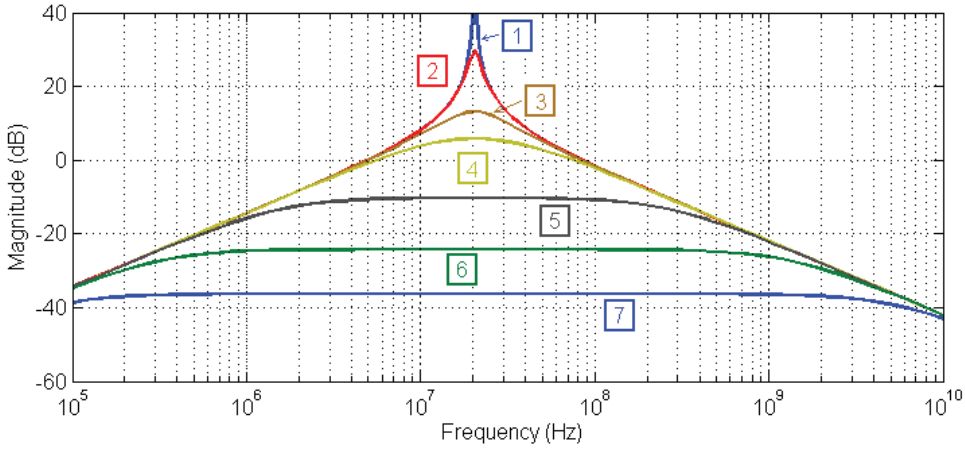

Figure 4.15. Magnitude plot of second order circuit.
Plotted circuit parameters are provided in Table 4.8 below.

Table 4.8. Properties of circuit with response presented in Figure 4.15, when $L_S = 10$ µH; $C_S + C_W + C_M = 6$ pF; $R_S = 0{,}3$ Ω; $R_M = 1\,000\,000$ Ω.

Plot # on Figure 4.15	1	2	3	4	5	6	7
R_T (Ω)	100 000	10 000	1500	641	100	20	5
ξ	$6{,}4 \cdot 10^{-3}$	0,064	0,43	1,0	6,4	32	128
f_{p1} (MHz)	20,4	20,4	20,4	20,4	1,61	0,323	0,0844
f_{p2} (MHz)	20,4	20,4	20,4	20,4	259,4	1308,3	5236,2

The plot presented uses similar approach as presented in [113] with several different responses are presented on one graph. From Figure 4.15, it can be observed that the decrease of value of R_T is providing the self-integration operating mode in heavily overdamped area ($\xi >> 1$). One of the facts to point out is that plot on the logarithmic frequency scale is symmetrical towards the natural oscillating frequency f_{res} of the coil (when $R_T \to \infty$). This makes selection of sensor coil parameters L_S and C_S more straightforward, as it is rather simple to determine required parameters from

$$f_{res} = \frac{1}{2 \cdot \pi \sqrt{L_S (C_S + C_W + C_M)}}. \tag{4.53}$$

This topic will be addressed further in detain in chapter "6.4.2. Coil parameters selection", where selection of operating bandwidth is discussed in more detail.

4.4 Summary

The medium-frequency inductive sensor model provides also solutions for an ideal case of operation. It is usable from some tens kHz up to few MHz range of sensor operation. This kind of model is widely discussed in literature and in scientific works as true high-speed model, but it actually does not take into account the high-frequency stray components to the sufficient level, for describing the high-frequency operation.

This model presents some of the most important aspects for the sensor modelling and design of sensor operating bandwidth. While this chapter included mostly classical operation of such circuit, it is presented in detailed manner for terms of discussion for high-frequency model in Chapter 5 and for the sensor design, described in Chapter 6. Regardless of the medium-frequency model bandwidth limits, this model presents the operating bandwidth calculation essentials and is a vital part of the sensor design.

5 Air-core sensor high-frequency model

5.1 Overview of high-frequency stray components

The limit of observing the high-frequency model should be, depending on sensor and system parameters, around 10 … 30 MHz. Starting from this frequency and in in higher frequency range operation, even the smallest capacitance and inductance begin to matter, and higher frequency will also mean more stray effects to take into account (an example of an inductor GHz frequency range high frequency model with very high number of stray components is presented in [59]). A question arises on the precision of the stray components and which of them to take into account, this can be settled by setting an upper freqeuency limit to the model. In present application, the sensor coil highest operating frequency is targeted at 100 MHz; therefore the components providing effects above this frequency could be neglected.

Other aspect that the the high-frequeny operation models should take into account is the matter of physical dimensions, such as total winding wire length, side length etc. Namely, when the wavelength of some frequency is close to some physical dimension, the circuit cannot be observed only by having lumped components, but rather as a long system with distributed parameters. For example, at 30 MHz the wavelength is (2.7)

$$\lambda = \frac{\upsilon}{f} = \frac{299 \cdot 10^6}{30 \cdot 10^6} \sim 10 \text{ m},$$

which would, for example, mean a coil with 20 turns, each turn being 50 cm long (circula coil with diameter around 15 cm).

In approach presented in this thesis there are actually two models used to describe the high-frequency operation. First, a distributed model of the sensor coil is presented without the measurements system. For the base of the new model, the segment consisting of one turn of the sensor coil should be discussed [40]. It is presented in Figure 5.1 and it basically shows the same components as described for medium-frequency model before. Difference here is that the components are provided with their per-turn values.

Power line wire being measured affects the coil via per-turn mutual inductance $M_{S,T}$ and line-to-shield capacitance $C_{LS,T}$. If the shield is built properly, there is no capacitive influence to the coil; only the added shield-to-sensor capacitance $C_{SS,T}$ affects the coil. This presents much higher capacitance to the coil than the effect of turn-to-turn capacitance C_{TT}. Every winding turn has its own inductance $L_{S,T}$ (NB! Not loop inductance) and skin resistance $R_{SSkin,T}$. The mutual inductance between turns M_{TT} provides magnetically coupled connection to every turn of the coil.

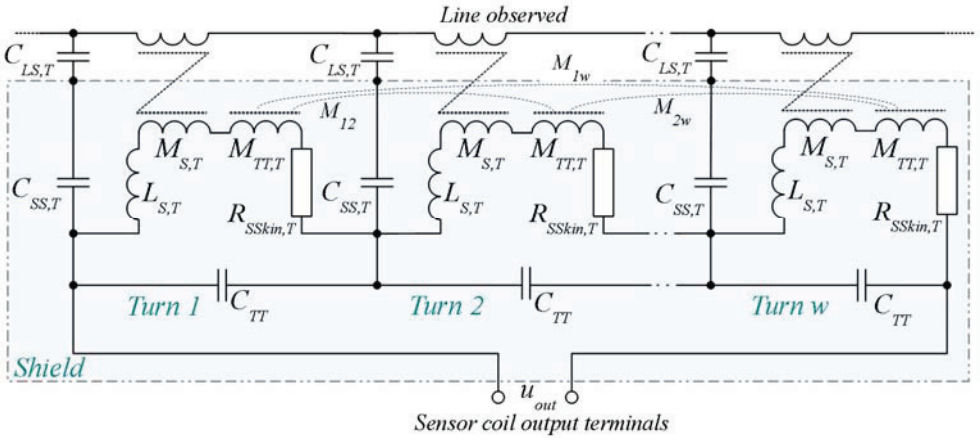

Figure 5.1. Distributed inductive sensor model for high-frequency operation analysis.

This model can be also elaborated in a more detailed transmission-line model, which some investigators also have done [32] [111] [115] [124]. This is one part of the transmission line model that actually defines the limits of the sensor coil operation. In particular, the transmission line model presents the understanding of resonance due to the physical length of the coil wire. It will be addressed in further detail in the end of this chapter (see "5.6. Transmission line effects of the sensor coil").

When the external components are considered and their effects to the sensor coil operation observed, this model can turn out to be quite complicated for the analysis of effects of different components. Therefore, in addition to the sensor distributed model, a high-frequency model lumped model is observed. This model has emphasis on describing the external components of the measurements system that can present some significant influence on the sensor operation.

The high-frequency lumped model is actually much like the medium-frequency model (see also "4.1. Components in medium-frequency model"). Still, the medium-frequency model does not represent following high-frequency effects:

- skin effect of the sensor coil wire, which produces higher losses in the sensor coil;
- terminating resistance high-frequency stray components, like equivalent series inductance;
- connecting cables inductance effects;
- capacitive coupling to the measured wire, shield connection and capacitance symmetricity issues.

Based on the sensor distributed parameters model above equivalent lumped model can be defined as presented in Figure 5.2.

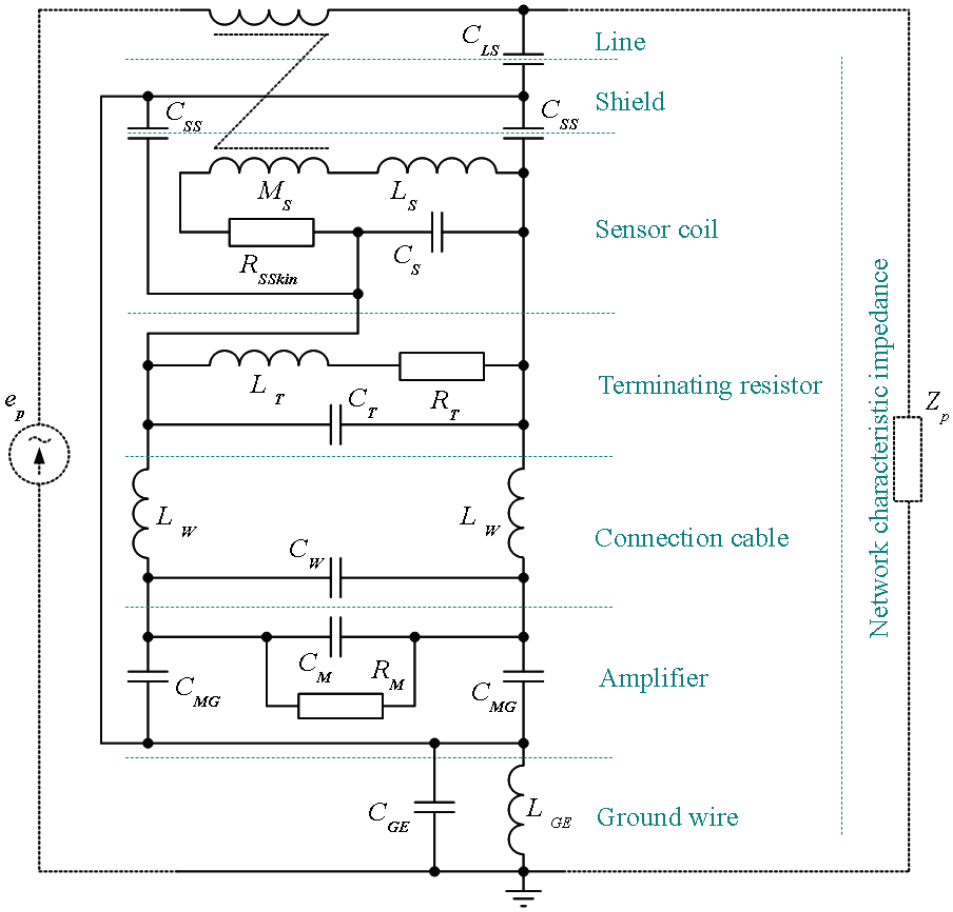

Figure 5.2. Lumped high-frequency model of the inductive sensor.

More detailed index of the components present in the high-frequency lumped model is presented in Table 5.1.

Table 5.1. Lumped high-speed model components of an inductive current sensor coil

Compo-nent	Description	Impact / analysis
C_{LS}	Line-to-shield capacitance of the sensor	Small effect if properly grounded
C_{SS}	Shield-to-sensor coil capacitance	Effect on bandwidth, decreases resonant frequency, see “5.5.2. Shielding of the sensor”
M_S	Mutual inductance between the sensor coil	Provides the magnetic effect output of sensor, see “3.3. Number of turns and mutual inductance”
L_S	Sensor coil self-inductance	Determines bandwidth, criterion for design, see “6.4. Sensor electrical design”

Compo-nent	Description	Impact / analysis
C_S	Sensor coil self-capacitance	Determines bandwidth, criterion for design, see "6.4. Sensor electrical design"
R_{SSkin}	Sensor coil wire resitance with skin effect	Resistance has some effect of bandwidth; skin effect resistance has only minor effect, see "5.2. Skin effect"
R_T	Terminating resistance	Determines bandwidth, criterion for design, see "6.4. Sensor electrical design"
L_T	Terminating resistor stray inductance	Has effect on the high-frequency operation to the magnitude and phase response, see "5.3. Terminating resistance properties"
C_T	Terminating resistor stray capacitance	Relatively small compared to sensor coil self-capacitance. Minor effect on bandwidth
L_W	Measurement circuitry input connection wires stray inductance	Has effect on the high-frequency operation to the magnitude and phase response, see "5.4. Effect of measurement system connection"
C_W	Measurement circuitry input connection wires stray capacitance	Also present in the middle-frequency model. Has effect on the high-frequency operation to the magnitude and phase response, see "5.4. Effect of measurement system connection"
C_M	Measurement circuitry input differential mode capacitance	Determines bandwidth, criterion for design, see "5.4. Effect of measurement system connection"
R_M	Measurement circuitry input differential mode resistance	Minor effect, if the input resistance is very large compared to the terminating resistance
C_{MG}	Measurement device input common mode capacitance (towards ground)	Can be observed as part of C_M; usually rather small effect for differential measurements, see "5.4. Effect of measurement system connection"
C_{GE}	Capacitive coupling of measurement system ground to real earth/common ground	Minor effect if the grounding connection is good and has small inductance and resistance
L_{GE}	Inductance of the grounding wire connecting measurement system ground to real earth/common ground	Minor effect if the measurement system is using differential measurement of the coil output

The interest in researching the model would be calculations of transfer functions, from the pulse source to the active input of the signal processing unit. For this purpose, the lumped model provides easier solution than the distributed components mode.

The effects of different stray components are analyzed one-by-one, not including other components. Main reason for such simplification is that the relations between these components are rather complex and number of variables will be high. The

approach taken in the following analysis is to introduce the effects of stray components one-by-one to the simpler medium-frequency model and then in the end, these can be summed together for the full high-frequency model.

5.2 Skin effect

In higher frequencies, magnetic field interaction inside the wire causes actual current flow to divert from the centre of the wire material. This effect is called skin effect due to the nature of current flow to remain in the outmost material layers of the wire material.

Some researchers have also included the skin effect resistance in their analysis, though stating it as neglible [124] or that it is included [98] in the sensor model. Still, the direct influence of the skin resistance has not been presented.

5.2.1 Analytical approach

With current fluctuation frequency becoming higher, current density distribution inside the material will obtain more and more in form of exponent. This distribution is characterized by skin depth or depth of penetration, defined as the distance from material surface in which the current density has decreased to value of $1/exp(1)$ compared to value on the surface [48]. Skin depth is calculated as

$$\delta = \sqrt{\frac{1}{\pi \cdot f \cdot \mu \cdot \sigma}}, \tag{5.1}$$

where f – frequency of the current fluctuation (Hz), μ – absolute magnetic permeability of material, σ – characteristic conductance of material.

Value of

$$\alpha = \frac{1}{\delta} = \sqrt{\pi \cdot f \cdot \mu \cdot \sigma} \tag{5.2}$$

is known as attenuation constant, referring to origin from high-frequency wave attenuation properties (see also "2.5. High-frequency transients' propagation on power lines"). With skin effect, current density distribution inside the wire is in exponential relation to the radius

$$J(r) = J_0 \cdot e^{-\alpha(r_w - r)}, \tag{5.3}$$

where J_0 – current density on the surface of the conductor (A/m^2) and r – distance from the conductor geometrical centre. This way, the skin effect can be also described as series of rings of wire each having different resistance value. Current through the ring with thickness dr can be calculated as

$$di = 2\pi \cdot r \cdot dr \cdot J(r) = 2\pi \cdot r \cdot J_0 \cdot e^{-\alpha(r_w - r)} dr. \tag{5.4}$$

For overall current through the wire, the integration over wire radius provides us with

$$i = 2\pi \cdot J_0 \cdot e^{-\alpha \cdot r_w} \int_0^{r_w} r \cdot e^{\alpha \cdot r_w} dr = 2\pi \cdot J_0 e^{-\alpha \cdot r_w} \left[\frac{e^{\alpha \cdot r_w}}{\alpha^2} (\alpha \cdot r_w - 1) + \frac{1}{\alpha^2} \right]. \quad (5.5)$$

In another view, this can also be described as effective area $A_{w,eqv}$ of the wire, still possessing resistance at the initial material DC-resistance value

$$A_{w,eqv} = \frac{i}{J_0} = 2\pi \cdot \left[\frac{1}{\alpha^2} (\alpha \cdot r_w - 1) + \frac{e^{-\alpha \cdot r_w}}{\alpha^2} \right]. \quad (5.6)$$

Comparing the effective area, resistance value for a particular frequency can be obtained by

$$R_{skin} = \frac{A_{w,eqv}}{\sigma} = \left[\frac{1}{\alpha^2} (\alpha \cdot r_w - 1) + \frac{e^{-\alpha \cdot r_w}}{\alpha^2} \right] \cdot \frac{2\pi}{\sigma} \cdot \quad (5.7)$$

5.2.2 Circuit representation

While conductor DC-resistance can easily be expressed in simple static form of resistor, transferring this to the schematic as a property of component is not so trivial. The last formula is quite complex and it is rather difficult to include it in a model circuit which uses Laplace frequency domain representation. Some work has already been done in this field, for example [23] obtaining an equivalent circuit suitable for including in a circuit. One of the most feasible ones is a method of 3-stage ladder representation [56].

Behind the idea of the ladder representation is discretization of physical current model of the wire (Figure 5.3). At high frequencies, a wire can be seen as the array of co centric rings (the inner part is a cylinder), each carrying some current. Each ring is represented as resistance R_{Ring} on the ladder diagram; the inductance L_{Ring} is the self-inductance of each of the rings.

Like observing every kind of discrete description about continuous phenomenon, the more there are rings in this model, the more accurate it will be. In case of limited frequency range for observation, it is not useful to obtain a large number of discrete ladder elements. For example, in both [23] and [56] a quite accurate result is reported based on 4-stage ladder, even in broad frequency band.

There are several ways on how to divide the wire into rings; one case favourable [23] is to have the resistance of each ring calculated as a certain multiple of previous ring's resistance. Same applies to inductance. The equivalent schematic for the wire resistance covering high frequency range is presented in Figure 5.4 below.

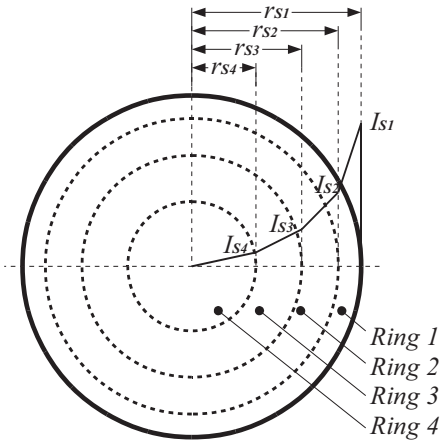

Figure 5.3. Ring structure of a wire for skin effect representation.

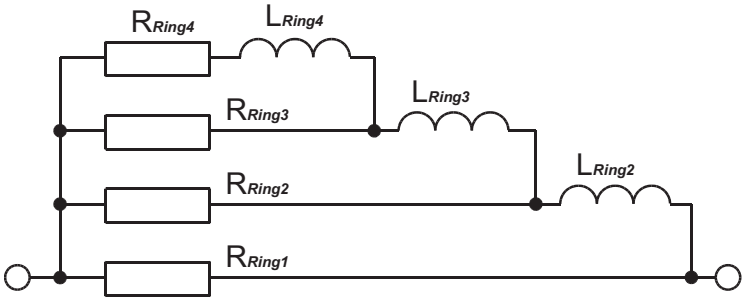

Figure 5.4. Representation of the ladder equivalent schematic for the skin effect.

Components in the ladder diagram have then following relation:

$$R_{Ring(i)} = RR_{skin} \cdot R_{Ring(i+1)}, \tag{5.8}$$

where RR_{skin} is the skin effect resistance ratio. Smallest resistance value possible for a wire is the resistance value at DC. Considering Figure 5.4 the smallest resistance value should be held by R_{Ring4}. Considering that at DC all inductances have practically zero reactance, all the resistors of the rings would be connected in parallel and thus an equation can be elaborated

$$\frac{1}{R_{Ring4} \cdot RR_{skin}^3} + \frac{1}{R_{Ring4} \cdot RR_{skin}^2} + \frac{1}{R_{Ring4} \cdot RR_{skin}} + \frac{1}{R_{Ring4}} = \frac{1}{R_{wDC}}, \tag{5.9}$$

where R_{wDC} is the wire resistance at DC.

Similar relation applies to the self-inductances of the wire. It is a known fact [79], that the internal inductance of a wire is dependent on the frequency of current applied to the coil, and that the self-inductance of the coil is highest at low frequency. Therefore, the parallel connection of all inductances should yield in this

case inductance of a wire at DC. Using similar approach as for ring resistance values, a skin effect inductance ratio LR_{skin} can be defined for calculating the inductances:

$$L_{Ring(i+1)} = LR_{skin} \cdot R_{Ring(i)}, \tag{5.10}$$

Similar equation to (5.9) to calculate the inductances would be

$$\frac{1}{L_{Ring2} \cdot LR_{skin}^{\ 2}} + \frac{1}{L_{Ring2} \cdot LR_{skin}^{\ 1}} + \frac{1}{L_{Ring2}} = \frac{1}{L_{wDC}}, \tag{5.11}$$

where L_{wDC} is the wire self-inductance at DC.

Self-inductance for a circular wire can be calculated as [79]

$$L_{wDC} = \frac{\mu_0}{8 \cdot \pi}, \tag{5.12}$$

which is constant for all circular wires.

It is rather difficult to find out the internal inductance value at high frequency. Instead, there is a rather straightforward approach to assist in this matter [56]. The overall internal inductance is not observed, but an empirical approach has been presented.

To solve the (5.9), a formula is described as

$$RR_{skin}^{\ 3} + RR_{skin}^{\ 2} + RR_{skin} + (1 - \alpha_R) = 0. \tag{5.13}$$

In this,

$$\alpha_R = \frac{R_{Ring1}}{R_{wDC}}. \tag{5.14}$$

The suitable value for this is defined as

$$\alpha_R = 0.53 \frac{r_w}{\delta_{\max}}, \tag{5.15}$$

where $\delta_{\max}$ is defined by formula (5.2) as skin depth at the maximum frequency $f_{\max}$ the skin resistance is observed

$$\delta_{\max} = \sqrt{\frac{1}{\pi \cdot f_{\max} \cdot \mu \cdot \sigma}}. \tag{5.16}$$

The value for calculating inductance values is more complex and does not provide as straightforward solution. The skin effect inductance ratio LR_S will be solved from equation

$$\frac{1}{LR_{skin}^{\ 2}}+\left(1+\frac{1}{RR_{skin}}\right)^2\frac{1}{LR_{skin}}+\left(\frac{1}{RR_{skin}^2}+\frac{1}{RR_{skin}}+1\right)^2-$$
$$-\alpha_L\left[\left(1+\frac{1}{RR_{skin}}\right)\cdot\left(\frac{1}{RR_{skin}^2}+1\right)\right]^2=0\,, \tag{5.17}$$

where $\alpha_L = 0{,}315\cdot\alpha_R$.

The value of both α_L and α_R is empirical and as observed in (5.15) it depends on wire radius. In the paper [56] the authors identify the error to be in range of 15 – 20% from the exact skin resistance calculations, which in real application can be considered acceptable.

For the analysis of practical skin effect, the ladder schematic is observed as in Figure 5.4. Once again, it is best to take an approach using Laplace transform and provide the skin effect resistance also as a function of s. The ladder circuit can be analyzed as Cauer network [15], with a schematic for it described as in Figure 5.5.

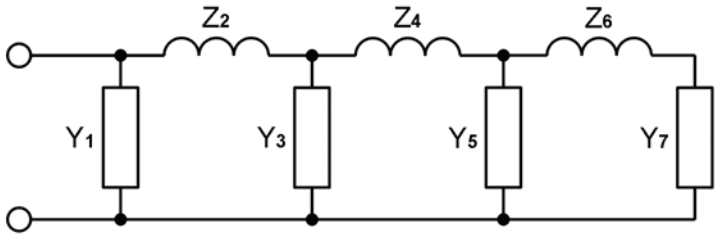

Figure 5.5. Skin effect ladder circuit as Cauer network, where $Y_1 = 1 / R_{skin1}$; $Y_3 = 1 / R_{skin2}$; $Y_5 = 1 / R_{skin3}$; $Y_7 = 1 / R_{skin4}$; $Z_2 = j\cdot\omega\cdot L_{skin2}$; $Z_4 = j\cdot\omega\cdot L_{skin3}$; $Z_6 = j\cdot\omega\cdot L_{skin4}$.

Cauer network for such circuit representing skin impedance Z_{skin} can be written as

$$Z_{skin}=\cfrac{1}{Y_1+\cfrac{1}{Z_2+\cfrac{1}{Y_3+\cfrac{1}{Z_4+\cfrac{1}{Y_5+\cfrac{1}{Z_6+\cfrac{1}{Y_7}}}}}}}\,. \tag{5.18}$$

5.2.3 Skin effect on practical wires

It is fairly complicated to solve this, especially considering substitutions made for calculating each component. Instead of further analytical approach, it is here best to make analysis based on a numerical example for a particular type of wire. Assuming the sensor coil wire could have a diameter of 0,1 mm – 0,4 mm, the equivalent

circuit components for the skin effect were calculated and the values for such components are stated in Table 5.2.

Table 5.2. Calculated skin effect circuit component values.

Wire diameter (mm)	0,1	0,2	0,4
Wire radius r_w (mm)	0,05	0,1	0,2
Wire cross-section area A_w (mm^2)	$7{,}85 \cdot 10^{-3}$	$3{,}14 \cdot 10^{-2}$	0,126
R'_{wDC} (Ω/m)	2,14	0,535	0,134
α_R	12,9	25,7	51,4
α_L	4,05	8,09	16,2
RR_S	1,87	2,51	3,31
LR_S	0,392	0,288	0,210
R'_{Ring1} (Ω/m)	27,5	13,7	6,87
R'_{Ring2} (Ω/m)	14,7	5,46	2,08
R'_{Ring3} (Ω/m)	7,89	2,18	0,629
R'_{Ring4} (Ω/m)	4,23	0,866	0,190
L'_{Ring2} (nH/m)	12,4	6,18	3,09
L'_{Ring3} (nH/m)	31,5	21,5	14,7
L'_{Ring4} (nH/m)	80,1	74,5	70,8

The skin impedance calculation results for highest frequency range $f_{max} = 1$ GHz based on (5.18) are presented in graph in Figure 5.6 below.

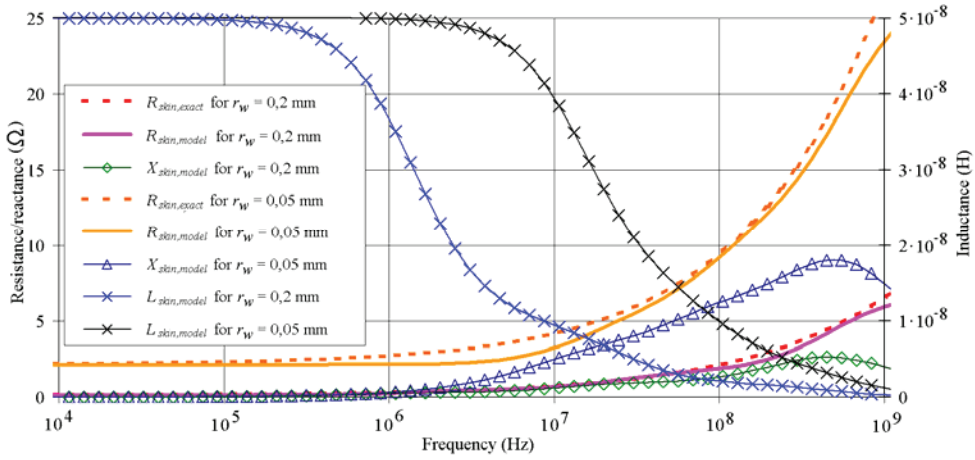

Figure 5.6. Graphs presenting the skin effect resistance obtained by (5.7) and by (5.18).

As it can is expected, such circuit provides quite significant reactance because of inductive components included. Reactance is caused by the internal impedance and this value is rather low, remaining in range of 10^{-8} H. Compared to the sensor coils expected inductance value L_S, which is significantly over 1 μH, the internal induc-

tance has only minimal effect. Thus it can be said that this model of skin effect for the inductive sensor actually represents the skin effect active resistance of the wire, as it is needed in current model.

In the high-frequency model circuit (see Figure 5.2), the inductor inductance L_S and wire resistance R_{SSkin} are in series. The wire resistance should be substituted with the skin effect circuit as in Figure 5.4 or Figure 5.5, R_{SSkin} is represented by Z_{SSkin}. In one way, it could be practical to analyze the L_S and Z_{SSkin} in circuit together and this is elaborated into same ladder circuit as in Figure 5.5. However, when observing the overall sensor design aspects, it would be good to keep the inductor as a component separately, as it is varied for range of inductances based on sensor geometry and number of turns of wire.

The ladder circuit (see Figure 5.5) can be elaborated into transfer function shape, which provides the poles and zeros for the circuit analysis. Once again, it has to be said that this is very difficult task, as the (5.18) provides extremely complex shape function. It is best to find the transfer function by using, for example, Mathcad software which is capable of finding the solutions in symbolic form. Using similar approach to calculations of values for the circuit, the values of poles and zeros for the ladder circuit are presented in Table 5.3. As the transfer function polynomial has order of 3, there are 3 zeros and 3 poles for the circuit.

Table 5.3. Poles and zeros for skin impedance transfer function form

Wire diameter (mm)	0,1	0,2	0,4
Zero #1, z_1 ($\times 10^6$ rad/s)	–31,6	–8,21	–2,13
Zero #2, z_2 ($\times 10^6$ rad/s)	–286	–109	–44,4
Zero #3, z_3 ($\times 10^6$ rad/s)	–1740	–1160	–821
Pole #1, p_1 ($\times 10^6$ rad/s)	–96,8	–29,2	–8,98
Pole #2, p_2 ($\times 10^6$ rad/s)	–579	–288	–152
Pole #3, p_3 ($\times 10^6$ rad/s)	–3610	–3188	–2930

In the sensor overall transfer function calculations, the wire resistance R_S has to be substituted with the transfer function as

$$R_S \longrightarrow \frac{(s+z_1)(s+z_2)(s+z_3)}{(s+p_1)(s+p_2)(s+p_3)} = \frac{Z^3}{P^3}, \tag{5.19}$$

where Z^3 – zeros' polynomial of 3rd degree; P^3 – poles' polynomial of 3rd degree.

This makes the overall transfer function quite complex. Using the simplest approach based on medium-frequency model, the transfer function will be elaborated from (4.30) into

$$U_{out}(s) = \frac{s \cdot M}{L_C \cdot C_C \cdot s^2 + s\left(\frac{Z^3}{P^3} \cdot C_C + \frac{L_C}{R_T}\right) + 1 + \frac{\frac{Z^3}{P^3}}{R_T}} I(s), \quad (5.20)$$

which can be developed into

$$U_{out}(s) = \frac{s \cdot M \cdot P^3 \cdot R_T}{s^2 \cdot P^3 \cdot L_C \cdot C_C \cdot R_T + s \cdot \left(Z^3 \cdot R_T \cdot C_C + L_C \cdot P^3\right) + P^3 \cdot R_T + Z^3} I(s). \quad (5.21)$$

This transfer function has zeros' polynomial of 4th degree and poles' polynomial of 5th degree, thus there are 4 zeros and 5 poles for this transfer function. Based on the comparison of calculation, the initial resistance ladder values are fairly correct, as the high-frequency and the low-frequency resistances match quite closely.

5.2.4 Simulation results and conclusions

It would be reasonable to present the results of skin-effect modelling with all the wires' data presented in Table 5.2 and Table 5.3. As the results of the simulation results using (5.21) show, the effect of the wire skin effect resistance is actually miniscule, if considering frequencies up to 1 GHz and the wires' data used for analysis.

The results for simulation of the coil model with skin effect are provided on frequency and magnitude plot in Figure 5.7. Values of the components of the equivalent circuit are $L_S = 350$ µH; $C_E = 7$ pF; $R_E = 20$ Ω; $w = 50$; $l_{wire} = 15$ m; $r_w = 0{,}1$ mm. These parameters are relatively close of a sensor coil that is presented later, in chapter "6.4. Sensor electrical design based on determination of inductance". The coil with rather large number of turns is selected so that it would present higher skin resistance due to longer wire length.

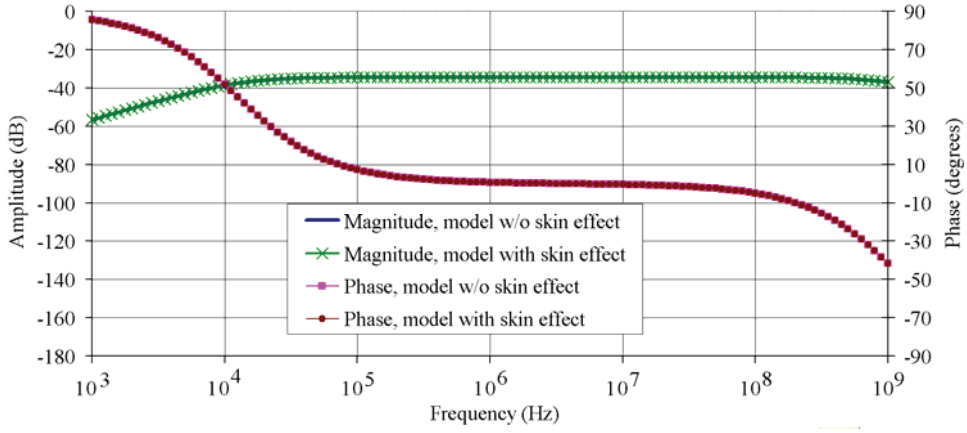

Figure 5.7. Magnitude and phase plot of inductive sensor with skin effect circuit model, in comparison to a plot of the sensor model without skin effect implemented.

Results presented in Figure 5.7 are very similar to results obtained when using different wire size for the coil winding. There are practically no differences between the results from model with skin effect and without skin effect, leading to the conclusion that the skin effect does not present any effect, needed to be taken into account during sensor coil operation analysis for frequency range of up to 100 MHz.

It is therefore safe to conclude, that although there is substantial evidence of the skin effect of the coil wires, it still does not bring remarkable effects to coil operation at frequency below 1 GHz. The reason for this most likely is that the wire diameter compared to the skin depth is still small in the frequency areas of interest. Also, the reactance of the coil is significantly larger than the skin effect resistance, bringing only minimal effect to the already great coil impedance at this frequency.

In conclusion, as the target frequency of the sensor coil observed in this thesis is up to 100 MHz, it can be said that the skin effect can actually be neglected in the sensor high-frequency model.

5.3 Terminating resistance properties

Terminating resistance as external component itself has a high-frequency equivalent circuit representation, having series inductance (ESL) L_T and parallel capacitance C_T (Figure 5.8). The parallel capacitance is quite small and actually does not influence the operation of the circuit. Reason for this is that as C_T is connected in parallel to the coil capacitance and the latter is expectidly significantly larger in quantity being significantly larger than the resistor parallel capacitance.

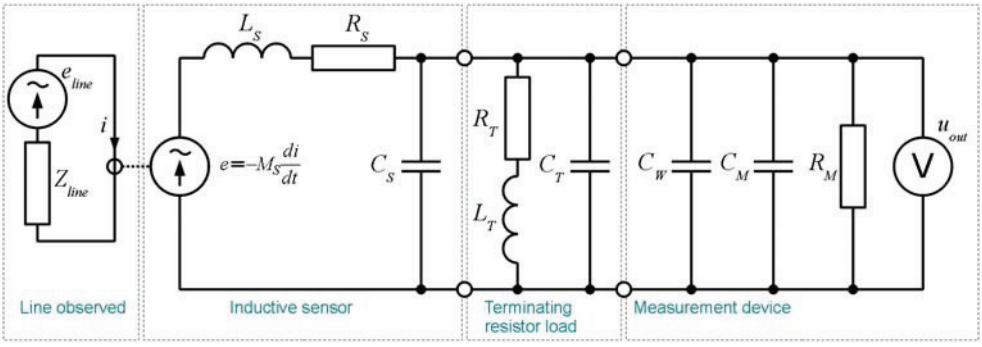

Figure 5.8. Sensor model circuit with terminating resistor high-frequency model.

Commercially available low-inductance resistors data presents ESL component value of less than 0,08 μH [121]. This is indeed a rather small value and represents wire of length of approximately 5 cm (see also "5.4. Effect of measurement system connection"). At high frequencies such inductance is providing significant effect to the circuit [90], as it provides reactance of nearly 14 Ω at 30 MHz.

The transfer function, calculated for model circuit in Figure 5.8, will present a transfer function

$$U_{out}(s) = \frac{s \cdot M_S \cdot \left(s + \frac{R_T}{L_T} \right)}{L_S \cdot L_T \cdot C_E \left[s^3 + \left(\frac{R_T}{L_T} + \frac{R_S}{L_S} \right) s^2 + \left(\frac{1}{L_S \cdot C_E} + \frac{1}{L_T \cdot C_E} \right) s + \left(\frac{R_S + R_T}{L_S \cdot L_T \cdot C_E} \right) \right]} I(s). \quad (5.22)$$

It provides two zeros, at

$$f_{z1} = 0; \quad (5.23)$$

$$f_{z2} = \frac{R_T}{2 \cdot \pi \cdot L_T}. \quad (5.24)$$

The poles' polynomial is now of 3rd degree, meaning there will be three poles to the transfer function. Determining the poles' locations means solving a cubic equation and this can be a rather difficult task. To provide some simplification to the solution, let it be assumed, that the values for components would be in range $C_E \approx 10^{-11}$ F; $L_S \approx 10^{-5}$ H; $L_T \approx 10^{-8}$ H; $R_S \approx 1\,\Omega$; $R_T \approx 100\,\Omega$. In this case, the approximation of the poles' frequencies can be found as

$$f_{p1} = \frac{1}{2\pi} \cdot \frac{R_S + R_E}{L_T + L_S + R_S \cdot R_E \cdot C_E}, \quad (5.25)$$

$$f_{p2}, f_{p3} = \frac{1}{2\pi} \cdot \frac{1}{\sqrt{L_T \cdot C_E}}. \quad (5.26)$$

A solution to cubic function is one real value, accompanied by two complex values forming a set of conjugate complex values. While (5.26) presents that the two poles have same frequency, these actually are conjugate complex poles. This refers to resonance occurrence and it can be verified from the magnitude and phase plots in Figure 5.9 and Figure 5.10 that resonance is present.

To present the effects of L_T to the measurement results a practical example will be used. In a sample sensor coil system, $C_E = 6 \cdot 10^{-12}$ F; $L_S = 5 \cdot 10^{-5}$ H; $R_S = 3\,\Omega$; $R_T = 30\,\Omega$ is used. The results of calculation are presented in Table 5.4 and frequency plots of circuit behaviour are presented in Figure 5.9 and Figure 5.10 for various L_T values.

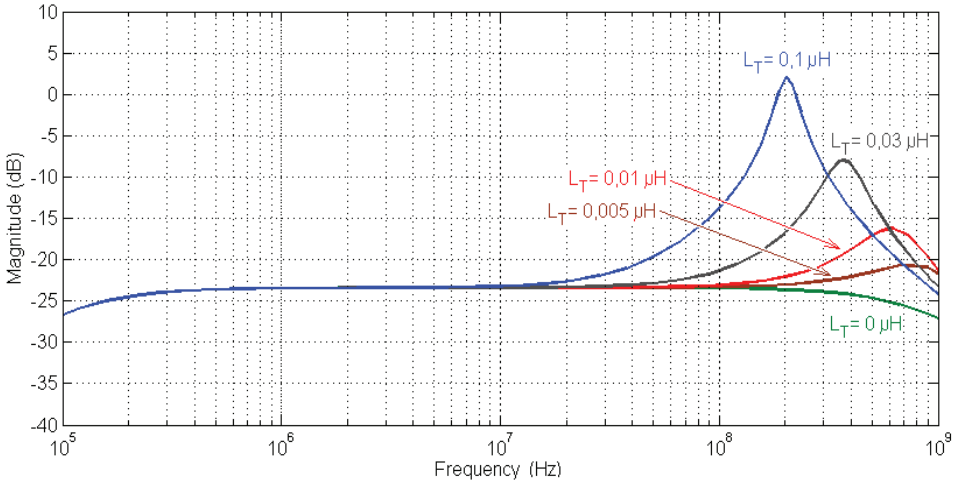

Figure 5.9. Magnitude plot for circuit with different L_T values.

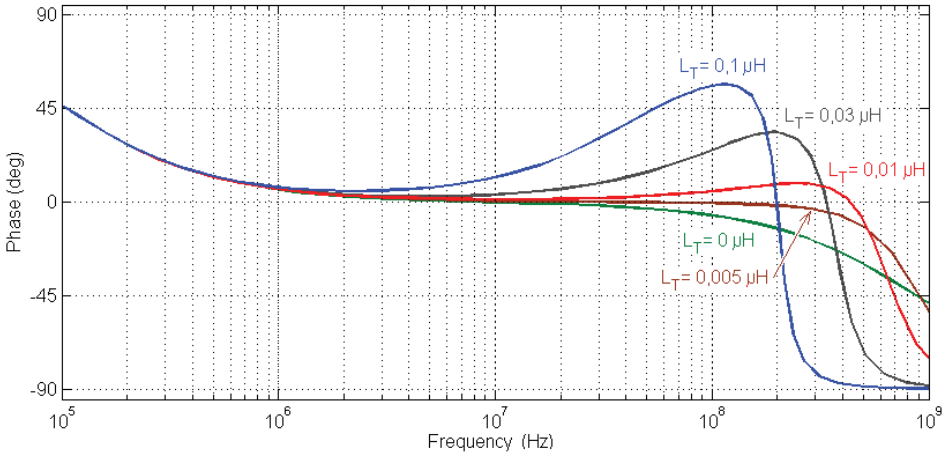

Figure 5.10. Phase plot for circuit with different L_T values.

Table 5.4. Frequencies of zeros and poles of the circuit at different L_T values.

L_T (µH)	f_{z2} (MHz)	f_{p1} (MHz)	f_{p2}, f_{p3} (MHz)
0	–	1,05	873*
0,005	955	1,05	914
0,01	477	1,05	647
0,03	159	1,05	373
0,1	47,7	1,05	204

* Frequency of 2nd pole; the circuit does not have 3rd pole if there is no L_T in the system.

In real application when coil system is built with care, the value of L_T could remain in range 0,01 … 0,03 µH, if wires/leads to connect to L_T are also taken into account. This means that even with R_T has a value of 30 Ω, the zero frequency is still in

range 470 … 160 MHz respectively; the effect of zero will cause phase shift starting from 47 … 16 MHz and this means that at highest operating range frequency of 100 MHz, the phase plot is not at steady zero. This can also be clearly seen on phase plot in Figure 5.10.

As frequency of the zero depends fully on the parameters of the terminating resistor, there is little to do in practice about other components in the system to keep the effect of the zero as small as possible. However accurate measurements of pulsed signal require stable phase plot at 0 degrees, therefore some solutions to decrease the effect of L_T has to be provided.

Overcoming this effect can be achieved three ways:

1) Keep R_T as high as possible, but this would mean set-backs in sensor bandwidth design, see "6.4. Sensor electrical design".
2) Keep L_T as small as possible; however this can be complicated due to connecting wires inductance, see "5.4. Effect of measurement system connection".
3) Provide a circuit element in the system that would provide a pole on the same frequency as the zero. Such is, for example, simple RC-lowpass filter.

The effect of poles itself do not provide serious set-backs when value of L_T is in the range below 0,03 μH. The frequency of poles will be above 300 MHz, which could cause some phase shift from 30 MHz; however as the higher frequency poles form a conjugate complex pair, the phase shift is expected to be sharper and remain out of 100 MHz range.

5.4 Effect of measurement system connection

High-speed circuit representation of measurement system connected to the sensor coil output is rather complex. Reason for this can be found in various components imposing capacitance and inductance in very small values that in electric circuits are generally not considered. Quite invisibly, if the measurement system is connected with wires with length l_W of 3 cm away from the coil, will have wire inductance included in the signal path. It should be noted, that even 1 cm of wire has about 0,015 μH of inductance. Given frequency of 30 MHz, this inductance provides reactance in range of 2,8 Ω. This can be greater value than the resistance of coil wire. Assuming coil output wires with radius r_w of 0,2 mm are in parallel with spacing s_w = 10 mm, the connecting wires together have inductance of [79]

$$L_W \approx \frac{\mu_0 \cdot l_w}{\pi} \ln \frac{s_w}{r_w} \approx 0{,}047 \mu H \,. \tag{5.27}$$

The formula presents also one clue, on how to keep the inductance low – for this purpose the wires from the coil should be as close together as possible.

A wire with length of, for example, 3 cm has typically so small resistance that this will not cause any effects in frequency range up to 100 MHz. More effect will be brought by the value of capacitance of the cable (discussed previously in "4.1.5. Measurement system"), however this is added to the measurement system capacitance.

For a differential measurement input, as recommended for use with sensor, a separation between differential measurement input capacitance C_{MD} and input capacitance to ground plain C_{MG} can be separated. The role of these capacitances is different, but they add together as a parallel capacitance between the input terminals (or then, sensor coil output terminals). The overall capacitance of the measurement system can be summed together as equivalent parallel capacitance $C_E = C_{MD} + C_W + C_{MG/2}$.

Components described above are presented in Figure 5.11, without the sensor coil (please refer to Figure 5.8 for sensor coil circuit presentation) as a simpler lumped model and for analysis is presented also as classical *LC*-filter. This allows for a simpler analysis of the effects of the sensor coil, as the transfer function of the *LC*-filter is well-known. It can be even observed like an inductive component model, just as the sensor coil itself on Figure 4.1, but here the wire resistance is presume to have zero value, when the connecting wires are kept very short.

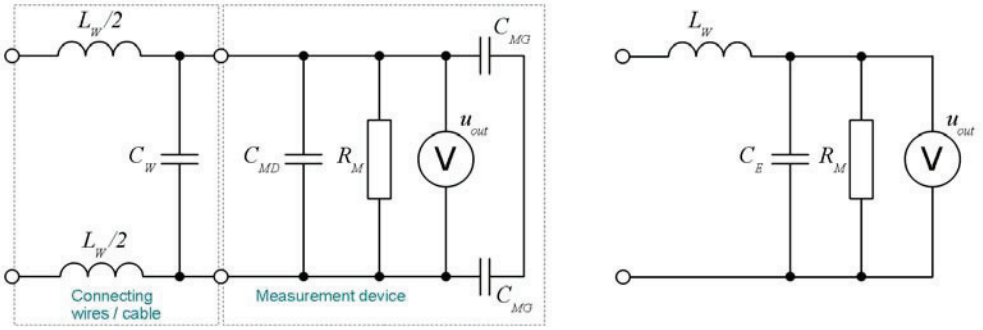

Figure 5.11. Measurement system high-speed model components (on the left) and representation as LC-filter circuit (on the right).

The measurement system equivalent parallel capacitance C_E is expected to have a value of close to 5 pF. When observing the sensor coil behaviour, this capacitance will be key part also for the sensor operation, as discussed in "4.1.5. Measurement system". However with longer wires and higher frequency values the results can become unexpected, as the wire inductance L_W could then decouple the measurement system capacitance from the coil self-capacitance. Considering that this could be the case for the high-frequency operation, the lower frequency poles of the coil likely remain in the same place. The high-frequency pole of the coil will move towards even higher frequencies due to this, but this actually does not cause significant problems. The measurement system capacitance decoupling is not visible on

the magnitude and phase plots on Figure 5.12 and Figure 5.13 but is better observed from calculation results in Table 5.5.

Provided the measurement input resistance is very large (which is the case in practice) the transfer function of the *LC*-filter is straightforward and is described by two poles and no zeros. Poles form a conjugate complex pair, which means that the poles are located at the same frequency

$$f_{p1}, f_{p2} = \frac{1}{2\pi \cdot \sqrt{L_W \cdot C_E}} \tag{5.28}$$

and transfer function of the LC-filter will be

$$U_{out,LC}(s) = \frac{1}{\left(s + \sqrt{L_W \cdot C_E}\right)\left(s + \sqrt{L_W \cdot C_E}\right)} U_{in,LC}(s), \tag{5.29}$$

where $U_{in,LC}$ and $U_{out,LC}$ are the input and the output voltage of *LC*-filter respectively.

As the transfer function of whole coil system is becoming very complex, it is better if the transfer function is observed in a way, that sensor coil transfer function, but also measurement system transfer function model is in polynomial form. For pointing out the effects of measurement system connection, the sensor is observed without termination resistor high-frequency model, but in a classical second order system model as in medium-frequency model "4.2.3. Poles and zeros of the model".

Measurement system is connected to the coil in series and this way the transfer function of the coil and measurement system can be multiplied for resulting function

$$U_{out}(s) = \frac{Z_C}{P_C \cdot P_{LC}} I(s), \tag{5.30}$$

where Z_C – zeros' polynomial of sensor coil, P_C, P_{LC} – poles' polynomials of sensor coil and *LC*-filter respectively.

The properties of such transfer function and effect of measurement system to the sensor coil operation is best to present on the graphical form. In this example, a sensor coil system with $C_E = 5 \cdot 10^{-12}$ F; $C_S = 1 \cdot 10^{-12}$ F; $L_S = 5 \cdot 10^{-5}$ H; $R_S \approx 3\ \Omega$; $R_T \approx 30\ \Omega$ is used. The results of poles' calculation are presented in Table 5.5 while the magnitude frequency plot of such system is presented in Figure 5.12 and phase plot is presented in Figure 5.13.

Table 5.5. Frequencies of poles of coil circuit with measurement system.

L_w (μH)	f_{p1} (MHz)	f_{p2} (MHz)	f_{p3}, f_{p4} (MHz)
0	1,05	873	–
0,015	1,05	4590	602
0,05	1,05	4820	322
0,15	1,05	4889	185

0,5	1,05	4900	101

The transfer function used for obtaining results in Table 5.5 is actually a bit more complicated than (5.30), as it can also provide results for occasion when $L_W = 0$. It also presents the decoupling effect of C_E from coil capacitance C_S. Namely, the sensor coil model without L_W included has the highest pole located at frequency (4.38)

$$f_{p2} \approx \frac{1}{2\pi} \frac{L_S + R_S \cdot R_E \cdot C_{S,M}}{R_E \cdot C_{S,M} \cdot L_S},$$

where in present analysis $C_{S,M}$ is the combined capacitance of coil and measurement system. This pole frequency is 873 MHz for the present example. However, when the coil self-capacitance is decoupled from measurement system by L_W, the pole frequency will be (4.38)

$$f_{p2} \approx \frac{1}{2\pi} \frac{L_S + R_S \cdot R_E \cdot C_S}{R_E \cdot C_S \cdot L_S}$$

and in this example it provides frequency 4,91 GHz. It can be seen from Table 5.5, that the higher the measurement system connection inductance is, the higher will be the pole frequency and it will become closer to the ideal coil pole frequency.

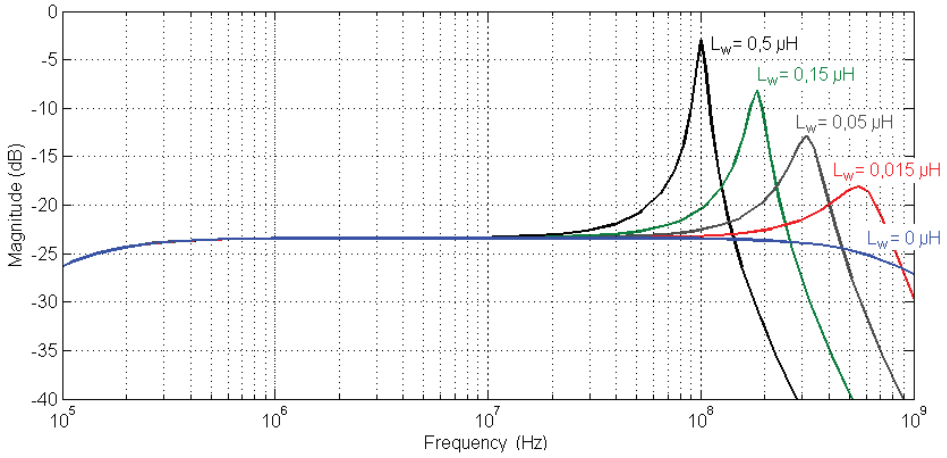

Figure 5.12. Magnitude plot for circuit with various cable inductance values.

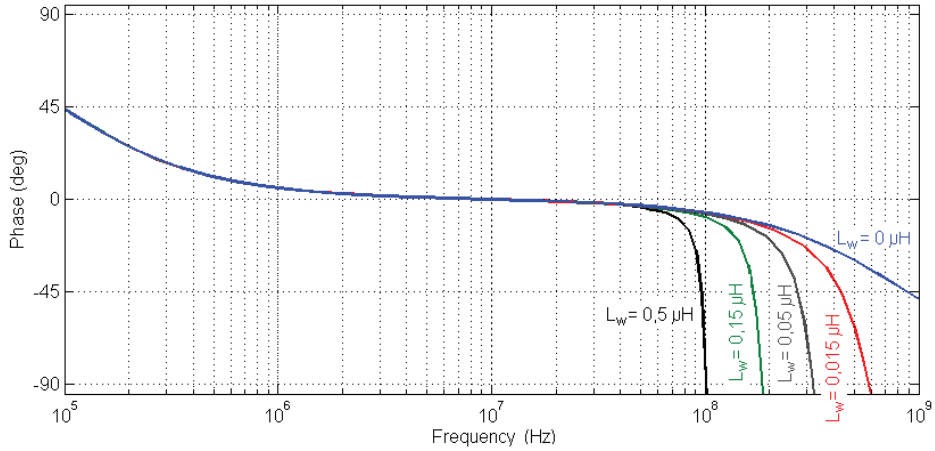

Figure 5.13. Phase plot for circuit with various cable inductance values.

The phase and magnitude plots on Figure 5.12 and Figure 5.13 present quite clearly the *LC*-circuit pole locations. It should be pointed out that in the real system the situation can be more complex and the phase plot might not be as friendly as presented in the simulation results. As explained in "4.3.2. Effect of poles and zeros on system behaviour", the effect of a pole to the system phase plot can begin one frequency decade away from the pole frequency. This means that the pole frequency of 600 MHz as presented in case the wire is only 30 mm long, is already on a critical limit, if one considers that for measurement of pulsed signal the phase plot should be constant over the full bandwidth range.

5.5 Capacitance effects of the sensor coil

Every two electrical conductors provide some value of capacitance between them and this is also case for the inductive sensor coil. One implication of this is the self-capacitance of the sensor coil. There is also capacitive coupling between the sensor coil and wire being measured, which in high-frequency operation will matter. The effect of capacitive coupling can be decreased with the help of shielding, but shielding itself has several aspects that need to be taken into account for performing accurate measurements.

5.5.1 Capacitive coupling to wire

Shielding of the inductive sensors has been discussed with Rogowski coil operations in [45] [26] [115]. Discussion on shielding does not reach very deep, and is considered to be necessary to eliminate external and environmental noise. It is rare to find some indication that there is some coupling to the wire being measured, or analyzed in more detail towards the physical value of capacitance. There is some discussion of the fact of capacitive coupling in [90] and in another case capacitance between coil and wire [45] is also seen as source. It could be suspected that the

authors of [45] observed the capacitive coupling as “preshoot” in the sensor output in their previous work [85]. Still, there is no more detailed analysis available.

For estimating the capacitive coupling between wire and sensor coil the simplest approach is presented. In this case, power line wire with radius r_{line} is monitored with a sensor coil having thickness of d_C, placed at a distance $h_{line,C}$ (see Figure 5.14). Assuming that $h_{line,C} >> r_{line}$ and that $r_{line} \approx d_C$ the capacitive coupling between the sensor coil and the wire being measured can be represented using the same principle idea as the transmission line with two wires (see also “4.1.5. Measurement system”).

In case of rectangular coil the transmission line length affected would have length of the coil length l_C and the capacitive coupling can be calculated as (4.9)

$$C_{SW} = \frac{2 \cdot \pi \cdot l_C \cdot \varepsilon}{\ln\left(\frac{h_{line,C}}{2 \cdot r_{line}} + \sqrt{\left(\frac{h_{line,C}}{2 \cdot r_{line}} \right)^2 - 1} \right)}. \quad (4.9)$$

For example, when $h_{line,C} = 0{,}1$ m, $r_{line} = d_C = 0{,}01$ m and $l_C = 0{,}1$ m, the capacitance between the sensor coil and the power line wire would be $C_{SW} = 2{,}86$ pF. Compared to the other capacitances in the system, this is actually quite large value.

The capacitive coupling is especially effective for the high-frequency operation, as every other capacitance to, for example, ground, will provide capacitive voltage dividers, which will then also affect the outcome of the measurement at the coil terminals. This is presented in simplified schematic in Figure 5.14.

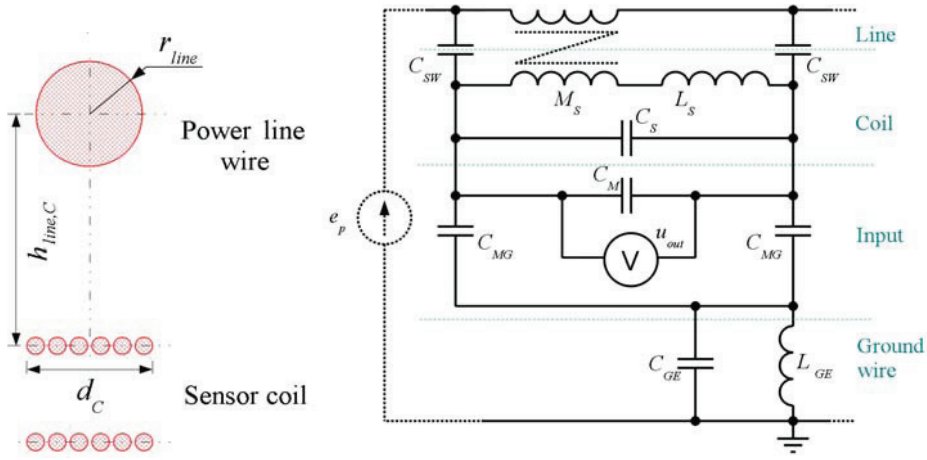

Figure 5.14. General representation of sensor coil under the power line wire being measured, for capacitive coupling estimation (on the left) and simplified schematic of capacitances forming voltage dividers (on the right).

As it can be seen, the capacitive coupling does not have much effect, provided the capacitance values of C_{SW} and C_{MG} are equal in pairs. In reality, this is very difficult to achieve and small capacitance unbalance can provide significant effect to the measurement input voltage.

5.5.2 Shielding of the sensor

In order to cancel the capacitive coupling between the sensor coil and the power-line wire, a rather simple shield can be built. Shielding the coil can on one hand cancel the capacitive connection to the wire measured; however it leads also to increase of the sensor coil total capacitance. This means that for the same band-width, the coil inductance should be lower; for this the number of turns will be lower and also then sensitivity of the coil will be lower.

The construction of a shield can be rather simple with simple materials, for example an aluminium foil could be used. The shield should be all around the coil winding, but for maintaining the level of sensitivity, there should be a gap in the upper end of the coil (see Figure 5.15) that would cancel the conductive turn of the shield. This is necessary, as when there is no gap included there will be current passing through short-circuited path through the shield, the latter operating with the same principle as the sensor coil. The field due to such short-circuited turn provides opposite magnetic field inside and around it, cancelling out much of the magnetic field inside the shield. Usually sources of literature that present the shielding of the sensor coil do not present necessity of having a gap in the shield [26] [46].

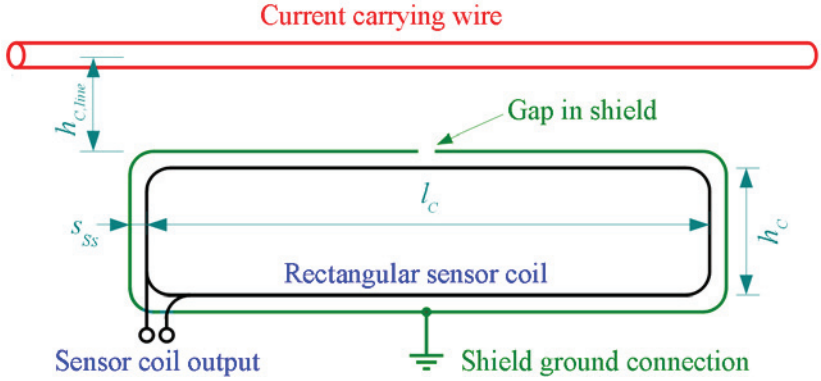

Figure 5.15. Shield construction for the sensor coil.

The location of the gap and the ground connection of the shield are essential for the sensor coil application. Like current of the short-circuited turn presented by a shield without a gap, the magnetic field inside the sensor coil will also be created by any other current present in the shield. As the shield still has the capacitive coupling to the power line wire, capacitive current will be passing through the

shield. The magnetic field due to this capacitive coupling current can also present influence to measurement outcome, if not symmetrically balanced.

The effect of providing the gap and ground connection symmetricity is presented in Figure 5.16. For a better visualization, the capacitive coupling effort is represented by distributed capacitors connected to the shield, each providing a part of capacitive current flow. In case of symmetrical shield set-up, the left and right side shield currents $i_{sh,l}$ and $i_{sh,r}$ are exactly equal; their summary effect to the coil centre area is 0, as the magnetic fields from both sides are equal and cancel each other due to different sign (see Figure 5.16). In case the left and right currents in shield at same height from power-line wire are different (see Figure 5.16), sum of their magnetic fields is not 0 and this will cause deviation to the sensor output also.

The topic is addressed also in [103] with real-world case examples, presenting the measurement results of a B-dot sensor and position of the gap in shield. Similar considerations to left- and right side shield current effects have also to be observed when selecting placement of the shield ground connection.

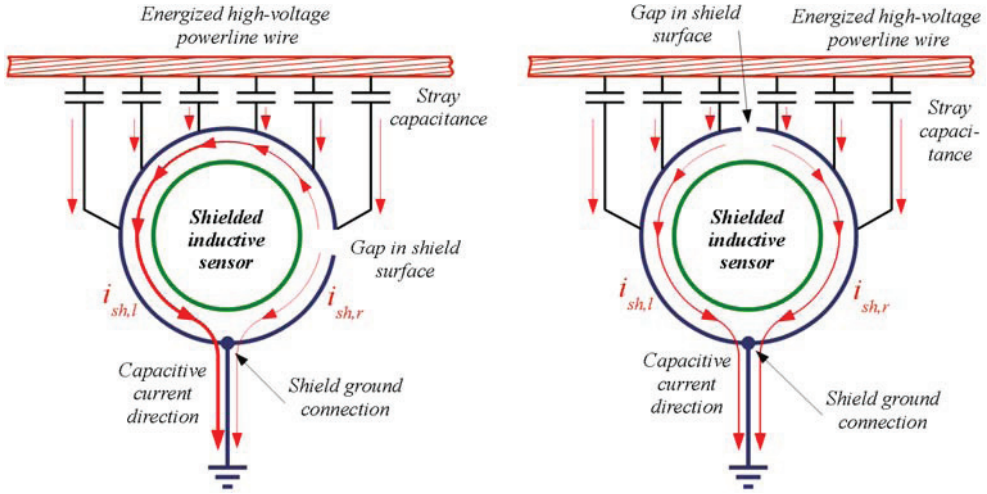

Figure 5.16. Shield with unsymmetrical (on the left) and symmetrical placement of the gap (on the right).

Shielded sensor coil model circuit

For the sensor coil model with shield capacitance, the shield capacitance is added to the coil symmetrically on both output terminals of the coil. As shield is grounded, the shielded coil will now have capacitive coupling to the ground, which will effectively increase the loading of the sensor coil.

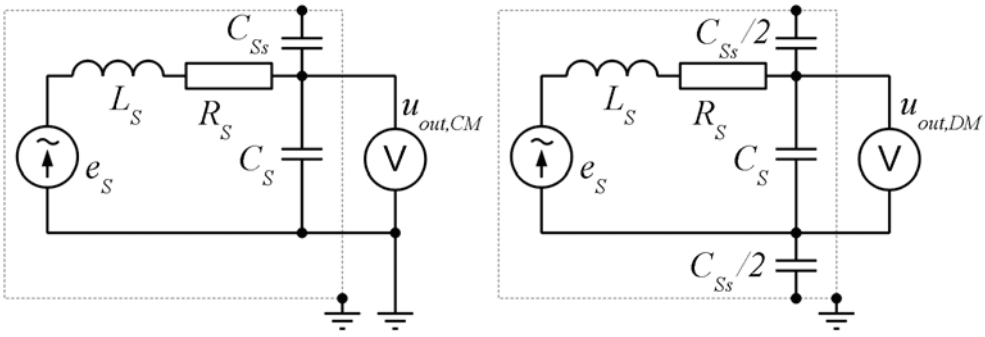

Figure 5.17. Sensor coil with single-ended / grounded mode (on the left) and differential mode connection (on the right).

If the coil shield has been built symmetrically, the sensor-to-shield capacitance C_{Ss} is equally distributed between the two terminals of the sensor coil. There is a difference however if one of the terminals is grounded (single-ended/grounded mode) or both of the terminals are decoupled from ground (differential mode). Presentation of the sensor coil equivalent circuit with shield in Figure 5.17 shows more clearly the difference in the operation. The total grounded-mode capacitive effect of the coil towards the shield in this case is equal to the wire-to-shield capacitance. Situation is more optimistic if differential mode effect is observed. Sensor coil self-capacitance is now the differential load for coil, and the two wire-to-shield capacitances are connected in series for this mode. The total coil loading capacitance for differential mode C_{Sdiff} can be calculated as

$$C_{Sdiff} = C_S + \frac{C_{Ss}}{4}. \tag{5.31}$$

The C_{Sdiff} value presents the value for the sensor coil self-capacitance in differential mode operation. Value of C_{Ss} is would be greater than the value of C_S for multi-turn coils and therefore it is especially beneficial if the effect of this capacitance is kept low.

Shield effect to coil capacitance

As the shield is a conductive and it is connected to ground (this is recommended in practice), there will be capacitive coupling also between the sensor coil wire to the shield and this way also to ground (previously, the sensor coil was observed as totally independent component from ground). The capacitance is distributed in its nature and for establishing a symmetrical structure of the sensor, the shield is advised to be placed at the same distance from the winding at all places.

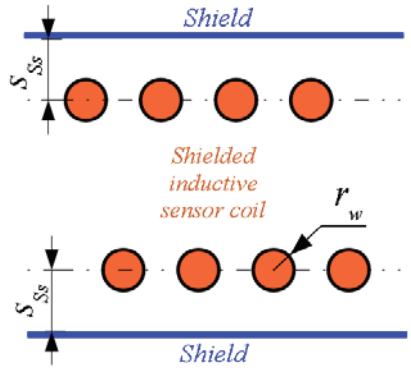

Figure 5.18. Cross-section of a shielded coil.

The topic of investigations of shielded coils is not well covered in literature. One more straightforward source [40] uses approach of a simpler model, assuming every section of winding wire is laying at a separation distance s_{Ss} above ground plain (see Figure 5.18). In this case, the wire capacitance C_{Ss} can be calculated as [40], [48]

$$C_{Ss} = \frac{l_w \cdot \pi \cdot \varepsilon_0}{\ln\left(\frac{s_{Ss} + \sqrt{{s_{Ss}}^2 - {r_w}^2}}{r_w}\right)}, \tag{5.32}$$

where l_w is the total winding wire length.

However, verified by testing done, this approach provides huge error. If observing the electric field distribution, then it can be said for the range of coils used for sensors, in context of this thesis it is better to follow results obtained during testing.

For verification of (5.32) differential self-capacitance of several coils were measured. The testing procedure followed the test case presented in "4.1.2. Capacitance of the sensors", coils' self-resonance was observed for finding the value of self-capacitance. As a reference, a precision capacitance meter was also used to determine the capacitance C_{Ss}. C_{Ss} was calculated based on (5.32); C_{Sdiff} was calculated from measurements using (4.12). The C_S is presented also for the same coil, with shield removed, to obtain the value of C_{Ss} from resonant measurements. Results of the measurements and calculations are presented below in Table 5.6.

Table 5.6. Capacitance measurements and calculations for dense rectangle coils.

r_w (mm)	l_S (mm)	h_S (mm)	S_{Ss} (mm)	w	C_{Ss} (pF) measured	C_{Ss} (pF) calculated by (5.32)	$C_{\mu s}$ (pF) calculated by (5.33)	C_{Sdiff} (pF) measured/ calculated by (4.12)	C_S (pF) calculated by (4.12)	C_{Ss} (pF) calculated by (4.12)	C_{Ss} measured / C_{Ss} calculated by (4.12)
0,15	100	30	2	50	30,8	33,1	34,2	4,92	3,0	4,07	7,6
0,15	100	30	5	20	10,7	39,7	8,0	3,82	2,6	1,29	8,3
0,15	100	30	2	20	15,3	53,0	16,0	4,53	3,0	2,52	6,1
0,15	100	30	7	50	14,8	90,8	12,3	3,88	2,7	1,12	13,2
0,15	100	50	2	20	18,3	61,2	18,5	4,79	3,0	3,57	5,1
0,15	100	50	4	50	19,3	122	22,1	5,76	2,6	9,03	2,1
0,27	100	50	4	20	12,4	56,9	17,0	4,77	3,1	3,09	4,0

Testing verifies that the formula (5.32) presents very pessimistic capacitance values compared to the values observed from measurements. The measurement results show that due to shield that is relatively far away from the winding, the added capacitance ranges up to 5 times the non-shielded capacitance value. This can be even only 1/10 of the value proposed by (5.32).

Finding the formula that would correlate the testing results is actually closer than might be expected. This has also physical background, but in this thesis this is not addressed in more detail. Let it be said for physical phenomenon reference, that electrostatic shielding can be achieved using just a net of wire. Similarity to the coil winding is such, that the wires close together form an equipotential surface and this could be observed as a sheet conductor (see Figure 5.19). In this case, the system can be observed as a microstrip, having air for dielectric.

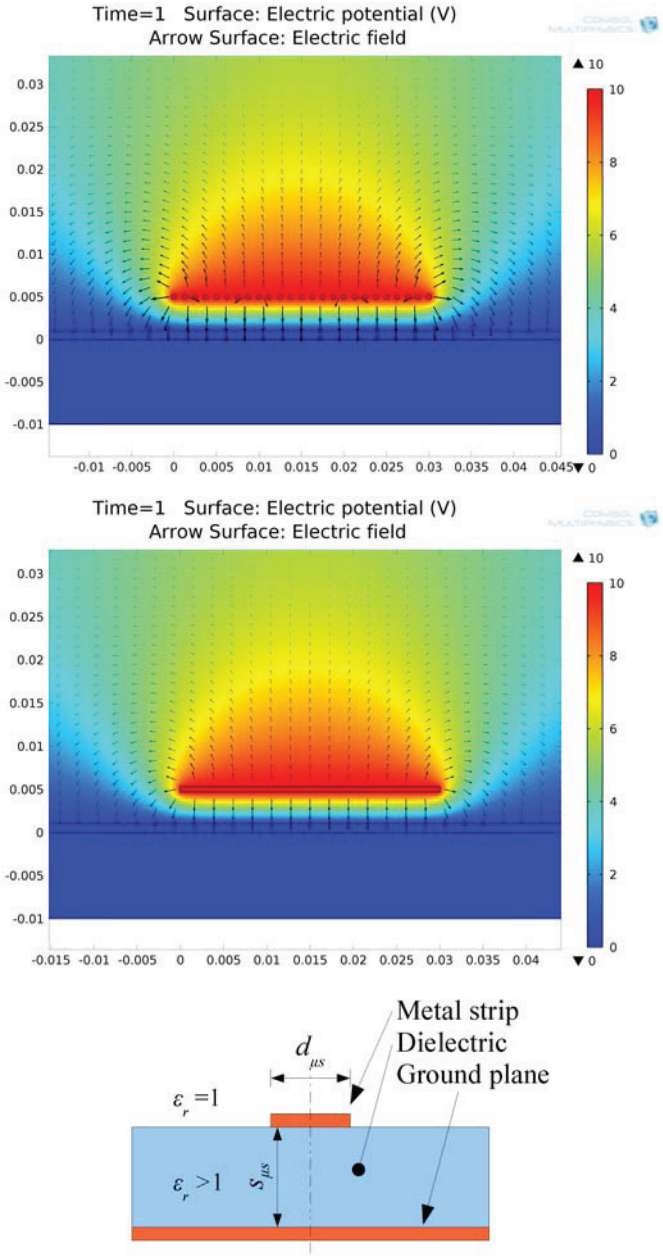

Figure 5.19. Presentation of electric field in case of shielded coil (on the top), microstrip line (in the middle) and microstrip line geometry (on the bottom).

Capacitance of the microstrip is rather well investigated topic, with several approximations to complex formulas. One of such more simple approximations is [75] [104]

$$C'_{\mu s} \cong \frac{\varepsilon_r \cdot \varepsilon_0 \cdot d_{\mu s}}{s_{\mu s}} \left\{ 1 + \frac{2 \cdot s_{\mu s}}{\pi \cdot \varepsilon_r \cdot d_{\mu s}} \left[\ln \frac{d_{\mu s}}{2 \cdot s_{\mu s}} + 1{,}416 \cdot \varepsilon_r + \right. \right.$$
$$\left. \left. + 1{,}547 + (1{,}112 - 0{,}028 \cdot \varepsilon_r) \frac{d_{\mu s}}{s_{\mu s}} \right] \right\}, \tag{5.33}$$

where ε_r is the relative dielectric permittivity of the dielectric material between the metal strip and the ground plain.

This equation is proved to be of high accuracy compared to other approximations [99] [103] but in case of sensor coils simplifications can be added. Equation (5.33) specifies that the capacitance of the microstrip system is increased as the dielectric material between the strip and the ground plane. It is most likely that the dielectric separating the winding and the shield, is actually air in case of sensor coil with $\varepsilon_r = 1$. After the simplification and substitution for the sensor coil dimensions, (5.33) becomes

$$C_{Ss} \cong \frac{\varepsilon_0 \cdot d_C}{s_{Ss}} \left\{ 1 + \frac{2 \cdot s_{Ss}}{\pi \cdot d_C} \left[\ln \frac{d_C}{2 \cdot s_{Ss}} + 2{,}963 + \frac{1{,}084 \cdot d_C}{s_{Ss}} \right] \right\}. \tag{5.34}$$

Use of this formula presents a rather good relation between testing results presented in Table 5.6. The results by (5.34) seem to confirm the measurements of C_{Ss}, this is the static capacitance between the sensor coil and its shield. However, as seen from the table, this still can not shed light on the exact self-capacitance of the shielded coil, as the ratio of C_{Ss} measured to the C_{Ss} calculated from resonance tests is varying to high extent.

A rather holding pattern emerges, as for most of the measured coils the effective $C_{Sdiff} \approx 1{,}5\ C_S$, regardless of the distance of the shield. Assuming the measured coils are similar to the coils of design target, this relation will be used for the coil design. Similarly to statement in "4.1.2. Capacitance of the sensors" this assumption provides less error than using any of the formulas provided above.

Dependence of capacitance on separation of shield and wire

Equation (5.33) presents that the larger the separation is, the smaller will be the value of capacitance between shield and winding wire. For sensor coil shielding design it presents that the shield should be kept a bit further away from the winging to effectively decrease the value of capacitance. Effects of spacing are presented in more detail in Figure 5.20, where results of a coil with $r_w = 0{,}05$ mm and $w = 50$ turns is presented. The view of capacitance is presented for a dense coil, with relation to value of capacitance to the spacing distance in multiples of wire radius. It can be presented that this also applies to wires of different radiuses. A base comparison value C_{Ss0} is the capacitance value obtained when the spacing is equal to the wire

radius; the C_{Ss} presented on the graph is calculated for all shield spacing values from $s_{Ss} = r_w \ldots 100 \times r_w$.

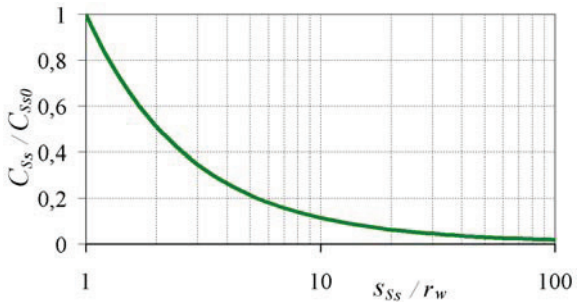

Figure 5.20. Relation of capacitance decrease C_{Ss} / C_{Ss0} with increased shield-to-wire spacing s_{Ss}.

It can be seen, that the fastest decrease of capacitance occurs with the initial increase of the spacing between wire and shield. When the spacing s_{Ss} reaches value of 10 times the wire radius r_w, the capacitance effect has decreased to 5% of the initial.

5.6 Transmission line effects of the sensor coil

At high-frequency operation, the sensor coil geometrical aspects become more and more effective. Reason for this is the fact that every field can propagate with a finite velocity; the electric and magnetic fields also propagate at the velocity of speed of light, though this can vary depending on the propagation environment (see also "2.5. High-frequency transients' propagation on power lines".

This presents a very strong influence to the operation of the sensor coil also. For analysis of transmission line effects, the coil should also be observed as a transmission line with distributed components. Such model circuit of a sensor coil was also presented in Figure 5.1, with every turn specified as the smallest piece of the transmission line. The analysis of the transmission line model will be based on [31], observing the wire as very long straight line.

For observing the nature of the coil as transmission line, a simpler model than in Figure 5.1 could be used. For transmission line effects analysis, it can be shown, a simpler model presented in Figure 5.21 would be sufficient. The model presents the distributed sensor coil inductance L'_S, which is basically inductance per small section of wire. Similarly, each section of wire provides some distributed mutual inductance M'_S, some distributed turn-to-turn capacitance C'_{TT} and some distributed wire resistance, taking into account also skin effect R'_{SSkin}. The coil is assumed to be shielded with distributed sensor-to-shield capacitance C'_{Ss}.

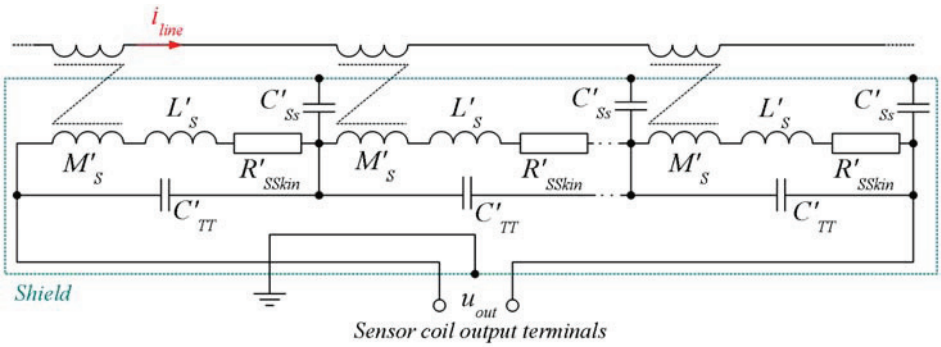

Figure 5.21. Simple transmission line model for use for analyzing the transmission line effects on a sensor coil.

Previously, the transmission line effects were observed for the power lines in "2.5 High-frequency transients' propagation on power lines". The transmission line equations for a schematic presented in Figure 5.21 will be [31]

$$\frac{du(x)}{dx} = -Z_S \cdot i(x) + j \cdot \omega \cdot M'_S \cdot i_{line} \tag{5.35}$$

$$\frac{di(x)}{dx} = -j \cdot \omega \cdot C'_{Ss} \cdot u(x) \tag{5.36}$$

where $u(x)$ is voltage in a location along the coil wire and the sensor's impedance

$$Z_S = \frac{\left(R'_{SSkin} + j \cdot \omega \cdot L'_S\right) \dfrac{1}{j \cdot \omega \cdot C'_{TT}}}{R'_{SSkin} + j \cdot \omega \cdot L'_S + \dfrac{1}{j \cdot \omega \cdot C'_{TT}}}. \tag{5.37}$$

Solving these equations and taking into account the value of terminating resistor, the frequency-dependent transfer function will be in form

$$\frac{u_{out}}{i_{line}} = \frac{j \cdot \omega \cdot M'_S \cdot R_T \cdot Z_{S0} \cdot \sinh(\gamma \cdot l_w)}{Z_S \cdot \left[Z_{S0} \cdot \sinh(\gamma \cdot l_w) + R_T \cdot \cosh(\gamma \cdot l_w)\right]}, \tag{5.38}$$

where γ is called a propagation constant

$$\gamma = \sqrt{\frac{R'_{SSkin} + j \cdot \omega \cdot L'_S}{R'_{SSkin} + j \cdot \omega \cdot L'_S + \dfrac{1}{j \cdot \omega \cdot C'_{TT}}} \cdot \frac{C'_{Ss}}{C'_{TT}}} \tag{5.39}$$

and Z_{S0} is the wave impedance of the coil

$$Z_{S0} = \sqrt{-\frac{R'_{SSkin} + j \cdot \omega \cdot L'_S}{\omega^2 \cdot C'_{TT} \cdot C'_{Ss} \left(R'_{SSkin} + j \cdot \omega \cdot L'_S{}' + \frac{1}{j \cdot \omega \cdot C'_{TT}} \right)}}. \qquad (5.40)$$

In order to present the aspects of distributed model of the sensor coil, the magnitude and phase response of the transfer function can be calculated using (5.40). The results of the calculations have been presented for a shielded practical coil, which parameters are previously known (see Table 5.6). The coil under observation has length l_C = 100 mm, height h_C = 30 mm, number of turns w = 20, shich results in wire length l_w = 5,2 m. The coil winding to shield separation distance s_{Ss} = 5 mm, and electrical parameters are C_S = 2,6 pF; C_{Ss} = 1,3 pF and L_S = 46,8 μH. The results of calculations are presented in Figure 5.22 and Figure 5.23, using the per-length values of the electrical parameters. First resonance here can be observed at a frequency of 72,9 MHz. The wavelength of such frequency is actually shorter than the coil length (4,1 m vs. 5,2 m). Still, observing effects of the different input variables of the formulas, the results are directly dependent on the length of the transmission line l_w specified. The other parameter with great influence to the coil self-resonant frequency is the value of C_{Ss}. For the investigated coil ranges, the highest first resonance is seen, when the value of C_{Ss} is very low. For the practical coils, the C_{Ss} measured would be varying depending on the shield distance from the coil winding. While analysis of the exact phenomena is rather complex, the results form calculations of actual coils presents, that it would be safe to assume that the first resonance would be found at frequency, with wavelength less than 1,1 times the coil wire length.

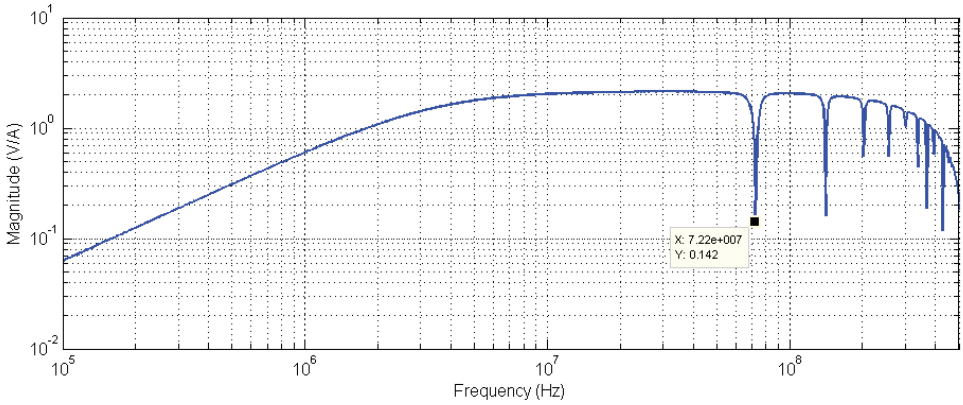

Figure 5.22. Magnitude transfer plot frequency plot according to (5.40).

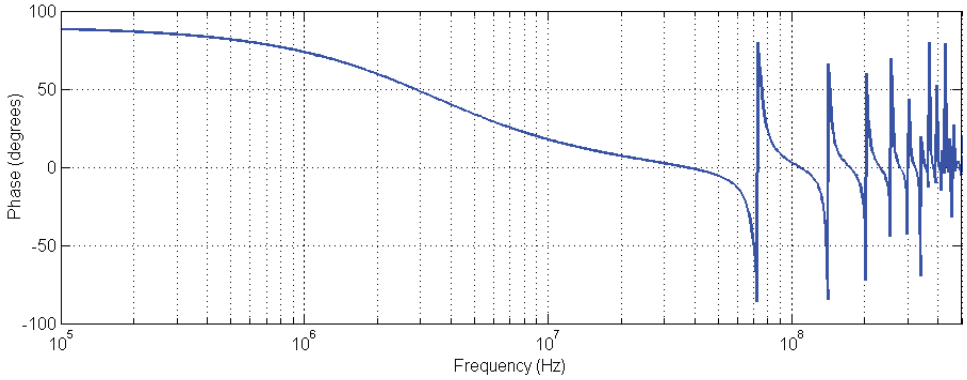

Figure 5.23. Phase response frequency plot according to (5.40).

The outcome of the transfer function presents some sensitivity decrease at the point of resonances, which actually does not present very great harm to the measurement results. This is because there would not be a dominating frequency component that is magnified due to the resonance. But as for the requirements to the pulsed measurements, the phase response should also be observed. This plot presents that every location of resonance would provide 180° phase shift, which is unacceptable for the accurate measurements. Also an aspect to point out is the bandwidth of resonance – in this case the magnitude and phase plots show that the resonance point is quite sharp. The decrease of transfer magnitude but also the phase shift will have effect only shortly before the resonance.

The distributed model for coil in this way presents, that the first resonance due to the coil physical length would be the limit for the coil bandwidth. As there definitely would be some signal components reaching above the resonance limits, quite sharp filtering should be applied to remove the signal components having phase shift different than the other signal components.

5.7 Summary

The sensor high-speed model presents the stray components that can affect the performance above frequency of 10 … 30 MHz. As presented, most critical effects to take into account are rather invisible in the initial approach. The inductance of wires and terminating resistor inductance are not discussed in literature at all, yet there are many claims of performing accurate measurements even up to hundreds of MHz range. In reality, reaching high frequency operation with inductive sensor, such as also Rogowski coils, requires much precision and attention to the physical sensor design but also to the external circuitry design.

The importance of the sensor coil high-frequency model is to provide information about stray components that are decreasing the overall accuracy and sensitivity of the sensor. There are often limited options available to control the stray components, these mostly have to be taken into account and find some ways to overcome the effects in signal processing stages.

6 Sensor design criteria and methods

In general the target of the sensor design can be specified as follows, but not limited to:

1. Geometrical aspects, also related to sensitivity
   - sensor should have as high sensitivity as possible to capture the weak PD-events;
   - sensor should be capable of performing accurate measurements at offset from the wire, as it is intended for power lines;
   - sensor should have dimensions that are reasonable and feasible for manufacturing, use and maintenance.
2. Electrical operation aspects
   - sensor should cause as little distortions to the signal as possible;
   - sensor should have sufficient bandwidth for performing measurements.
3. Measurement qualification aspects
   - sensor model should be accurate and represent the sensor actual behaviour;
   - sensor output should be equipped with signal processing unit(s) that provides the original waveform of the measured signal;
   - signal processing unit should be able to compensate for the native measurement error of the sensor.

These are the design criteria that should be analysed to give some estimation on the suitable build-up of the sensor and its capabilities. The sensor design procedure presented here starts with the geometrical design to determine the mutual inductance of the sensor, following the limits for the wire length.

One of the most important parts for sensor electrical properties design is the sensor bandwidth design. Intention of this stage is to provide a sensor physical construction so that the sensor coil would operate in the required bandwidth. Criteria for the operating bandwidth have been previously discussed in “4.3.3. Damping and effect on bandwidth”, and the bandwidth requirements were discussed in “6.1. Requirements for a sensor”. The operating bandwidth design is specified under electrical performance design topics, and there are two directions of accomplishing this – either by observing the inductance or the sensitivity as the most important criterion. The sensor design procedure is presented for both cases with examples and results of simulations are presented.

6.1 Requirements for a sensor and design procedures

Requirements for the sensor presented is based largely on the results of signal analysis described in "2.2. Frequency spectrum analysis of transient signals". The summary of requirements used in the following work:

- Sensitivity: the weaker PD signals can provide voltage trace with amplitude of only some volts. Assuming line characteristic impedance of 400 Ω, a PD signal with peak at 2 V provides only 5 mA current peak. This should not vanish into noise of the sensor.
- Limiting dimensions: using the sensor and the measurement device in real networks does not mean that the sensor should be as small as possible. For outdoors/overhead lines applications rather suitable would be if the sensor coil frame was around up to 5 cm thick, 20 cm wide and 20 cm long. This would also provide necessary robustness and mechanical strength of the supporting material, suitable fixing places and isolation. This roughly means that sensor could be up to 15 × 15 × 3 cm size. For the indoors/cable applications, the sensor outline could be 2 × 5 × 15 cm, for convenient mounting in tighter places. As the isolation on the cables is usually very good, sensor mechanical design does not have to provide as good electrical withstand capabilities. The reasonable sensor coil dimensions in this application could be, for exaple, 1 × 4 × 14 cm.
- Bandwidth: the sensor for capturing the fast pulse transients does not require measurements on low frequencies. Assuming various high-frequency effects, listed in "5. Air-core sensor high-frequency model" and others, it is rather feasible to limit the sensor bandwidth to 100 MHz. Results presented using filtering of captured signals in "2.4. Bandwidth analysis" confirm, that the 100 MHz upper bandwidth is suitable for the accurate measurements.

There requirements are the constraints to provide the analysis of parameter selection. The number of combinations without limitations would be too large to provide a reasonable analytical approach for the design aspects.

The design procedure itself would consist of several stages. First, the sensor geometry design will determine the essential mutual inductance, which will in turn be one of the major aspects for the calculation of sensitivity. Second, the sensor coil electrical design will be carried out to determine the electrical characteristics, as inductance, total capacitance and also external terminating resistor. There are two directions for carrying out the electrical design – first is the bandwidth design using inductance as the determining value and not observing the geometry of the coil as the design constraint. Second approach is by carrying out the design using sensitivity and coil parameters as base criteria. In this way, the sensor inductance is calculated later and the coil wire length is the most important aspect of the coil design. The last stage of the design is the verification of designed sensor electrical

characteristics by measuring the parameters and carrying out the verification simulations. All the design steps above will be described in more detail.

6.2 Sensor geometry design

The sensor geometry design should follow the requirements presented above, observing mechanical and practical criteria. Options for the electrical design phase of the sensor coil are also presented by the geometry design, as the physical wire length is the factor that determines the bandwidth limit (see "5.6. Transmission line effects of the sensor coil").

Sensitivity of the sensor is dependent on the factor of mutual inductance between the sensor coil and the wire being measured (see "6.3. Sensitivity of the sensor coil"). For designing a sensor with the best sensitivity, the mutual inductance value should be the highest. Related to electrical design of the sensor, the mutual inductance depends on the number of turns of the coil, but higher number of turns will mean longer wire of the sensor coil winding. It could be even estimated, that the sensor wire length is more critical than the inductance of the coil in determining the operating bandwidth (this will later be presented also).

Knowing the sensor coil upper operating frequency, the limiting factor to the geometrical design should be the wire length. It should be as long as the wavelength of the highest operating frequency, for assuring that the coil is made of maximum number of turns possible, thus ensuring the highest sensitivity.

As a basis of the analysis, a rectangular sensor coil could be observed. This coil would have side length of l_C and winding height of h_C. The coil would be placed under a wire, with a distance $h_{C,line}$ from the wire. In this case the mutual inductance could be calculated as

$$M_S = \frac{\mu_0 \cdot w \cdot l_C}{2\pi} \ln \frac{h_C + h_{C,line}}{h_{C,line}} \tag{3.14}$$

Target of such analysis would be to find out the maximum value of mutual inductance M_S for a specific length of wire of a winding turn, at a specific height from line $h_{C,line}$. For the outcome, however, one of the most important characteristics is the shape ratio RR_C of the coil, which presents the relation between the length of the coil l_C and height of the coil h_C as

$$RR_C = \frac{h_C}{l_C} \ . \tag{6.1}$$

Knowing a particular wire length l_w, the coil length, for example, can be found as

$$l_C = \frac{l_w}{2(RR_C + 1)} \tag{6.2}$$

and the coil height

$$h_C = \frac{l_w \cdot RR_C}{2(RR_C + 1)}. \tag{6.3}$$

Substituting these values into the mutual inductance formula, it results

$$M_S = \frac{\mu_0 \cdot w \cdot l_w}{2\pi \cdot 2(RR_C + 1)} \ln \frac{\frac{l_w \cdot RR_C}{2(RR_C + 1)} + h_{C,line}}{h_{C,line}}. \tag{6.4}$$

The function presents that the shape ratio RR_C in dependence on the height from the line h_C but also on wire length l_w. Typically the insulation thickness $h_{C,line}$ between sensor coil and wire are provided. For presenting the analysis of the optimal shape ratio, the wire length is observed as constant at different heights from the line h_C. The results of such calculations have been presented in Figure 6.1.

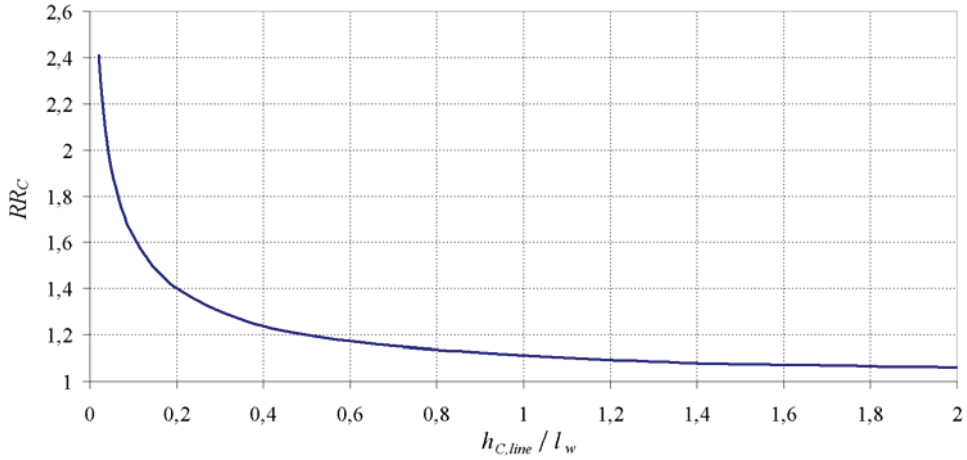

Figure 6.1. Selection shape-ratio of a sensor coil depending on the single-turn wire length and sensor height from the wire measured.

From graph in Figure 6.1 conclusions on the coil optimal shape can be drawn. Namely, when the separation distance of the coil is relatively large compared to the coil dimension, more square-shape coil would be optimal, with shape ratio $RR_C \approx 1$. When the coil dimensions become comparable to the separation distance ($h_{C,line} / l_w$) < 0,5 it is more beneficial to use a coil with rectangular form, with shape ratio RR_C up to 2,5.

6.3 Sensitivity of the sensor coil

In discussion about sensor low-frequency model in “3.3. Number of turns and mutual inductance” the dependence of mutual inductance on the value of number of turns of the coil (3.14) states that more there are turns to the coil, the higher its mutual inductance is. Expressing sensor coil output voltage as (3.13)

$$e = -M\frac{di}{dt}$$

and counting the mutual inductance value to be constant, the key factor determining the output will be rate of current variation (di/dt). In the magnitude plots of the sensor coils presented, this can be seen at lower frequency values, when the output is growing proportional to the frequency of the current signal, also showing phase shift of 90 degrees for sine waveform. This trend comes to an end when current signal frequency value reaches the value of frequency of the first pole of the sensor coil transfer function (see Figure 4.14).

The magnitude plot will become stable at the same level it is approximately at the first pole frequency, and stays stable at this value until the frequency of the second pole of the sensor coil transfer function. It provides a very straightforward approach for finding the sensitivity of the sensor coil for the operating bandwidth. Namely, when the magnitude plot is stable from the first pole on, it is reasonable to find the output voltage and measured current ratio at the frequency corresponding to the frequency of the first pole.

Assuming sinewave for testing, the current variation rate at frequency of f_{p1} will be

$$\frac{di_{line}}{dt} = \frac{d\left[\ i_{line,mag}\sin(2\cdot\pi\cdot f_{p1}\cdot t)\ \right]}{dt} = i_{line,mag}\cdot 2\cdot\pi\cdot f_{p1}\cdot\cos(2\cdot\pi\cdot f_{p1}\cdot t), \quad (6.5)$$

where $i_{line,mag}$ – magnitude value of current of a line being measured.

Peak output value will be provided at time $t = 0$, when the current variation rate will be

$$\left.\frac{di_{line}}{dt}\right|_{\max} = i_{line,mag}\cdot 2\pi\cdot f_{p1}. \quad (6.6)$$

Sensitivity of the coil in the self-integrationg range can be given in V/A (volts per ampere), for which the term transimpedance is proposed [5] or in other form transfer impedance [108], measured in Ω. In this context it is appropriate to define the sensor coil sensitivity value as

$$K_S = \frac{-u_{out,\max}}{i_{line,\max}} = \frac{-u_{out}}{i_{line}}, \quad (6.7)$$

where both input current and output voltage will be represented by their instantaneous values, and when using (3.12)

$$-u_{out} = f_{p1}\cdot 2\pi\cdot M_S\cdot i_{line}. \quad (6.8)$$

Observing the sensor output as absolute value [96],

$$K_S = \frac{u_{out}}{i_{line}} = f_{p1}\cdot 2\pi\cdot M_S. \quad (6.9)$$

This sensitivity value is only valid for the operating bandwidth. For more universal method of calculating the coil sensitivity, when the coil electrical parameters like capacitance and inductance values are known, (4.34) can be used for calculation of f_{p1}

$$K_S \approx M_S \frac{R_S + R_T}{L_S + R_S \cdot R_T \cdot C_E} \ . \tag{6.10}$$

6.4 Sensor electrical design based on determination of inductance

The approach of an inductive sensor design using inductance determination assumes at first that the coil length would be short enough that the coil actually will not be presenting any resonance in the operating frequency range due to coil physical length. In this case, the coil inductance is the main design criterion. This approach is suitable for example, for coils with high number of turns but small dimensions. It can be proposed in this case that the coil would have shape close to a rectangle, as presented in analysis above in "6.2. Sensor geometry design".

For the design of operating bandwidth, the medium-frequency model is used. There are three components in this model that determine the sensor behaviour – sensor coil self-inductance L_S, self-capacitance C_S and termination resistor R_T resistance. During bandwidth design, values for all these three components should be determined. First, however, some essential features are discussed for the inductance geometrical design. A shielded coil is needed for the high-frequency operation, therefore aspects of a shielded coil design are only focused on.

6.4.1 Inductance of multi-turn coil

Initial formulas for calculating the coil inductance were presented in "4.1.1. Inductance of the sensor". Discussion there involves methods of inductance calculations, while number of turns and coil geometry is known. In the sensor electrical design, the geometry could be known to more extent; however the number of turns remains key variable to be determined. The formulas for multi-turn coils, present also coil thickness as one variable, dependent on number of turns. Derivation of expression for selecting suitable number of turns is rather difficult and taking into account basic relations for sensor coil electrical design, such formulas are even not feasible due to their complexity. There are some starting points in presented in "4.1.1. Inductance of the sensor" that can be helpful in providing the relations useful for the sensor electrical design. In particular, similar approach to ones provided in Table 4.2 and Table 4.4 should be observed.

Considering ideal case, inductance of a coil should be in relation the number of turns squared as (4.2)

$$L_{coil} = w^2 \cdot L_{loop} ,$$

the number of turns, provided the coil inductance and loop inductance are known can be calculated as

$$w = \sqrt{\frac{L_{coil}}{L_{loop}}}\,. \tag{6.11}$$

Equation (6.11) has its virtue in simplicity, yet already Table 4.2 and Table 4.4 present, that the results obtained using formulas by Wheeler [119] (4.4) and (4.8) are not the same at number of turns of 10. The difference of inductance calculation by (4.2) is growing with the number of turns increasing. Inductance formulas by Wheeler [119] (4.4) and (4.8) are quite accurate also for coils with large number of turns; therefore the latter should be used as reference. However, expressing the number of turns from (4.4) and (4.8) is rather difficult. Another possibility would be the use of correcting function to number of turns and still use (6.11) as

$$w = \sqrt{\frac{L_{coil}}{L_{loop}}} \cdot K_L\,, \tag{6.12}$$

where K_L is the correction function.

Idea behind this is to find the number of turns, which would provide by (4.4) or (4.8) the same inductance as was searched for with (6.11). For example, if by (6.11) the determined number of turns is w_1, then by (4.4) or (4.8) the resulting inductance is significantly smaller. If the result of (6.11) is multiplied by correction factor, then a new number of turns w_2 is aquired, which provides the initial searched L_{coil} inductance value when using (4.4) or (4.8). The correction function in this case can be evaluated as

$$K_w = \frac{w_2}{w_1}\,. \tag{6.13}$$

To find the correction factor, a numerical analysis is carried out. In order to limit the K_L range, the inductance of circular and square coils are observed, which in practice are of interest for the sensor coil. For circular coils the investigated coil radiuses r_C are 25, 50 and 100 mm; for square coils the investigated coil side lengths l_C are 30, 50, 100 and 300 mm. All coils are calculated as dense coils with winding wires are close to each other, wire radius varying from 0,05 … 0,2 mm. In the first case, equation (4.2) is used to obtain the coil inductance, initial loop inductance is calculated using (4.3) and (4.7) respectively and selecting number of turns w_1. Then, using (4.4) and (4.8) respectively, and investigating the results while varying number of turns, the closest value to number of turns w_2 is determined for reaching the same inductance value as by (4.2). Value of w_2 is always higher, which presents the need to adjust the number of turns by (6.11) to positive direction. Results of analysis are presented in Table 6.1.

Table 6.1. Analysis of correction function for number of turns.

Specified w_1 (4.2)	Closest matching w_2 found for (4.4)	Average difference @ w_1 by (4.4) vs. w_1 by (4.2)	Max. difference @ w_1 by (4.4) vs. w_1 by (4.2)	Average difference @ w_2 by (4.4) vs. w_1 by (4.2)	Max. difference @ w_1 by (4.4) vs. w_1 by (4.2)	$K_w = w_2 / w_1$	Estimated w_{corr} by (6.15)	Average difference @ w_1 by (4.4) vs. w_{corr} by (4.2)	Max. difference @ w_1 by (4.4) vs. w_{corr} by (4.2)
9	10	24%	32%	9%	19%	1,11	10	9%	19%
12	15	29%	38%	8%	17%	1,25	15	8%	17%
15	19	33%	43%	7%	17%	1,27	19	7%	17%
20	27	38%	49%	10%	22%	1,35	27	10%	22%
25	35	42%	54%	11%	24%	1,40	35	11%	24%
35	52	47%	61%	14%	31%	1,49	53	15%	33%
50	76	53%	68%	16%	43%	1,52	80	17%	40%
75	128	60%	75%	20%	50%	1,71	127	20%	51%
100	171	64%	80%	25%	61%	1,71	177	24%	59%
150	280	68%	82%	31%	69%	1,87	281	31%	69%

For dense coils, the difference between (4.2) and (4.4), if observed at same number of turns is becoming obvious at around 10 turns, therefore the analysis starting point is also 9 turns. As the number of turns is getting higher, the correlation between different wire sizes is becoming smaller and the difference is growing. Therefore the results presented in Table 6.1 can be considered reliable up to 100 turns, as the maximum difference on edge values (smallest wire, largest dimensions and vice versa) is becoming very large and shadows the average correlation.

The correction function presented in Table 6.1 holds a logarithmic relation to specified number of turns w_1. The function was determined using logarithmic fit tools and a very good correlation to K_w is provided by

$$K_w = 0{,}2643 \cdot \ln(7{,}134 \cdot w_1) \,. \tag{6.14}$$

When the coil inductance is known, and loop inductance is known the specified initial number of turns can be found by (6.11)

$$w_1 = \sqrt{\frac{L_{coil}}{L_{loop}}} \,,$$

and after applying correcting function as in (6.12), the final corrected number of turns w_{corr} in the coil would be

$$w_{corr} = \sqrt{\frac{L_{coil}}{L_{loop}}} \cdot \left[0{,}2643 \cdot \ln\left(7{,}134 \cdot \sqrt{\frac{L_{coil}}{L_{loop}}} \right) \right]. \quad (6.15)$$

The results of finding number of turns using (6.15) have also been presented in Table 6.1, confirming that the correction function is sufficiently accurate. In the following, this function soon becomes key element in determining the number of turns for a coil.

Adding a closed shield around a coil will cause the value of inductance to decrease significantly [126]. In the application of the magnetic sensor coil, such closed shield would decrease the sensitivity significantly and therefore closed shield is not an option. Instead, a gap is introduced to the shield, which means that there is no shorted path for the current that would cause drastic reduction of inductance. In literature available, such shielding has practically been not discussed. During practical tests also a search for simple empirical solution was not found for the calculation of inductance of the shielded coil with a gap in shield. It can be presented that the inductance decrease due to added shield is up to 20% in some cases; this is much lower value than presented in [126]. It is therefore recommended to measure the exact inductance of a prototype coil and then make some corrections if needed, when designing a shielded coil.

6.4.2 Coil parameters selection

The electrical design will start with assuming the self-capacitance value of the coil to have value of 2,0 pF (as explained in "4.1.2. Capacitance of the sensors") and the shielded coil total capacitance at value of 3,0 pF (as explained in "5.5.2. Shielding of the sensor"). The wire used in this example has radius r_w = 0,15 mm. Let the loop dimensions be l_C = 30 mm and h_C = 30 mm, the loop is mounted at height of $h_{C,line}$ = 20 mm from the measured line. The measurement system input capacitance C_M = 4 pF and the connecting cable capacitance C_W = 1 pF are used in this design.

In the following example a sensor coil is designed, assuming limits on upper operating frequency $f_{\max}$ = 100 MHz and on lower bandwidth f_{min} = 100 kHz.

First it can be said that the logarithmic operating bandwidth spans over

$$\Delta f_{\log} = \log \frac{f_{\max}}{f_{\min}} = \log \frac{100 \cdot 10^6}{100 \cdot 10^3} = 3 \text{ decades}. \quad (6.16)$$

Following discussion in "4.3.3. Damping and effect on bandwidth" the operating bandwidth can be considered as symmetrical on logarithmical frequency scale towards resonance. In present case with bandwidth span $\Delta f_{\log}$ of 3 decades, the resonant frequency should be 1,5 decade (31,6 times) higher than the f_{min}, that is

$$f_{res} = 10^{\Delta f_{\log}/2} \cdot f_{\min} = 31{,}6 \cdot 100 \cdot 10^3 = 3{,}16 \cdot 10^6 \text{ Hz}. \quad (6.17)$$

When stable phase shift region is specified as operating bandwidth, the poles should be 1 decade lower than $f_{\min}$ and 1 decade higher than $f_{\max}$:

- pole #1 should be located at frequency f_{P1} = 10 kHz;
- pole #2 should be located at frequency f_{P2} = 1 GHz.

Next, attention should be turned to resonance frequency calculation formula for the inductive sensor model

$$f_{res} = \frac{1}{2\pi \cdot \sqrt{L_S(C_S + C_W + C_M)}} \cdot \tag{4.53}$$

For calculating the resonance both capacitance and inductance need to be known; in other case when capacitance is known the inductance value can be determined.

Considering that measuring system $C_W + C_M$ holds in this example 5 pF, the majority of the capacitance will not originate from the sensor coil. Sum of the capacitances in the system in the first case would be quite constant regardless of the number of turns of the coil. Therefore one can specify that the overall capacitance $C_E = C_S + C_W + C_M \approx 8$ pF.

Required resonance frequency was determined previously; also now as coil system capacitance is specified the required inductance of the coil can be calculated. From resonance equation (4.53), the sensor coil inductance would need to have value of

$$L_S = \frac{1}{4 \cdot \pi^2 \cdot {f_{res}}^2 \cdot (C_S + C_W + C_M)} = \frac{1}{4 \cdot \pi^2 \cdot \left(3{,}16 \cdot 10^6\right)^2 \cdot 8 \cdot 10^{-12}} \approx 317 \cdot 10^{-6}\,\text{H}.$$

Assuming the coil is shielded, the inductance of the unshielded designed coil should be about 20% higher. Thus the target inductance value will be L_S = 380 μH.

Inductance of a coil can be determined by number of turns and loop inductance. As discussed in ”6.4.1. Inductance of multi-turn coil” the initial characteristic needed is single-turn loop inductance L_{loop}. For a rectangle loop with dimensions l_C = 30 mm and h_C = 30 mm, the loop inductance calculated by (4.7)

$$L_{loop} = \frac{2 \cdot \mu_0 \cdot 0{,}030}{\pi}\left[\ln\left(\frac{0{,}030}{0{,}00015}\right) - 0{,}774\right] \sim 109 \cdot 10^9\ \text{H}.$$

The number of turns for the sensor coil can now be calculated using (6.15)

$$w_S = \sqrt{\frac{380 \cdot 10^{-6}}{109 \cdot 10^{-9}}} \cdot \left[0{,}2643 \cdot \ln\left(7{,}134 \cdot \sqrt{\frac{380 \cdot 10^{-6}}{109 \cdot 10^{-9}}}\right)\right] = 63\ \text{turns} \cdot$$

Coil wire resistance can be found using (4.13)

$$R_S = \frac{l_{w0} \cdot w_s \cdot \rho_{Cu}}{A_{Sw}} = \frac{2 \cdot (0{,}03 + 0{,}03) \cdot 63 \cdot 1{,}68 \cdot 10^{-8}}{\pi \cdot \left(0{,}15 \cdot 10^{-3}\right)^2} = 1{,}80\ \Omega.$$

Value of terminating resistance can now be found from the poles formula (4.34)

$$R_T = \frac{2\pi \cdot f_{p1} \cdot L_S - R_S}{1 - R_S \cdot C_E \cdot 2\pi \cdot f_{p1}} = \frac{2 \cdot \pi \cdot 10^4 \cdot 317 \cdot 10^{-6} - 1{,}8}{1 - 1{,}8 \cdot 8 \cdot 10^{-12} \cdot 2 \cdot \pi \cdot 10^4} = 18{,}1\ \Omega.$$

Frequency of the second pole will be (4.37)

$$f_{p2} = \frac{1}{2\pi}\left(\frac{L_S + R_S \cdot R_E \cdot C_E}{R_E \cdot C_E \cdot L_S} + \frac{R_S + R_E}{L_S + R_S \cdot R_E \cdot C_E}\right) = 1{,}09 \cdot 10^9\ \text{Hz} = 1{,}09\ \text{GHz}.$$

The mutual inductance of the sensor coil with the determined parameters will be

$$M_S = \frac{\mu_0 \cdot w_S \cdot l_C}{2\pi} \ln \frac{h_{C,line} + h_C}{h_{C,line}} = \frac{\mu_0 \cdot 63 \cdot 0{,}03}{2\pi} \ln \frac{0{,}05}{0{,}02} = 364 \cdot 10^{-9}\,\text{H} = 346\ \text{nH}.$$

The sensor sensitivity will be (6.9)

$$K_S = f_{p1} \cdot 2\pi \cdot M_S = 10 \cdot 10^3 \cdot 2\pi \cdot 346 \cdot 10^{-9} = 0{,}0217\ \text{V/A}. (-33{,}7\ \text{dB})$$

A summary of parameters of the designed sensor are presented in Table 6.2.

Table 6.2. Summary of designed sensor coil initial and design parameters.

Initial parameters		Design parameters	
l_C (mm)	30	L_S (μH)	317
h_C (mm)	30	w_S	63
r_w (mm)	0,15	R_S (Ω)	1,80
$h_{C,line}$ (mm)	20	R_T (Ω)	18,1
$f_{\max}$ (MHz)	100	M_S (nH)	346
$f_{\min}$ (MHz)	0,1	K_S (V/A)	0,0217
C_S (pF)	2		
C_{SDiff} (pF)	3		

The magnitude and phase plot for this sensor coil are presented on graphs in Figure 6.2.

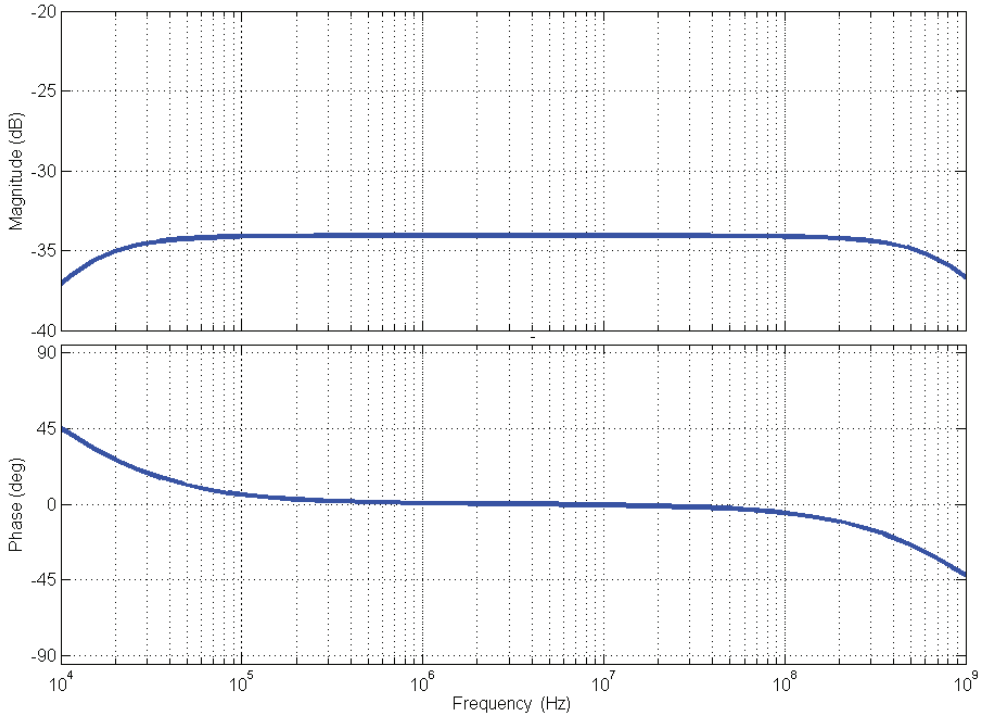

Figure 6.2. Magnitude and phase plot of the designed sensor.

The plots in Figure 6.2 present that the designed coil indeed has poles at f_{p1} = 10 kHz and f_{p2} = 1 GHz. This concluding part of the sensor coil inductance-based design is the verification of the coil length and estimating the first resonance emerging from the transmission line approach. The length of the coil wire is

$$l_w = 2 \cdot (l_C + h_C) \cdot w = 2 \cdot (0{,}03 + 0{,}03) \cdot 63 = 7{,}56 \text{ m}.$$

Based on analysis in "5.6. Transmission line effects of the sensor coil", the limiting first resonant frequency of the coil would be

$$f = \frac{2{,}99 \cdot 10^8}{1{,}1 \cdot 7{,}56} = 35{,}9 \text{ MHz},$$

which is almost three times lower than the target highest bandwidth. This presents the risks of the pure inductance approach for the sensor coil design, as the proposed coil would not be usable for measurements in the frequency range set in the design specification.

6.5 Sensor electrical design based on sensitivity criteria

The sensor design criteria can be also sensitivity of the sensor, which presents an alternative method for the sensor electrical design. In this case, the sensitivity requeirements are determined first.

To determine the sensitivity requirements for the sensor, the measured waveform characteristics should be determined first. An example of a PD waveform is available in "2.2.1. Fast transient signal waveforms, windows of analysis and frequency spectrum". The sensor for the measurement of PD transients would need to capture waveforms with peak value of 14 V.

Assuming the power line characteristic impedance value of 400 Ω, the magnitude of expected current would be (2.11)

$$i = \frac{u}{Z} = \frac{14}{400} = 0{,}035 \text{ A} \cdot$$

The resolution of the PD pulse is the next criterion. The sensor coil will pick up distortions from the environment, the noise level in the sensor output should be determined for each case by initial measurements. For the present design, the noise level is assumed to be 1 mV, a quite small value. However, the PD measurement result would need to be high above the noise level, for example, 10 times higher than the noise. In this case, the peak voltage in the sensor output should be at least 10 mV.

The output voltage divided by the input current will determine the sensitivity of the sensor and this will be (6.7)

$$K_S = \frac{u_{out}}{i_{line}} = \frac{10}{35} = 0{,}286 \text{ V/A} \cdot$$

Observing the theoretical approach in "6.3. Sensitivity of the sensor coil", the sensitivity is defined by the value of the pole of the lowest frequency and by the value of mutual inductance. Assuming the frequency of the lowest pole as $f_{p1} = 10 \cdot 10^3$ Hz, the mutual inductance value can be found based on (6.9) as

$$M_S = \frac{K_S}{2\pi \cdot f_{p1}} = \frac{0{,}286}{2\pi \cdot 10 \cdot 10^3} = 4{,}55 \cdot 10^{-6} \text{H} = 4{,}55 \,\mu\text{H}.$$

This value of mutual inductance presents the total mutual inductance of the sensor coil. Knowing the single turn mutual inductance towards the measured wire, the number of turns can be calculated. This is also useful as it presents the condition to find out the wire length for the sensor coil, needed to reach the highest design target frequency.

At 100 MHz, the wavelength λ of the signal is almost 3 m. As discussed in "5.6. Transmission line effects of the sensor coil" sensor coil wire should have length less than $\lambda/1.1$. The coil wire total length would need to be $l_w < 2{,}72$ m. Using a sensor coil with loop dimensions of $l_C = 100$ mm and $h_C = 30$ mm, one turn of the loop would have length of $l_{w,loop} = 0{,}26$ m. Total number of turns for the coil would be 10 turns, with more turns in coil the wire length requirement to operating frequency bandwidth will not be met.

If such a loop is placed at height $h_{C,line}$ = 0,05 m from the line being measured, the mutual inductance of the loop would be (3.14)

$$M_{loop} = \frac{\mu_0 \cdot l_C}{2\pi} \ln \frac{h_{C,line} + h_C}{h_{C,line}} = \frac{\mu_0 \cdot 0{,}1}{2\pi} \ln \frac{0{,}08}{0{,}05} = 9{,}40 \cdot 10^{-9}\,\text{H} = 9{,}4\,\text{nH}\,.$$

For a coil with w = 10 turns, the mutual inductance value will be

$$M_S = M_{loop} \cdot w = 94{,}0 \cdot 10^{-9}\ \text{H} = 94\,\text{nH}\,.$$

This is almost one fifth of the sensor mutual inductance value observed as the necessary for fulfilling the sensitivity requirement. It can be increased, taking the sensor closer to the power line wire measured, but this might not be allowed by the insulation requirements. One way of reaching such high sensitivity values would be using wide bandwidth amplifiers in the output of the sensor.

Once the coil geometry is determined, the coil electrical characteristics can be determined. A presented loop with l_C = 100 mm and h_C = 30 mm would have inductance by (4.6) of L_{loop} = 280 nH. The 10-turn sensor coil would present total inductance value (4.2) (6.13) L_S = 22,7 µH. Observing the coil capacitance value as constant C_S = 3 pF, measurement system input capacitance C_M = 4 pF and the connecting cable capacitance C_W = 1 pF, the coil resonant frequency by (4.53)

$$f_{res} = \frac{1}{2\pi \cdot \sqrt{22{,}7 \cdot 10^{-6} \cdot 8 \cdot 10^{-12}}} = 11{,}8\ \text{MHz}.$$

As the resonant frequency of such a coil is rather high and refers that the inductance of the coil could be even higher in this application. Knowing the number of turns, the wire resistance, terminating resistance and highest frequency poles can be determined by following same steps as presented in “6.4.2. Coil parameters selection”.

6.6 Discussion

The sensor design methods presented do not present a solution to meet both the sensitivity and bandwidth design requirements. A solution could be use of a wideband amplifier in the output of the sensor, to amplify the output voltage signal. The design procedure could then start also from the definition of amplifier capabilities.

The methods of sensor coil physical design here are presented as an examples of two aspects and it has been presented in a manner to show the different limitations to the capabilities of sensor coils. Taking into account the aspects discussed above, the application specific properties could determine the conditions for the sensor design. For example, for achieving sufficient level of sensitivity, the sensor could be designed with very high sensitivity, but this could be schieved with a penalty in operating bandwidth.

7 Verification of the sensor by laboratory measurements

In the previous chapter, a sensor coil was designed for the measurement of fast transients. In this chapter, similar path is taken to prepare a sensor dedicated for the fast transients' measurement in the high-voltage laboratory. During laboratory tests the sensor's suitability for the on-line monitoring system will be studied.

The sensor coil used for carrying out the verification measurements was especially designed for the measurements and its characteristics were investigated. At the very start of measurements of the actual fast transients phenomena, a calibration of the sensor was carried out, to obtain the correct partial discharge patterns and quantities for evaluation. Only after this the actual high-voltage testing was carried out for the real PD phenomane detection and recording.

7.1 Inductive sensor coil preparation and parameter identification

This chapter focuses on the design and determination of the parameters of the built measurement coils. Most important point of interest is the fact on how well the sensor coil performs in a real transient measurement setup, which is presented in the second part of this chapter.

During preparations for testing in the high-voltage laboratory and sensor calibration, it turned out the one of the sensors weaknesses played a very critical part. Namely, the sensor is quite senitive to noise and electromagnetic fields from the surrounding environment. In this view a sensor was prepared, that would be more sensitive, in exchange for the bandwidth. For verification of the sensor in the real-life measurement scenario and later in presentation of the output signal processing, such sensor would still be reasonable.

7.1.1 Construction of the sensor coil

The sensor coil used for measurement of the partial discharge signals during these tests was built on a porous polystyrene core, which presents electrical characteristics similar to air – it has very high resistance, its dielectric constant is close to 1 and its magnetic permittivity is also 1. This material presents a mechanically relatively strong base to hold the windings, but also provide some ways of fixing the coil to its place. The dimensions of the coil support core were $l_C = 100$ mm; $h_C = 50$ mm. The sensor coil for testing was wound using PVC-insulated winding wire, with total diameter of 0,30 mm, and copper conductor diameter of 0,25 mm (r_w = 0,25 mm). An overwiew of the constructed coil geometry is presented in Figure 7.1.

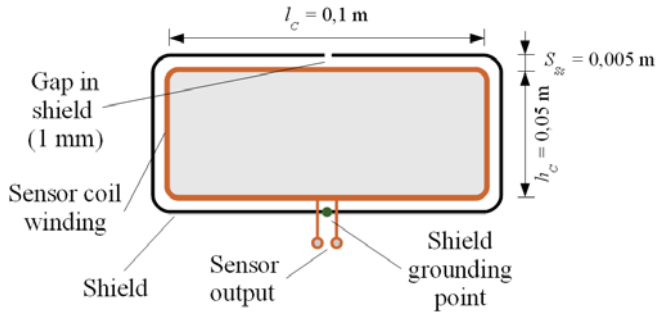

Figure 7.1. Sensor coil geometry (on the left) and the completed sensor coil (on the right).

The coil electrical design was assuming quite high noise level, this limit was also set by the capabilities of the measurement probes. The target sensitivity of the coil was around 0,15 V/A. As this could not have been reached with a coil having small number of turns, the coil had total of 37 turns with the total winding length of 11,1 m. The frequency, which wavelength is equal to the coil's wire length, is 27,0 MHz. This presents the limiting upper operating frequency of the coil used.

Shielding of the sensor coil was made from aluminium foil with thickness of 0,7 mm. Separation between shield and the sensor coil s_{Ss} was 5 mm all over the coil perimeter.

7.1.2 Measurement of inductance, capacitance, wire resistance

A sensor coil parameter that can be measured directly by a measurement device is inductance. The inductance measurement result was 174 μH, which is a supporting parameter for proceeding with the self-capacitance measuements.

Self-capacitance of the investigated sensor coil was measured in resonance tests (see also "4.1.2. Capacitance of the sensors"). The tests confirm that the shielded coil self-capacitance value was at 4,3 pF, while the coil total capacintance including measurement probe was 6,7 pF.

This configuration will provide the self-resonant frequency at

$$f_{res} = \frac{1}{2 \cdot \pi \cdot \sqrt{L_S \cdot C_E}} = 4{,}66 \text{ MHz}. \tag{4.53}$$

However, more interesting for the measurement application are actually the locations of poles of the sensor coil circuit. For this, the wire DC resistance should also be measured, this was done using ohmmeter and the result was 1,0 Ω, very close to the result when calculating using wire length (0,95 Ω).

The limiting electrical operation parameter is the wire length of the coil, which is expected to present a limit at the frequency of 24,5 MHz (this is 27 MHz / 1,1).

This is actually quite suitably located at 0,72 decades away from the sensor coil system self-resonant frequency. The resonant 4,66 MHz is also 0,66 decades away from the lowest operating frequency. As discussed with the sensor coil design (see "6.4.2. Coil parameters selection") the highest pole should reach at least 10 times of higher limiting frequency. Assuming the higest pole to be located at frequency of 245 MHz, the suitable termination resistor value can be calculated observing (4.38) as

$$R_T \approx \frac{L_S}{C_E(2 \cdot \pi \cdot L_S \cdot f_{p2} - R_S)} \tag{7.1}$$

$$R_T \approx \frac{174 \cdot 10^{-6}}{6{,}7 \cdot 10^{-12} \cdot (2 \cdot \pi \cdot 174 \cdot 10^{-6} \cdot 245 \cdot 10^{6} - 1)} = 97{,}0\ \Omega$$

The closest value of resistors available is 100 Ω, which means that there would be a slight correction to the pole frequency as

$$f_{p2} = \frac{1}{2\pi}\left(\frac{L_S + R_S \cdot R_E \cdot C_E}{R_E \cdot C_E \cdot L_S} + \frac{R_S + R_E}{L_S + R_S \cdot R_E \cdot C_E}\right) = 237\ \text{MHz}. \tag{4.37}$$

This is quite close to the target frequency of 245 MHz, so the 100 Ω resistor can be confirmet to be suitable for this application. The lower frequency pole of this sensor coil in present case is

$$f_{p1} = \frac{1}{2\pi} \cdot \frac{R_S + R_E}{L_S + R_S \cdot R_E \cdot C_E} = 92{,}3\ \text{kHz}. \tag{4.34}$$

The operating range for the present sensor coil would start one decade higher than the lowest pole frequency and respectively upper range is one decade less than upper pole frequency. The operating frequency range of such a sensor therefore in this case will be from 1 MHz up to 23,7 MHz. While the penalty on the upper frequency range is quite heavy (design targets have been set at 100 MHz) this sensor configuration will have a very good sensitivity for measurements in a noisier environment.

7.1.3 Transfer plots sensors characteristic verification

The coil transfer plots can be found by mathematical approach when pole frequencies f_{p1} and f_{p2} are known. In present case, the coil transfer plot was also recorded during laboratory testing.

In order to verify the sensor suitability for the measurements, the magnitude and phase transfer plots should be observed. For recoring such transfer plots, there are special measurement devices – network analyzers, capable of direct measurement of the transfer characteristics. In these devices, a sweeping signal generator is providing sinewave output starting from low and ending with high frequency; at the same time a receiver in the input of the analyzer is observing the magnitude and

phase of the input signal. Such network analyzers usually provide capabilities of grounded mode measurements though; in this case however the output of the sensor coil would need to be measured using the differential probe.

As the differential probe available could not be used for connection to the network analyzer, the set-up consisting of generator and oscilloscope was used, presented in Figure 7.2. From the oscilloscope, it is easy to observe the sine wave amplitude to provide the information about the magnitude transfer. For the sinewave signal generator, Tektronix AFG3252 signal generator was used, capable of providing output signals with up to 240 MHz frequency. Current sinewave in the loop was measured using high-frequency current probe.

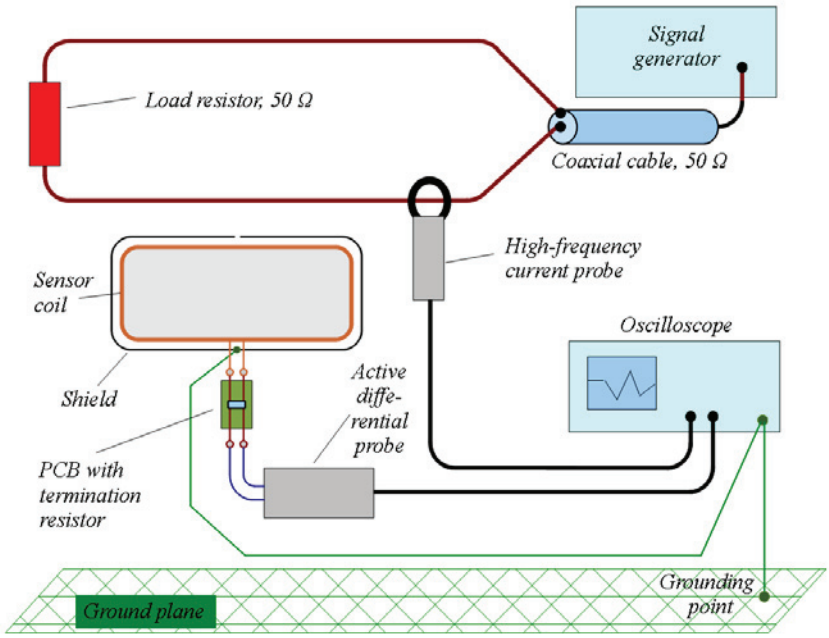

Figure 7.2. Sensor coil transfer characteristics measurement set-up.

Due to difficulties of calibrating the differential probe and current probe delays, the phase transfer function was not captured reliably. The verification will thus rely only on the magnitude transfer comparison. Measurement of the transfer function was carried out starting from frequency 100 kHz up to the limit resonant frequency 27 MHz. Results of the measurement are presented in Figure 7.3.

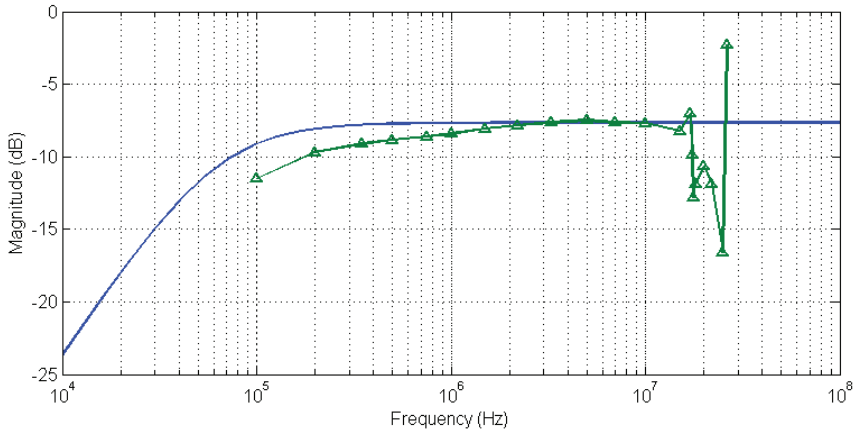

Figure 7.3. Comparison of magnitude transfer functions by using theoretical model and from measurements of a real sensor coil.

The plot in Figure 7.3 presents that there is some differencies when the real sensor coil response and theoretical model response are observed. However, it seems to confirm, that the lower pole is found in the vicinity of frequency 100 kHz, as predicted by calculation. There is one resonance effect seen at 17,6 MHz for which at this time there is no clear explanation available. As there is no phase information available, the effect of this resonance will be studied when observing the real measurement results. In first approach resonance should not harm the outcome as much, as it decreases the output by 5 dB, however there is no phase information available for area around this resonance. The limiting resonance is found at 26,4 MHz, increasing the output suddenly at least by 15 dB; at this limit the signal should be filtered.

7.2 Partial discharge transients measurement

For thesting the sensor capabilities for on-line measurement, partial discharge measurements were carried out in the high-voltage laboratory in Aalto University (HV laboratory in further text).

7.2.1 Measurement set-up

In order to measure the partial discharge transients on the electric power lines, a HV test was carried out. The intention of this test was to create similar PD phenomena as in the real distribution network, and compare measurement results from the capacitive divider as well as the designed fast sensor coil.

The test set-up consisted of a controllable mains frequency HV source, capacitive divider for HV voltage measurements, a section of power line using covered conductor power line wire and a simulation of defect providing the PD occurrence, presented in Figure 7.4. As the laboratory space was limited, the power line was not completely straight, but set-up in a U-shaped form, with rather long straight

sections. The power line wire was relatively evenly set up at height about 1 m from the floor level. The whole floor of the HV laboratory had good conductivity and was grounded. The expected characteristic impedance of the power line was calculated at 330 Ω. One end of the power line wire was unconnected and the other end of the wire was connected to the capacitive coupler. Such line is unterminated and would cause significant reflections, as the high-frequency transient propagate like a travelling wave on the power line. For reducing the effect of reflections from line ends to the meauremet results, the sensor was set up in a location on the half way of the power line (Figure 7.4). In such location, the reflections from the ends of the power line would not have effect at the same time instance as the initial transient is observable to the sensor.

A PD source was set up as a grounded wire, 1 m long, being tied around the power line wire in one end of the line. Insulation on the covered-conductor overhead line was quite thin and had several defects, which caused quite intensive PD occurrence. The intensity of the PD phenomena increased as the supply voltage on the line was raised. The value of the PD intensity was measured by PD monitoring device, using the voltage signal from the capacitive coupler. This provided the peak PD value present on the line, and the peak PD pulses were the ones that were also captured from the power line.

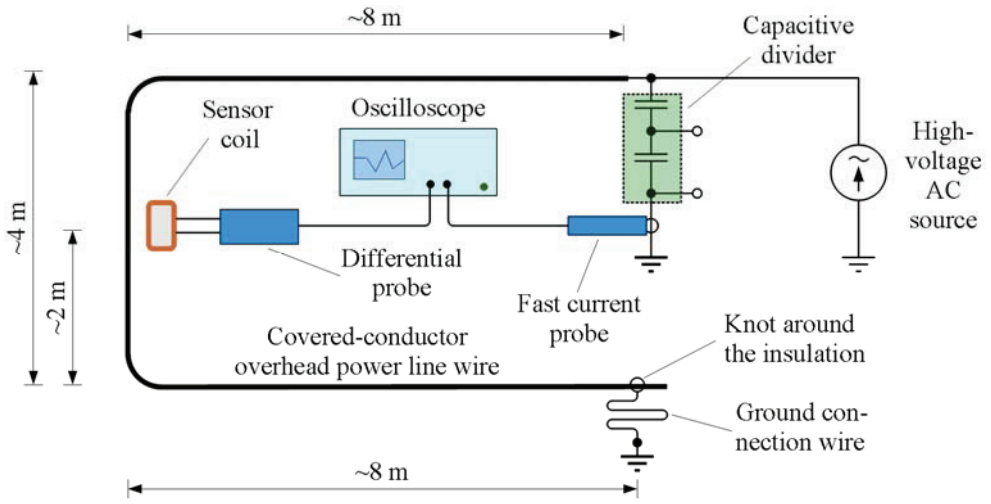

Figure 7.4. Partial discharge measurement HV test set-up overview.

Measurement of the actual waveform on the line was performed, using fast current probe Tektronix TCP0030 with 120 MHz bandwidth to measure the current passing through the capacitive coupler. It can be argued that the current of the capacitive coupler differs from the current measured by the sensor significantly, as

1) current in the capacitive coupler is caused by voltage on the line, not current itself;

2) capacitive coupler is further away from the sensor's location, therefore the signals could be damped during the propagation;

3) capacitive coupler presents an impedance change to the transmission line and it can cause reflections; this means that the current in capacitive coupler could differ from the actual travelling wave on the power line wire.

Still, the power line wire represents a long transmission line for the transients, the current and voltage should be in relation defined by line impedance (2.11)

$$\frac{u(x)}{i(x)} = Z_{line} \cdot$$

This was the closest option in this test to obtain the waveform of the actual phenomena, and current reading from the capacitive coupler would provide an overview of the nature of the phenomena present on the power line.

The sensor itself was loaded with 100 Ω low-inductance resistor and connected to differential probe HAMEG HM009. This probe provides measurement bandwidth up to 40 MHz (–3 dB level), which is suitable for carrying out the measurements with the sensor designed.

During the test, actually 2 oscilloscopes were used and their triggers synchronized. The reason for this was the great distance between the sensor and the current probe. First oscilloscope was LeCroy WaveRunner 6 Zi, which was used for capturing the inductive current sensor output. This oscilloscope was set up with measurement triggering to the sensor output signal and had the capability of outputting trigger signal to external measurement devices. Second oscilloscope type Tektronix MSO2024 was connected to current probe and triggered the measurement on the external signal. This way it was assured, that the same PD waveform was captured by both devices.

Grounding of the sensor was done using a low-inductance copper foil connection. The conductor was first connected between the oscilloscope and ground and from the oscilloscope grounding terminal, the grounding connection was provided to the sensor coil shield. This way, the sensor coil had potential closest to the oscilloscope and stray currents due to different capacitances were at minimum.

The sensor was set up at the distance of 115 mm from the perimeter of the power line wire to the shield of the sensor (Figure 7.5). As the separation between shield and sensor was 5 mm, the sensor coil winding was set at distance $h_{C,line}$ of 120 mm from the conductor. With this data, the mutual inductance between the sensor coil and the power line wire can be determined. The calculated value of mutual inductance in this configuration was (4.13)

$$M_S = \frac{\mu_0 \cdot w_S \cdot l_C}{2\pi} \ln \frac{h_{C,line} + h_C}{h_{C,line}} = \frac{\mu_0 \cdot 37 \cdot 0{,}1}{2\pi} \ln \frac{0{,}17}{0{,}12} = 258 \cdot 10^{-9}\,\text{H} = 258\ \text{nH} \cdot$$

Using the previously calculated lower pole frequency f_{p1} = 92,3 kHz, total sensitivity of the sensor coil in the operating frequency range was (6.9)

$$K_S = \frac{u_{out}}{i_{line}} = f_{p1} \cdot 2\pi \cdot M_S = 0{,}15 \text{ V/A}.$$

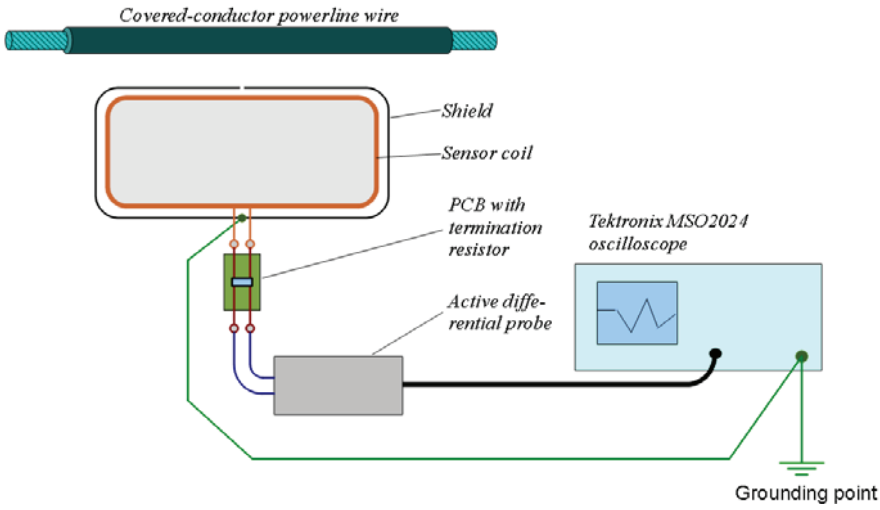

Figure 7.5. Detailed sensor set-up for the PD measurement.

Before carrying out measurements of the actual HV PD phenomena, the sensor would have to be calibrated first, to verify the sensors capabilities and the actual sensitivity value.

7.2.2 Calibration of the sensor

For calibration of the inductive sensor, a test setup was prepared with similar configuration as the final test. The sensor was set up at the same location from a wire as it was during the HV test, and the sensor output was observed in a more noise free configuration.

The calibration test set-up is presented in Figure 7.6. As a transient source, a partial discharge calibrator was used, providing PD pulses equivalent to particular PD intensity value. The PD calibrator CAL1E from Power Diagnostix was used, with the charge setting at 10 nC. The PD calibrator was connected to the power line wire and this presented it a matched load. Actual current pulse present in the wire was measured using Tektronix TCP0030 fast current probe. The sensor coil was connected to terminating resistor with 100 Ω resistance, and Hameg HM009 differential probe was used for the sensor output signal measurement.

The waveforms obtained during the measurement are presented in Figure 7.7. The waveform of the actual current on the power line, measured with fast current probe and the sensor output show a very good match. This is the most direct example of the capabilities of the sensor, as the waveform of current on the wire and sensor

output in this case are measured at the same location. The sensor output presented here is not filtered, but nevertheless does not show any significant oscillations or high noise levels. The waveform captured by the inductive sensor presents transient's edge timing and slope exactly the same as the current probe output. From these results it can be concluded that the sensor designed is suitable for the measurements of fast transients and it is also fast enough to capture the PD calibrator output accurately.

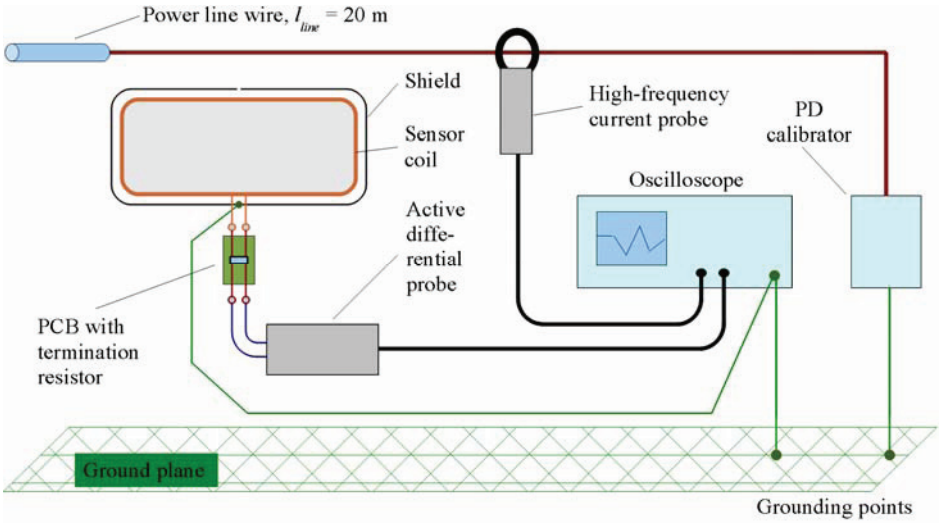

Figure 7.6. Testing set-up for the calibration of the inductive sensor.

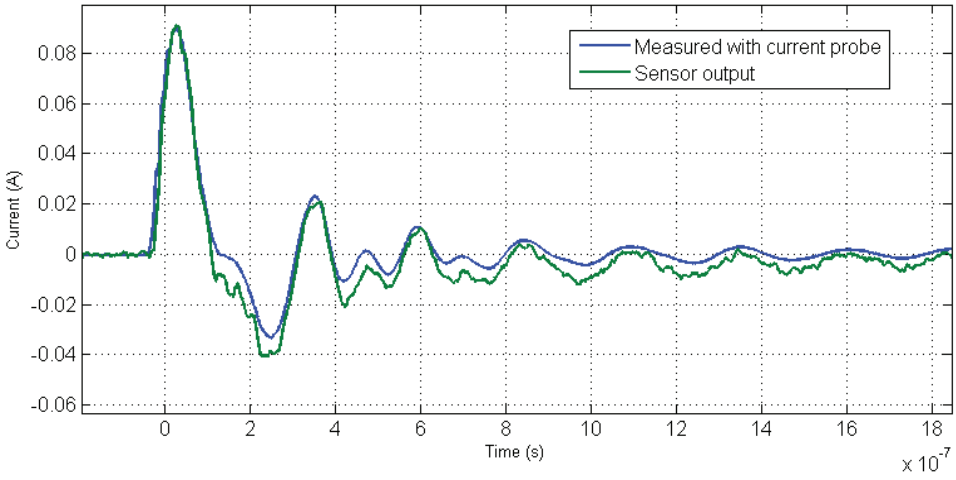

Figure 7.7. Waveforms obtained during sensor calibration.

From the measured waveforms the sensor sensitivity value can be found. In this case the sensor sensitivity was 0,435 V/A. This is actually 3 times higher than the value of the calculated sensitivity, a positive effect. This actually presents a good

overview about the magnitude of the current present in the tested line, the pulse peak values should remain under 100 mA. Considering the sensitivity of the sensor the output voltage observed should remain below 50 mV.

Knowing the value of current, a value of charge passing through a wire can be calculated by integrating current measured over a defined time period

$$q = \int_{t0}^{t1} idt \tag{7.1}$$

The usual practice for the PD charge measurement is through the capacitive couplers and by observing the voltage variation on the coupler output. However, as there is direct current information available at this time, the charge van be calculated directly. Observing the waveform, it can be noted that most of the current has passed the sensor and the probe by the time of 500 ns. After this, there is some more current present on the wire, although this has oscillatory nature and is most likely present due to oscillations on the power line wire. The charge passing through the measured wire during first 500 ns of the transient are presented in Table 7.1. Results could be used for further calibration of the designed inductive sensor designed, in order that both measurement sensors would provide exactly the same output.

Results in Table 7.1 present some further questions, as the PD calibrator, used during the test was set to 10 nC output and also calibrated before the test.

Table 7.1. Recorded charge during the sensor calibration measurement

Measurement device	Recorded charge (nC)
Inductive sensor	5,97
Fast current probe	5,43

7.2.3 Calibration of the high-voltage line measurements

As a start of the measurements, the line was set up and tested without switching on the HV source. The power line, the inductive sensor, capacitive coupler etc. were set up the same way as for the final test with HV. In the initial calibration, the PD calibrator was used as a transient source and it was connected to the open end of the power line wire. The other end of the power line wire was connected to capacitive coupler as presented in Figure 7.4.

The PD calibrator was set to output pulses equivalent to 20 nC partial discharges. Measurement results were observed synchronously from both the capacitive coupler and the sensor coil. It was mechanically impossible to attach the fast current probe to the power line wire, which in this test presents a question on comparing the actual results. Namely, there would be reflections of the current from the unterminated line ends included, making the measurement at the location

of the inductive sensor more complicated – the sensor would be subjected to more reflections than the measurement coupler in the end of the line.

A diagram for estimating the reflections from the line end is shown in Figure 7.8, with one scenario of the pulsed signal propagation. This Lattice diagram presents the time-location relation of the travelling wave edges. In the current set-up, there are two main points that introduce reflections; these are the open line end and the line end connected to the capacitive coupler. It is expected that the capacitive coupler has the same influence to the travelling waves as the shorted line end. The shorted line end reflects the current wave back with the same sign, and the open end of the line provides current reflection with opposite sign. It should be noted however, that in the shorted end, the current value is twice the size. The oscillation from reflection (or in other words the current waves having different sign), arrive to the sensor with period of

$$T = \frac{2 \cdot l_{line}}{\upsilon}, \tag{7.2}$$

where l_{line} is the line length and υ is the electromagnetic wave propagation velocity.

In the case of present set-up with power line wire length l_{line} = 20 m and assuming the current wave is propagating with velocity of $\upsilon = 2{,}99 \cdot 10^8$ m/s, the reflection period is expected to be around 133 ns. This value should be kept in mind when observing the results of the measurements on the HV power line.

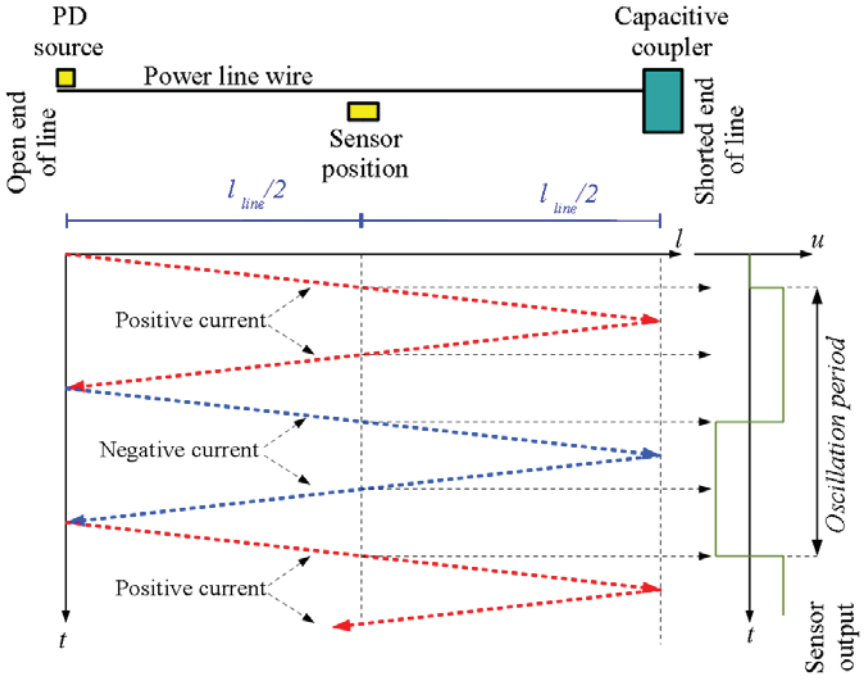

Figure 7.8. Diagram for estimation of effects of current reflections.

These measurements would be the first ones indicating the waveforms of the partial discharges occurring on the line during the HV tests. Measurement results with 20 nC test charge are presented in Figure 7.9, while in this graph, the sensor output voltage has been presented rather than current value.

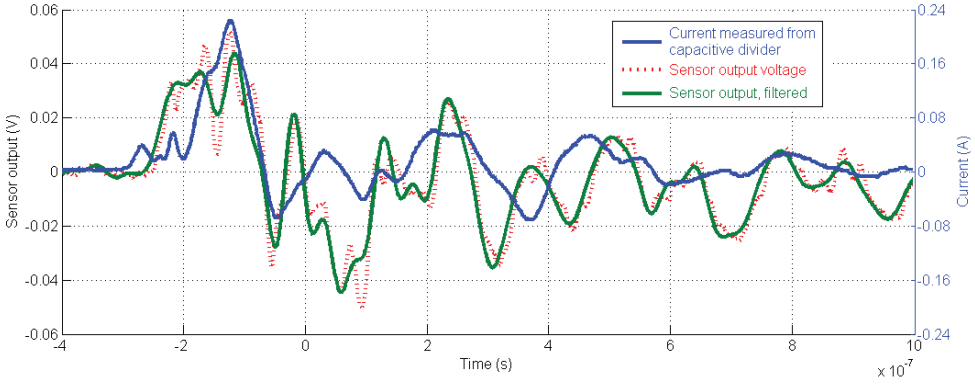

Figure 7.9. Results of the calibration measurements from the capacitive coupler and from the inductive sensor, using 20 pC test charge.

The sensor output to the calibration signals presents heavy oscillations, which can be observed as a sign of the reflections from both ends of the line. The inductive sensor output signal was filtered to eliminate the high-frequency noise caused by resonance of the sensor – the non-filtered sensor waveform in Figure 7.9 the 26 MHz sensor presents some self-resonant oscillations. However, the period of the more significant oscillations visible also in the filtered signal have period of 136 ns, which is basically exatly the same as observed by (7.2). Such oscillations present so much role that the result of the sensor actually cannot be verified. It has to be pointed out, that the current waveform for the comparison is obtained from the capacitive coupler, in remote location from the sensor and that the current of the capacitive coupler is dependent on the voltage on the line rather than the actual current. As a result, there is not much correlation between the actual current and the sensor output.

For evaluation of the PD charge would use the same time-frame as presented above for the sensor calibration measurements (see “7.2.2. Calibration of the sensor”), i.e. 500 ns from the start of the transient. The charge, that has passed the line during the test, has been calculated by (7.1) and the results of the charge evaluation are presented in Table 7.2.

Table 7.2. Recorded charge during the sensor calibration measurement

Measurement device	Recorded charge (nC)
Inductive sensor	2,86
Fast current probe	19,2

It is curious, that in case the charge calculated by the current probe in the capacitive coupler output, the captured charge value is very close to the PD calibrator setting value. The inductive sensor in this case is not able to provide the correct result. Here an improvement to the test can be presented – for comparison; another inductive sensor should be connected to the capacitive coupler, to compare the current waveform sen by the current probe.

There is also an interesting effect to point out in the very start of the transient. Namely, the high peak occurs at the capacitive coupler, but this is not visible in the sensor output. This can also be seen from a calibration test result, which used smaller PD test charge (Figure 7.10).

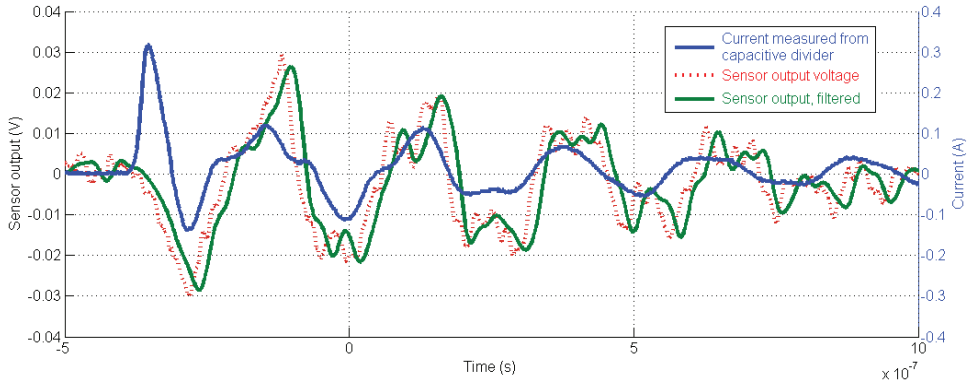

Figure 7.10. Results of the calibration measurements from the capacitive coupler and from the inductive sensor, using 10 nC test charge.

Another calibration scenario was used the same set-up, but different output charge setting of the PD calibrator, 10 nC. The waveform observed during the calibration measurements is presented in Figure 7.10, with a comparison of the sensor output waveform and the waveform seen on the capacitive coupler. The waveform shows clear oscillations due to reflections and the sensor output is presenting more reflections than the current probe measurement on the capacitive coupler as the filtered sensor output signal still seems to have higher frequencies included than the current measured at the capacitive voltage divider.

The sensor output waveform in Figure 7.10 is much more similar to the measured current at capacitive coupler than in results in Figure 7.9. Yet here also, the initial peak in the PD transient is completely missing in the sensor output.

During the calibration it has become clear that the sensor output waveforms and the capacitive coupler outputs differ from each other quite significantly, as for first, they are in physically different locations of the model power line. There are many reflections on the line that the inductive sensor observes and capacitive coupler does not observe. Therefore, in the following presentations of the HV PD measurements, the current signal from the coupler should be seen as indication of reference to the nature of the PD event, not the actual current waveform.

7.2.4 Measurement of high-voltage partial discharges

For the HV partial discharge phenomena measurement, the testing set-up was energized and set up to 6 kV. For producing the PD, a wire connected to ground was used, which was tightly attached to the power line wire, in particular around the power line wire insulation (the wire used during the test was a covered-conductor wire). The power line wire insulation had defects at the same location, therefore adding a grounded wire caused significant dielectric stress and the PD transients were clearly visible.

All measurements done were recorded synchronously, i.e. the output of the sensor and the current from the capacitive coupler were sampled for the same event. However, as the capacitive coupler does not present the actual current of the power line wire, the current signal from the coupler should be seen as indication of reference to the nature of the PD event, not the actual current waveform.

Measurement results in Figure 7.11 and in Figure 7.12 present also oscillations due to reflections present on the line. Here also it has to be stated that the line for the measurement is not long enough to keep the reflections from affecting the sensor measurement result. However, a PD waveform observed at the location of the capacitive coupler presents waveform similar to the PD calibrator output signal.

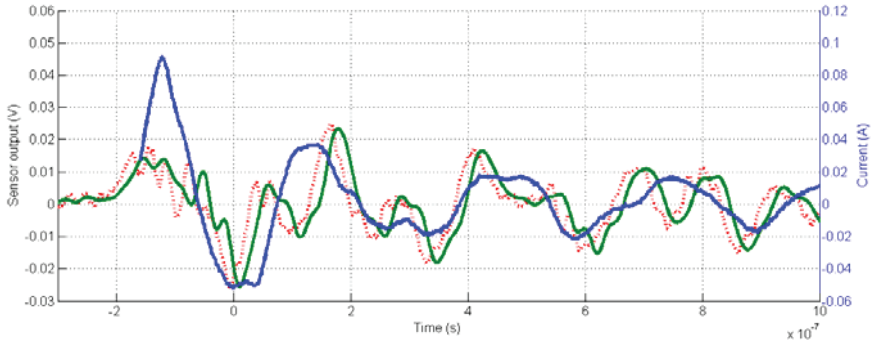

Figure 7.11. PD waveform measured from HV tests, 30 nC.

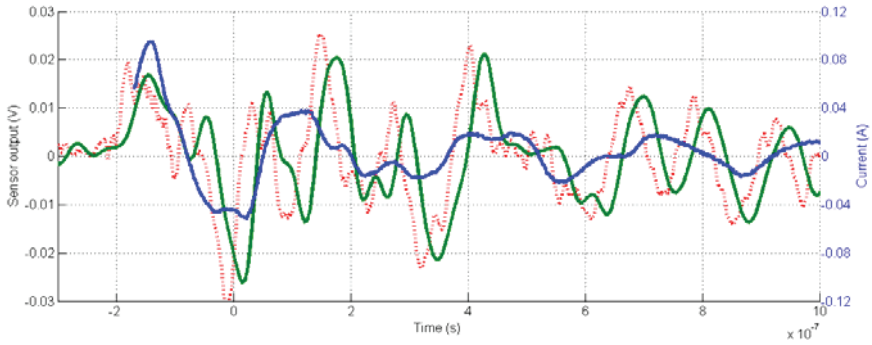

Figure 7.12. PD waveform measured from HV tests, 20 nC.

7.3 Conclusions

The inductive sensor verification testing was carried out with a HV set-up in order to verify the suitability of the sensor for measurements on a real power line. During the tests, it became obvious that the HV set-up did not provide the perquisites for carrying out the accurate fast transients measurements.

The calibration of the actual inductive sensor provided very good result, indicating that the senor would be indeed capable and suitable for capturing the real partial discharge (PD) transients on the power lines. It was verified that the inductive sensor output waveform slope and timing were exactly the same as seen in the results of the measurements with fast current probe. The calibration results were however obtained with PD calibrator device in a noise and reflection free set-up.

The measurements carried out using a model power line presented challenges as reflections from of the transient from the ends of the power line model presented some significant noise for the sensor. It has to be concluded that the test set-up for carrying out similar test scenarios would need to use a longer power line model. Namely, the PD phenomena observed in the tests produced transients that had significantly longer duration than was the time for the transient to reflect from the line ends. The power line wire length, set up for the sensor verification test, should not provide reflections for the duration of 500 ns ($\approx$ 80 meters line) at the sensor location.

8 Conclusions and discussion

8.1 Key results of the work

In this thesis several considerations and solutions were presented for the design of an inductive current sensor for the fast transients' measurements on electrical distribution network. The phenomena targeted with such measurements are the partial discharge and also fault-originated transients. If a power line on-line measurement system was built, that could capture such transients accurately, the power line condition monitoring and fault locating would be much more accurate. For most effective distribution network power line diagnostics, there should be a high number of on-line monitoring units present on the power line, which present a need for a cheap, reliable and robust sensor. Such sensor can be, for example, inductive air-core current sensor.

The investigation started with determining the requirements for the sensor. The bandwidth necessary for the sensor was studied and **it is presented that operating frequency of the sensor should range from 1 up to 100 MHz** (the lower bandwidth is a matter of dispute though). The sensor operating bandwidth stated would be sufficient for carrying out the measurements of both partial discharge transients and fault-initiated transients. Having a sensor with such bandwidth would be sufficient for capturing the waveform of the mentioned transients with high accuracy.

As 100 MHz is quite high frequency for an electice circuit, **the sensor electric operation is presented three-level model**. The low frequency model is valid until some tens of kHz range, and it presents the essential magnetic effect of the sensor. From the low-level model, the sensor magnetic coupling, or mutual inductance, can be determined, which is also one of the factors determining the sensitivity of the sensor.

The **medium-frequency model** is used to present the sensor operation in the range from 50 kHz up to 10 MHz. This model can be used for the design of the sensor operating bandwidth, and includes discussion about the influence of self-inductance and self-capacitance of the sensor coil, and external components like termination resistor, measurement system and the measurement amplifier input.

The **high-frequency model** has been presented for describing the operation of the sensor for the ranges **from 10 MHz up to 100 MHz**. The inductive sensor high-frequency model with lumped components can be used to determine the effects of the external components, connected to the sensor coil output. The analyzed external stray components include the effect of termination resistor stray inductance, effect on measurement system connection wires; also capacitive coupling of the sensor is presented and aspects of shielding of the sensor are presented. For describing the sensor coil operaton at high frequency, one has to take into account the physical dimensions of the sensor coil and this is presented by using a distributed component model of the sensor coil. Such model presents that the

length of the wire used for the sensor coil will be also presenting some bandwidth limitations due to resonances.

Using the results of the three-level sensor and measurement system modelling, **design methodology of the sensor** is proposed. Some further requirements are presented, related to the real-world application of the inductive sensors, such as mechanical constraints of the application. Aspects of coil shape design, self-inductance and self-capacitance are discussed. A design procedure of the inductive current sensor is proposed and a sample sensor coil design presented.

The **operation of the inductive sensor is verified** by testing of the partial discharge phenomena in a HV laboratory. The calibration tests of a constructed inductive sensor are carried out and the initial tests present quite accurate match between the inductive sensor output and the actual waveform present on the line measured. However the testing set-up does not make use of a long enough power line section to remove influences of reflections from the results. It is therefore very difficult to determine the sensor operation during the HV testing. Nevertheless, the objective of this thesis can be considered fulfilled, as the sensor verification in a reflection-free set-up proved that the sensor is accurately able to capture the transient current waveform on the line.

8.2 Future research and development

During the thesis, many different aspects were gone through, that actually did not receive a scientific answer. These will be the aspects for the future work and sensor development.

1. **Sensor coil parameters more accurate determination.** Such issues may seem trivial at first sight, but actually there is only very little usable information about the matters like solenoid self-capacitance, influence of electric shielding to solenoid self-capacitance, effect of adding a shield with a gap on inductance and many more. Some scientists have indeed proposed solutions to these problems, but reliability of their results is very low. Right now it is stated in this thesis that the measured or empirical results are much more accurate than any of the proposed formulas. During more comprehensive research it would be beneficial to clarify these matters in scientific sense and work out calculations of the parameters with theoretical calculations.
2. **Testing of the sensor with improved test set-up.** Performance tests with the sensor and the real HV PD measurement will continue. Results of the calibration tests of the sensor present very good results, therefore it its performance should be tested and verified using different other test scenarios. Goal of the laboratory testing would be determining the exact conditions of measurements, but also developing signal processing algorithms for noise filtering.

3. **Development of the measurement amplifier circuitry**. The sensor presented was built keeping in mind higher sensitivity but it results in the limiting resonant frequency being rather low, 23 MHz instead of the limit (100 MHz) specified as the requirement for the sensor design. The main reason for this was the voltage measurement probes connected to the sensor output provide only 1:1 transfer from the coil output. In order to achieve this, the sensor should be equipped with a wideband low-noise signal amplifier. This way the inductive sensor coil could reach higher sensitivity with less turns of the coil. As the coil wire length would be shorter, the limiting bandwidth could be higher. In addition, tests with coils having wider bandwidth can provide some more data for the scientific research of the PD phenomena.
4. **Power line on-line condition monitoring tests**. Target application of the sensor is medium voltage power lines' on-line condition monitoring and fault locating. Tests on real power lines would follow immediately after the laboratory tests have been done. Testing in the real power network would be much more difficult and significantly higher noise would be present in the environment, therefore the laboratory tests should be carried out in advance to clarify all operating conditions and set-up details for accurate measurements.
5. **Power line fault locating tests.** Besides the PD activity monitoring, another application for fast transients is the fault initiated transients measurements. Accurate measurement of the time of arrival will provide most valuable information for the fault locating. The fault transients provide greater current in travelling wave, therefore these are easier to detect and distinguish from noise.

The listed tasks would be the examples on proceeding with the future work, but these tasks present the significant perspective of the topic. This is also important for perspective industrial applications, for example after finishing the tests on real power lines some practical equipment for the power line on-line monitoring can be developed using the sensor.

9 Abstract

With the requirements to power distribution networks' supply reliability becoming more strict, the conventional relay protection methods alone are not sufficient to guarantee the continuous supply of high level. For achieving more reliable power supply and smallest interruption duration new equipment and power line diagnostics methods are required.

For the previous period, power line diagnostics for detecting problems of line condition or fault location has relied on mains frequency (50 / 60 Hz) measurements. Highest frequencies measured are usually up to few kHz, with exceptional devices reaching up to few tens kHz. This limits the ability of the automation devices to detect and correctly analyze short-duration events, which actually present very valuable information on both the power line condition and/or diagnostics upon power line faults.

On-line powerline condition monitoring is presently being discussed more actively, as it often relies on high-speed transient phenomena and high-speed signal processing devices are becoming more and more economically feasible. Today there seem to be no problems related to signal processing capabilities of the electronic systems, however there does not seem to be a good and cheap sensor available to carry out the high-speed measurements. The sensors available are expensive and often also not suitable for outdoor harsh condition operation.

This thesis presents a detailed analysis for building an air-cored inductive sensor suitable for use for powerline high-frequency measurements. The inductive sensor proposed is intended to be as cheap as possible, also robust as possible to guarantee reliability of operation. Simple sensor still presents quite many challenges to overcome, its operating model at high-frequency is still rather complex.

Chapter 2 focuses on the requirements for accurate measurements of high-frequency signals present on power lines. A non-classical approach to determine the necessary sensor bandwidth is presented, as the pulsed transient signal bandwidth obtained by Fourier transform alone can not present a clear overview of the required measurement parameters. It is presented that sensor and signal processing system bandwidth of 100 MHz can be considered sufficient. In addition, some powerline effects are discussed for explaining the propagation of high-frequency transients on the transmission lines.

Chapter 3 presents the inductive sensor low-frequency model overview. The low-frequency model presents the magnetic effect analysis of the sensor, which presents essential component – mutual inductance – for the calculations of the sensor sensitivity. Regardless of the medium- and high-frequency model of the sensor, the sensitivity is determined by this magnetic effect.

Chapter 4 presents medium-frequency model for the sensor, usable from some tens kHz up to few MHz range of sensor operation. This kind of model is widely

discussed in literature and in scientific works as true high-speed model, but it can be proved that it is not sufficient for truly describing the high-frequency operation. As this kind of model presents some of the most important aspects for the sensor modelling and design, it is analyzed deeply. While this chapter mostly is dealing with classical overview of operation of such circuit, it is presented in detailed manner for terms of discussion for high-frequency model in Chapter 5 and for the sensor design, described in Chapter 6. Regardless of the medium-frequency model bandwidth limits, this model presents the operating bandwidth and sensor response shaping principles.

Chapter 5 presents a novel more detailed high-frequency model of the sensor; it is targeted to operate at frequencies up to 100 MHz. The high-frequency model includes some of the more invisible stray effects of external components of the inductive sensor measurement system, that present effects only above some MHz. Skin effect of the winding wire is analyzed deeply, though it is thereby proved that it has only minor effect to the operation; it is very small compared to reactance of the sensors coil. Termination resistor and connecting wires effects are observed and some compensation circuits are proposed. Analysis focuses also on the capacitive coupling effects of the sensor to the power line, shielding and overall capacitive balancing of the sensor are discussed. The high-frequency model presents essentially stray components of the sensor system, that likely can not be completely eliminated by design, but rather have to be taken into account and to find some means to compensate for the effects to achieve accuracy of pulsed measurements.

Chapter 6 is dedicated for design of the inductive sensor, taking into account the low-, medium- and high-speed sensor models. Design requirements are presented for geometrical design, electrical basic design and electrical external design. Further discussion presents the inductance and sensitivity design of the sensor, with practical examples of the sensor. It is presented, that there should be some compromise between the sensitivity and bandwidth. A sensor coil with wide operating bandwidth would not have high sensitivity and vice versa.

Chapter 7 is more practical and presents measurement and validation results of the sensor built based on design from previous chapter. Testing set-up is discussed and testing scenarios presented. Practical measurements of the power line transients, obtained with this type of sensor have been presented.

Most valuable research outcome and main conclusions of this research can be summarized as follows:

- Bandwidth analysis of the high-speed transients is presented, giving ground to requirements for sensor design.
- High-speed model of the inductive sensor is presented, allowing accurate modelling of sensor above 30 MHz range.
- Detailed skin effect analysis of the inductive sensor is presented.

- Detailed stray effects analysis of the external components is presented.
- Capacitive coupling and shielding of the sensor are presented; importance of capacitive balancing is presented.
- Sensor design criterion including sensor coil inductance and sensitivity design are presented.
- Sensor design is validated using practical measurements and signal processing of the sensor output is discussed.

References

[1] 1130A 1.5 GHz InfiniiMax Differential and Single-ended Probes, User Guide; Agilent Technologies Inc. Publication Number 01130-97003, May 2009; available from http://cp.literature.agilent.com/litweb/pdf/01130-97003.pdf (checked May 10th, 2012)

[2] ADS4126, ADS4129, ADS4146, ADS4149 – 12-/14-Bit, 160/250MSPS, Ultralow-Power ADC; Product Datasheet SBAS483G, NOVEMBER 2009, REVISED JANUARY 2011; Texas Instruments Inc.; available from http://www.ti.com/lit/ds/symlink/ads4149.pdf (checked May 10th, 2012).

[3] Ametani, A.; Ono, T.; Honaga, Y.; Ouchi, Y.; Surge propagation on Japanese 500 kV untransposed transmission line; Proceedings of the Institution of Electrical Engineers, Feb 1974, Vol. 121, Iss. 2; ISSN 0020-3270; pp: 136 – 138.

[4] Ametani, A.; Stratified Earth Effects on Wave Propagation - Frequency-Dependent Parameters; IEEE Transactions on Power Apparatus and Systems, Sept 1974, Vol. PAS-93, Iss. 5; ISSN 0018-9510; pp. 1233 – 1239.

[5] Andersson, A.; Destefan, D.; Ramboz, J.D.; Weiss, S.; DeHaan, J.M.; Unique EHV current probe for calibration and monitoring; Transmission and Distribution Conference and Exposition, 2001 IEEE/PES; Vol. 1; ISBN 0-7803-7285-9; pp. 379 – 384.

[6] Argüeso, M.; Robles, G.; Sanz, J.; Implementation of a Rogowski coil for the measurement of partial discharges; Review of Scientific Instruments, 2005, Vol. 76, Iss. 6; http://dx.doi.org/10.1063/1.1921427.

[7] Ariastina, W.G.; Blackburn, T.R.; Frequency Characteristics Of Partial Discharges In Aged Insulation Systems; Australasian Universities Power Engineering Conference (AUPEC-2001); available from http://itee.uq.edu.au/~aupec/aupec01/128_ARIASTINA_AUPEC01paper_revised.pdf (checked May 10th, 2012).

[8] Baker, P.C.; McArthur, S.D.J.; Judd, M.D.; A frequency-based RF partial discharge detector for low-power wireless sensing; IEEE Transactions on Dielectrics and Electrical Insulation, Feb 2010, Vol. 17, No. 1; ISSN 1070-9878; pp. 133 – 140.

[9] Bao Hai; Xu Weihua; Yang Yihan; A research about a new Rogowski coil model based on the control principle; International Conference on Sustainable Power Generation and Supply, 2009 (SUPERGEN'09); ISBN 978-1-4244-4934-7; pp. 1 – 6.

[10] Baocheng Wang; Deyu Wang; Weiyang Wu; A Rogowski coil current transducer designed for wide bandwidth current pulse measurement; IEEE 6th International Power Electronics and Motion Control Conference, 2009 (IPEMC '09); ISBN 978-1-4244-3556-2; pp. 1246 – 1249.

[11] Bin Wei; Chengrong Li; Lijian Ding ; Changyu Li; Dong Liu; VHF PD detection of 110 kV XLPE cable accessories; Conference Record of the 2004 IEEE International Symposium on Electrical Insulation; ISBN 0-7803-8447-4/04; pp. 366 – 371.

[12] Bo, Z.Q.; Weller, G.; Jiang, F.; Yang, Q.X.; Application of GPS based fault location scheme for distribution system; 1998 International Conference on Power System Technology (POWERCON '98); Vol. 1; ISBN 0-7803-4754-4; pp. 53 – 57.

[13] Boggs, S.A.; Stone, G.C.; Fundamental Limitations in the Measurement of Corona and Partial Discharge; IEEE Transactions on Electrical Insulation, Apr 1982, Vol. EI-17, Iss. 2; ISSN 0018-9367; pp. 143 – 150.

[14] Marungsri, B., Boonpoke, S.; Applications of Simplified Fuzzy ARTMAP to Partial Discharge Classification and Pattern Recognition; WSEAS Transactions on Systems, Mar 2011, Iss. 3, Vol. 10; ISSN 1109-2777; pp. 69 – 80.

[15] Budak, A.; Passive and Active Network Analysis and Synthesis; Houghton Mifflin, 1974; ISBN 0-395-17203-9.

[16] C37.114-2004 – IEEE Guide for Determining Fault Location on AC Transmission and Distribution Lines; Current Version: 20 June 2005; ISBN: 0-7381-4653-6.

[17] C37.235-2007 – IEEE Guide for the Application of Rogowski Coils Used for Protective Relaying Purposes; IEEE Standard, issue date Feb 22, 2008; ISBN 978-0-7381-5714-6.

[18] Chen Qing; Li Hong-bin; Chen Xiao; Deng Yin; Liu Yan-bin; PCB Rogowski Sensor Designs for Plasma Current Measurement; IEEE 22nd Symposium on Fusion Engineering, 2007 (SOFE 2007); ISBN 1-4244-1194-7/07; pp. 1 – 4.

[19] Chen Xiaolin; Cheng Yonghong; Rong Mingzhe; Zhang Shaofeng; Xie Hengkun; Study on Wideband Sensor of Partial Discharge for XLPE Power Cable; Proceedings of the 7th International Conference on Properties and Applications of Dielectric Materials, 2003; Vol. 1; ISBN 0-7803-7725-7; pp. 203 – 206.

[20] Chenguo Yao, Qianbo Xiao, Yan Mi, Tao Yuan, Chengxiang Li and Wenxia Sima; Contactless measurement of lightning current using self-integrating B-dot probe; IEEE Transactions on Dielectrics and Electrical Insulation, Aug 2011, Vol. 18, No. 4; ISSN 1070-9878; pp. 1323 – 1327.

[21] Chu Xianghu; Zeng Xiangjun; Deng Feng; Li Ling; Novel PCB sensor based on Rogowski coil for transmission lines fault detection; IEEE Power & Energy Society General Meeting, 2009 (PES '09); ISBN: 978-1-4244-4241-6; pp. 1 – 4.

[22] Chu Xianghui; Zeng Xiangjun; Ma Hongjiang; Li Zewen; Li Ling; Deng Feng; Rogowski sensor for power grid traveling wave based fault location; IET 9th International Conference on Developments in Power Systems Protection (DPSP 2008); ISBN 978-0-86341-902-7; pp. 438 – 443.

[23] Chu-Sun Yen; Fazarinc, Z.; Wheeler, R.L.; Time-domain skin-effect model for transient analysis of lossy transmission lines; Proceedings of the IEEE, Jul 1982, Vol. 70, Iss. 7; ISSN 0018-9219; pp. 750 – 757.

[24] Coggins, D.; Thomas, D.; Hayes-Gill, B.; Yiqun Zhu; Pereira, E.T.; Cabral, S.; Initial Experiences with a New FPGA Based Traveling Wave Fault Recorder Installed on a MV Distribution Network; Joint International Conference on Power System Technology and IEEE Power India Conference, 2008 (POWERCON 2008); ISBN 978-1-4244-1763-6; pp. 1 – 6.

[25] Coggins, D.P.; Thomas, D.W.P.; Hayes-Gill, B.R.; Zhu, Y.; Pereira, E.T.; Cabral, S.H.L.; A New High Speed FPGA based Travelling Wave Fault Recorder for MV Distribution Systems; IET 9th International Conference on Developments in Power System Protection, 2008 (DPSP 2008); ISBN 978-0-86341-902-7; pp. 579 – 583.

[26] Cooper, J.; On the high-frequency response of a Rogowski coil; Journal of Nuclear Energy. Part C, Plasma Physics, Accelerators, Thermonuclear Research, 1963, Vol. 5, No. 5; doi:10.1088/0368-3281/5/5/302; pp. 285 – 289.

[27] de B Santos, E.A.; de Oliveira, A.J.B.; de Melo, M.T.; e Silva, J.C.C.; Wavrik, J.F.A.G.; Design and construction of a system for detection of lightning discharges on power transmission lines; International Symposium on Lightning Protection (XI SIPDA), 2011; ISBN 978-1-4577-1898-4; pp. 278 – 283.

[28] Deng, Xiangyang; Li, Zeren; Peng, Qixian; Liu, Jun; Tian, Jianhua; Research on the magneto-optic current sensor for high-current pulses; Review of Scientific Instruments, Aug 2008, Vol. 79, no. 8; ISSN 0034-6748.

[29] Doig, P.; Gunn, C.; Durante, L.; Burns, C.; Cochrane, M.; Reclassification of Relay-Class Current Transformers for Revenue Metering Applications; 2005/2006 IEEE PES Transmission and Distribution Conference and Exhibition; ISBN 0-7803-9194-2; pp. 1244 – 1251.

[30] Draxler, K.; Styblikova, R.; Hlavacek, J.; Prochazka, R.; Calibration of Rogowski Coils With an Integrator at High Currents; IEEE Transactions on Instrumentation and Measurement, Jul 2011, Vol. 60, Iss. 7; ISSN 0018-9456; pp. 2434 – 2438;

[31] Dubickas, V.; Edin, H.; High-Frequency Model of the Rogowski Coil with a Small Number of Turns; IEEE Transactions on Instrumentation and Measurement; Dec 2007, Vol. 56, Iss. 6; ISSN 0018-9456; pp. 2284 – 2288.

[32] Dubickas, V.; On-line time domain reflectometry diagnostics of medium voltage XLPE power cables, Licentiate Thesis; KTH Royal Institute of Technology, 2006; ISBN 91-7178-327-X.

[33] Electrical Engineering Handbook; Siemens AG, 1981; ISBN 3-8009-1076-4.

[34] Elhaffar, A.; Lehtonen, M.; High Frequency Current Transformer Modeling for Traveling Waves Detection; IEEE Power Engineering Society General Meeting, 2007; ISBN: 1-4244-1296-X; pp. 1 – 6.

[35] Elhaffar, A.; Lehtonen, M.; Travelling waves based earth fault location in 400 kV transmission network using single end measurement; Large Engineering Systems Conference on Power Engineering, 2004 (LESCOPE-04); ISBN: 0-7803-8386-9; pp. 53 – 56.

[36] Elhaffar, A.M.; Power Transmission Line Fault Location based on Current Traveling Waves; Doctoral Dissertation; Helsinki University of Technology, 2008; ISBN 978-951-22-9244-8.

[37] Englert, T.J.; Chowdhury, B.H.; Grigsby, E.; A laboratory investigation of electro-optic Kerr effect for detection of electric transmission line faults; IEEE Transactions on Power Delivery, Jul 1991, Vol. 6, No. 3; ISSN 0885-8977; pp. 979 – 985.

[38] Fei Long; Jianhuan Zhang; Chunrong Xie; Zhiwei Yuan; Application of the Pockels Effect to High Voltage Measurement; 8th International Conference on Electronic Measurement and Instruments, 2007 (ICEMI '07); ISBN 978-1-4244-1136-8; pp. 4-495 – 4-499.

[39] Ferkovic, L.; Ilic, D.; Malaric, R.; Mutual Inductance of a Precise Rogowski Coil in Dependence of the Position of Primary Conductor; IEEE Transactions on Instrumentation and Measurement, Jan 2009, Vol. 58, Iss. 1; ISSN 0018-9456; pp. 122 – 128.

[40] Grandi, G.; Kazimierczuk, M.K.; Massarini, A.; Reggiani, U.; Stray Capacitances of Single-Layer Solenoid Air-Core Inductors; Vol. 35, Iss. 5, Sept/Oct 1999; ISSN 0093-9994/99; pp. 1162 – 1168.

[41] Grandi, G.; Reggiani, U. ; Kazimierczuk, M.K.; Massarini, A.; Optimal design of single-layer solenoid pair-core inductors for high frequency applications; Proceedings of the 40th Midwest Symposium on Circuits and Systems, 1997; ISBN 0-7803-3694-1; pp. 358 – 361.

[42] Grover, F.W.; Inductance calculations: working formulas and tables; Dover 2009 (reprint of 1946 edition); ISBN 0-486-47440-2.

[43] Hashmi, G.M.; Lehtonen, M.; Nordman, M.; Calibration of on-line partial discharge measuring system using Rogowski coil in covered-conductor overhead distribution networks; IET Science, Measurement & Technology, Jan 2011, Vol. 5, Iss. 1; ISSN 1751-8822; pp. 5 – 13.

[44] Hashmi, G.M.; Partial Discharge Detection for Condition Monitoring of Covered-Conductor Overhead Distribution Networks using Rogowski Coil; Doctoral Dissertation; Helsinki University of Technology, 2008; ISBN 978-951-22-9446-6.

[45] Hewson, C.; Ray, W.R.; The effect of electrostatic screening of Rogowski coils designed for wide-bandwidth current measurement in power electronic applications; IEEE 35th Annual Power Electronics Specialists Conference, 2004 (PESC 04); Vol. 2; ISBN 0-7803-8399-0; pp. 1143 – 1148.

[46] Hewson, C.R.; Ray, W.F.; Optimising the high frequency bandwidth and immuntity to interference of Rogowski coils in measurement applications with large local dV-dt; Twenty-Fifth Annual IEEE Applied Power Electronics Conference and Exposition (APEC), 2010; ISBN 978-1-4244-4783-1/10; pp. 2050 – 2056.

[47] Hlavacek, J.; Prochazka, R.; Draxler, K.; Kvasnicka, V.; The Rogowski Coil Design Software; 16th IMEKO TC4 Symposium Exploring New Frontiers of Instrumentation and Methods for Electrical and Electronic Measurements 2008; Available from www.imeko.org/publications/tc4-2008/IMEKO-TC4-2008-148.pdf (checked May 10th, 2012).

[48] Ida, N.; Electromagnetic Engineering; Springer-Verlag 2004; ISBN 0-387-20156-4.

[49] Ifeachor, E.C.; Jervis, B.W; Digital Signal Processing: A Practical Approach (2nd Edition); Prentice Hall, 2001; ISBN 0201-59619-9.

[50] Isa, M.; Hashmi, G.M.; Lehtonen, M.; Comparative study of on-line three phase PD monitoring systems for overhead covered conductor distribution lines; Proceedings of the 44th International Universities Power Engineering Conference (UPEC), 2009; ISBN 978-1-4244-6823-2; pp. 1 – 5.

[51] Judd, M.D.; Li Yang; Hunter, I.B.B.; Partial discharge monitoring for power transformer using UHF sensors Part 2: field experience; IEEE Electrical Insulation Magazine, May-June 2005, Vol. 21, No. 3; ISSN 0883-7554; pp. 5 – 13.

[52] Järvik, J., Panov, V.; Fault Location in Unearthed MV Networks Based on Analyses of Wave Transients; 4-th International Conference Electric Power Quality and Supply Reliability 2004 (PQ2004); pp. 163 – 168.

[53] Kamen, E.W.; Fundamentals with Signals and Systems with MATLAB; Prentice-Hall 1997; ISBN 0-02-361942-2.

[54] Kanda, M.; Standard probes for electromagnetic field measurements; IEEE Transactions on Antennas and Propagation, Oct 1993, Vol. 41, No. 10; ISSN 0018-926X; pp. 1349 – 1364.

[55] Karrer, N.; Hofer-Noser, P.; PCB Rogowski coils for high di/dt current measurement; IEEE 31st Annual Power Electronics Specialists Conference, 2000 (PESC 00); Vol. 3; ISBN 0-7803-5692-6; pp. 1296 – 1301.

[56] Kim, S.; Neikirk, D.P.; Compact equivalent circuit model for the skin effect; IEEE MTT-S International Microwave Symposium Digest, 1996; Vol. 3; ISBN: 0-7803-3246-6; pp. 1815 – 1818.

[57] Kreuger, F.H.; Wezelenburg, M.G.; Wiemer, A.G.; Sonneveld, W.A.; Partial discharge. XVIII. Errors in the location of partial discharges in high voltage solid dielectric cables; IEEE Electrical Insulation Magazine, Nov-Dec 1993, Vol. 9, Iss. 6; ISSN 0883-7554; pp. 15 – 22.

[58] Liao Jingsheng; Guo Xiaohua; Luo Cheng; Zhu Mingjun; Yang Zefu; Studies of Rogowski coil current transducer for low amplitude current (100A) measurement; IEEE Canadian Conference on Electrical and Computer Engineering, 2003 (CCECE 2003); Vol. 1; ISBN 0-7803-7781-8; pp. 463 – 466.

[59] Lim, S. F.; Yeo, K. S.; Ma, J. G.; Do, M. A.; Geng, C. Q.; Chew, K. W.; Chu, S.-F.; A comprehensive study and modeling of centre-tap differentially driven single-turn integrated inductors for 10-GHz applications; Microwave and Optical Technology Letters, Aug 2003, Vol. 38, Iss. 3; DOI: 10.1002/mop.11008; pp. 182 – 185.

[60] Liu, Y.D.; Sheng, G.H.; He, Z.M.; Xu, X.Y.; Jiang, X.C.; Method of fault location based on the distributed traveling-wave detection device on overhead transmission line; IEEE Power Engineering and Automation Conference (PEAM), 2011; ISBN 978-1-4244-9691-4; pp. 136 – 140.

[61] Luciano, A.M.; Savastano, M.; Wide band transformer based on a split-conductor current sensor and a Rogowski coil for high current measurement; IEEE Instrumentation and Measurement Technology Conference, 1995 (IMTC/95); ISBN 0-7803-2615-6; pp. 454 – 458.

[62] Macintyre, S. A.; Magnetic Field Sensor Design; Sensor Review, 1991, Vol. 11, Iss. 2; DOI: 10.1108/eb007841; pp. 7 – 11.

[63] Magnusson, P.C.; Alexander, G.C; Tripathi, V.K.; Weishaar, A.; Transmission Lined and Wave Propagation, 4th Edition; CRC press 2001; ISBN 0-8493-0269-2.

[64] Manson J.; Targosz R.; European Power Quality Survey Report; November 2008; Leonargo Energy, 2008; available from http://www.leonardo-energy.org/european-power-quality-survey-report (checked May 10th, 2012).

[65] Marracci, M.; Tellini, B.; Zappacosta, C.; Robles, G.; Critical Parameters for Mutual Inductance Between Rogowski Coil and Primary Conductor; IEEE Transactions on Instrumentation and Measurement, Feb. 2011, Vol. 60; Iss. 2; ISSN 0018-9456; pp. 625 – 632.

[66] Mason, S.J.; Topological analysis of linear non-reciprocal networks; Proceedings of the IRE, Jun 1957, Vol. 45, Iss. 6; ISSN 0096-8390; pp. 829 – 838.

[67] Massarini, A.; Kazimierczuk, M. K.; Self-Capacitance of Inductors; IEEE Transactions on Power Electronics, Jul 1997, Vol. 12, Iss. 4; ISSN 0885-8993/97; pp. 671 – 676.

[68] Massarini, A.; Kazimierczuk, M.K.; Grandi, G.; Lumped parameter models for single- and multiple-layer inductors; 27th Annual IEEE Power Electronics Specialists Conference, 1996 (PESC '96); Vol. 1; ISBN 0-7803-3500-7/96; pp. 295 – 301.

[69] Medhurst, R. G.; H. F. Resistance and Self-Capacitance of Single-Layer Solenoids; Wireless Engineer, Feb 1947; pp. 35 – 43.

[70] Medhurst, R. G.; H. F. Resistance and Self-Capacitance of Single-Layer Solenoids; Wireless Engineer, Mar 1947; pp. 80 – 92.

[71] Metwally, I.A.; Self-Integrating Rogowski Coil for High-Impulse Current Measurement; IEEE Transactions on Instrumentation and Measurement, Feb 2010, Vol. 59, Iss. 2; ISSN 0018-9456; pp. 353 – 370.

[72] Mirzaei, M.; A Ab Kadir, M.Z.; Moazami, E.; Hizam, H.; Review of Fault Location Methods for Distribution Power System; Australian Journal of Basic and Applied Sciences, 2009, Vol. 3; ISSN 1991-8178; pp. 2670 – 2676.

[73] Mostafa, A.E.-S.; Gohar, M.K.; Determination of Voltage, Current, and Mlagnetic Field Distributions Together with the Self-Capacitance, Inductance and HF Resistance of Single-Layer Coils; Proceedings of the IRE, Apr 1953, Vol. 41, No. 4; ISSN 0096-8390; pp. 537 – 547.

[74] Nanming Chen; Kun-Long Chen; Yuan-Pin Tsai; Replacing current transformers with power current microsensors based on hall ICs without iron cores; 2010 IEEE International Workshop on Applied Measurements For Power Systems (AMPS); ISBN 978-1-4244-7372-4; pp. 22 – 26.

[75] Noyan Kinayman, Aksun, M.I.; Modern Microwave Circuits; Artech House 2005; ISBN 1-58053-725-1.

[76] Ohrstrom, M.; Geidl, M.; Soder, L.; Andersson, G.; Evaluation of travelling wave based protection schemes for implementation in medium voltage distribution systems; 18th International Conference and Exhibition on Electricity Distribution, 2005 (CIRED 2005); pp. 1 – 5; available in IEEE Xplore database.

[77] Palermo, A.J.; Distributed Capacity of Single-Layer Coils; Proceedings of the Institute of Radio Engineers, Jul 1934, Vol. 22, Iss. 7; ISSN 0731-5996; pp. 897 – 905.

[78] Paoletti, G.J.; Golubev, A.; Partial discharge theory and technologies related to medium-voltage electrical equipment; IEEE Transactions on Industry Applications, Jan/Feb 2001, Vol. 37, No. 1; ISSN 0093-9994; pp. 90 – 103.

[79] Paul, C.R.; Inductance: loop and partial; John Wiley & Sons 2010; ISBN 978-0-470-46188-4.

[80] Pellinen D. G.; Di Capua M. S.; Sampayan S. E.; Gerbracht H.; Wang M.; Rogowski coil for measuring fast, high-level pulsed currents; Review of Scientific Instruments, 1980, Vol. 51, Iss. 11; ISSN 0034-6748/80/111535-06; pp. 1535 – 1540.

[81] Peretto, L.; Sasdelli, R.; Scala, E.; Tinarelli, R.; Performance Characterization of a Measurement System for Locating Transient Voltage Sources in Power Distribution Networks; IEEE Transactions on Instrumentation and Measurement, Feb 2009, Vol. 58, No. 2; ISSN 0018-9456; pp. 450 – 456.

[82] Qin Yu; Holmes, T.W.; Stray capacitance modeling of inductors by using the finite element method; IEEE Transactions on Electromagnetic Compatibility, Feb 2001, Vol. 43, Iss. 1; pp. 88 – 93.

[83] Rachidi, F., (ed.); Tkachenko, S.V., (ed.); Electromagnetic Field Interaction with Transmission Lines, From Classical Theory to HF Radiation Effects; WIT press, 2008; ISBN 978-1-84564-063-7.

[84] Rautiainen, A.; Helisto, P.; Mansten, T.; Seppa, H.; 50 Hz current measurements with Rogowski coils; Conference on Precision Electromagnetic Measurements, 2002; ISBN 0-7803-7242-5; pp. 350 – 351.

[85] Ray, F.V.; Davis, R.M.; High Frequency Improvements in Wide Band-width Rogowski Current Transducers; EPE 99 Conference Proceedings, Lausanne, Sept 1999; Available from www.pemuk.com/pdf/816epe99.pdf (checked May 10th, 2012).

[86] Ray, W.F.; Hewson, C.R.; Metcalfe, J.M.; High frequency effects in current measurement using Rogowski coils; European Conference on Power Electronics and Applications, 2005; ISBN 90-75815-09-3; pp. 9 – 17.

[87] Ray, W.F.; The use of Rogowski coils for low amplitude current waveform measurement; IEE Colloquium on Measurement Techniques for Power Electronics, 1992; pp: 4/1 – 4/5 (available in IEEE Xplore database).

[88] Reach of protection for an electrical installation and rules of operating within its limits (in Estonian) / Elektripaigaldise kaitsevööndi ulatus ja kaitsevööndis tegutsemise kord; Regulation of Estonian Ministry of Economic Affairs and Communications; approved 26.03.2007 nr 19, in effect since 20.07.2007.

[89] Reed Edgel, W.; I vs I-dot; PRODYN Application note 890; date unknown; available from http://www.prodyntech.com/download/appnotes/PAN 890-I vs I Dot Sensors.pdf (checked May 10th, 2012).

[90] Reilly, M.P.; Lewis, W.; Miley, G.H; Magnetic field probes for use in radio frequency plasma; Review of Scientific Instruments, 80, 053508 (2009); doi: 10.1063/1.3136907.

[91] Rezaee, M.; Heydari, H.; Mutual inductances comparison in Rogowski coil with circular and rectangular cross-sections and its improvement; 3rd IEEE Conference on Industrial Electronics and Applications, 2008 (ICIEA 2008); ISBN 978-1-4244-1717-9; pp. 1507 – 1511.

[92] Robles G.; Martinez J. M.; Rojas M.; Sanz J.; Inductively coupled probe for the measurement of partial discharges; Review of Scientific Instruments 2008, Vol. 79, Iss. 5; DOI: 10.1063/1.2924207; pp. 79 – 83.

[93] Robles, G.; Argueso, M.; Sanz, J.; Giannetti, R.; Tellini, B.; Identification of parameters in a Rogowski coil used for the measurement of partial discharges; IEEE Instrumentation and Measurement Technology Conference Proceedings, IMTC 2007; ISBN 1-4244-0589-0/07; pp. 1 – 4.

[94] Robles, G.; Martinez-Tarifa, J.M.; Rojas-Moreno, M.V.; Sanz-Feito, J.; Inductive Sensor for Measuring High Frequency Partial Discharges Within Electrical Insulation; IEEE Transactions on Instrumentation and Measurement, Nov 2009; Vol. 58; Iss. 11; ISSN 0018-9456; pp. 3907 – 3913.

[95] Rodrigo, A.; Llovera, P.; Fuster, V.; Quijano, A.; Influence of high frequency current transformers bandwidth on charge evaluation in partial discharge measurements; IEEE Transactions on Dielectrics and Electrical Insulation, Oct 2011, Vol. 18, Iss. 5; ISSN 1070-9878; pp. 1798 – 1802.

[96] Rojas-Moreno, M.V.; Robles, G.; Martinez-Tarifa, J.M.; Sanz-Feito J.; Self-integrating inductive loop for measuring high frequency pulses; Review of Scientific Instruments 2011, Vol. 82, Iss. 8; doi:10.1063/1.3622521.

[97] Rojas-Moreno, M.V.; Robles, G.; Tellini, B.; Zappacosta, C.; Martinez-Tarifa, J.M.; Sanz-Feito, J.; Study of an Inductive Sensor for Measuring High Frequency Current Pulses; IEEE Transactions on Instrumentation and Measurement, May 2011, Vol. 60, Iss. 5; ISSN 0018-9456; pp. 1893 – 1900.

[98] Rojas, M.; Robles, G.; Tellini, B.; Zappacosta, C.; Martinez, J.M.; Sanz, J.; An inductive transducer for the measurement of high frequency pulses with applicability in the detection of partial discharges; IEEE Instrumentation and Measurement Technology Conference (I2MTC), 2010; ISBN 978-1-4244-2832-8; pp. 375 – 379.

[99] Sadiku, M.N.O.; Musa, S.M.; Nelatury, S.R.; Comparison of approximate formulas for the capacitance of microstrip line; IEEE SoutheastCon, 2007; ISBN 1-4244-1029-0; pp. 427 – 432.

[100] Shepard, D.E.; Yauch, D.W.; An overview of Rogowski coil current sensing technology; LEM DynAmp Inc.; available from http://www.dynamp.com/dynamp/LDADocum.nsf/c2270fbdd892ac3e86256e75000ad88a/e710af6d3e0f6255862565d7004b19db/$FILE/Report.pdf (Checked May 10th, 2012).

[101] Shi Shenxing; Jiang Bo; Dong Xinzhou; Bo Zhiqian; Protection of microgrid; 'Managing the Change' 10th IET International Conference on Developments in Power System Protection (DPSP 2010); doi: 10.1049/cp.2010.0209; pp. 1 – 4.

[102] Shim, I.; Soraghan, J.J.; Siew, W.H.; Digital signal processing applied to the detection of partial discharge: an overview; IEEE Electrical Insulation Magazine, May/Jun 2000, Vol. 16 , Iss. 3; ISSN 0883-7554; pp. 6 – 12.

[103] Smith, D.C.; Signal and noise measurement techniques using magnetic field probes; IEEE International Symposium on Electromagnetic Compatibility, 1999; Vol. 1; ISBN: 0-7803-5057-X; pp. 559 – 563.

[104] Soon Yun Poh; Weng Cho Chew; Jin Au Kong; Approximate Formulas for Line Capacitance and Characteristic Impedance of Microstrip Line; IEEE Transactions on Microwave Theory and Techniques, Feb 1981, Vol. 29, No. 2; ISSN 0018-9480; pp. 135 – 142.

[105] Spoor, D.J.; Zhu, J.; Frequency considerations when employing travelling wave fault location algorithms; 39th International Universities Power Engineering Conference, 2004 (UPEC 2004); Vol. 3; ISBN 1-86043-365-0; pp. 1116 – 1120.

[106] Stone, G.; Importance of bandwidth in PD measurement in operating motors and generators; IEEE Transactions on Dielectrics and Electrical Insulation, Vol. 7, Iss. 1, February 2000; ISSN 1070-9878/0; pp: 6 – 11.

[107] Zhang Q.; Zhu J.; Jia J.; Tao F.; Yang L.; Design of a current transducer with a magnetic core for use in measurements of nanosecond current pulse; Measurement Science and Technology, 2006, Vol. 17, No. 4; doi:10.1088/0957-0233/17/4/039; pp. 895 – 900.

[108] Zhang, Z.S. ; Xiao, D.M.; Li, Y.; Rogowski air coil sensor technique for on-line partial discharge measurement of power cables; IET Science, Measurement & Technology, May 2009, Vol. 3, Iss. 3; ISSN 1751-8822; pp. 187 – 196.

[109] Zhu Jun-jie; Zhang Xiao-feng; Qiao Ming-zhong; Shen Zhe; Common-mode current measurement of high voltage inverter based on Rogowski coil; IEEE 6th International Power Electronics and Motion Control Conference, 2009 (IPEMC '09); ISBN 978-1-4244-3557-9/09; pp. 1604 – 1608.

[110] Zhu Jundong; Zhang Qiaogen; Jia Jiangbo; Tao Fengbo; Yang Liandian; Yang Lanjun; Design of a Rogowski Coil with a Magnetic Core Used for Measurements of Nanosecond Current Pulses; Plasma Science and Technology, 2006, Vol. 8, No. 4; doi:10.1088/1009-0630/8/4/19; pp 457 – 460.

[111] Zhu, J.; Yang, L. ; Jia, J. ; Zhang, Q.; The Design of Rogowski Coil with Wide Band Using for Partial Discharge Measurements; Proceedings of 2005 International Symposium on Electrical Insulating Materials, 2005 (ISEIM 2005); Vol. 2; ISBN 4-88686-063-X; pp. 518 – 521.

[112] Thomas, D.W.P.; Carvalho, R.J.O.; Pereira, E.T.; Fault location in distribution systems based on traveling waves; IEEE Power Tech Conference Proceedings, 2003; Vol. 2; ISBN 0-7803-7967-5.

[113] Tumanski, S.; Induction coil sensors – a review; Measurement Science and Technology, 2007; Vol. 18, No. 3; doi:10.1088/0957-0233/18/3/R01.

[114] Turner, G.R.; Hofsajer, I.W.; Rogowski coils for short duration (<10 uS) pulsed current (>10 kA) measurements; 1999 IEEE AFRICON; Vol. 2; ISBN 0-7803-5546-6; pp. 759 – 764.

[115] Van den Bossche, A.; Ghijselen, J.; EMC combined di/dt current probe; IEEE International Symposium on Electromagnetic Compatibility, 2000; Vol. 2; ISBN 0-7803-5677-2; pp. 569 – 573.

[116] Ward, D.A.; Exon, J.L.T.; Experience with using Rogowski coils for transient measurements; IEE Colloquium on Pulsed Power Technology, 1992; pp. 6/1 – 6/4.

[117] Ward, D.A.; Exon, J.La.T.; Using Rogowski coils for transient current measurements; Engineering Science and Education Journal, Jun 1993, Vol. 2, Iss. 3; ISSN 0963-7346; pp. 105 – 113.

[118] Ward, D.A.; Measurement of Current Using Rogowski Coils; IEE Colloquium on Instrumentation in the Electrical Supply Industry, 1993, pp. 1/1 – 1/3.

[119] Wheeler, H.A.; Inductance formulas for circular and square coils; Proceedings of the IEEE, Dec 1982, Vol. 70, Iss.12, ISSN 0018-9219/82/1200-1449; pp. 1449 – 1450.

[120] Wheeler, H.A.; Simple Inductance Formulas for Radio Coils; Proceedings of the Institute of Radio Engineers, Oct 1928, Vol. 16, No. 10; ISSN 0731-5996; pp. 1398 – 1400.

[121] WSE Series Power Metal Strip Resistors (Extended Range), Product data-sheet; Vishay Intertechnology Inc., Document Number 30109, Revision 15-Feb-11; available from http://www.vishay.com/docs/30109/wse.pdf (checked May 10th, 2012)

[122] Xin Li; Chengrong Li; Wei Wang; Bin Wei; Weijiang Wan; Partial Discharge Measurement in XLPE Cable Joint by Using VHF Sensor; Proceedings of the 2004 IEEE International Conference on Solid Dielectrics, 2004 (ICSD 2004); Vol.2; ISBN 0-7803-8348-6; pp. 669 – 671.

[123] Yadong Liu; Gehao Sheng; Zhimin He; Xiuchen Jiang; Study on new method for distributed fault location of overhead transmission line; IEEE Power and Energy Society General Meeting, 2011; ISBN 978-1-4577-1000-1; pp. 1 – 8.

[124] Yangchun Cheng; Yinghui Yan; Chengrong Li; The high frequency characteristic of wideband Rogowski coil with asymmetric windings; 2010 Annual Report Conference on Electrical Insulation and Dielectric Phenomena (CEIDP2010); ISBN 978-1-4244-9468-2; pp. 1 – 4.

[125] Yi Liu; Fuchang Lin; Qin Zhang; Heqing Zhong; Design and Construction of a Rogowski Coil for Measuring Wide Pulsed Current; IEEE Sensors Journal, Jan 2011, Vol. 11, Iss. 1; ISSN 1530-437X; pp. 123 – 130.

[126] Young, J.C.; Butler, C.M.; Inductance of a shielded coil; IEEE Transactions on Antennas and Propagation; Jun 2001, Vol. 49, No. 6; ISSN 0018-926X; pp. 944 - 953.

10 Kokkuvõte

Käesolevas töö keskendub õhksüdamikuga induktiivse voolutajuri analüüsile ja uurimisele, samuti konkreetse tajuri projekteerimisele ning katsetamisele. Antud voolutajuri peamiseks ülesandeks on elektrijaotusvõrgus keskpingeliinidel aset leidvate kõrgsageduslike siirdeprotsesside täpne mõõtmine. Selliste protsesside mõõtmise kaudu on võimalik teostada elektriliini isolatsiooni seisukorra hindamist, samuti määrata tekkinud rikke asukohta võrgus. Nimetatud meetmete abil oleks võimalik olulisel tõsta elektrivarustuse töökindlust – vähendada katkestuste arvu ning ka katkestuste koguaega.

Elektrivõrkude varustuskindlusele esitatavad nõuded muutuvad iga aastaga järjest kõrgemaks. Nende täitmine eeldab kaasaegsete ja kvaliteetsete kaitseaparaatide ja –releekaitsemetoodika rakendamist, kuid alajaamadele pakutava aparatuuri põhiline eesmärk on ikkagi reageerimine alles siis, kui rike on juba tekkinud või lühikest aega kestnud. Varustuskindluse kõrge saavutamine aga ei ole ainult nimetatud meetmeid rakendades võimalik, kuna antud juhul ei vaadelda tunnuseid, mis viitaksid näiteks rikke peatsele võimalikkusele. Töökindluse kasvu edasiseks tõstmiseks ning katkestusaegade vähendamiseks oleksid samas liini seisukorra hindamise vahendid väga olulised, kuna potentsiaalse rikke asukohas saaks näiteks ennetavalt läbi viia remondi ning seeläbi vältida rikke tekkimist, kuna viimane võiks kaasa tuua märksa pikema katkestuse ning suuremad kulud.

Elektrivõrgus esinev rike toob rikkega liinile ühendatud tarbijatele tüüpiliselt kaasa toitekatkestuse, kuid mõjub ka suuremas võrgu osas, seda näiteks järsu võrgupinge kukkumisena e. pingelohuna. Seda tüüpi siirdeprotsessid võivad olla katkestusest isegi kahjulikumad, seisates tootmisliine ning põhjustades rikkeid seadmetes. Uuringu [64] tulemusena on hinnatud, et Euroopa Liidus võib pingelohkudest ning katkestustest tekkinud kahju ulatuda kuni 75 miljardi euroni igal aastal.

Rikkeid elektrivõrgus võib jagada jämedalt kahte rühma. Esimesse kuuluvad rikked, millele eelnevalt elektrivõrgus pole elektrilisi märke rikke peatsest esinemisest. Taolised rikked on põhjustatud inimfaktorist, mehaanilistest probleemidest kuid ka loodusmõjudest (tormid, linnud jms.). Teise gruppi kuuluvad rikked, millele eelnevalt on elektrivõrgus võimalik mõõta tunnuseid, mis üheselt viitavad peatsele probleemile. Sellisteks on näiteks enamik isolatsiooni-rikkeid, kuid ka näiteks puude liinile liiga lähedale paindumine jm. Selliste rikete peatsele toimumisele viitavateks tunnusteks on osalahenduste (s.o miniatuursed dielektrilised läbilöögid) esinemine, mille toimumisest annab märku elektirliinilt mõõdetav väga lühiajaline (kestvus mõni kuni mõnikümmend nanosekundit) ning suhteliselt väikese tipuväärtusega (kuni paarkümmend volti) siirdeprotsess. Taoliste siirdeprotsesside intensiivistumine ning sagenemine elektriliinil on peatsele isolatsioonirikkele viitav tunnus.

Kiired siirdeprotsessid kaasnevad ka iga rikkega, mis elektrivõrgus toimub, tänu levimisviisile ning suurele levikiirusele nimetatakse antud protsesse laineprot-sessideks. Rikkega kaasnevate siirdeprotsesside tunnuseks on suur intensiivsus

(pingemuutumise kiirus isegi üle 100 kV / μs) ning amplituud kümnetes kilovoltides. Kui rikke järel esinev lühisvool on tohutu amplituudiga (suurused üle kiloamprite) kui suhteliselt aeglaselt kujunev, siis nimetatud kiired siirdeprotsessid levivad üle kogu elektrivõrgu valguse kiirusel. Uurides rikkega kaasnevate siirdeprotsesside levimist ning nende leviaega erinevate mõõtepunktide vahel, on täpse mõõtmise korral võimalik määrata nende alg-levipunkt, ehk siis rikke toimumise koht, elektrivõrgus. Teades täpset rikke asukohta, saab rikke parandamiseks kuluvat remondiaega oluliselt vähendada, kuna jääb ära parandamist vajava koha aeganõudev selgitamine.

Alajaamades hetkel kasutatavad kaitseautomaatikaseadmed mõõdavad liinil olevat võrgusageduslikku (50 või 60 Hz) voolu ning pinget ja rikke tekkimise järel reageerivad liinil olevale lühisvoolule. Selline ülesanne ei eelda aparatuurilt väga kiirete protsesside mõõtmist, elektrivõrkudes esinev inerts on suur ning liinil aset leidvad suurima amplituudiga lühisvooludega seotud siirdeprotsessid on suhteliselt aeglased. Nende mõõtmiseks ei ole vaja kiireid seadmeid ning ka signaalitöötluspõhimõtted on lihtsamad. Mõõteahelate tüüpiline ribalaius, s.t sisendsignaali sagedusvahemik, milles mõõtmisi on võimalik usaldusväärselt läbi viia, tipneb mõne kuni mõnekümne kilohertsiga (kHz).

Käesoleva töö teine peatükk esitab ülevaate mõõdetavatest siirdeprotsessidest ning samuti uuritakse, millise ribalaiusega tajurit oleks vaja, et mõõtmise järel oleks võimalik tagada väljundis samasugune signaalikuju, kui oli mõõdetaval liinil. Uuritavateks on kõrgepingelise osalahenduse tekitatud ning samuti lühise korral esinev siirdeprotsess. Analüüsi läbiviimiseks töödeldakse siirdeprotsessi signaali erineva lõikesagedusega filtritega ning saadud signaali ning originaali võrdlusel määratakse sobiv ribalaius. Saab näidata, et vajaliku sagedusriba ülempiir jääb 70 - 90 MHz vahemikku, soovitavaks eesmärgiks on määratud 100 MHz. Sagedusriba alampiir on määratud mõõdetava impulsi pikkusega, kuid ka signaalitöötlusseadmete (analoog-digitaalmuundur jms) parameetritega, s.h võendussagedusega ja see peaks olema vahemikus 0,1 – 1 MHz. Tutvustatakse ka impulss-signaalide mõõtmise nõudeid, mida hiljem töös arvestada tuleb.

Kolmandas peatükis antakse ülevaade induktiivse voolutajuri tööpõhimõtetest ning tutvustatakse selle tööpõhimõtteid madalsagedusliku vahelduvvoolu mõõtmisel. Esitatud on magnetvälja põhiseosed, magnetvoo arvutamisvõtted ning olulise terminina tutvustatakse vastastikuse induktiivsuse määramist juhtme ning tajuri vahel. Madalsagedusliku mudeli väljund on määratud Faraday seadusega ning kuna madalatel sagedustel on induktiivtajuri omainduktiivsus ning omamahtuvus väikesed, siis nimetatud komponendid määravat rooli tajuri töös ei mängi.

Neljandas peatükis on ülevaade tajuri dünaamilistest omadustest, rakendades kesksagedsulikku mudelit nimetatud omaduste analüüsiks. Selles mudelis on oluliselt kohal nii pooli omamahtuvus kui ka –induktiivsus, kuid sellele lisanduvad veel ka mõõtesüsteemi mahtuvus ning välise komponendina täiendav koormustakisti. Aseskeem sellisele mudelile on teist järku ahel, mille analüüsiks

kasutatava ülekandefunktsiooni arvutamist on samuti tutvustatud. Tähelepanu on pööratud antud ahela pooluste leidmisele, mille alusel saab leida ahela käitumise erinevatel sagedustel. Täpsemini vaadatakse amplituudi- ning faasiülekande karakteristikute kujundamist, et oleks võimalik täita impulssmõõtmiste läbiviimiseks määratud nõuded – amplituudi ülekande karakteristik püsiva väärtusega ning faasiülekande karakteristik nullisel väärtusel kogu töösagedusriba ulatuses. Osutub, et selleks on vaja tagada, et madalama sageduega poolu oleks sagedusel, mis jääb alusmisest töösagedusest 10 korda väiksemaks ja vastavalt kõrgem poolus peaks paiknema sagedusel, mis on 10 korda ülemisest töösagedusala piirist kõrgem.

Viies peatükk tutvustab kõrgsageduslikku induktiivtajuri mudelit. Selles on kajastatud väiksed induktiivsed- ning mahtuvuslikud mõjutused, mida madalamatel sagedustel kui 10 ... 30 MHz tavaliselt ei vaadelda. Ülevaade algab poolis kasutatava mähisetraadi pinnaefekti analüüsist, eesmärgiga leida selle mõju tajuri sagedukarakteristikule. Selgub, et sagedusalas kuni 100 MHz ei ole pinnaefekti tüttu suureneval takistusel märkimisväärset mõju. Vaadeldakse tajuri väljundisse ühendatud koormustakistuse jadainduktiivsuse mõju, tajuri ja mõõtesüsteemi vahelist ühendusjuhtmete mõju ning ka tajuri varjestamise küsimusi. Peatüki lõpus on toodud ülevaade induktiivpooli ülekandeliini talitluse mudelist, mis määrab ära tajuri suurima võimaliku töösageduse arvestades juhtme pikkusest tulenevate mõjudega. Kõrgsagedusmudelis esitatud parasiitkomponentide mõju saab vähendada, kuid neid ei saa vältida. Antud peatükis esitatud analüüs võimaldab hinnata tajuri väljundisse ühendatud kompnentide mõju ning esitada nõudmised tajuri väljundisse ühendatavatele komponentidele.

Kuues peatükk käsitleb induktiivse voolutajuri väljatöötamist ning kujundamist. Pikemalt on kirjeldatud tajuri kujundamise lähtetingimustel ning selgitatakse ka erinevaid praktilise rakendamise asjaolusid. Selgitatakse tajuri ühe oluliseima omaduse – tundlikkuse – määramist. Tajuri kujundamist induktiivsuse määramise kaudu, mille eesmärgiks on induktiivtajuri pooli keerdude arvu selgitamine. Sellisel lähenemisel saadud tajurit iseloomustab küllalt suur tundlikkus, kuid piiratud töösagedusala tänu pooli traadi suurele pikkusele. Teise lähenemisteena tajuri kujundamisel on lähtutud vajalikut tööribalaiuses, milles piirangu seab tajuris kasutatava mähisetraadi pikkus. Sellisel juhul tulemusena saadav tajur ei oma samas suurt tundlikkust. Lahendusena saaks antud juhul rakendada tajuri väljundis laiaribalist võimendit, kuna tundlikkust pole võimalik tõsta ilma traadi pikkust suurendamata.

Seitsmes peatükk annab ülevaate valmistatud laia töössagedusribaga induktiivtajurist ning selle katsetamisest kõrgepingelaboris. Katsete tulemused müra- ja peegeldusvabas keskkonnas näitavad loodud tajuri ning täpse kõrgsagedusliku vooluprooviku mõõtetulemuste kokkulangemist. See annab märku antud tajuri sobivusest kõrgsageduslike siirdeprotsesside mõõtmiseks. Edasised katsed kõrgepinglaboris võrreldavaid tulemusi ei anna, kuid võimaldavad saada aimu tegelike elektriliinidel aset leidvate siirdeprotsesside iseloomust.

Laboratoorsete katsete tulemused annavad selge vihje antud voolutajuri sobivusest kõrgsageduslike siirdeprotsesside mõõtmiseks jaotusvõrgu elektriliinidel. Sobivalt välja töötatud tajuri rakendamist elektriliinide seisukorra määramiseks ning ka rikke asukoha määramiseks tuleks katsetada nii edasiste laboratoorsete katsetega kui ka katsetega elektrivõrgus. Selle järel saab teha järeldused ning asuda tajurit kasutatavate seadmete väljatöötamisele.

Author's publications

[A1] Kütt, L.; Järvik, J.; Kilter, J.; Shafiq, M.; Lehtonen, M.; Air-core Inductive Current Sensor for Fast Transients Measurements in Distribution Networks; 8th Conference 2012 Electric Power Quality and Supply Reliability (PQ2012); June 11-13, 2012; Tartu, Estonia; ISBN 978-1-4673-1979-9.

[A2] Kütt, L.; Järvik, J.; Vaimann, T.; Shafiq, M.; Lehtonen, M.; Kilter, J.; High-Frequency Current Sensor for Power Network On-line Measurements; Proceedings of the 13th Scientific Conference Electric Power Engineering 2012 (EPE 2012); May 23-25, 2012; Brno, Czech Republic; ISBN 978-80-214-4514-7; pp. 367 - 371.

[A3] Kütt, L.; Järvik, J.; Mõlder, H.; Kilter, J.; Muhammad, S.; Magnetic Current Sensor Stray Components in High Frequency Operation and their Effects; 11th Conference on Environment and Electrical Engineering (EEEIC 2012); May 18-25, 2012; Venice, Italy; ISBN 978-1-4577-1828-1.

[A4] Vinnal, T.; Janson, K.; Kalda, H.; Kütt, L.; Supply Voltage Level Optimisation in Low Voltage Networks Using Shunt Capacitors; Proceedings of the 7th International Conference on Electrical and Control Technologies (ECT-2012); May 3-5, 2012; Kaunas, Lithuania; ISSN 1882-5934; pp. 206 - 211.

[A5] Kütt, L.; Järvik, J.; Kilter, J.; Shafiq, M.; Lehtonen, M.; Design of High-Frequency Transient Current Sensor for Powerline On-Line Measurement; Proceedings of the 7th International Conference on Electrical and Control Technologies (ECT-2012); May 3-5, 2012; Kaunas, Lithuania; ISSN 1882-5934, pp. 212 - 216.

[A6] Kütt, L.; Järvik, J.; Experiments with Travelling Wave Transients for Verification of Suitability of Sensor; 11th International Symposium "Topical Problems in the Field of Electrical and Power Engineering" and "Doctoral School of Energy and Geotechnology II"; January 16-21, 2012; Pärnu, Estonia; ISBN 978-9985-69-051-2; pp. 149 - 152.

[A7] Kütt, L.; Shafiq, M.; Magnetic Sensor Coil Shape Geometry and Bandwidth Assessment; Proceedings of 7th International Conference-Workshop Compatibility and Power Electronics (CPE2011); June 1-3, 2011; Tallinn, Estonia; ISBN 978-1-4244-8806-3.

[A8] Kütt, L.; Järvik, J.; Magnetic field sensor coil in fast transient measurement application; 10th International Symposium "Topical problems in the field of electrical and power engineering" and "Doctoral school of energy and Geotechnology II"; January 10-15, 2011; Pärnu, Estonia; ISBN 978-9985-9089-4-5; pp. 117 - 121.

[A9] Vinnal, T.; Janson, K.; Kalda, H.; Kütt, L;. Analyses of Supply Voltage Quality, Power Consumption and Losses Affected by Shunt Capacitors for

Power Factor Correction; 7th International Conference 2010 Electric Power Quality and Supply Reliability (PQ2010); June 16-18, 2010; Kuressaare, Estonia; ISBN 978-1-4244-6978-9.

[A10] Kütt, L.; Kilter, J.; Palu, I.; Short-Circuit Wave Transient Measurements in HV Power Network; 9th International Symposium Pärnu 2010 "Topical Problems in the Field of Electrical and Power Engineering" and "Doctoral School of Energy and Geotechnology II"; June 14 - 19, 2010; Pärnu, Estonia; ISBN 978-9985-9089-3-8; pp. 37 - 41.

[A11] Mõlder, H.; Lellsaar, M.; Kütt, L.; Compact fluorescent lamp harmonic disruption effect of transformer losses", 8th International Symposium "Topical problems in the field of electrical and power engineering. Doctoral school of energy and geotechnology II"; January 11-16, 2010; Pärnu, Estonia; ISBN 978-9985-69-049-9; pp. 277 - 280.

[A12] Kütt, L.; Järvik, J.; Analysis on Faulty Phase Grounding in Medium-Voltage Networks with Isolated Neutral; 8th International Symposium "Topical problems in the field of electrical and power engineering. Doctoral school of energy and geotechnology II"; January 11-16, 2010; Pärnu, Estonia; ISBN 978-9985-69-049-9; pp. 281 - 284.

[A13] Vinnal, T.; Kütt, L.; Kalda, H.; Analysis of Power Consumption and Losses in Relation to Supply Voltage Levels; 2008 Power Quality and Supply Reliability Conference (PQ2008); 27-29 August 2008; Pärnu, Estonia; ISBN 978-1-4244-2500-6; pp. 23 - 28.

[A14] Kallaste, A.; Kütt, L.; Bolgov, V.; Janson, K.; Reactive Power Compensation for Spot Welding Machine Using Thyristor Switched Capacitor; 2008 Power Quality and Supply Reliability Conference; August 27-29, 2008; Pärnu, Estonia; ISBN 978-1-4244-2500-6; pp. 241 - 245.

[A15] Janson, K.; Järvik, J.; Kütt, L.; Soosalu, A.; Improvement of Voltage Transformers Overvoltage Problems in MV Networks; 2008 Power Quality and Supply Reliability Conference (PQ2008); 27-29 August, 2008; Pärnu, Estonia; ISBN 978-1-4244-2500-6; pp. 247 - 251.

[A16] Janson, K.; Bolgov, V.; Kütt, L.; Kallaste, A.; Mõlder, H.; New Practical Approach to Input Current Shaping in AC-DC Power Converters; 13th International Power Electronics and Motion Control Conference (EPE-PEMC 2008); September 1-3, 2008; Poznan, Poland; ISBN 978-1-4244-1741-4; pp. 154 - 158.

[A17] Janson, K.; Bolgov, V.; Kütt, L.; Kallaste, A.; Mõlder, H; Passive Shaping of Line Current Waveform by Converter with Alternating of Parallel and Series Resonance in AC-DC Switch Mode Power Supplies; The 15th IEEE International Conference On Electronics, Circuits and Systems (ICECS 2008); Aug 31 - Sept 3, 2008; Malta; ISBN 978-1-4244-2181-7; pp. 77 - 80.

APPENDIX / LISA A. Curriculum Vitae

Name	Lauri Kütt
Date of birth	24.05.1980
Mailing address	Department of Fundamentals of Electrical Engineering and Electrical Machines Tallinn University of Technology Ehitajate tee 5 19086 Tallinn Estonia
E-mail address	lauri.kutt@ttu.ee

Education	
2004	Master of Science in Technology, electric power engineering, Tallinn University of Technology, thesis title "Device for Single-Phase Earth Fault Protection and Detection Device for Distribution Networks with Unearthed Neutral"
2002	Bachelor of Science in Technology, computer and automation engineering, Tallinn University of Technology, thesis title "Design of Digital Synchronous Test Data Receiver and Storage Device".
1998	Secondary education, Tallinn School No. 21
1995	Basic education, Tallinn Tondiraba Secondary School
Employment	
2007 -	Researcher, Department of Fundamentals of Electrical Engineering and Electrical Machines, Tallinn University of Technology, Estonia
2000 - 2010	Electronic engineer, Liewenthal Electronics Ltd., Estonia
1999 - 2002	Specialist, EMI-IT Ltd., Estonia
1999 - 2001	Computer administrator, Estonian Railway Administration
Additional training and education	
2010 - 2011	Aalto University School of Electrical Engineering (Espoo, Finland), Post-graduate research (5 months).
2011	Power quality. Post-graduate intensive course. Espoo, Finland (3 days). Aalto University.
2011	Microcontrollers for power electronics applications. Post-

	graduate intensive course. Tallinn, Estonia (3 days). Tallinn University of Technology.
2011	Overvoltages, overvoltage protection and insulation co-ordination in high voltage power systems for transmission and distribution of electric energy. Post-graduate intensive course. Lappeenranta, Finland (3 days). Lappeenranta University of Technology.
2010	Reliability Assessment in the Electrical Power System. Post-Graduate intensive course. Espoo, Finland (4 days). Aalto University.
2010	Fault Detection and Location in Distribution Networks. Post-Graduate intensive course. Espoo, Finland (3 days). Aalto University.
2010	Product Develpoment. Post-graduate intensive course. Pärnu, Estonia (2 days). Tallinn University of Technology.
2010	Power Quality Issues in Contemporary and Future Power Networks. Intensive course. Manchester, Great Britain (3 days). University of Manchester.
2009	Lighting Technology. Intensive course. Tallinn, Estonia (2 days). Tallinn University of Technology.
2008	Automation and Modelling of Fuelcell-based Energy Systems. Spring School. Stralsund, Germany (2 weeks). FHS Stralsund
2008	Laboratory Tasks in Subject of Electromagnetic Compatibility. Work in Gdansk University of Technology laboratory. Gdansk, Poland (1 week).
Scientific administrative practice	
2012	Leading member of the organizing committee of an international scientific conference "2012 Electric Power Quality and Supply Reliability" (PQ2012).
2010	Leading member of the organizing committee of an international scientific conference "2010 Electric Power Quality and Supply Reliability" (PQ2010).
2008	Member of the organizing committee of an international scientific conference "2008 Power Quality and Supply Reliability" (PQ2010).
2006	Member of the organizing committee of an international scientific conference "Power Quality and Supply Reliability 2006" (PQ2006).
Honours and Awards	

2011	Tallinn University Of Technology Post-Graduate Scholarship from Mati Jostov Foundation
2011	Best Presenter Award in Power Electronics and SmartGrids session, 10th International Symposium "Topical Problems in the Field of Electrical and Power Engineering", Pärnu, January 2011
2011	Best Paper Award, CPE 2011 Conference Student Forum
2010	Lauri Kütt; Best Presenter Award, 9th International Symposium "Topical Problems in the Field of Electrical and Power Engineering", Pärnu, June 2010.
2010	Tallinn University Of Technology Post-Graduate Scholarship from Estonian Power Company (Eesti Energia)
Theses supervised	
2012	Paavo Prii, Master's Degree in Power Electronics and Electrical Drives, 2012, (sup) Lauri Kütt, thesis title “Air-Core Inductive Components”, Tallinn University of Technology
2011	Mihhail Mitrofanov, Master's Degree in Electrical Power Engineering, 2011, (sup) Lauri Kütt, thesis title “Algorithm for Fault Location in Distribution Networks using Traveling Wave Method”, Tallinn University of Technology
Main fields of activity	
Electrical engineering Electric power quality Electrical measurement Electromagnetic compatibility	

APPENDIX / LISA B. Elulookirjeldus

Nimi	Lauri Kütt
Sünniaeg	24.05.1980
Postiaadress	Elektrotehnika aluste ja elektrimasinate instituut Tallinna Tehnikaülikool Ehitajate tee 5 19086 Tallinn Eesti
E-posti address	lauri.kutt@ttu.ee

Haridustee	
2004	Tehnikateaduste magister elektroenergeetika erialal, Tallinna Tehnikaülikool, lõputöö teema "Ühefaasiliste maalühiste detektor-konditsioneer isoleeritud neutraaliga keskpingevõrkudele"
2002	Tehnikateaduste bakalaureus arvuti- ja süsteemitehnika erialal, Tallinna Tehnikaülikool, lõputöö teema "Digitaalsignaali vastuvõtja-salvesti"
1998	Keskharidus, Tallinna 21. kool
1995	Põhiharidus, Tallinna Tondiraba Keskkool

Teenistuskäik	
2007 -	Teadur, Elektrotehnika aluste ja elektrimasinate instituut, Tallinna Tehnikaülikool
2000 - 2010	Elektroonikainsener, Liewenthal Electronics OÜ
1999 - 2002	Tehniline spetsialist, EMI-IT OÜ
1999 - 2001	Arvutikonsultant, Raudteeamet

Täiendkoolitus ja kursused	
2010 - 2011	Aalto Ülikooli Elektrotehnika Kool, (Aalto University School of Electrical Engineering), Espoo, Soome. Uurimistöö doktoritöö raames (5 kuud).
2011	Elektritoite kvaliteet. Doktoriõppe intensiivkursus. Espoo, Soome (3 päeva). Aalto Ülikool.
2011	Mikrokontrollerid jõuelektroonikarakendustes. Doktoriõppe intensiivkursus. Tallinn, Eesti (3 päeva). Tallinna Tehnikaülikool.
2011	Liigpinged, liigpingekaitse ja isolatsiooni koordinatsioon

	kõrgepingelistes elektrienergia ülekande- ja jaotussüsteemides. Doktoriõppe intensiivkursus. Lappeenranta, Soome (3 päeva). Lappeenranta Tehnikaülikool.
2010	Elektrisüsteemi töökindluse hindamine. Doktoriõppe intensiivkursus. Espoo, Soome (4 päeva). Aalto Ülikool.
2010	Rikete asukoha määramine elektrivõrkudes. Doktoriõppe intensiivkursus. Espoo, Soome (3 päeva). Aalto Ülikool.
2010	Tooteloome. Doktoriõppe intensiivkursus. Pärnu, Eesti (2 päeva). Tallinna Tehnikaülikool.
2010	Elektritoite kvaliteedi tänapäev ja tulevik. Intensiivkursus. Manchester, Inglismaa (3 päeva). University of Manchester.
2009	Valgustustehnika. Doktoriõppe intensiivkursus. Tallinn, Eesti (2 päeva). Tallinna Tehnikaülikool.
2008	Kütuseelemendid ja nende rakendamine. Intensiivkursus. Stralsund, Saksamaa (2 nädalat). FHS Stralsund.
2008	Elektromagnetilise ühilduvuse labrotööd. Töö Gdanski Tehnikaülikooli laboratooriumis. Gdansk, Poola (1 nädal).
Teadusorganisatsiooniline ja -administratiivne tegevus	
2012	Rahvusvahelise teaduskonverentsi "2012 Electric power quality and supply reliability" (PQ2012) organiseeriva töörühma juht
2010	Rahvusvahelise teaduskonverentsi "2010 Electric power quality and supply reliability" (PQ2010) organiseeriva töörühma juht
2008	Rahvusvahelise teaduskonverentsi "2008 Power quality and supply reliability" (PQ2008) organiseeriva töörühma liige
2006	Rahvusvahelise teaduskonverentsi "Electric Power quality and supply reliability 2006" (PQ2006) organiseeriva töörühma liige
Tunnustused ja preemiad	
2011	Mati Jostovi nimeline TTÜ Arengufondi Doktoriõppe Stipendium
2011	Parim ettekanne "Jõuelektroonika mikro- ja tarkvõrkudes" temaatikal, 10. rahvusvaheline sümpoosium "Topical Problems in the Field of Electrical and Power Engineering, Pärnu, jaanuar 2011
2011	Parima teadusartikli auhind, CPE 2011 konverentsi Üliõpilasfoorum
2010	Parim ettekanne, 9. rahvusvaheline sümpoosium "Topical Problems in the Field of Electrical and Power Engineering", Pärnu, juuni 2010

2010	Eesti Energia TTÜ Arengufondi Doktoriõppe Stipendium
Juhendatud lõputööd	
2012	Paavo Prii, tehnikateaduse magistritöö elektriajamite ja jõuelektroonika erialal, 2012, (juh) Lauri Kütt, lõputöö teema "Õhksüdamikuga induktiivkomponendid", Tallinna Tehnika-ülikool
2011	Mihhail Mitrofanov, tehnikateaduse magistritöö elektroenergeetika erialal, 2011, (juh) Lauri Kütt, lõputöö teema "Algoritm laineprotsesside meetodil rikkekoha määramiseks jaotusvõrgus", Tallinna Tehnikaülikool
Peamised teadusteemad	
Elektrotehnika alused Elektritoite kvaliteet Elektrimõõtmised Elektromagnetiline ühilduvus	

DISSERTATIONS DEFENDED AT TALLINN UNIVERSITY OF TECHNOLOGY ON *POWER ENGINEERING, ELECTRICAL ENGINEERING, MINING ENGINEERING*

1. **Jaan Tehver**. Boiling on Porous Surface. 1992.

3. **Endel Risthein.** Electricity Supply of Industrial Plants. 1993.

4. **Tõnu Trump**. Some New Aspects of Digital Filtering. 1993.

5. **Vello Sarv.** Synthesis and Design of Power Converters with Reduced Distortions Using Optimal Energy Exchange Control. 1994.

6. **Ivan Klevtsov**. Strained Condition Diagnosis and Fatigue Life Prediction for Metals under Cyclic Temperature Oscillations. 1994.

7. **Ants Meister**. Some Phase-Sensitive and Spectral Methods in Biomedical Engineering. 1994.

8. **Mati Meldorf**. Steady-State Monitoring of Power System. 1995.

9. **Jüri-Rivaldo Pastarus**. Large Cavern Stability in the Maardu Granite Deposit. 1996.

10. **Enn Velmre**. Modeling and Simulation of Bipolar Semiconductor Devices. 1996.

11. **Kalju Meigas**. Coherent Photodetection with a Laser. 1997.

12. **Andres Udal**. Development of Numerical Semiconductor Device Models and Their Application in Device Theory and Design. 1998.

13. **Kuno Janson**. Paralleel- ja järjestikresonantsi parameetrilise vaheldumisega võrgusageduslik resonantsmuundur ja tema rakendamine. 2001.

14. **Jüri Joller**. Research and Development of Energy Saving Traction Drives for Trams. 2001.

15. **Ingo Valgma**. Geographical Information System for Oil Shale Mining – MGIS. 2002.

16. **Raik Jansikene**. Research, Design and Application of Magnetohydrodynamical (MHD) Devices for Automation of Casting Industry. 2003.

17. **Oleg Nikitin**. Optimization of the Room-and-Pillar Mining Technology for Oil-Shale Mines. 2003.

18. **Viktor Bolgov**. Load Current Stabilization and Suppression of Flicker in AC Arc Furnace Power Supply by Series-Connected Saturable Reactor. 2004.

19. **Raine Pajo**. Power System Stability Monitoring – an Approach of Electrical Load Modelling. 2004.

20. **Jelena Shuvalova**. Optimal Approximation of Input-Output Characteristics of Power Units and Plants. 2004.

21. **Nikolai Dorovatovski**. Thermographic Diagnostics of Electrical Equipment of Eesti Energia Ltd. 2004.

22. **Katrin Erg**. Groundwater Sulphate Content Changes in Estonian Underground Oil Shale Mines. 2005.

23. **Argo Rosin**. Control, Supervision and Operation Diagnostics of Light Rail Electric Transport. 2005.

24. **Dmitri Vinnikov**. Research, Design and Implementation of Auxiliary Power Supplies for the Light Rail Vehicles. 2005.

25. **Madis Lehtla**. Microprocessor Control Systems of Light Rail Vehicle Traction Drives. 2006.

26. **Jevgeni Šklovski**. LC Circuit with Parallel and Series Resonance Alternation in Switch-Mode Converters. 2007.

27. **Sten Suuroja**. Comparative Morphological Analysis of the Early Paleozoic Marine Impact Structures Kärdla and Neugrund, Estonia. 2007.

28. **Sergei Sabanov**. Risk Assessment Methods in Estonian Oil Shale Mining Industry. 2008.

29. **Vitali Boiko**. Development and Research of the Traction Asynchronous Multimotor Drive. 2008.

30. **Tauno Tammeoja**. Economic Model of Oil Shale Flows and Cost. 2008.

31. **Jelena Armas**. Quality Criterion of road Lighting Measurement and Exploring. 2008.

32. **Olavi Tammemäe**. Basics for Geotechnical Engineering Explorations Considering Needed Legal Changes. 2008.

33. **Mart Landsberg**. Long-Term Capacity Planning and Feasibility of Nuclear Power in Estonia under Certain Conditions. 2008.

34. **Hardi Torn**. Engineering-Geological Modelling of the Sillamäe Radioactive Tailings Pond Area. 2008.

35. **Aleksander Kilk**. Paljupooluseline püsimagnetitega sünkroongeneraator tuuleagregaatidele. 2008.

36. **Olga Ruban**. Analysis and Development of the PLC Control System with the Distributed I/Os. 2008.

37. **Jako Kilter**. Monitoring of Electrical Distribution Network Operation. 2009.

38. **Ivo Palu**. Impact of Wind Parks on Power System Containing Thermal Power Plants. 2009.

39. **Hannes Agabus**. Large-Scale Integration of Wind Energy into the Power System Considering the Uncertainty Information. 2009.

40. **Kalle Kilk**. Variations of Power Demand and Wind Power Generation and Their Influence to the Operation of Power Systems. 2009.

41. **Indrek Roasto**. Research and Development of Digital Control Systems and Algorithms for High Power, High Voltage Isolated DC/DC Converters. 2009.

42. **Hardi Hõimoja**. Energiatõhususe hindamise ja energiasalvestite arvutuse metoodika linna elektertranspordile. 2009.

43. **Tanel Jalakas**. Research and Development of High-Power High-Voltage DC/DC Converters. 2010.

44. **Helena Lind**. Groundwater Flow Model of the Western Part of the Estonian Oil Shale Deposit. 2010.

45. **Arvi Hamburg**. Analysis of Energy Development Perspectives. 2010.

46. **Mall Orru**. Dependence of Estonian Peat Deposit Properties on Landscape Types and Feeding Conditions. 2010.

47. **Erik Väli**. Best Available Technology for the Environmentally Friendly Mining with Surface Miner. 2011.

48. **Tarmo Tohver**. Utilization of Waste Rock from Oil Shale Mining. 2011.

49. **Mikhail Egorov**. Research and Development of Control Methods for Low-Loss IGBT Inverter-Fed Induction Motor Drives. 2011.

50. **Toomas Vinnal**. Eesti ettevõtete elektritarbimise uurimine ja soovituste väljatöötamine tarbimise optimeerimiseks. 2011.

51. **Veiko Karu**. Potential Usage of Underground Mined Areas in Estonian Oil Shale Deposit. 2012.

52. **Zoja Raud**. Research and Development of an Active Learning Technology for University-Level Education in the Field of Electronics and Power Electronics. 2012.

53. **Andrei Blinov**. Research of Switching Properties and Performance Improvement Methods of High-Voltage IGBT based DC/DC Converters. 2012.

54. **Paul Taklaja**. 110 kV õhuliinide isolatsiooni töökindluse analüüs ja töökindluse tõstmise meetodid. 2012.